ABSTRACT

Title of Dissertation: CHARACTERIZATION, MODELING, AND
                                OPTIMIZATION OF POLYMER COMPOSITE
                                PIN FINS

                                Raj Bahadur, Doctor of Philosophy, 2005

Directed By: Professor, Avram Bar-Cohen, Mechanical
                                Engineering

  Increasing electronic product manufacturing volumes and cooling requirements

necessitate the use of new materials and innovative techniques to meet the thermal

management challenges and to contribute towards sustainable development in the

electronic industry. Thermally conductive polymer composites, using high thermal

conductivity fillers such as carbon fibers, are becoming commercially available and

provide favorable attributes for electronic heat sinks, such as low density and

fabrication energy requirements. These polymer composites are inherently anisotropic

but can be designed to provide high thermal conductivity values in particular

directions to address application-specific thermal requirements.

  This Thesis presents a systematic approach to the characterization, analysis, design,

and optimization of orthotropic polymer composite fins used in electronic heat sinks.

Morphological characterization and thermal conductivity measurements of thermally

conductive Poly-Phenylene Sulphide composites are used to determine the significant

directional thermal conductivity in such composites. An axisymmetric orthotropic thermal conductivity pin fin equation is derived to study the orthotropic thermal conductivity effects on pin fin heat transfer rate and temperature distribution. FEM simulation and water cooled experiments, focusing on the radial temperature variations in single pin fins, are used to validate the analytical model. Theoretical models, CFD modeling, and experiments are used to characterize the thermal performance of heat sinks, fabricated of PPS composite pin fins, in air natural convection and forced convection modes. Simplified solutions, for the orthotropic fin heat transfer rate that are easy to use and can be easily implemented in a heat sink design and optimization scheme, are presented.

CHARACTERIZATION, MODELING, AND OPTIMIZATION OF POLYMER

COMPOSITE PIN FINS

By

Raj Bahadur

Dissertation submitted to the Faculty of the Graduate School of the
University of Maryland, College Park, in partial fulfillment
of the requirements for the degree of
Doctor of Philosophy
2005

Advisory Committee:
Professor Avram Bar-Cohen, Chair
Professor Reinhard Radermacher
Professor Peter Kofinas
Professor Hugh Bruck
Professor Bao Yang

Dedication

To my ever loving family for giving me everything

Acknowledgements

Table of Contents

List of Tables

List of Figures

Nomenclature

A	Heat sink area	m^2
Bi	Biot number	hR/k
c_p	specific heat of air	[W/kg-K]
COP	coefficient of performance	[W/W]
d	diameter of pin-fin	[m]
E	fabrication energy	[J]
f	Darcy friction factor	Eq. (6.12)
g	gravitational acceleration	9.81 m/s^2
h	heat transfer coefficient	[W/m^2-K]
G	detector amplifier gain	
H	height of the pin-fin	[m]
IP	input power	[W]
J	Bessel function	
k	thermal conductivity	[W/m-K]
k*	fin conductivity ratio	k_r/k_z
L	length of the array	[m]
m	mass	[kg]
m_{fin}	fin parameter	$(2h/kR)^{1/2}$ [m^{-1}]
M	mass of heat sink	[kg]
n	number	
N	pin fin density	[fins/cm^2]
N'	plate fin density	[fins/cm]
NA	not applicable/available	
Nu	Nusselt number	
P	pressure	[N/m^2]
Pr	Prandtl number [$\mu c_p/k_f$]	
q	cooling rate	[W]
q*	heat flow parameter	$q/k\theta_b R$
Q	heat	[J]
r, z	polar coordinates	[m]
R	pin fin radius	[m]
Re	Reynolds' number	
R_{hs}	heat sink thermal resistance	[K/W]
Ra_{Sh}	$g\beta Pr_b\theta_b S_h^4/Lv^2$, Raleigh's no. based on S_h	
Ra_L	$g\beta Pr_b\theta_b L^3/v^2$, Raleigh's no. based on L	
s	air gap between adjacent fins	[m]
S	center to center spacing	[m]
Sh	horizontal pin fin center to center spacing	[m]
Sv	vertical pin fin center to center spacing	[m]
t	time	[s]
t_p	plate thickness	[m]

T	temperature	[K]
V	volume	[m^3]
V$_{air}$	volumetric air flow rate	[m^3/s]
Vo	voltage	[Volts]
W	width of the array	[m]
W$_T$	total fabrication energy	[J]

Greek Symbols

α	thermal diffusivity	[m^2/s]
β	thermal coefficient of expansion	[K^{-1}]
γ	aspect ratio	
Δ	rise above ambient, difference	
δ	standard deviation	
η	fin efficiency	
θ	excess temperature	[K]
λ	eigenvalues	Eq. (7.8)
μ	mean dynamic viscosity of fluid	[kg/μm-s]
ν	mean kinematic viscosity of fluid	[m^2/s]
ρ	mean fluid density	[kg/m^3]
τ	sample thickness	[m]
σ	standard deviation	
Φ	volume fraction	[Eq. (3.6)]
Ψ	fraction factor	[Eq. (3.12)]

Subscripts and superscripts

a	array
amb	ambient
air	air
avg	average
b	fin array base
bi	bias error
d	pin fin diameter
f	fluid
fin	fin
gm	geometric mean, $(k_r k_z)^{1/2}$
h	horizontal
hm	harmonic mean $(2k_r k_z)/(k_r + k_z)$
lm	least material
m	mass
opt	optimum
p	pin-fin
pr	precision error
r	radial
sc	space claim

T	total
v	vertical
z	axial
'	correction
0	zero order
1	1st order

Chapter 1: Polymer Composites in Electronics Cooling

1.1 Introduction

Increasing electronic product manufacturing volumes and cooling requirements necessitate the use of new materials and innovative techniques to meet the thermal management challenges and to contribute towards sustainable development in the electronic industry. Thermally conductive polymer composites, using high thermal conductivity fillers such as carbon fibers, are becoming commercially available and provide favorable attributes for electronic heat sinks, such as low density and fabrication energy requirements. These polymer composites are inherently anisotropic but can be designed to provide high thermal conductivity values in particular directions to address application-specific thermal requirements.

There are many technical challenges associated with polymer composites, apart from fabrication and synthesis, such as managing thermal anisotropy and optimizing the filler volume. Polymer matrix composites provide thermal conductivity as high as 300 W/m-K in the direction of carbon fibers, but up to two orders of magnitude lower thermal conductivity is obtained perpendicular to the fiber direction (Table 1.1). Since the fillers such as carbon fiber are dense and require energy intensive fabrication processes, lesser is the filler volume used, lower is the fabrication energy and lighter is the polymer composite. These polymer composites can be tailor-made to have desired thermal conductivity values in specific directions based on thermal requirements [6]. This can be achieved by controlling the filler orientation and volume fraction during processing.

In this research orthotropic thermal conductivity pin fin design and optimization is studied with a focus on a thermally conductive polyphenylene sulphide composite using short discontinuous pitch-based carbon fibers. A two dimensional axisymmetric orthotropic thermal conductivity pin fin equation is derived to study the orthotropic thermal conductivity effects on the polymer composite pin fin heat transfer rate and temperature distribution. FEM simulation, as well as experimental measurements, is used to validate the analytical model. An orthotropic least material pin fin equation is derived to calculate the radius of the fin that maximizes heat transfer per unit volume over a range of parameters such as the external heat transfer coefficient and conductivity ratio. Theoretical models, numerical modeling, and experiments are used to characterize the thermal performance of a PPS pin fin heat sink in air cooled natural convection and forced convection modes. Natural convection water cooled experiments are conducted to verify the orthotropic thermal conductivity effects on PPS composite pin fin heat transfer rate and temperature distribution.

To compare the air cooled thermal performance of polyphenylene sulphide-carbon fiber composite heat sinks with aluminum and copper heat sinks, use is made of metrics such as Coefficient of Performance (COP) and the Total Coefficient of Performance, (COP_T) which includes the fabrication energy invested in the heat sink,
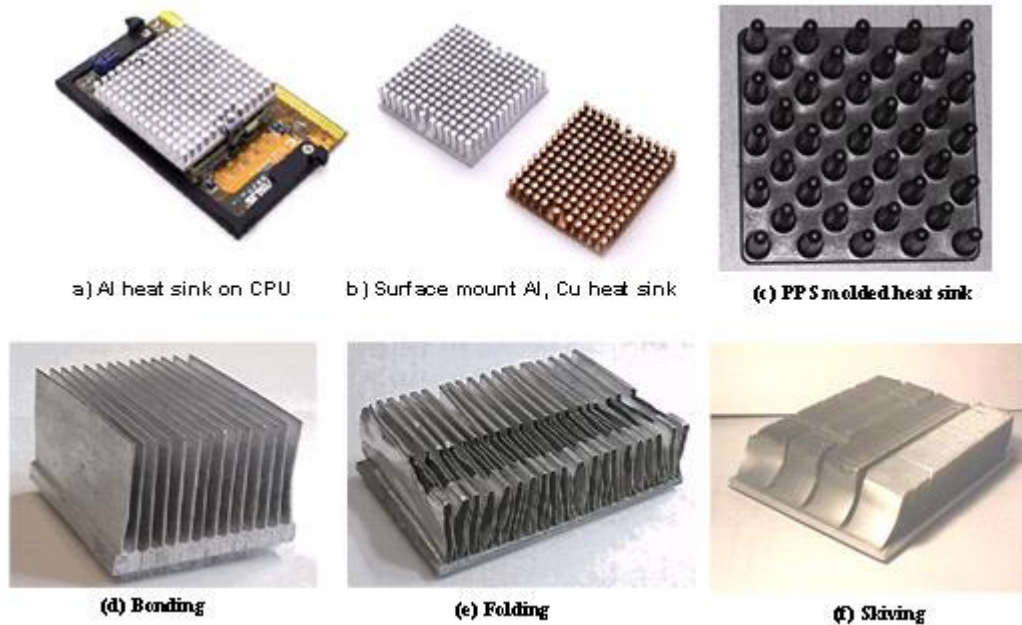
Figure 1.1 Heat sink forms

This chapter first, briefly describes the present cooling requirements in the electronics industry and resulting energy consumption rates, and the newly available thermally conductive polymer composites which provides an opportunity for significant mass and fabrication energy savings. The motivations and need for research are then discussed, followed by a brief outline of thesis objectives, scope, and overview.

1.2 Thermal Management of Electronics

The explosion in information technology during the past two decades led to as many as 600 million computers [1] being in use worldwide in the year 2001, with personal computers (PC) constituting approximately 50% of the total. Personal computer worldwide sales have reached some 140 million in 2002 and in excess of

152 million in 2003 [2], suggesting that approximately 450 million high-end PC's might have been in use in 2003. The substantial material stream, energy consumption, and entropy generation rate associated with the cooling of these desktop computers, as well as other categories of computers and electronic equipment threatens to dramatically increase the depletion rate of key resources and lends urgency to the efficient design of heat sinks (Fig. 1.1) commonly used to provide thermal management for such electronic systems.

Fabrication energy involves the amount of energy invested to process the material in its usable form from its natural state. From the data available in the literature and media, as well as on corporate and governmental websites, 230-310 MJ/kg [3] and 100-180 MJ/kg [4] are required to form, assemble, and transport aluminum and copper heat sinks, respectively, dropping to 200 MJ/kg for aluminum and 71 MJ/kg for copper, after taking reusability (recyclability) into account [5].

The "creation" of a single 125g aluminum heat sink – with formation/fabrication energy of 200 MJ/kg (56kW-h/kg) – would require 25.2 MJ (7 kW-hr) and the energy required to form/fabricate the approximately 150 million heat sinks sold in 2003 (consuming some 19 million kg of aluminum) would have required nearly 3.96×10^6 MJ (1.1 Terra W-hours). Considering the operational requirements of 450 million PC's, at approximately 3.96×10^6 MJ (1.35 Terawatt-hours) and the need to form and fabricate approximately 150 million heat sinks at an energy "cost" of 3.96×10^6 MJ (1.1 Terawatts-hours), leads to a total energy investment in PC cooling of some 8.8×10^9 MJ (2.45 Terra watts-hours) in 2003. This work investment is approximately

equal to the entire annual output of a 500MW power plant operating at 56% of capacity throughout the year (8.8×10^9 MJ).

1.3 Enhanced Thermal Conductivity Polymeric Materials

Recent advances in polymer composites, using carbon fibers [6] and graphite fillers, [7] to increase the thermal conductivity, have made such materials viable alternatives to conventional metals in the design and fabrication of heat sinks and heat exchangers, as shown in Table 1.1. Ongoing research into the use of carbon nano tubes (CNT's), [8], [9] may yield further improvements in such polymer composites. In addition to the manufacturing advantages offered by such moldable, high thermal conductivity composites, their relatively low density can provide a significant weight reduction and require less energy for formation and fabrication than copper and aluminum – yielding an important contribution to sustainability. Polyphenylene sulphide (PPS) matrix composites, filled with short discontinuous pitch based carbon fibers, offer enhanced thermal conductivity (20 W/m-K) and are attracting growing attention for use in heat sinks and thermal spreaders [10]. Such PPS heat sinks with an 80% mass fraction of carbon fiber typically require approximately 115 MJ/kg (32 kW-hr, Appendix G), without considering recyclability but assuming that the energy requirement of the 80% mass fraction of the carbon fibers will reach 100 MJ/Kg (28 kW-hr).

1.4 Motivation and Background

Reducing fabrication energy requirements, along with reduced mass and greater flexibility in manufacturing and assembly, is the major motivation for considering

5

polymer composite pin fins over conventional metals. For a typical polymer matrix filled with discontinuous carbon fibers, metal-like thermal conductivity values 10-300 W/m-K in the fiber direction are achievable as shown in Table 1.1. The thermal conductivity value perpendicular to carbon fiber axis direction ranges from 3-10 W/m-K, lower but still far superior to the 0.4W/mK typical of the polymer itself. Since the thermal performance in air cooled heat sinks is limited mostly by the external convective thermal resistance, it may well be possible to achieve comparable thermal performance to copper and aluminum heat sinks in air cooling using optimized thermally conductive polymer composite fins.

Table 1.1 Polymer composite properties

Reinforcement	Matrix	Along fiber axis thermal conductivity (k_z, W/m-K)	Perpendicular to carbon fiber axis thermal conductivity (k_r, W/m-K)	CTE (α, 10^{-6}/K)	Density (ρ, kg/m^3)
Milled glass fiber [6]	Polymer	0.2-2.6	0.2-2.6	20-40	1400-1600
Continous carbon fiber [6]	Polymer	330	3-10	-1	1800
Discontinous carbon fiber [6]	Polymer	10-100	3-10	4-7	1700
Graphite [7]	Epoxy	370	6.5	-0.8-53	1940
Single Walled Nano Tubes [8]	Epoxy	0.5	NA	NA	NA

The PPS composite density is 1700 kg/m^3 [10] compared to aluminum 2700 kg/m^3 and copper 8900 kg/m^3. Therefore, for an available or specified heat sink volume, a PPS composite heat sink would weigh only 60% of an aluminum heat sink and only

19% of a copper heat sink. The CTE of the PPS composite is reported to be 6-10 ppm/K [10] (Al~20ppm/K) that is better matched to the silicon CTE of 2.5 ppm/K. For a heat sink attached directly to a silicon chip, this increases the reliability of the overall package by reducing the loading and stresses on the package/heat sink interface. Furthermore polymers are noncorrosive and can be used in harsh environments such as automobile under-the-hood electronics. Finally, significantly smaller enhanced PPS volumetric energy requirements, of 195,500 MJ/m^3 [11], only 37% of that of aluminum and 31% of that required using copper, may lead to significant energy savings.

1.5 Need for Research

The PPS (polyphenylene sulphide) in itself has a very small thermal conductivity value approximately 0.4 W/m-K and one or two order higher CTE (10^{-4} ppm/K) than silicon, low glass transition temperature resulting in phase change at relatively moderate temperatures (82 ^{o}C). The introduction of carbon fibers in the PPS matrix increases thermal conductivity, reduces the CTE, and increases the glass transition temperature. However, carbon fiber has a high energy content and density. Therefore, increasing the carbon fiber content, to improve the thermal conductivity, increases the energy content and the mass of the polymer matrix composite. Clearly, application-driven optimal carbon fiber content is necessary in order to achieve a light weight, energy efficient heat sink.

The introduction of carbon fiber increases thermal conductivity significantly in the fiber axis direction. Perpendicular to the fiber axis there is a relatively lower thermal conductivity value. Therefore, while increasing the axial thermal conductivity the

introduction of fiber increases thermal anisotropy in polymer matrix. Careful thermal design is necessary in order to manage the effects of the low thermal conductivity in the orthogonal direction. For instance fiber alignment in the heat sink base needs to parallel to the base in order to increase the "in plane" thermal conductivity for enhanced heat spreading. Alternatively, in the heat sink fins, carbon fiber alignment along the fin axis is most beneficial, because it enhances conduction of heat away from the base, thereby increasing heat transfer rates.

The reported enhanced PPS composite heat sink thermal conductivity is approximately 20 W/m-K [10], one order of magnitude smaller than traditional aluminum and copper heat sinks. Thermal performance characterization and design optimization is necessary to find suitable thermal applications for these new enhanced PPS composite heat sinks. Thermal anisotropy effects also need to be quantified in natural and forced convection modes of heat transfer.

1.6 Thesis Objectives, Scope and Overview

1.6.1 Thesis Objectives

The polymer composite pin fins may result in energy efficient heat sinks. However, several challenges need to be met before they can be successfully utilized in heat sink design. In order to support achievement of the overall goal there are five primary objectives that needs to be met,

1. Establish the scope and impact of thermal anisotropy in these materials. Study the morphology of thermally conductive polymer composites using

8

test tools such as SEM, and TGA. Quantify the thermal conductivity values using theoretical model predictions and laser flash measurements.

2. Quantify the thermal performance of the high thermal conductivity polymer composite pin fin arrays through analytical, numerical, and experimental techniques.

3. Derive orthotropic thermal conductivity single pin fin equations. Determine the effect of orthotropic thermal conductivity on the thermal performance of single pin fins.

4. Determine the heat transfer rate and aspect ratio of a least material anisotropic pin fin and develop a methodology for orthotropic thermal conductivity based least material pin fin array optimization.

5. Experimentally verify the orthotropic thermal conductivity effects in PPS composite pin fin heat flow rate and temperature distribution.

1.6.2 Scope and Overview of Thesis

This Thesis presents a systematic approach to the characterization, analysis, design, and optimization of orthotropic polymer composite fins used in heat sinks. The thesis is divided into ten chapters, beginning with the introduction, which explores the need for the current research, and subsequently details the thesis objectives and the scope of the study. Chapter 2 describes high thermal conductivity polymer composites and presents the results of a morphological analysis of fiber-filled PPS, using SEM (scanning electron microscope) images and TGA (Thermo gravimetric analysis). Thermal conductivity measurements using the laser flash technique and a theoretical

9

prediction using the Nielsen model is described in Chapter 3 for carbon fiber filled PPS (polyphenylene sulphide) composite. Chapter 4 describes a general design and optimization scheme for air cooled pin finned heat sinks, including the introduction of thermal performance metrics and description of a design optimization methodology. Detailed natural convection pin fin experimental results along with CFD results are presented in Chapter 5. In Chapter 6, air cooled forced convection pin fin CFD results are presented and compared with some of the available experimental results in the literature. The single orthotropic thermal conductivity pin fin heat transfer is covered in Chapter 7, including the detailed derivation of the orthotropic pin fin heat transfer rate and temperature distribution equations. The orthotropic least material pin fin analysis is presented in Chapter 8 that includes simplified orthotropic thermal conductivity pin fin heat transfer rate equations and orthotropic least material equation. A detailed set of single pin fin experiments are reported in Chapter 9 for the verification of orthotropic thermal conductivity effects on the pin fin heat transfer rate. Finally major contribution of the work and recommendations for future effort are presented in Chapter 10.

Chapter 2: Thermally Conductive Polymer Matrix Composites

2.1 Brief Overview of Thermally Conductive Composites

Composites are usually classified by the type of material used for the matrix. The four primary categories of composites for thermal applications are: polymer matrix composites (PMC's), metal matrix composites (MMC's), ceramic matrix composites (CMC's), and carbon matrix composites (CAMC's). The last category, CAMC's, includes carbon-carbon composites (CCC's), which consist of carbon matrices reinforced with carbon fibers. Presently, carbon-fiber-reinforced PMC's, MMC's and possibly CCC's are all important candidate materials for high-volume thermal management applications. It is anticipated that PMC's will be the dominant materials, followed by MMC's. Significant use of CCC's will depend on major manufacturing cost reductions. Table 2.1 illustrates MMC's thermal conductivity value to be much higher and density lower than traditionally used metals such as aluminum (200W/m-K, 2.7g/cc) and copper (400W/m-K, 8.9g/cc). Also there is noticeable amount of anisotropy associated with these composites.

Table 2.1 Thermal conductivity of various composites

Matrix	Filler (wt%)	Parallel to fibers (W/m-K)	Normal to fibers (W/m-K)	Density (g/cc)
Aluminum	Discontinuous carbon fiber	190-230 [6]	120-150 [6]	2.5 [6]
Copper	Discontinuous carbon fiber	300 [6]	200 [6]	6.8 [6]
Carbon	Carbon	36-43 [115]	4-7 [115]	1.4-1.8 [115]
Graphite	Graphite	370 [7]	6-7 [7]	1.9 [7]
Lexan HF 1110-11N	Graphite	11.4 [23]	0.74 [23]	1.5 [23]

The focus of this thesis is primarily on polymer matrix composites because of their lower fabrication energy requirements and relatively lower cost, which makes it possible for thermally conductive polymer composites to replace traditionally, used metals in many thermal applications. The advantages of thermally conductive PMC's relative to metals are described in Table 2.2, and include reduced density and coefficient of thermal expansion, as well as higher glass transition temperature, and corrosion, oxidation, and chemical resistance; along with moldability and customizable properties to fit the application.

Table 2.2 Advantages/disadvantages of polymer matrix composites

Advantages	Disadvantages
Low cost	Anisotropy analysis
Weight reduction	Reuse and disposal is difficult
Moldability	Cost of fibers
Tailorable properties	Low Transverse properties
Corrosion resistance	Matrix subject to environmental degradation
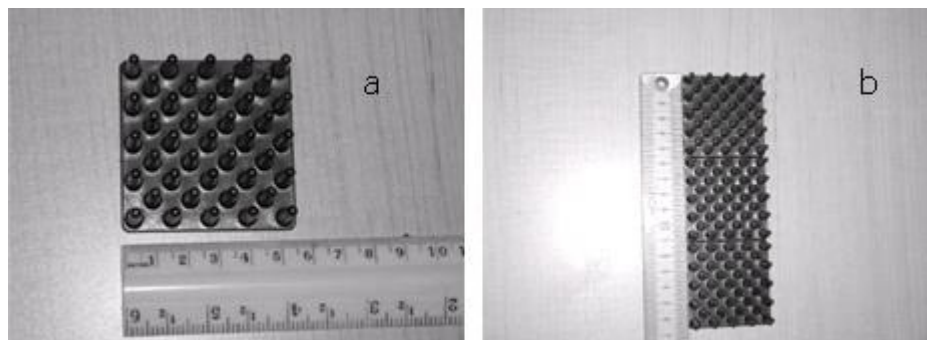
Figure 2.1 PPS composite staggered pin fin array (CoolPolymer, [10])

2.2 High Thermal Conductivity Polymer Matrix Composites

Typical unfilled polymer resin thermal conductivity values are in the range of 0.1~0.3 W/m-K, depending on the carbon-carbon bonds and the amount of cross linking. Many studies have investigated the addition of fillers to increase the thermal conductivity of polymer-based composites [12-23].

As a result polymer matrix composites with high thermal conductivity values up to 100 W/m-K are commercially available as shown in Table 2.3. Successful commercial applications of injection moldable thermally conductive polymer compounds include heat exchangers, heat sinks, and sensors/switches, bases/frames, ceramic replacement, encapsulation, hard disk drive coils [10].

Table 2.3 Thermal conductivity of various materials [6]

Materials	Thermal conductivity (W/m-K)	Density (g/cc)
Polymers	0.19-0.3	1.1-1.4
PAN based carbon fibers	8-70	1.8
Pitch based carbon fibers	20-1000	2.1-2.2
Stainless steel	11-24	7.9
Aluminum	200	2.7
Copper	385	8.9
Diamond	2600	3.5
Polymer-carbon fiber composites	1-100	1.2-2

High thermal conductivity polymer matrix composites are typically obtained by filling polymer resin with high thermal conductivity carbon fibers. Carbon fibers with a wide range of thermal conductivity values are commercially available. In general the thermal conductivity of the composite depends on the thermal conductivity of the

base resin and fiber, and the fiber aspect ratio, length, and volume fraction. Generally, the higher the volume percentage of the fibers in the matrix, the higher is the thermal conductivity of the composite. The fiber aspect ratio depends on the fiber manufacturing processes and short to continuous fibers can be obtained. Continuous fibers are costlier than short carbon fibers because of the tighter and complex processes required for obtaining longer fibers. The fiber orientation is strictly molding process dependant. Use of continuous fibers also results in composites that are more anisotropic than obtained with discontinuous fibers.

2.2.1 Polymer Resin

Polymers are extremely long chained molecules that have repeating units [18-19]. The carbon atoms in the long chain are held together by strong carbon-carbon covalent bonds. Among various neighboring chains only weak Van der Wall interactions exist. Still many polymers are solids due to entanglements and cross linking of the long molecules. To have stable entanglements that restrict the flow of the polymer, chain polymers must have a critical molecular weight that is dependent on the flexibility of the backbone and the steric hindrance within the molecule.

The importance of the entanglements on the cohesion can be explained in an illustration. If an assortment of different length strings are mixed into a ball the short pieces of string could be easily removed. The intermediate length pieces of string could be removed only with some effort but it would take a substantial amount of effort to remove the longest strings. These entanglements influence the physical properties of the polymer [18].

Polymers are significantly less crystalline than other crystalline materials, such as metals or low-molecular-weight compounds, and many are amorphous [18]. Figure 2.2a is a representation of how polymer chains arrange in an amorphous (non-crystalline) polymer matrix. A good way to think of the amorphous polymer matrix is as a plate of cooked spaghetti. Some characteristics of amorphous polymers are that they have good mechanical properties and good dimensional stability. Amorphous polymers also shrink consistently during cooling [19].

(a)   (b)
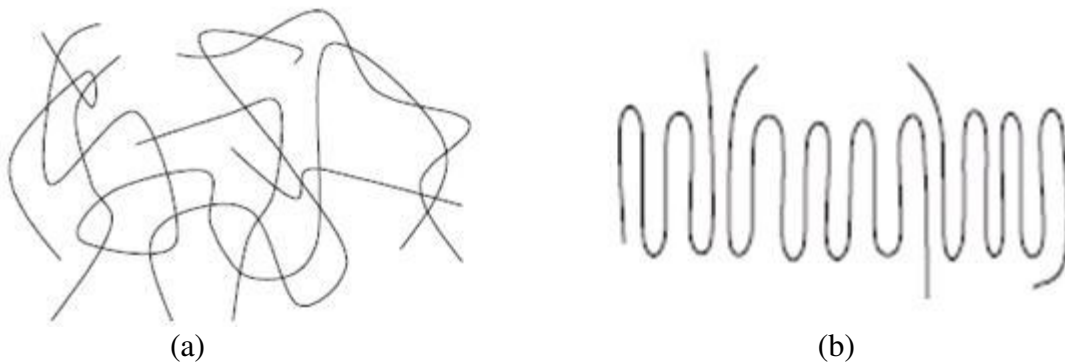
Figure 2.2 Representation of polymer chains in an (a) amorphous (b) semi crystalline polymer [20, 21]

Semi-crystalline polymers generally orient themselves in a lamellae structure [18], as seen in Fig. 2.2 b. The gills of a fish or a mushroom are examples of lamellar structures. For a polymer to crystallize, the conditions during the cooling of a polymer melt have to allow the polymer chains to arrange themselves. The crystal sheets may be as thin as 100 to 200Å; between these crystalline sheets, there are amorphous regions [18]. It was found that as the lamellar structure's thickness increased, the thermal conductivity of polyethylene increased [13].

Semi-crystalline polymers have anisotropic shrinkage, very good electrical properties, and are chemically resistance to some harsh environments [19]. Thermal conductivity has been experimentally shown to increase with increasing crystallinity or orientation of the polymer chains [13, 20, and 22]. This can be extrapolated to suggest that an amorphous polymer will be less conductive than semi-crystalline polymers. It was also experimentally shown that filled amorphous polymers are less thermally conductive then filled semi-crystalline polymers [21]. The carbon fiber filled nylon based composites are more conductive than the Polycarbonate-based samples, as can be seen in Figure 2.3 [23]. The nylon is semi-crystalline which conducts heat more effectively than an amorphous polymer like polycarbonate.
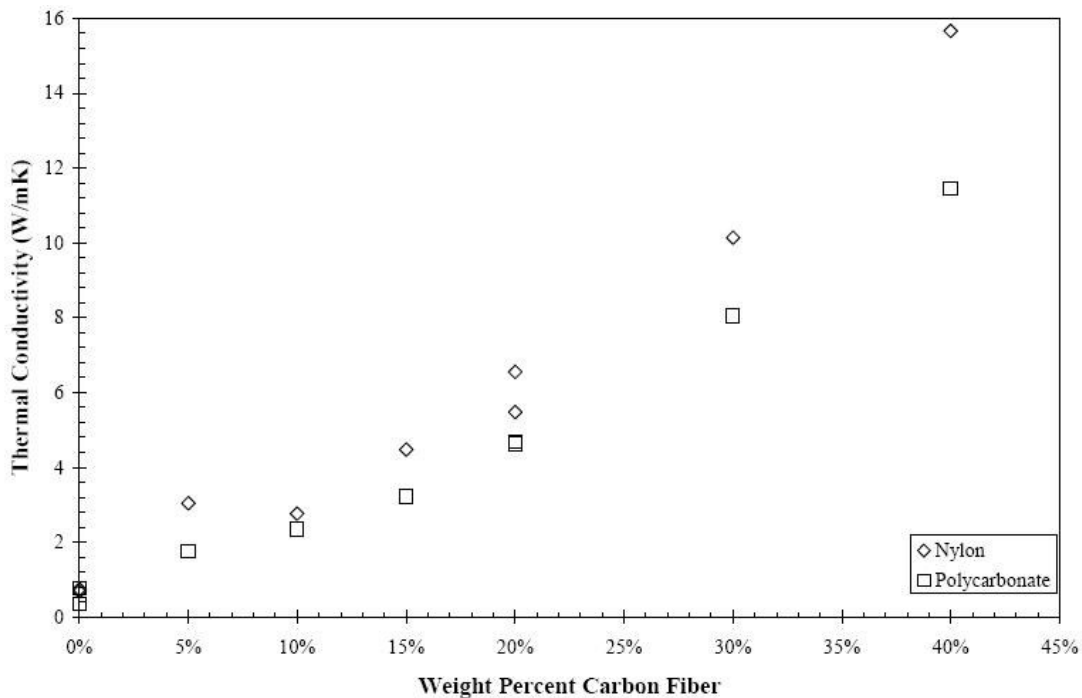
Figure 2.3 Longitudinal thermal conductivity of carbon fiber filled composite [23]

The addition of 40 % by weight carbon fiber has been found to increase the longitudinal thermal conductivity to 15.7 and 11.4 W/m-K for nylon and

polycarbonate, respectively [23], yielding a longitudinal thermal conductivity 16.5 and 15.4 times the value of the transverse thermal conductivity of these resins, respectively. This anisotropy ratio of 16 is most likely due to the alignment of the carbon fibers in the longitudinal direction.

As seen in Table 2.4, Polyphenylene sulphide (PPS, 0.3W/m-K) is one of the commercial polymers, from among those listed in Table 2.4, that is recommended for use in thermal applications including heat exchangers.

Table 2.4 Recommended polymers for heat exchanger applications [106], [107]

Suitable for propylene glycol and water	Suitable for water environment only
PPS: Polyphenylene sulphide PP: Polypropylene PTFE: Polytetrafluoroethylene PEEK: Poly-Ether-Ether-Ketone PLS: PolySulfone FEP: perFluoro Ethylene Propylene HTN: High temperature nylon PPA: PolyPthalAmide PFA: PerFluoro Alkoxy alkane PEX: Cross linked PolyEthylene	PPO: Polyphenylene oxide PVDF: PolyVinyliDine Fluoride

The selection was based on heat distortion temperature, thermal index (maximum service temperature at which the tensile strength of the polymer degrades to 50% of its original value in 50,000 hours), glass transition temperature, and water absorption. PPS is a high temperature semi-crystalline material. It has good mechanical properties and excellent chemical resistance at elevated temperatures. PPS has been compounded extensively and is available with many different properties. In the present thesis PPS thermally conductive composite pin fins have been tested.

Table 2.5 Commercially available thermally enhanced polymer resins [10]

Thermoplastic base resin	Acronym
Polypropylene	PP
Acrylic	PMMA
Polycarbonate	PC
Polypropylene sulfide	PPS
Liquid crystalline polymer	LCP
Polyvinylchloride	PVC
Polyamide	PA
Polyethylene terephthalate	PET
Acrylonitrile butadiene styrene	ABS
Polysulfone	PSU
Acetal	POM
Thermoplastic polyurethane	TPUR
Polyphenylene oxide	PPO
Aromatic polyamide	PPA, PAA, HTN
Polybutylene terephthalate	PBT
Polyethersulfone	PES
Polyetheretherketone	PEEK
Polyetherimide	PEI
Polyamideimide	PAI
Thermoplastic polyimide	TPI
Thermoplastic fluoropolymer	PFA, FEP, ETFE, PVDF

Table 2.6 Selection criteria for polymer resins

Good thermal conductivity No by products formation during curing Low shrinkage during cure High or low strength and flexibility Solvent and chemical resistance Resistance to creep and fatigue Wide range of curative options Adhesion to fibers	Insensitive to ultraviolet light Moisture resistance No toxicity Long shelf life Low cost Adjustable curing rates High strength Biodegradable

2.2.2 Carbon Fibers

Commercial carbon fibers are fabricated by using pitch or polyacrylonitrile (PAN) as the precursor. The processes for both precursors are shown in Fig. 2.4 [24]. Use of an isotropic pitch as the precursor, gives an isotropic carbon fiber, which belongs to the category of general-purpose carbon fibers, whereas anisotropic pitch (such as mesophase pitch) gives high-performance carbon fibers which have the carbon layers preferentially aligned with the fiber axis. While PAN based high strength carbon fiber find applications in structural components, pitch based low cost high modulus; and high thermal conductivity carbon fiber is more desirable for thermal management applications. The use of pitch-based carbon fibers is increasing, due to the lower cost and higher carbon content of pitch compared to PAN.
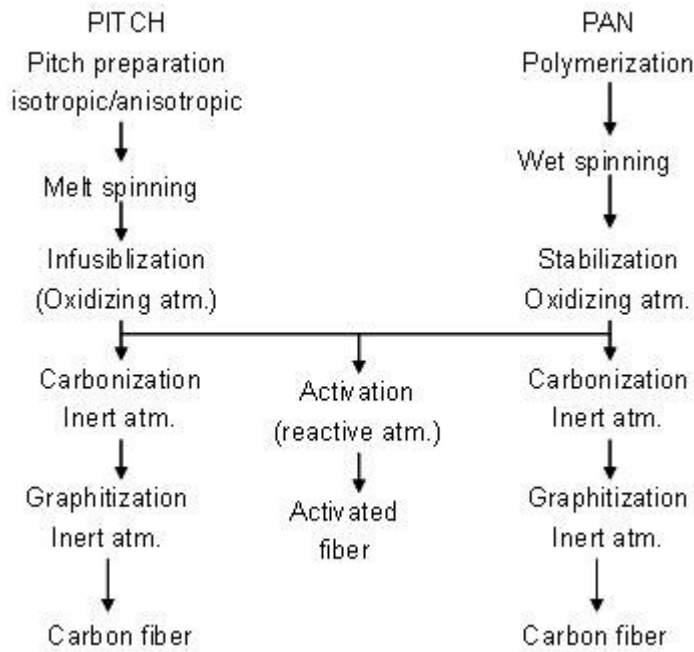
Figure 2.4 Process steps for making carbon fibers from pitch and PAN precursors [116]
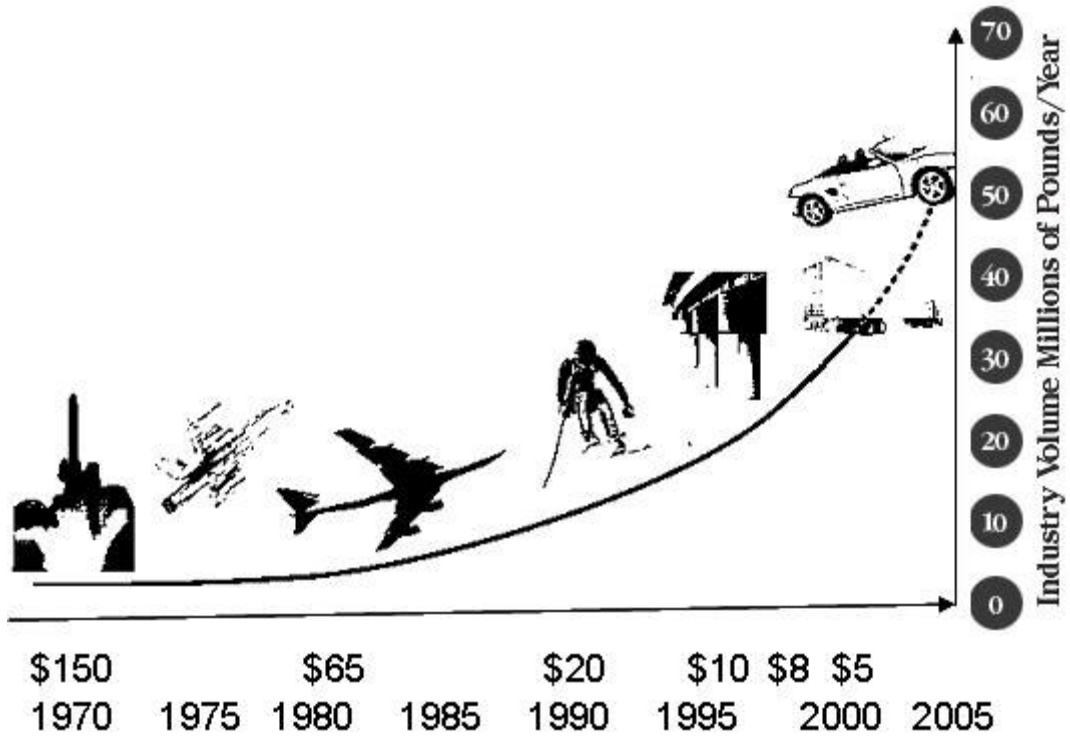
Figure 2.5 Carbon fiber volume consumption and prices [25]

The price of carbon fibers has been decreasing, while the consumption has been increasing, as shown in Figure 2.5 [25]. The decreasing price is broadening the applications of carbon fibers from military to civilian applications, from aerospace to automobile applications, and from biomedical devices to concrete structures.

Table 2.7 Thermal properties of pitch based carbon fiber [6]

Material	Longitudinal thermal conductivity	CTE	Density	Conductivity /density
Al -6063	218	23	2.7	81
Copper	400	17	8.9	45
P-100	520	-1.6	2.2	236
P-120	640	-1.6	2.1	305
K1100X	1100	-1.6	2.2	500
K1100X/Al (55% vol)	634	0.5	2.5	236
K1100X/epoxy (60%)	627	-1.4	1.8	344
K1100X/Cu (46% vol)	709	1.1	5.9	117
K1100X/C (53% vol)	696	-1.0	1.8	387

The longitudinal thermal conductivity, thermal expansion coefficient, density, and specific thermal conductivity (conductivity/density) of Amoco's Thornel mesophase high modulus pitch-based carbon fibers are shown in Table 2.7. The thermal conductivities of Amoco's P-100, P-120, and K1100X carbon fibers are all higher than that of copper and aluminum, while the thermal expansion coefficients and densities are much lower than those of copper. Thus, the thermal conductivity to density ratio is exceptionally high for these carbon fibers as shown in Table 2.7. Therefore, it is expected that use of these high thermal conductivity carbon fibers as fillers in polymer resins will lead to high thermal conductivity and low CTE polymer matrix composites.

2.2.3 Polymer Composite Fabrication Processes

Short carbon fiber composites are usually fabricated by mixing the fibers with a liquid resin to form slurry then molding to form a composite. The liquid resin is the polymer or the polymer dissolved in a solvent in the case of a thermoplast. The molding methods are those conventionally used for the neat polymers. For thermoplasts, the methods include injection molding (heating above the melting temperature of the thermoplast and forcing the slurry into a closed die by a plunger or a screw mechanism), extrusion (forcing the slurry through a die opening by using a screw mechanism), calendering (pouring the slurry into a set of rollers with a small opening between adjacent rollers to form a thin sheet), and thermoforming (heating above the softening temperature of the thermoplast and forming over a die (using matching dies, a vacuum, or air pressure), or without a die (using movable rollers)).

2.2.4: Morphological Characterization of PPS Composite Samples

2.2.4.1 Objective

  The objectives of the thermal characterization of the thermally conductive polyphenylene sulphide (PPS) composite samples were the determination of the fiber shape, size, orientation, fiber volume fraction, and thermal conductivity. It is essential to establish the fiber – resin relationship in the thermally conductive polymer composite in order to be able to quantify the effect of fiber aspect ratio, fiber orientation, fiber conductivity and volume fraction on the thermal conductivity of the polymer composite.

2.2.4.2 E-SEM Device Description

  High-vacuum conditions are required in the electron column of the environmental scanning electron microscope (E-SEM), because gas molecules can scatter electrons and degrade the beam (Figure 2.6). However, instead of using the single pressure-limiting aperture typical in conventional SEM, the E-SEM uses multiple pressure-limiting apertures (PLAs) to separate the sample chamber from the column, as shown in Figure 2.7. This allows the column to maintain high vacuum, while the chamber may sustain pressures as high as 50 Torr. E-SEM uses a proprietary secondary electron detector that can function in a nonvacuum environment, rather than the Everhart-Thornley detector used in SEM.

Figure 2.6 Picture of the E-SEM test apparatus
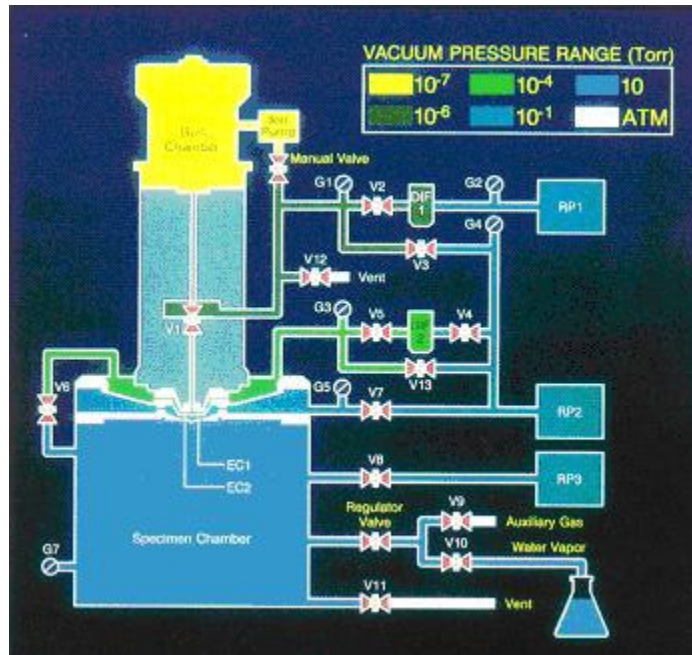
Figure 2.7 ESEM vacuum system consisting five stages of increasing vacuum

2.2.4.3 SEM Image Analysis of PPS Samples

a) Fiber Length (4.5 W/m-K)

b) Fiber Diameter (4.5 W/m-K)

c) Short Fibers (10 W/m-K)

d) Short Fibers (20 W/m-K)

e) PPS matrix (2.1 W/m-K)

f) PPS matrix (2.1 W/m-K)
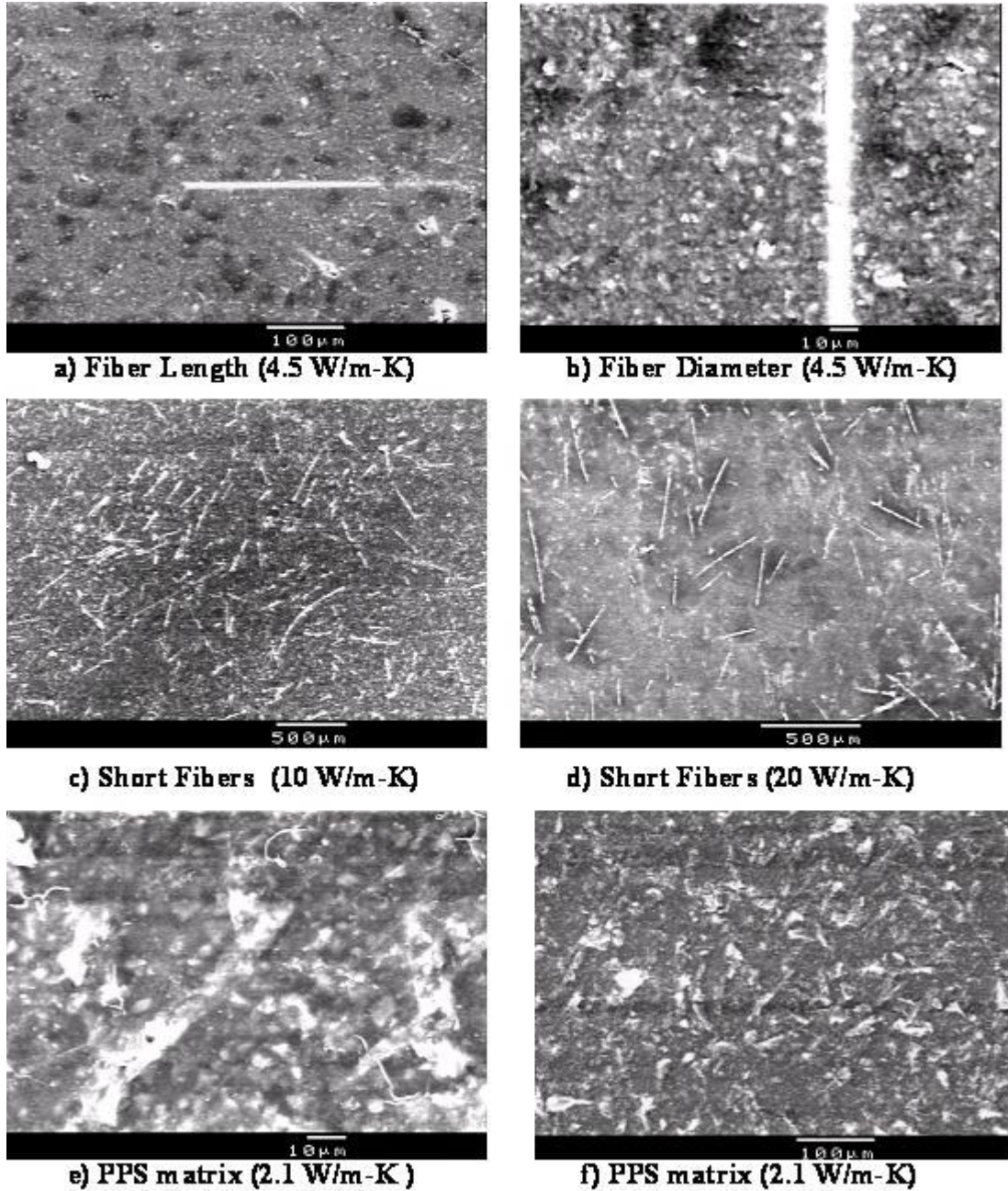
Figure 2.8 SEM images of various conductivity PPS samples

In Fig. 2.8 SEM images of thermally conductive PPS composite samples are shown. The shiny white portion in Figure 2.8 a)-f) is the carbon fiber and the darker portion

is the PPS matrix. In fig 2.8 a, the discontinuous single carbon fiber length is about 300μm and in b) the carbon fiber diameter is about 10 μm. Identical fibers are seen in Fig. 2.8 c) for a 10 W/m-K PPS carbon fiber filled sample. Use of this same fiber in other PPS composites have led to claimed thermal conductivity value of 1.5, 2.1, 4.5, 10 and 20 W/m-K [10]. More SEM images for various PPS composites are shown in Appendix B.

2.2.4.4 Processed SEM Images

a) PPS (k=20) Matrix b) PPS (k=20) Matrix

c) PPS (k=10) Matrix d) PPS (k=10) Matrix
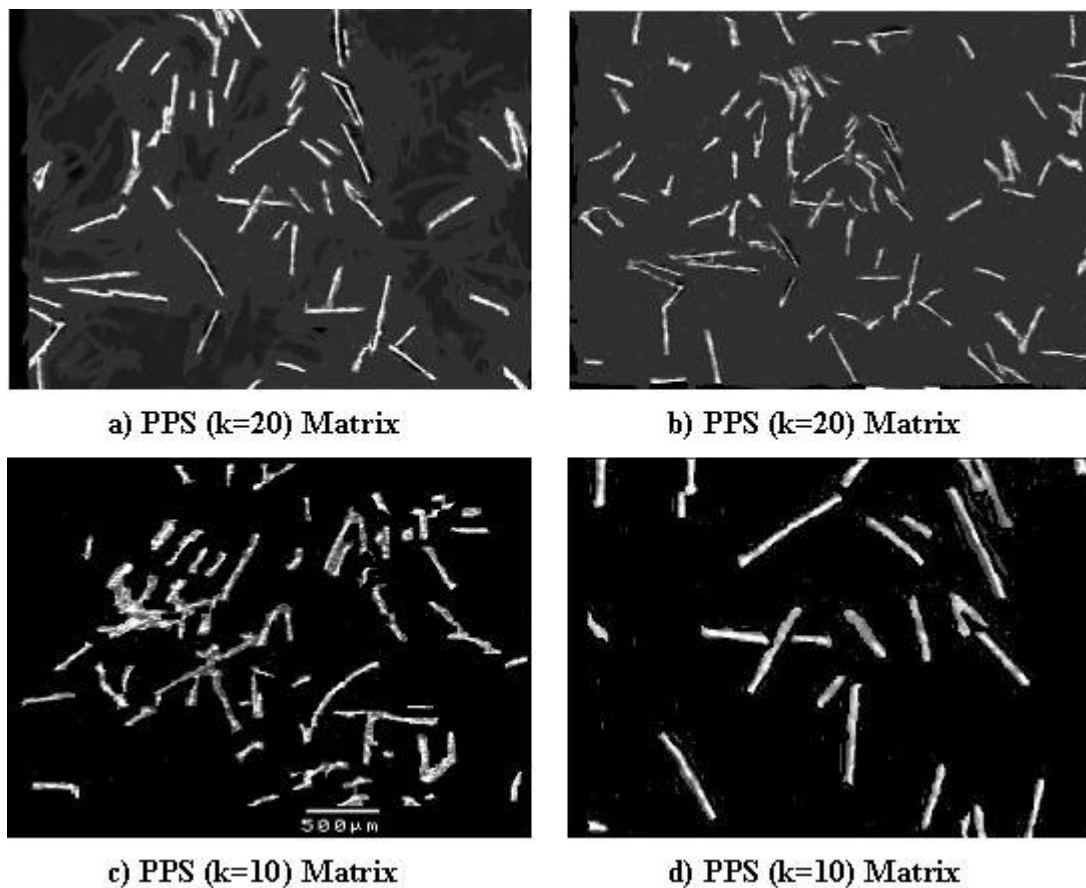
Figure 2.9 Processed SEM images of various conductivity PPS samples

25

In order to show the carbon fiber orientation and size more clearly the raw SEM TIFF images are processed with the Paint Shop software to make the resin matrix darker and highlight the carbon fibers in the matrix. Clearly, from Figs. 2.9 a)-d) the carbon fiber orientation is random in the PPS matrix and short discontinuous carbon fibers are used. The single carbon fiber diameter is of the order of 10 µm and fiber length is of the order of 200 µm, leading to a carbon fiber aspect ratio of about 20, but somewhat variable. The diameter appears to be more consistent, with an approximate value of ~10 um.

These SEM images depict somewhat random orientation of carbon fiber in the PPS matrix. The thermo gravimetric (TGA) analysis, described in the next section, is used to estimate the volume fraction of carbon fibers in the PPS matrix.

2.3 Thermo Gravimetric Analysis for Volumetric Percentage of Carbon Fibers

Thermogravimetry (TG) is used to measure the mass or change in mass of a sample as a function of temperature or time or both. Change of mass occurs due to vaporization of polymer resin.

2.3.1 Principle of Operation

The deflection of a beam carrying the specimen is held constant by means of an electromagnetic force feed back system. This compensation signal is used to determine the mass of the specimen via the force needed to maintain the beam in a horizontal position.

2.3.2 Equipment Construction

TG 2121 is used to do the TGA analysis that can withstand temperatures as high as 1100 ^{o}C [26]. The maximum sensitivity is one tenth of a microgram. The furnace follows precisely the user-created temperature profile of ramps and isotherms at the sample. A 'Type K' thermocouple, located under the sample, measures the temperature. Purge and furnace air gases are controlled by a user-defined method. The software interface allows for time, weight, and temperature data acquisition at different predefined time intervals. The recording balance has a closed loop servo network which automatically compensates for weight changes in the sample. The electrical current necessary to return the balance beam to its null position is directly proportional to weight. The sample always remains in the uniform temperature zone with the weight displayed on monitor screen and on the status and control panel. A cooling fan is used to remove the heat generated by the furnace right below the balance. The fan along with the thermal shield under the balance reduces the thermal drift in microbalance readings. The fan is continuously running during operation of the equipment. There are two gas ports to attach gas lines. A purge gas is available for purging the balance. A furnace air port allows for air flow through the furnace coils.

2.3.3 Specimen Preparation

The powdered PPS composite sample was obtained by machining PPS samples. High melting temperature quartz "round bucket" of 4.2 cm^3, that can hold up to 2.5 gm of sample weight, is used for holding the sample. Purge gas: N_2 at 20 ml/min is used to create an inert atmosphere for decomposition of the plastic.

Heating program A: First a dynamic heating cycle from 30 $^{\circ}$C to 600°C at ramp rate of 10°C/min is carried out. This is followed by an isothermal step at 600 $^{\circ}$C for a 10 min hold time. Finally, a dynamic cycle is carried out from 600 - 800°C at ramp rate of 10°C/min. The sampling period was kept fixed at 3 secs.

Evaluation: Decomposition temperatures and times, and changes of TG signal and mass.

Temperature calibration: A well calibrated 'K' type thermocouple is used to measure the temperature of the sample accurately.

Mass calibration: Equal weight of the test sample is placed at the balance weight side and the balance is tare to zero before each run.

2.3.4 TGA Single Step Analysis

The characteristic temperatures involved in a single step loss of mass are determined in accordance with ISO 11358 [26]. From the TG curve, the points A, B, and C, obtained by means of tangents, and the corresponding temperatures T_a (starting), T_b (end), and T_c (midpoint) are determined. In a mass time plot, the times t_a, t_b, and t_c are evaluated.

The percentage loss of mass M_l is calculated from the masses m_s (at the start, before heating) and m_f (at the end temperature T_b) using the following equation:

$$M_L = (\frac{m_s - m_f}{m_s})x100 \qquad\qquad (2.1)$$

A, starting point: Intersection of extrapolated starting mass with the tangent applied to the maximum slope of the TG curve

B, End point: Intersection of extrapolated end mass after reaction with the tangent applied to the maximum slope of the TG curve

C, Midpoint: Intersection of the TG curve with the line to the abscissa that is midway between A and B.
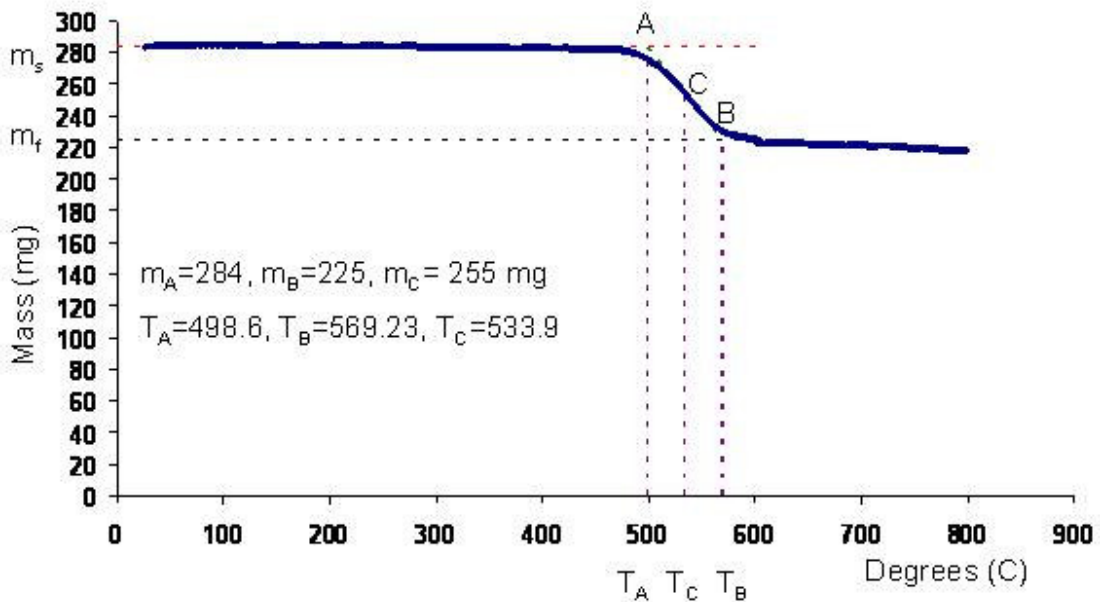
Figure 2.10 TGA run for PPS composite (RB020, CoolPolymer [10]) sample

T_A Temperature at the start time, T_B Temperature at the end, T_C Temperature at the midpoint, m_s starting mass, m_f End mass.

The resulting TGA plot for a starting PPS composite sample weight of 284 mg is shown in Fig. 2.10. As the temperature increases in the range 400 ^{o}C to 600 ^{o}C, the

polymer pyrolyzes. There is continuous decrease in the mass as the sample traverses this temperature range. The carbon fibers remain stable in such conditions. At 600 ^{o}C the heating phase is interrupted; it is followed by an isothermal holding cycle for 10 min during which pyrolysis goes to completion. All the polymer resin evaporates at that temperature.

The percentage change in mass for the entire cycle was 20.8%, as shown in Fig. 2.10, indicating the polymer content of the polymer composite. The rest of the material, or 79.2% of the mass, is assumed to be the carbon fiber fraction in the tested PPS composite sample. Three different runs results are tabulated in Table 2.8 below. The tabulated results indicate an average carbon fiber value of 78.2% and PPS resin value of 21.8% with a standard deviation of 1.2% in the tabulated results. The claimed thermal conductivity for the tested material is 20 W/m-K [10].

Table 2.8 TGA results for PPS composite (RB020) samples using cycle A

Run	Temperature cycle	Initial mass (mg)	Final mass (mg)	% Fiber	% PPS resin
1	A	283.99	225	79.2	20.8
2	A	285.85	221	77.3	22.7
3	A	289.81	226	78	22

In order to further verify the presented results a different thermal cycle was used for a second sample of the previously tested CoolPoly RB020 PPS composite. Also,

another material E5101 PPS composite sample was tested. Similar procedure and calibration was used.

Heating program B: Dynamic heating cycle from 30 ^{o}C to 800°C at ramp rate of 3°C/min is carried out for sampling period of 5 secs.

The percentage loss of mass M_L is calculated from the masses m_s (at the start, before heating) and m_f (at the end temperature 800 ^{o}C) using the Eq. (2.1).

The results by carrying out TG analysis using second temperature cycle B is indicated in Table 2.9 for similar PPS composite sample RB020.

Table 2.9 TGA results for PPS composite (RB 020) using cycle B

Run	Temperature cycle	Initial mass (mg)	Final mass (mg)	% Fiber	% PPS resin
4	B	166.304	132.223	79.5	20.5
5	B	169.46	133.74	78.9	21.1
6	B	171.633	133.264	77.6	22.4

The tabulated results indicate an average carbon fiber value of 78.7% and PPS resin value of 21.3% with a standard deviation of 1.2% in the tabulated results. The instrument provides sensitivity of 0.1 g. The mass percentage of carbon fiber in the tested (RB020, [10]) samples is, thus, about 80%. Since the density of the carbon fiber is about 2.2g/cm^3 , [38], compared to the PPS resin density of 1.34 g/cm^3 [37], the volume fraction of carbon fiber is about 70%.

Similarly another CoolPoly PPS composite sample E5101 of known thermal conductivity [10] value of claimed thermal conductivity 20 W/m-K was tested [10]. The TGA plot is depicted in Fig 2.11 achieved using temperature cycle B.
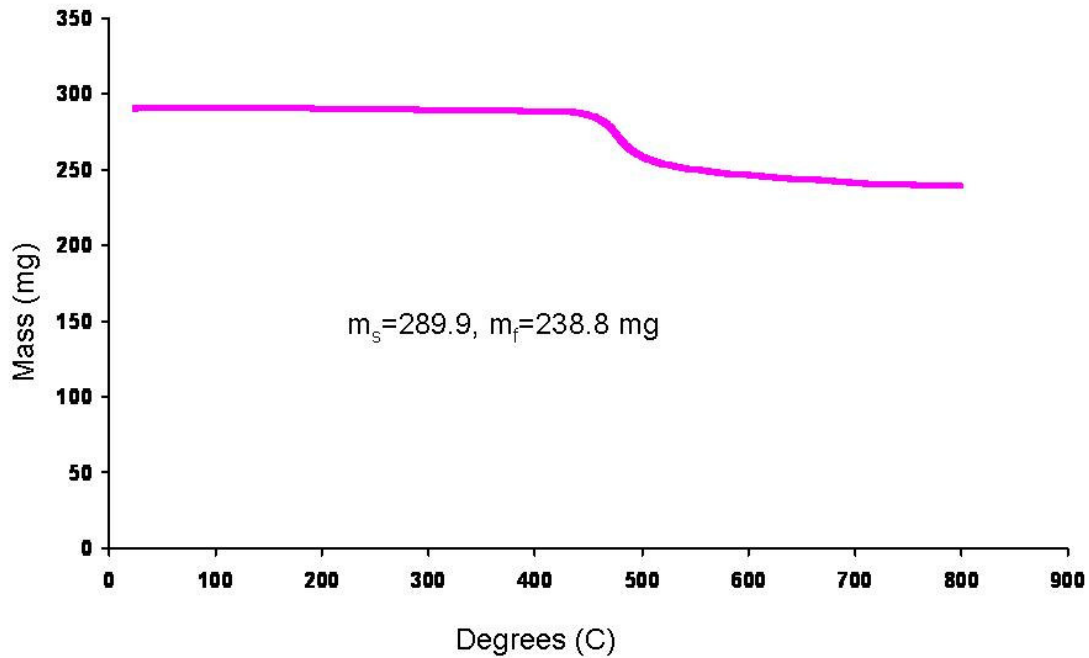
Figure 2.11 TGA run for PPS composite CoolPoly sample E5101 [10]

Table 2.10 TGA results for PPS composite (E5101, [10]) using cycle B

Run	Temperature cycle	Initial mass (mg)	Final mass (mg)	% Fiber	% PPS resin
1	B	289.914	238.764	82.4	17.6
2	B	253.238	209.608	82.8	17.2
3	B	217.624	180.052	82.7	17.3

Clearly, as indicated previously, the mass remains nearly constant up to 450 $^{\circ}$C, and then the PPS starts to melt and evaporate. The highest loss in PPS mass takes place in

the range 450-600 ^{o}C. After 600 ^{o}C only a small change in mass takes place up to 800

^{o}C. The results of 3 runs are shown in Table 2.10 for E5101 PPS composite sample.

The average fiber in the sample of E5101 is 82.6% and PPS resin is 17.4% with a

standard deviation of 0.4%.

Chapter 3: Thermal Conductivity Measurements and Modeling

3.1 Laser Flash Thermal Measurements

3.1.1 Introduction

A variety of methods, based on either steady or transient states, are available for characterizing material thermal diffusivity, specific heat capacity, and thermal conductivity. In recent years the flash diffusivity method (ASTM E1461 [27]) [28] [29], has been widely applied to the characterization of the materials used in electronics packaging. Other methods commonly employed include the guarded heat flow meter, ASTM E1530 [30], guarded comparative, ASTM E1225 [31] and its modification ASTM D5470 [32], various "probe" methods based on the transient hot wire technique [33]. The advantage of using a laser flash technique is that it does not involve thermal contact resistance effects between the sample and the heat source and/or intermediate layers.

In this work a Holometrix laser flash unit [34] was used to measure the thermal diffusivity and the specific heat of the Polyphenylene Sulphide (PPS) composite samples. These measured values are then used to calculate the thermal conductivity values of various PPS composite samples.

3.1.2 Principle of Operation

The laser flash method (Figure 3.1) involves irradiating the front surface of a small disk or slab of the material with a single pulse from a laser source, and monitoring the

resulting temperature rise on the back surface as a function of time. For the laser flash analysis undertaken, the PPS composite sample geometry was a square 8 mm on a side, with thicknesses ranging from 0.7 to 1.26 mm, depending on the thermal diffusivity of the material.
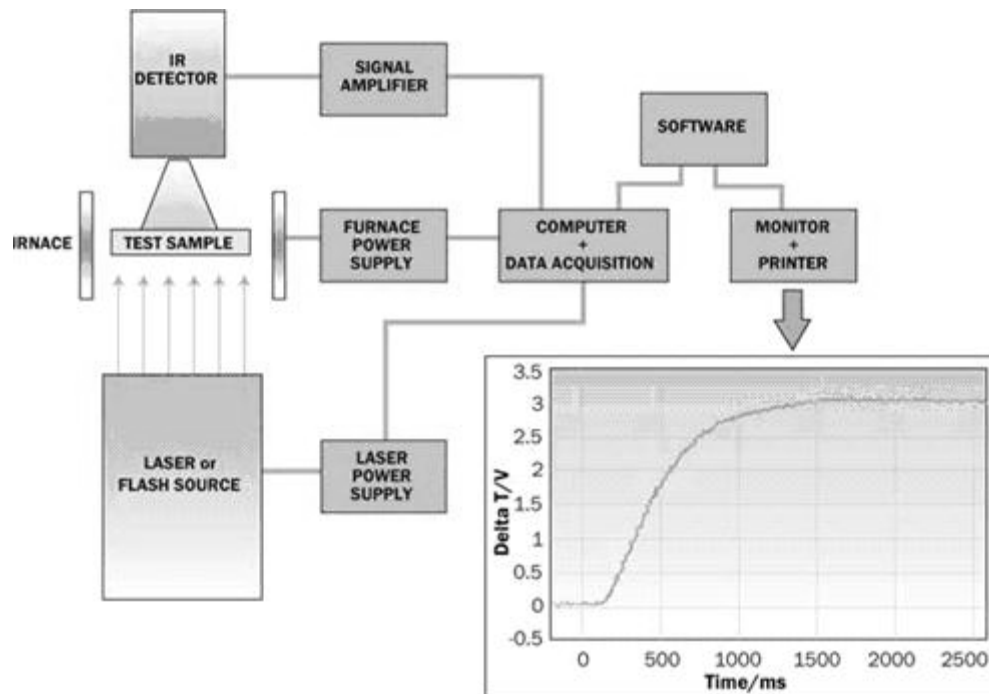
Figure 3.1 Schematic of Laser flash diffusivity measurement test setup [34].

The temperature of the back face is measured with an IR detector. The output of the temperature detector is amplified and adjusted for the initial, ambient conditions so that the recorded temperature rise curve, shown in Figure 3.1, is the change in the sample temperature resulting from the firing of the laser.

3.1.2.1 Thermal diffusivity

The recorded temperature rise data and sample thickness are used to directly calculate the thermal diffusivity. The earliest method of analysis was developed by Parker et al [32], who assumed that the sample was perfectly insulated from the environment during the test, that all the laser energy was absorbed instantaneously in a very thin layer of the sample material facing the laser (zero pulse width), and that the material properties are constant over the small temperature step of the measurement. The subsequent Cowan model [31] accounts for the heat losses from the backside of the sample. In this study Cowan's model predictions [31] were in agreement with those obtained using Parker's et al. model [32]. This suggests that the sample convective heat losses during measurements were negligible.

Under these conditions, the Parker model predicts that the time required for the temperature to rise to 50% of the peak value is given by:

$$t_{50} = 0.1388 \ \tau^2/\alpha \qquad\qquad (3.1)$$

where τ = sample thickness, α = thermal diffusivity

The thermal diffusivity is calculated from Eq. (3.1) by measuring (t_{50}), the time at which the dimensionless temperature θ^*, defined as $\Delta T/\Delta T_{peak}$, equals 0.5.

3.1.2.2 Specific Heat and Thermal Conductivity

The specific heat may be needed on its own as an input for transient thermal modeling, or in order to calculate the thermal conductivity. For homogeneous samples, the flash technique can be used to measure the specific heat [32]. This technique involves comparing the magnitude of the sample temperature rise due to the energy pulse (final detector voltage minus baseline detector voltage) to that of a

calibration sample of known specific heat, tested under the same conditions. Following the calibration run, the specific heat and thermal diffusivity of the test sample can be measured in a single run.

The specific heat of a material is defined as the amount of energy required to raise a unit mass of material by one unit of temperature at a constant pressure,

$$C_p = \frac{Q}{m\Delta T}$$

(3.2)

Where, m = mass, ΔT = change in temperature

Assuming that the pulse energy and its coupling to the sample, i.e. the net absorption, remain essentially unchanged between the calibration and unknown samples,

$$Q = (mC_p\Delta T)_{cal} = (mC_p\Delta T)_{sample}$$

(3.3)

and the unknown sample specific heat is calculated from

$$C_p = \frac{(mC_p\Delta T)_{cal}}{(m\Delta T)_{sample}} = \frac{(mC_p\Delta Vo)_{cal} G_{sample}}{(m\Delta Vo)_{sample} G_{cal}}$$

(3.4)

where,

ΔVo =   change in detector voltage (proportional to ΔT)

G   =   detector amplifier gain

Measurement of the thermal diffusivity and specific heat permits the calculation of the thermal conductivity, with an additional measurement or knowledge of the bulk density of the sample material as shown in Eq. (3.5)

$$k = (\alpha)\,(\rho)\,(c_p)$$

(3.5)

37

Where, k is the thermal conductivity, ρ is the bulk density, and c_P is the specific heat.

3.1.3 Laser Flash Test Samples

It is important to use a flat sample and to record an accurate value for the sample thickness as diffusivity depends directly on the square of the sample thickness in Eq. (3.1). Therefore any inaccuracy in sample thickness measurement will affect measured diffusivity value significantly. The optimum sample thickness (τ) in order to ensure that proper signal response holds depends on the diffusivity (α) of the material.

Table 3.1 Recommended sample thickness based on diffusivity estimation [34]

Diffusivity	Suggested thickness (mm)
Low diffusivity e.g. polymers (0.001cm²/S)	0.5 to 1
Medium diffusivity e.g. ceramics (0.05 cm²/S)	0.5 to 2.
High diffusivity e.g. copper (1 cm²/S)	2 to 3

In the methodology recommended for the Micro flash technique [34], the time (t_{50}) taken for the back surface to reach half its maximum temperature should be at least three times longer than the length of the laser pulse (0.33ms) and not longer than about 3 seconds [34]. If the sample is too thick it will take longer than 3s and the laser

flash plot is not correctly obtained. The guideline given in Table 3.1 was used in order to obtain appropriate sample thicknesses [34].

Sample mass was measured using digital weighing equipment (Mettler AE 100 [108]) that has a sensitivity of 0.1 mg. The sample thickness and dimensions were measured using a digital vernier caliper (Mitutoyo, [109]) with a resolution of 1 µm. For samples characterized, the length and breadth were 8mm and sample thickness ranges from 0.73 mm to 1.25 mm. The density of the sample (g/cm^3) is calculated from the measured mass and volume.
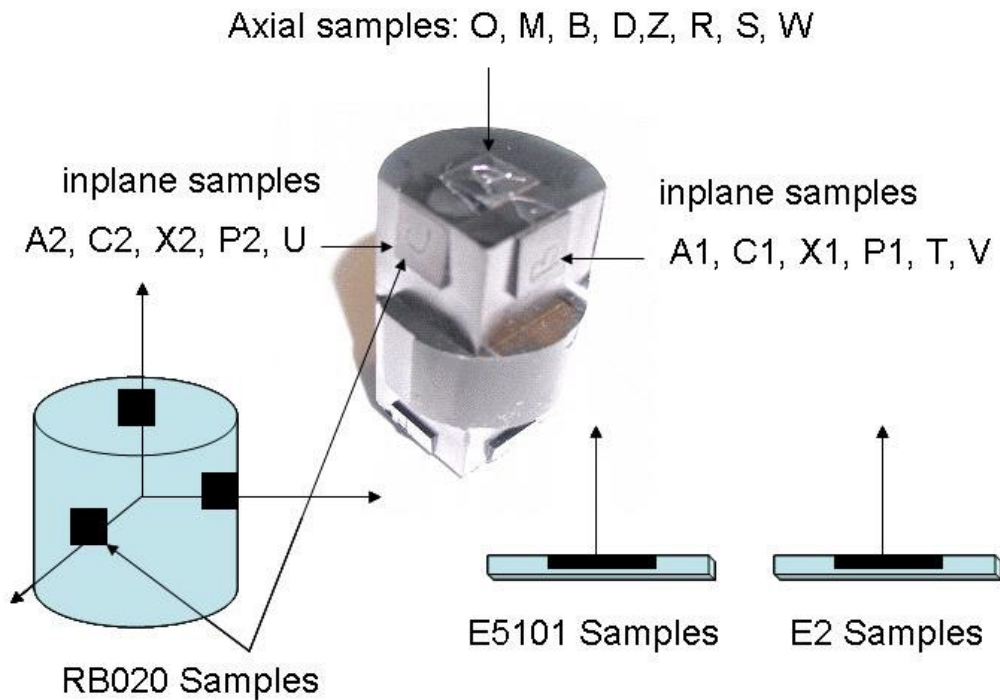
Figure 3.2 Enhanced PPS composite sample locations

Three different thermally conductive materials RB020, E 5101, E2 are tested for thermal diffusivity. The vendor claimed thermal conductivity value for each of the material is 20 W/m-K [10]. The RB020 thermal conductivity measurement samples were machined out from different orthogonal sections of a RB020 cylindrical fin of diameter 25.4 mm as shown in Fig. 3.2. The E5101 and E2 thermal diffusivity samples are made out from rectangular plaques of 2.5 mm thickness as shown in Fig. 3.2. The RB020 and E5101 have PPS matrix. The E2 has liquid crystal polymer as a matrix [10].

3.1.4 Laser Flash Tests

3.1.4.1 NIST traceable sample measurements

A NIST calibrated and traceable, round Pyroceram test sample - of the dimensions and properties shown in Table 3.2 - was used to "qualify" the laser flash test facility used in this experiment and to determine the specific heat of the PPS composite RB020 [10] test samples. Very good agreement between the data plots and the theoretical Parker curve were obtained for one of the various runs as shown in Fig. 3.3 [Appendix D]. The tests are repeated with the same settings on the same sample side and reversed, in order to capture repeatability of the tests.

Table 3.2 NIST traceable Pyroceram sample known properties

Sample	Thickness (mm)	Diameter (mm)	Density (g/cc)	Specific heat (J/kgK)	Thermal conductivity (W/m-K
NIST Pyroceram sample	1.002	12.7	2.6	780	4
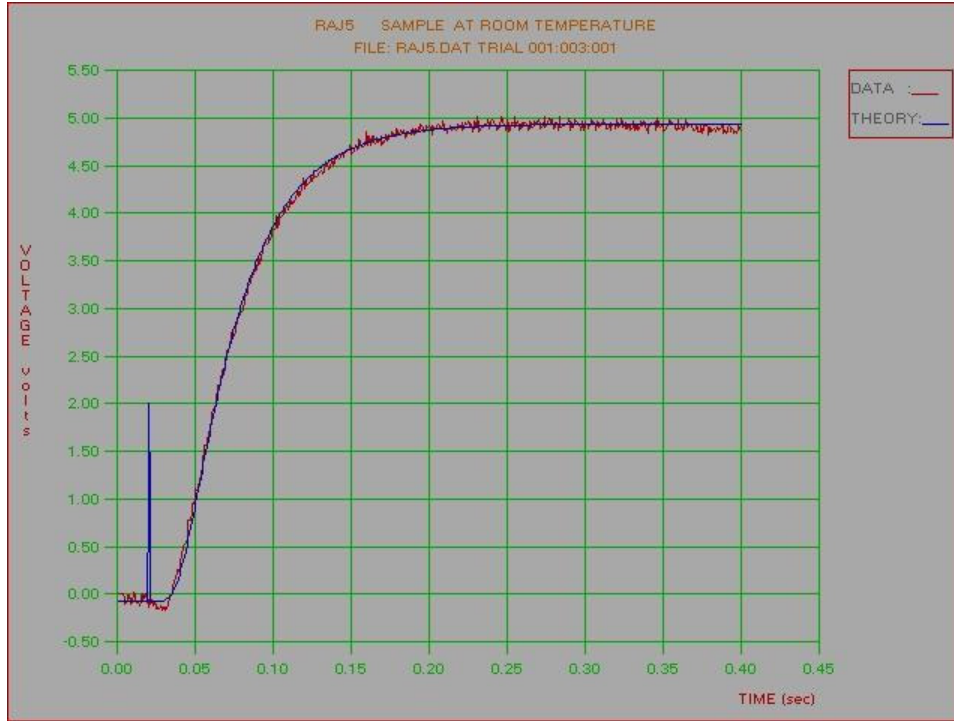
Figure 3.3 Voltage rise curve for PPS composite sample RB020 round sample 'M'

The results are shown in Table 3.3. The first row in Table 3.3 provides the measured thermal diffusivity and calculated thermal conductivity for the NIST sample. At a value of 3.99W/mK, the thermal conductivity is within 0.25% of the exact value of 4 W/m-K. The next row provides the values for the PPS RB020 axial composite round sample 'M' (Fig. 3.3), of diameter 12.7 mm and thickness value of 0.8 mm, tested under identical conditions. The measured specific heat and thermal diffusivity values are 906 J/kg-K and 0.05525cm^2/s, respectively, resulting in a thermal conductivity of 7.89W/mK. The test is repeated several time with NIST traceable sample and PPS composite RB020 sample 'M' in order to establish the accuracy, repeatability and sample side effects in the measurements. The four runs of NIST traceable samples and five runs of RB020 round sample 'M' were made in order to establish the accuracy and repeatability in the test setup

Table 3.3 Laser flash results using NIST traceable Pyroceram sample

Sample	Thickness (mm)	Diameter (mm)	Density (g/cc)	Thermal Diffusivity (cm²/s)	Specific heat (J/kgK)	Thermal conductivity (W/m-K
NIST (side1) Pyroceram sample run 1	1.002	12.7	2.6	0.01967	780	3.99
RB020round (side 1) sample run 1	0.8	12.7	1.576	0.05525	906	7.89
NIST (side 1) Pyroceram sample run 2	1.002	12.7	2.6	0.0198	780	4.02
RB020round (side 1) sample run 2	0.8	12.7	1.576	0.06196	912	8.91
RB020round (side 2) sample run3	0.8	12.7	1.576	0.0581	930	8.52
NIST (side 2) Pyroceram sample run 3	1.002	12.7	2.6	0.01967	794	4.06
NIST (side1) Pyroceram sample run 4	1.002	12.7	2.6	0.01953	780	3.96
RB020round (side 1) sample run4	0.8	12.7	1.576	0.05597	934	8.24
RB020round (side 2) sample run5	0.8	12.7	1.576	0.05287	941	7.84

Analyzing all the four runs made for NIST traceable Pyroceram samples. The measured average thermal diffusivity, and conductivity value for Pyroceram sample is 0.019668, 4.01 W/m-K respectively with percentage standard deviation value of 0.56, and 1.1% respectively. Analyzing all the five runs in Table 3.3, the average thermal diffusivity and specific heat for PPS composite RB020 round sample 'M' is 0.05683 (σ~6%) , 924.6 J/kg-K (σ ~1.6%) respectively, resulting in average thermal conductivity of 8.28 W/m-K (σ~5.4%). These preliminary experiments served to

establish the strong repeatability of the test setup for the thermal diffusivity and conductivity measurement of homogeneous NIST traceable sample with standard deviation values close to unity. The used equipment and procedure is capable of providing accuracy within 5% for thermal conductivity measurements. However, the runs for the inhomogeneous PPS RB020 composite samples yielded an average specific heat of 924.6 J/kg-K (σ ~1.6%) and average thermal conductivity of 8.28 W/m-K (σ~5.4%)..

3.1.4.2 Thermal diffusivity measurements

   Table 3.4 provides the results obtained using the thermal diffusivity test apparatus described above for two different rectangular PPS composite samples tested in the through thickness direction. The PPS composite samples included: one inplane samples of PPS composite E5101 [10] obtained from rectangular plaques in Fig. 3.2, and one additional inplane sample from a PPS E2 composite [10], obtained from rectangular plaques as shown in Fig. 3.2. The two materials are claimed to be of thermal conductivity value 20 W/m-K. The polymer matrix for E5101 is PPS and for E2 it is Liquid crystal polymer (LCP). The results in the Table 3.4 indicate results of four runs for each of the two materials. The average thermal diffusivity value from four runs for E5101 is 0.04488 with a percentage standard deviation value of 3.2%. The average thermal diffusivity value from four runs for E2 is 0.01965 with a percentage standard deviation value of 4.7%. It is believed that the through thickness direction is low conductivity direction for the rectangular plaques and inplane direction is the high thermal conductivity direction that is more close to claimed thermal conductivity value.

Table 3.4 Laser flash thermal diffusivity results in through thickness direction

Sample	Thickness (mm)	Length (mm)	Breadth (mm)	Diffusivity (cm^2/s)
E5101side1run1	1.24	8.01	8.04	0.04603
E5101side2run2	1.24	8.01	8.04	0.04618
E5101side1run3	1.24	8.01	8.04	0.04345
E5101side2run4	1.24	8.01	8.04	0.04387
E2side1run1	1.26	8.01	8.06	0.01867
E2side2run2	1.26	8.01	8.06	0.01973
E2side1run3	1.26	8.01	8.06	0.01935
E2side2run4	1.26	8.01	8.06	0.02086

3.1.4.3 Anisotropic thermal conductivity measurement

As previously discussed, it is expected that the PPS composite samples will display anisotropic thermal conductivity. In order to successfully capture this characteristic of the PPS composite pin fin material, rectangular samples were made from various orthogonal sections of the PPS composite pin fin. Three orthogonal samples were made from a 25.4 mm cylindrical sample of a PPS composite (RB020) pin fin, as shown in Fig. 3.2.

Table 3.5 Thermal conductivity tests for RB020 (A1, A2, B, C1, C2, D) samples

Sample	Thickness (mm)	Mass (gm)	Density (g/cc)	Thermal. Diffusivity (cm²/s)	Specific heat (J/kgK)	Thermal conductivity (W/m-K
RB020A1 inplane	1.245	0.1245	1.59	0.02913	924.6	4.27
RB020A2 inplane	1.245	0.1207	1.57	0.0343	924.6	4.98
RB020B axial	1.245	0.121	1.55	0.107	924.6	15.41
RB020C1 inplane	1.02	0.1029	1.6	0.0278	924.6	4.11
RB020C2 inplane	1.03	0.0987	1.55	0.0342	924.6	4.91
RB020D axial	1.01	0.0978	1.55	0.105	924.6	14.87

Table 3.5 presents the results obtained for 6 different samples. The results were obtained for three PPS composite (RB020) samples of thickness 1.245mm (A1, A2, B) and three of thickness 1.01-1.03 mm (C1, C2, D) obtained from orthogonal sections of the pin fin. In these tests the axial thermal conductivity (sample B and D) was found to vary from 14.87 to 15.41 W/m-K, averaging 15.1W/mK, while the in-plane thermal conductivity samples (A1, C1 and A2, C2) yielded an average value of 4.19W/mK for the x-direction conductivity and 4.95W/mK for the y-direction conductivity, respectively. Although a small variation (+/- 5.9%) in conductivity is

thus seen in the two in-plane directions, at an average of 4.6W/mK the in-plane values are just approximately 30% of the axial thermal conductivity of this PPS RB020 material.

To further explore the directional and spatial variability of the PPS RB020 thermal conductivity, additional samples, O, Z, R, S, W were taken from cross sections of the pin fin as shown in Fig. 3.2 at different places normal to pin fin axis.

Table 3.6 Thermal conductivity tests for RB020 pin fin axial samples

Sample	Thickness (mm)	Mass (gm)	Density (g/cc)	Thermal. Diffusivity (cm²/s)	Specific heat (J/kg-K)	Thermal conductivity (W/m-K
RB020O	1.25	0.121	1.55	0.1075	924.6	15.41
RB020Z axial	0.77	0.0728	1.49	0.05554	924.6	7.65
RB020R axial	1.02	0.1018	1.56	0.0302	924.6	4.36
RB020S axial	0.77	0.076	1.54	0.11625	924.6	16.6
RB020W axial	1.016	0.0969	1.54	0.08487	924.6	12.07

The results of the thermal conductivity tests for PPS composite RB020 samples that have cross sectional area normal to the pin fin axis are presented in Table 3.6. The axial thermal could range from 4.36 W/m-K to 16.6 W/m-K. Highest axial thermal conductivity value of 16.6 W/m-K is measured for RB020 sample 'S' in Table 3.6.

The average axial thermal conductivity value for samples obtained from different fin height locations in the PPS composite RB020 pin fin in Fig. 3.2 is 11W/m-K with ± 5 W/m-K ($\sigma \sim 46\%$). The variable axial thermal conductivity could be due to the non uniform distribution of carbon fibers in the PPS matrix during fabrication processes.

The additional thermal conductivity, PPS, RB020 [10] samples, X1, X2, P1, P2, T, U, V were taken from inplane cross sections of the pin fin as shown in Fig. 3.2 at different places along the fin height parallel to pin fin axis.

Table 3.7 Thermal conductivity tests for RB020 pin fin inplane samples

Sample	Thickness (mm)	Mass (gm)	Density (g/cc)	Thermal. Diffusivity (cm²/s)	Specific heat (J/kg-K)	Thermal conductivity (W/m-K)
RB020X1 inplane	0.77	0.0776	1.563	0.02004	924.6	2.90
RB020X2 inplane	0.77	0.0776	1.563	0.02125	924.6	3.07
RB020P1 inplane	1.02	0.1052	1.586	0.0383	924.6	5.62
RB020P2 inplane	1.02	0.1044	1.591	0.0185	924.6	2.72
RB020T inplane	1.2	0.1216	1.57	0.07959	924.6	11.56
RB020U inplane	1.02	0.1015	1.57	0.10913	924.6	15.81
RB020V inplane	1.02	0.1054	1.56	0. 109	924.6	15.8

The radial thermal conductivity could range from 2.72 -15.8 W/m-K. The average pin fin inplane or radial thermal conductivity value from Table 3.7 measurements is 8.2 W/m-K with ± 6 W/m-K ($\sigma \sim 73\%$) variation.

3.2 Polymer Composites Thermal Conductivity Prediction Models

The polymer composite thermal conductivity value depends on several distinct parameters such as fiber and resin thermal conductivity, fiber aspect ratio, fiber volume fraction, and fiber orientation. In order to explore the influence of these parameters on the thermal conductivity value of the composite and to explain the measured thermal conductivity values for the PPS composite samples, an existing empirical model, developed by Nielsen [17] is used.

3.2.1 Literature Review

The most simplistic thermal-conductivity models start with the standard mixture rule (Eq. 3.6) [35]. This model is typically used to predict the thermal conductivity of a unidirectional composite with continuous fibers.

In the filler direction, the composite thermal conductivity is estimated by the rule of mixtures.

$$k = \sum_{i=1}^{n} k_i \Phi_i \tag{3.6}$$

In the direction perpendicular to the fillers (through plane direction), the inverse mixing rule [35] (Eq. (3.7)) is used.

$$1/k = \sum_{i=1}^{n} \Phi_i / k_i \tag{3.7}$$

where 'k' is the thermal conductivity of the composite, 'n' the number of constituents in the composite, 'i' the index variable for the composite constituents, 'Φ' the volume fraction of the constituents, and 'k_i' the thermal conductivity of the ith constituent.

Another model similar to the two standard-mixing rule models is the geometric model shown in Eq. (3.8) [36].

$$k = \sum_{i=1}^{n} k_i^{\phi_i} \qquad (3.8)$$

Many more theoretical models have been proposed for the electrical and thermal conductivity of two-phase systems (Bruggeman, 1935; Kerner, 1956; Hamilton and Crosser, 1962; Tsao, 1961; Springer and Tsai, 1967; Behrens, 1968; Ashton et al., 1969; Cheng and Vachon, 1969; Sundstrom and Chen, 1970; Zinsmeister and Purohit, 1970)[89-98]. These models show the effect of the thermal conductivities of matrix and filler on the total composite thermal conductivity. However these models do not consider variables such as the shape and size of the particles, and how the particles are packed. Therefore these models are not suitable for precise prediction of the thermal conductivity of polymer matrix composites.

The first comprehensive theoretical model for the effective thermal conductivity of a two-component composite was proposed by Nielsen, 1974 [17] and includes the particle shape, size, and packing considerations. This model was derived from the theory of elastic moduli of composite materials based on the Halpin Tsai equations [98]. Progelhof, 1976 [16], X.Lu, 1997 [103]; Shoji Okamoto, 1999 [102]; C.P. Wong, 1999 [104]; each confirmed the Nielsen model results with experimental findings. Amit Devpura et. al., 2000 [105]; applied percolation theory for calculating thermal conductivity in thin interface material (TIM) randomly filled with spherical

49

particles and showed good agreement with Nielsen model up to a 40% particle

volume fraction. Erik H. Weber, 2003 [23]; showed the Nielsen model [17] to be in

good agreement with his experimental findings up to 40% fiber volume for resins

containing single fibers with aspect ratios ranging from 2 to 8. The Modified Nielsen

model [23] has also been proposed for dealing with the combination of different

fibers at various concentrations. In the presented analysis the theoretical "Nielsen"

model is used to establish the PPS composite thermal conductivity. This model is also

used to establish the effect of fiber thermal conductivity, aspect ratio, and fiber

volume fraction on the PPS composite thermal conductivity.

3.2.2 Nielsen Thermal Conductivity Model
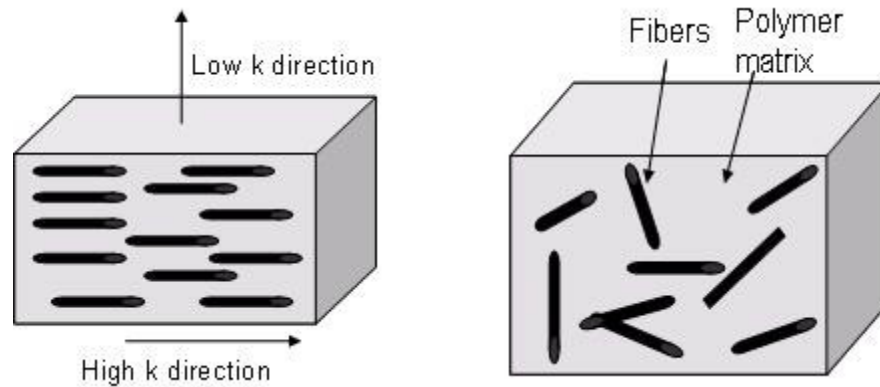
Figure 3.4 Polymer matrix composite block (a) uniaxially oriented fibers (b) randomly oriented fibers

The Nielsen composite thermal conductivity model for two phase systems is given as;

$$\frac{k}{k_1} = \frac{1 + AB\phi_2}{1 - B\varphi\phi_2} , \qquad (3.9)$$

Where, 'k', 'k_1' is the composite, and polymer resin thermal conductivity value,

respectively.

The coefficient A can be expressed as

$$A = k_E - 1, \tag{3.10}$$

where, 'k_E' is the Einstein coefficient, and 'A' is related to the generalized Einstein coefficient and is a function of the aspect ratio and orientation with respect to the heat flow (random vs. unidirectional). Table 3.8 below shows the values of 'A' for various types of fillers, with A ranging up to 8.58 for randomly oriented fibers of L/D equal to 15, but attaining much higher values (equal to 2L/D) in the fiber direction, along with much lower values (0.5) perpendicular to the fiber direction, for uniaxially aligned fibers. Using the tabulated data, it is possible to express the 'A' factor for randomly oriented fibers of various aspect ratios, in the following form

$$A = 1.281e^{0.1279\gamma} \tag{3.11}$$

where, γ is the aspect ratio of the randomly oriented fibers.

Table 3.8 Fiber aspect ratio and orientation constant [17]

Filler type	Direction of heat flow	Aspect ratio	A
Cubes	Any	1	2
Spheres	Any	1	1.5
Random fibers	Any	2	1.58
Random fibers	Any	4	2.08
Random fibers	Any	6	2.80
Random fibers	Any	10	4.93
Random fibers	Any	15	8.38
Uniaxially oriented fibers	Parallel to fibers	---	2L/D
Uniaxially oriented fibers	Perpendicular to fibers	---	0.5

Table 3.9 Maximum packing fractions for fillers packed in various ways [17]

Filler shape	Type of packing	ϕ_m
Spheres	Hexagonal close	0.7405
Spheres	Face centered cubic	0.7405
Spheres	Body centered cubic	0.6
Spheres	Simple cubic	0.524
Spheres	Random close	0.637
Spheres	Random loose	0.601
Rods or fibers	Uniaxial hexagonal close	0.907
Rods or fibers	Uniaxial simple cubic	0.785
Rods or fibers	Uniaxial random	0.82
Rods or fibers	Three dimensional random	0.52

The coefficient B can be expressed as

$$B = \frac{k_2/k_1 - 1}{k_2/k_1 + A},$$ (3.12)

where 'k_2' is the filler; and 'k_1' is the resin thermal conductivity.

And Ψ is given by,

$$\psi = 1 + \left(\frac{1 - \phi_m}{\phi_m^2} \right) \phi_2 ,$$ (3.13),

The filler volume fraction is ϕ_2 and ϕ_m is the maximum packing fraction, shown in Table 3.9, and defined as the true volume of the particles divided by the apparent volume when packed to the maximum extent. The factor ψ is determined by the maximum packing fraction ϕ_m of the fillers. The product $\psi\phi_2$ can be considered as a reduced concentration which approaches 1.0 when $\phi_2 = \phi_m$.

The fiber aspect ratio and orientation effects on the composite thermal conductivity are associated with parameter 'A' in the Nielsen model, as expressed in Eqs. (3.9) and (3.10).

3.2.3 Applying the Nielsen Model to PPS-Pitch RB020

To apply the Nielsen Model to the present PPS-pitch RB020 composite it is necessary to recall that the SEM images in Fig 2.8 of the previous chapter show the fibers to be randomly oriented, to possess a diameter close to 10 µm and a length that can vary up to approximately 300 µm. From the literature, it is known that typical PPS and pitch based discontinuous carbon fiber thermal conductivity values are 0.3 W/m-K [37] and 500 W/m-K [38], respectively, and that the PPS density is 1.34 g/cc [37] and the fiber 2.2 g/cc [38], respectively. Based on translation of the TGA results, described in section 2.3, the fiber volume fraction was found to equal 70%.

Interestingly, Table 3.9 reveals that fibers cannot achieve more than a 52% volume fraction in a completely random three-dimensional arrangement. However, a random uniaxial packing arrangement can reach an 82% volumetric fraction. Consequently, the present PPS-pitch composite would appear to consist of substantially-aligned fibers, as – in fact – reflected in the observed thermal anisotropy of this material. (see section 3.1.4)

Re-examining Fig. 3.5 in light of the measured thermal conductivity of the PPS-pitch composite suggests that the composite axial thermal conductivity value of 15 W/m-K is associated with an 'A' value of 11.
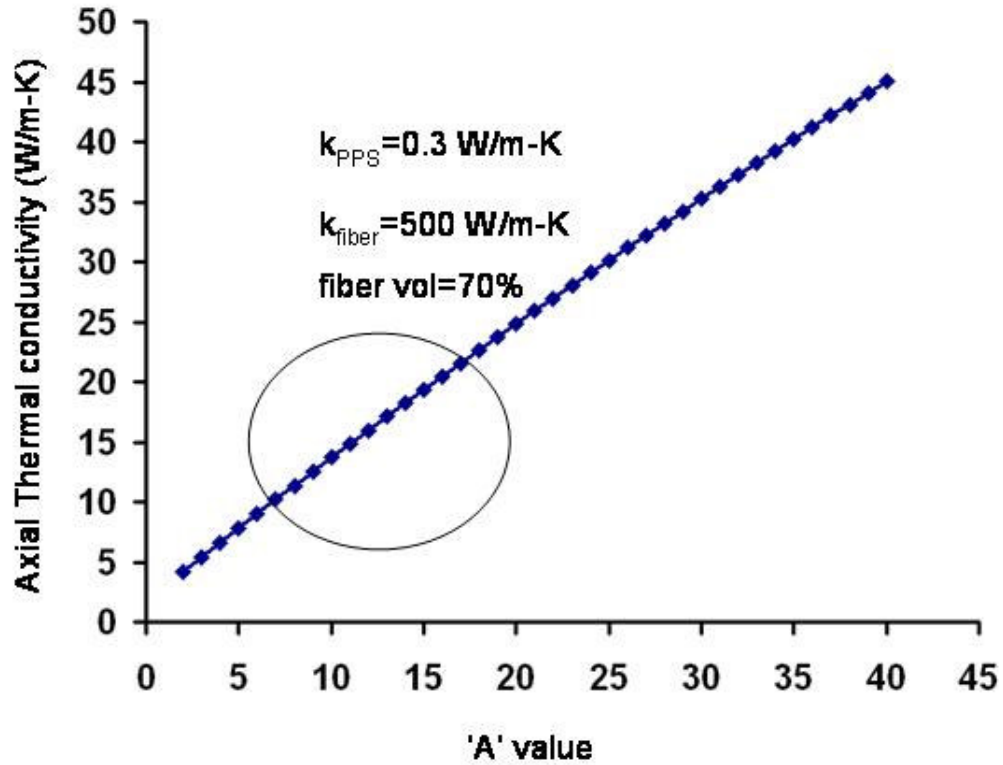
Figure 3.5 Axial thermal conductivity value variations with 'A' parameter

Using Eq. (3.11) the 'A' value of 11 corresponds to a fiber aspect ratio (γ) value of 22 which is within the observed SEM fiber length (<300 µm) to diameter (10 µm) maximum ratio of 30.

Additional improvements could be achieved by the use of commercially available, higher thermal conductivity fibers, with values ranging from 400 to 800 W/m-K, as shown in Table 2.7, However, for discontinuous fibers, it is unlikely that the modest improvement attained with fiber conductivity greater than 400W/mK (see Fig 3.7) would justify the added cost and fabrication energy requirements.
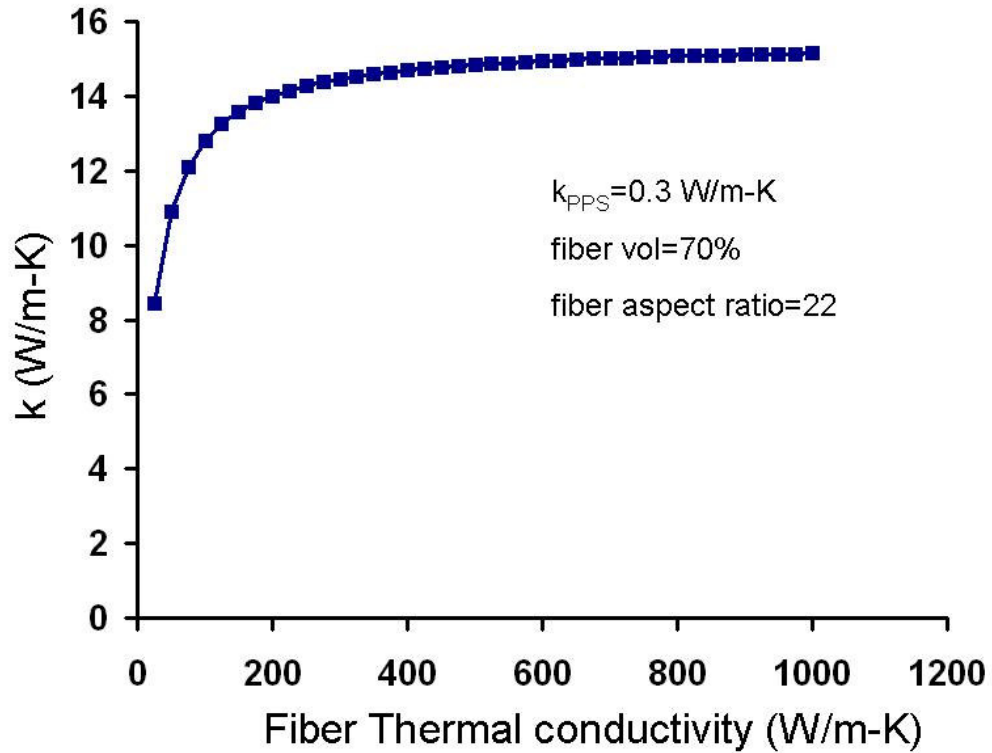
Figure 3.6 Overall thermal conductivity values with fiber conductivity value

In the tested PPS composite samples the total volume fraction of carbon fibers is 70% (section 2.3.4). The Nielsen model suggests that it is possible to achieve the measured axial thermal conductivity (15 W/m-K) at much lower fiber concentration by packing carbon fibers in a perfect uniaxial arrangement. For such a perfectly aligned composite, in the direction parallel to the fibers the 'A' value is 44 for carbon fibers with an aspect ratio of 22. Examining Fig 3.8, it may be seen that this results in a conductivity of 15 W/m-K at a 50% volume fraction of carbon fibers.

However, for the normal-to-fiber direction the thermal conductivity value at a 50% fiber fraction is just 0.9 W/m-K. This results in a highly-orthotropic PPS composite with a conductivity ratio of 0.06.
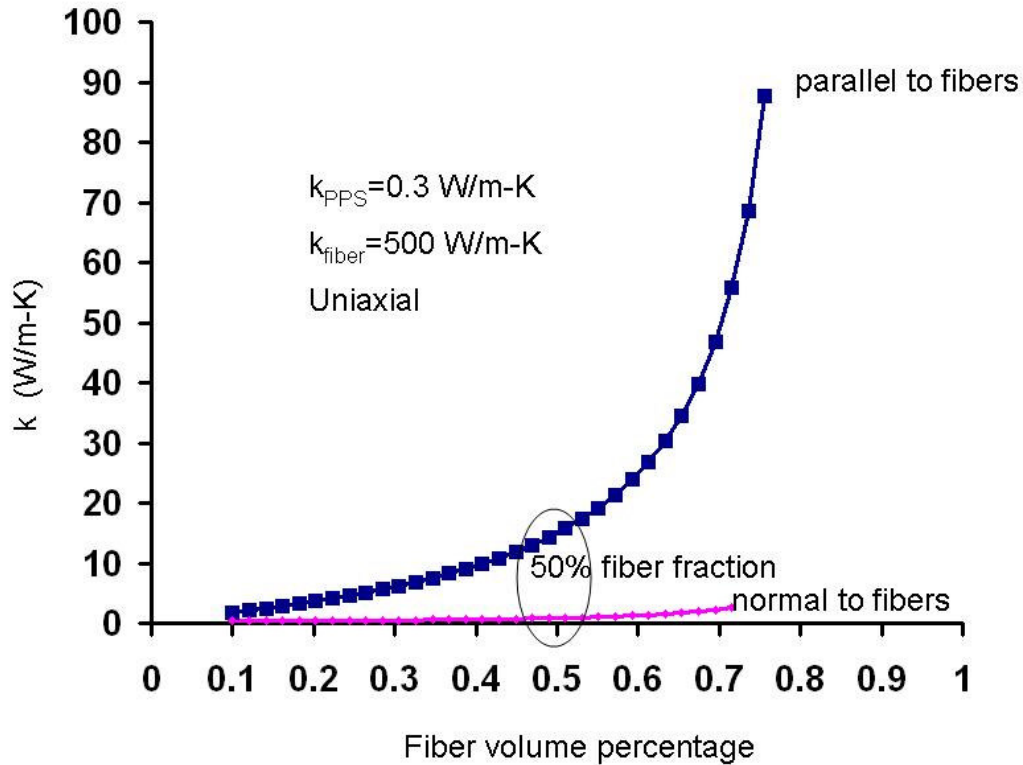
Figure 3.7 Uniaxial PPS composite thermal conductivity values

The foregoing reveals that the thermal conductivity of polymer-carbon composite increases as the volume fraction and the aspect ratio of the carbon fibers increase. The fiber thermal conductivity value (400-1000 W/m-K) exerts a far weaker effect on the composite thermal conductivity. Fiber orientation can play a significant role in establishing the thermal capability of such a composite, due to the impact of orientation on the maximum packing concentration. A uniaxial polymer matrix composite can achieve a 0.82 volumetric fraction, leading to a higher axial conductivity but far lower radial conductivity than achieved by a randomly oriented fiber polymer composite. The randomly oriented fiber PPS composite has a thermal conductivity value that falls between the uniaxial maximum and minimum thermal conductivity values. Therefore, it is not possible to have an isotropic high thermal

conductivity PPS-pitch composite and the rational use of these materials for fins and heat sinks must contend with their inherent anisotropic thermal conductivity. In achieving the desired performance, cost, and manufacturability, it is also important to recognize several key trades offs involving fiber material, aspect ratio, orientation, fiber, and volumetric concentration.

Chapter 4: Heat Sink Design and Optimization

The rapid proliferation of computers, as well as other categories of electronic equipment, has resulted in substantial material and energy consumption, as well as entropy generation, rates devoted to the thermal management of such electronic systems. Heat sinks, composed of arrays of variously-shaped fins, continue to serve as the "technology of choice" for the thermal packaging of most categories of electronic equipment. The application of "design for sustainability" principles to this industry must involve the least-mass and least-energy optimization of heat sinks and include both geometric and material selection considerations. The high thermal conductivity polymer-fiber composites offer a most promising alternative to conventional heat sink materials such as aluminum and copper. To achieve the goals of sustainable development, the design and use of such heat sinks involves a subtle balance between a superior thermal design, minimum material consumption, and minimum pumping power. This chapter deals with the design and optimization methodology used to achieve these goals. To concretize the potential benefits of using polymer matrix composite heat sinks, a comparison in thermal performance and metrics among heat sinks fabricated of copper, aluminum, and thermally conductive polymer is presented.

4.1 Literature Review

The desire to minimize the cost, weight, and volume of commercial heat sinks can often be addressed by the design of light-weight, volumetrically efficient, least-material fins in which the ratio of fin height to thickness (or diameter) has been

58

selected to minimize the mass required to dissipate the specified heat flow. The use of these individually-optimum plate and pin fins [42] to compose multiple fin arrays has been described in Bar-Cohen et al. [43], Iyengar and Bar-Cohen [44], and Bahadur and Bar-Cohen [45] for natural convection and in Iyengar and Bar-Cohen [46], Bahadur and Bar-Cohen [64] for forced convection cooling applications.

Heat dissipation from a high temperature heat source, such as an operating microprocessor, to a low temperature sink, such as ambient air, by means of a fan-cooled fin structure, will always be accompanied by the generation of entropy. This entropy generation results from the loss of thermodynamic availability due to heat transfer from a hot to a cold reservoir and the consumption of fluid pumping power to overcome frictional dissipation. Several research groups [47-50] have extended the Entropy Generation Minimization (EGM) methodology, first proposed by Bejan [51], to heat sink arrays and a detailed review of EGM is provided in [52]. While the least-energy optimization, explored in this work, does not account for the thermal availability loss in the system and its corresponding opportunity cost, the EGM methodology does not include any entropy generation in the creation of the fin mass or in the manufacturing process, thus excluding from consideration two important contributors to the heat sink energy consumption and entropy generation. It is, thus, to be expected that these two approaches to "design for sustainability" will lead to different optimal designs [53]. The recent appearance of commercial, high-conductivity, and moldable polymer matrix composites [6, 10] provides an opportunity to extend the least-mass and least-energy heat sink design and optimization methodology to these most promising materials. To initiate this process

the performance and metrics of a "classical" plate fin heat sink configuration, fabricated of enhanced polymer material and operating in natural convection, will be determined and compared to the performance and metrics of conventional aluminum and copper plate fin heat sinks.

It is to be noted that the least-energy optimization of air-cooled heat sinks will - in this study - focus on the mass and cooling capability of the fins, while the heat sink base will be assumed to be isothermal. Such an isothermal base is often encountered in a heat sink with a small base plate, or with a heat pipe or vapor chamber base plate, as shown by Zhao and Avedisian [39], and Garner and Toth [40]. It is, nevertheless, important to note that in a high-performance heat sink, the base thickness is typically in the range of 5mm-10mm and may represent between 25% and 50% of the total mass of the heat sink [41]. While the heat sink base can be optimized for minimum mass, as for example in [41], and for minimum energy, the minimum energy optimization of the heat sink base is not included in the present study.

4.2 Heat Sink Design Metrics

In a typical heat sink design the objective is to achieve target heat dissipation, while restricting the consumption of valuable resources such as mass, pumping power, pressure drop, space claim, noise, and ultimately cost. Any useful metric would need to capture a relevant performance-to-resource consumption trade-off. In evaluating and characterizing the cooling capacity of a heat sink, it is important to recognize the existence of several distinct fin array metrics, none of which can exclusively account for all the design constraints. Thus, although it might be possible to design heat sinks with any one or several of these parameters as the optimization criteria; to

constructively utilize the available resources, it is imperative to follow a systematic integrated methodology that intelligently incorporates these constraints early in the design process. To achieve this goal, it is important to pursue the design by using a set of carefully constructed metrics. The metrics presented in this section are expected to be applied to heat sink design, individually or in combination, depending on the specific motivation of the designer.

Thermal resistance, R_{hs}: This metric, defining the temperature rise penalty associated with the use of the heat sink, is the most commonly used thermal characteristic of heat sinks, i.e.

$$R_{hs} = \theta_b / q_T \quad \text{(K/W)} \tag{4.1}$$

Where θ_b is the excess temperature of the heat sink base (K) and q_T is the total heat sink heat dissipation (W). While system designers may find R_{hs} the most useful of the heat sink metrics, it usually masks the effect of heat sink area, as well as volume and material choice, on thermal performance.

Array heat transfer coefficient, h_a: This thermal metric is, perhaps, the parameter most reflective of the "intensity" of heat transport from an electronic component and can be expressed as,

$$h_a = q_T/LW\theta_b \quad \text{(W/m}^2\text{-K)} \tag{4.2}$$

Where, L and W are the length and width of the heat sink base, respectively. The overall thermal capability of a heat sink can be represented by the array heat transfer coefficient.

Space claim heat transfer coefficient, h_{sc}: Following Iyengar and Bar-Cohen [45], the "space claim" heat transfer coefficient, h_{sc}, which represents the thermal utilization of the volume occupied by the heat sink ($L \times W \times H$), can be determined as

$$h_{sc} = q_T / (LWH\theta_b) \tag{4.3}$$

Mass-based heat transfer coefficient, h_m: Due to the importance of minimizing the weight, as well as the cost, of a commercial heat sink, it is useful to evaluate the thermal utilization of the mass of the heat sink. This can be represented by the "mass based" heat transfer coefficient [45], as:

$$h_m = q_T / (\theta_b V_p \, \rho_p) \tag{4.4}$$

Coefficient-of-Performance, COP: By analogy to refrigeration systems, it is helpful to determine the COP of the heat sink, relating the cooling rate, q_T, to the fluid power imparted to the airflow by the fan, IP, i.e.,

$$COP = q_T / IP \tag{4.5}$$

Where IP does not include the fan inefficiency and is equal to,

$$IP = V_{air} \, \Delta P \tag{4.6}$$

Where V_{air} is the volumetric airflow rate and ΔP is the pressure drop across the heat sink.

Total Coefficient-of-Performance, COP_T: Extending the COP concept to address issues of sustainability, it is possible to define a COP_T, relating the cooling capability to the total energy invested in the formation and fabrication of the heat sink, as well as in the operation (as above) of the heat sink, i.e.

$$COP_T = q_T \, t_1 / W_T \tag{4.7}$$

where, $\quad W_T = E_m \times M + IP \times t_1$

Where, E_m, is the fabrication energy kJ/kg and IP is the input pumping power, W and total time of operation is t_1 in secs, M, is the total heat sink mass in kg.

The development and optimization of a particular heat sink design requires guidelines regarding the relative importance of the various thermal metrics. In many applications, it is necessary to perform the least-mass, least-space-claim, and COP optimization within the domain in which thermal performance requirements are met. However, insightful use of the h_m , h_{sc} , COP, and COP_T metrics early in the design process will serve to define the parametric zone of the design space in which thermal management opportunities and costs are most nearly in balance with the design requirements and constraints.

4.3 Heat Sink Design Methodology

The complete heat sink design and optimization methodology can be divided into three parts. The first part, as shown in Fig. 4.1, involves selecting the design objectives, available resources, identifying the parametric space, and setting the target values of the design metrics that will meet or exceed the system specifications during operation.

The second stage involves selecting an appropriate optimization technique and developing a solution engine in order to generate solution sets. At this stage the metric trades off are done and the final design parameters, both geometric and operational, are selected. Finally, the third stage involves CFD modeling, simulation, prototype building and experimental testing to verify the performance of the heat sink.

63
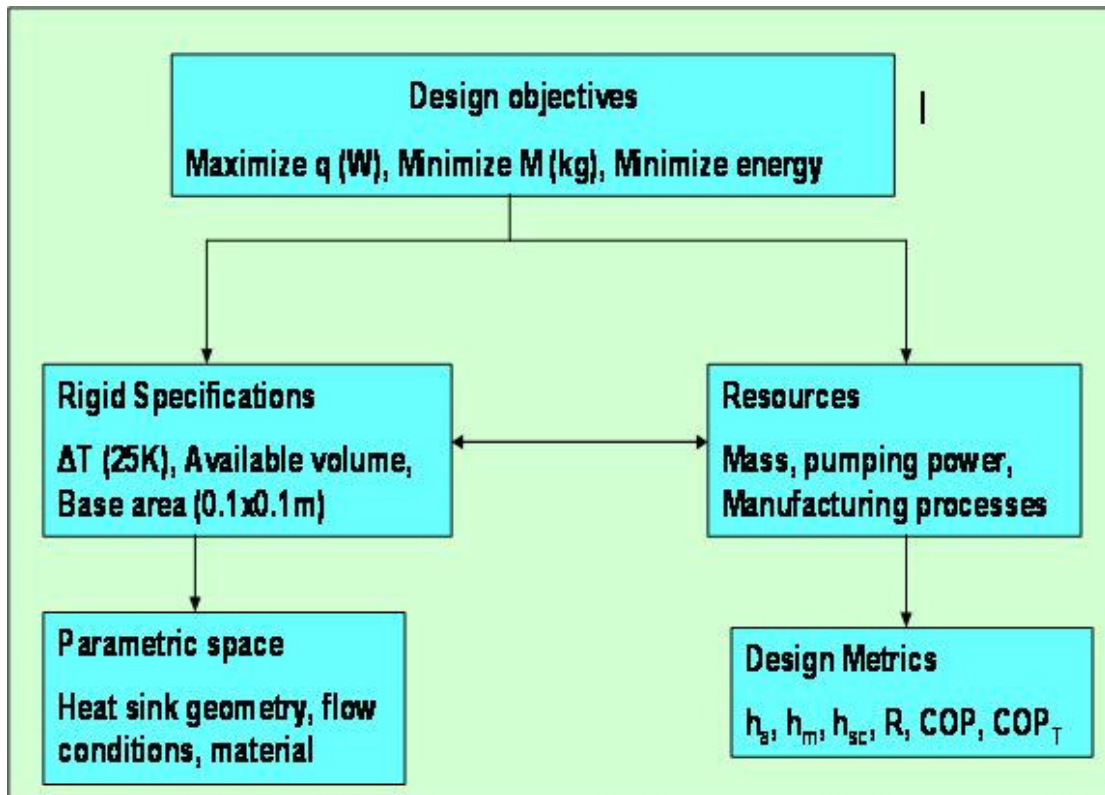
Figure 4.1 Flow chart depicting heat sink design planning scheme

To best explore a broad design space and multiple metrics at minimum cost and in a short time, extensive use is made of theoretical modeling early in the design process. Commercial software tools such as Engineering Equation Solver (EES) and Mathematica are used for performing such a broad multiple variable parametric studies. Such theoretical predictions have been found to give good prediction within prescribed parametric ranges [45, 65]. Experimental verification with thermal prototypes and numerical verification with CFD tools are used to obtain the precision and final design verification needed at the final stages of product development. Figure 4.1 and Figure 4.2 describe the complete design and optimization methodology (Appendix E and F).
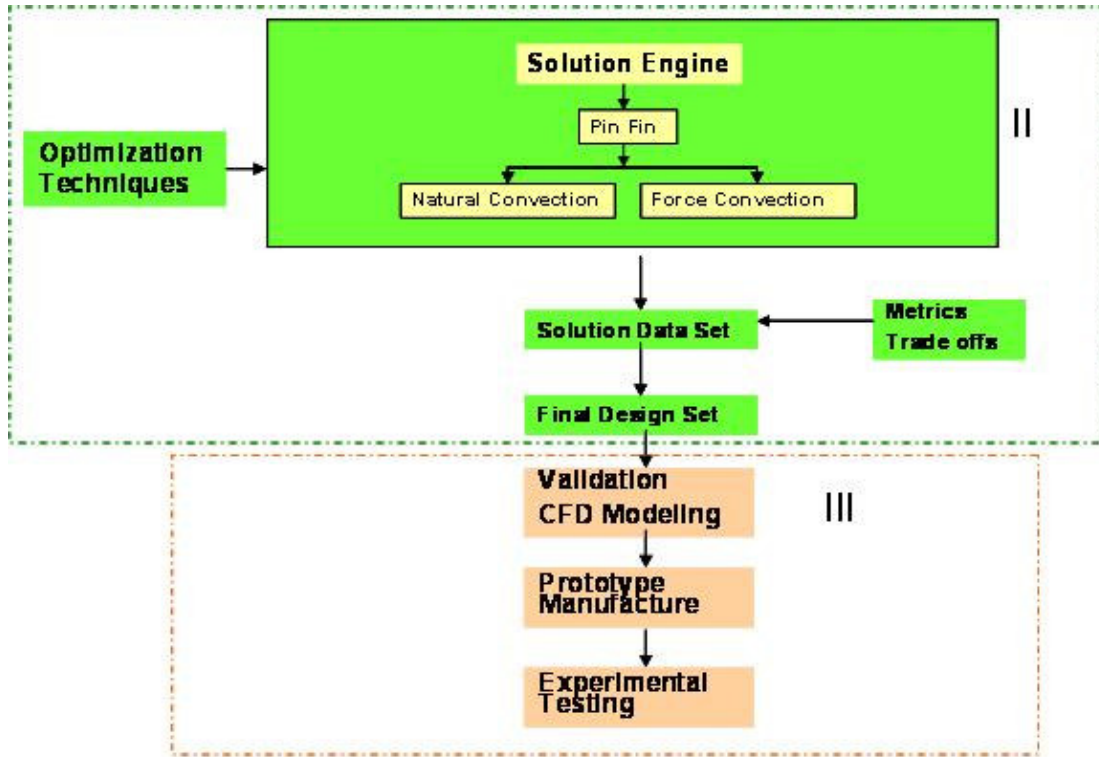
Figure 4.2 Flow chart depicting design optimization scheme

4.4. Natural Convection Plate Fin Heat Sinks

4.4.1 Analytical Modeling

Heat transfer from a fin array, can be represented to a good approximation by

$$q_T = n_{fin}(q_{fin} + h_{base}A_{b,f}\theta_b) \tag{4.8}$$

where it has been assumed that the number of fins equals the number of inter-fin gaps.

Applying the Murray-Gardner assumptions, provided in Kern and Kraus [54], and assuming an insulated fin tip, the heat dissipation capability of a single fin can be expressed as,

$$q_{fin} = Lk_{fin}t\theta_b m(\tanh mH) = (2h_{fin}k_{fin}t)^{1/2}L\theta_b(\tanh mH) \tag{4.9}$$

where, m is the fin parameter equal to $(2h_{fin}/k_{fin}t)^{1/2}$.

Following the pioneering work of Kern and Kraus [54], the least-material fin can be defined by a functional dependence between the fin thickness, t, and the fin height, H, which for individual rectangular, longitudinal (or commonly-called plate) fins, is expressed as,

$$t_p = 0.993 h_{fin} H^2 / k_{fin} \qquad (4.10)$$

Where k_{fin} is the fin thermal conductivity and h_{fin} is the average fin heat transfer coefficient. For such plate fins, the fin efficiency, subject to the usual assumptions [54], can be found via the familiar hyperbolic relation, with the fin height, H, used as the length scale, and given by,

$$\eta = \tanh(m_{fin}H) / m_{fin}H \qquad (4.11)$$

Where m_{fin} is the fin parameter and is defined as,

$$m_{fin} = [2h_{fin}/k_{fin}\, t_p]^{1/2} \qquad (4.12)$$

Kern and Kraus [54] showed that the least-material plate fin is characterized by a unique value of the $m_{fin}H$ product, equaling 1.4192. Since the fin efficiency of such a fin is solely dependent on the $m_{fin}H$ product, the efficiency of the least-material plate fin is a fixed value, equal to 0.627. It is this value of plate fin efficiency that is used in the present study to determine the preferred fin aspect ratio. Eq. (4.10) reveals that the least-material fin thickness is directly proportional to the heat transfer coefficient and to the fin height squared, but varies inversely with the thermal conductivity. Thus, in the presence of low heat transfer coefficients, high thermal conductivity materials (e.g. copper, aluminum) can be used to form very thin – and very high aspect ratio - plate fins. Alternatively, more commonly proportioned fins can perform

successfully even with only moderate thermal conductivities (e.g. polymer matrix composites).

Application of Eq. 4.8 to a natural convection heat sink, in which fluid flow and heat transfer are coupled and the convective heat transfer coefficient is not an independent variable, requires the use of a natural convection correlation. The Bar-Cohen-Rohsenow Nu correlation [57], for natural convection in parallel, vertical plate channels, modified for use with non-isothermal plates takes the form,

$$Nu_{fin}=h_{fin}s/k_{fin}=[576/(\eta_{fin}El)^2+.873/(\eta_{fin}El)^{1/2}]^{-1/2} \tag{4.13}$$

Where, El is the Elenbaas number [58] defined as $(g\beta\theta_b Pr \ s^4)/Lv^2$.
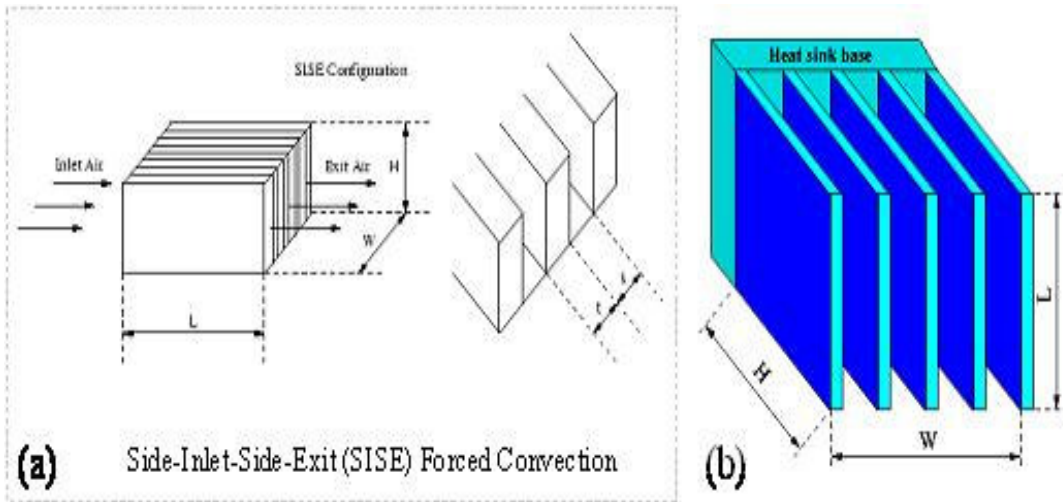
Figure 4.3(a) Side-Inlet-Side-Exit (SISE) Rectangular Plate Fin Heat Sink Configuration, (b) Vertical Natural Convection Plate-Fin Arrays

4.4.2 Optimal Plate Fin Lateral Spacing

Applying the equations described, programmed to be used within specified constraints (see Appendix E) and the terminology of Fig. 4.3, it is possible to generate the thermal performance metrics for heat sink geometries that meet the specified constraints. Figs.4.4, 4.5, and Fig. 4.6 displays the variation of h_a for arrays of vertical copper, aluminum, and enhanced PPS composite plate fins, respectively, for a heat

sink placed on a 10x10cm base operating at an excess temperature of 25K and having a fixed height of 4.5cm.

The h_a for the plate-fin array is seen to rise with increasing fin spacing, attain a maximum value and then drop down, with a further increase in the fin spacing. Fig. 4.4, Fig. 4.5 and Fig. 4.6 reveal that independently of the fin material, the optimum natural convection spacing for the copper, aluminum, and PPS-fiber composite plate fin arrays is nearly 0.8cm, when the fins are thin, and increases modestly to approximately 0.9cm when fin thickness increases to 0.5cm. Based on the earlier work of Elenbass [58], Bar-Cohen [59] provided an expression for the optimum spacing, s_{opt}, of relatively thin fins, as below,

$$s_{opt} = 2.66(Lv^2/g\beta\eta_{fin}\theta_b Pr)^{1/4} \tag{4.14}$$

It may be noted that the optimum spacing is, thus, a function of geometry and the air properties, but its dependence on the thermal conductivity of the fin material is only through the fin efficiency. For the stated conditions, Eq. (4.14) yields a S_{opt} value of 0.8cm, essentially identical to the optimum spacing visible in Fig. 4.4, Fig. 4.5 and Fig. 4.6. These figures also display the effect of fin thickness on the array heat transfer coefficient, h_a. For the high thermal conductivity materials, copper (k=400W/mK) and aluminum (k=200W/mK), the plate-fin array heat transfer rate drops with an increase in the fin thickness from 0.1cm to 0.5cm, since little improvement is realized in the performance of the individual fin and fewer fins can be accommodated. However, for the low thermal conductivity PPS (k=20W/mK), the significantly more efficient 0.2cm thick fins lead to higher overall heat transfer rates, despite the small reduction in fin count. Nevertheless, as the polymer fin thickness is

increased to 0.5cm, the loss in fin surface area, due to reduced fin count, again dominates and the thermal performance falls.
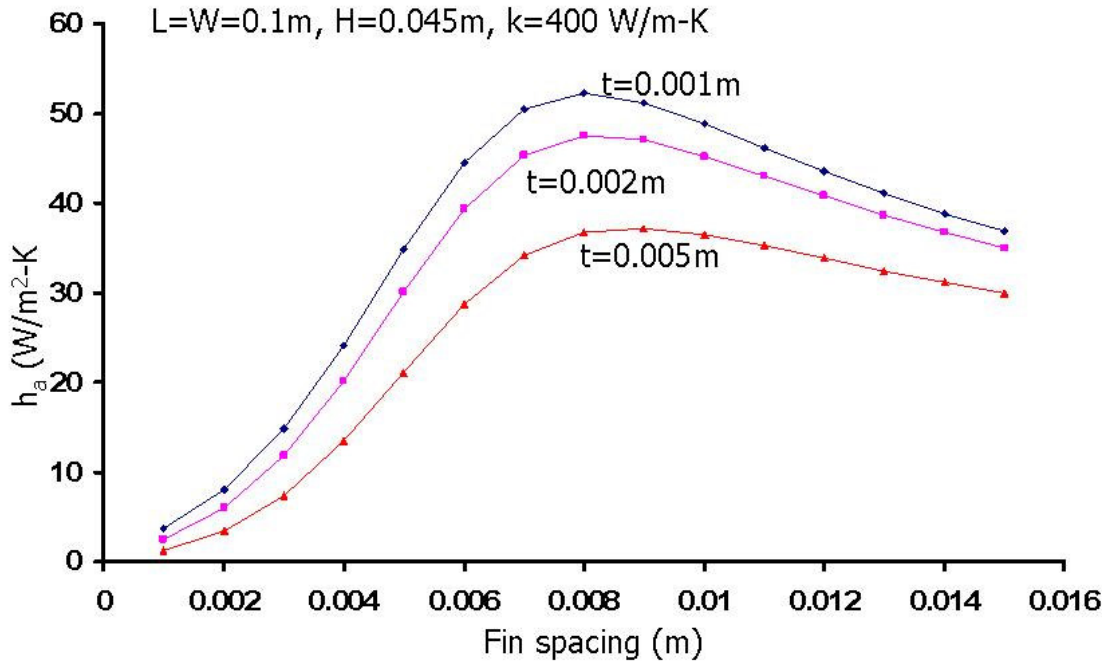
Figure 4.4 Natural Convection Copper Array Heat Transfer Coefficients - Variation with Fin Spacing for 45mm Height (θ_b=25K)
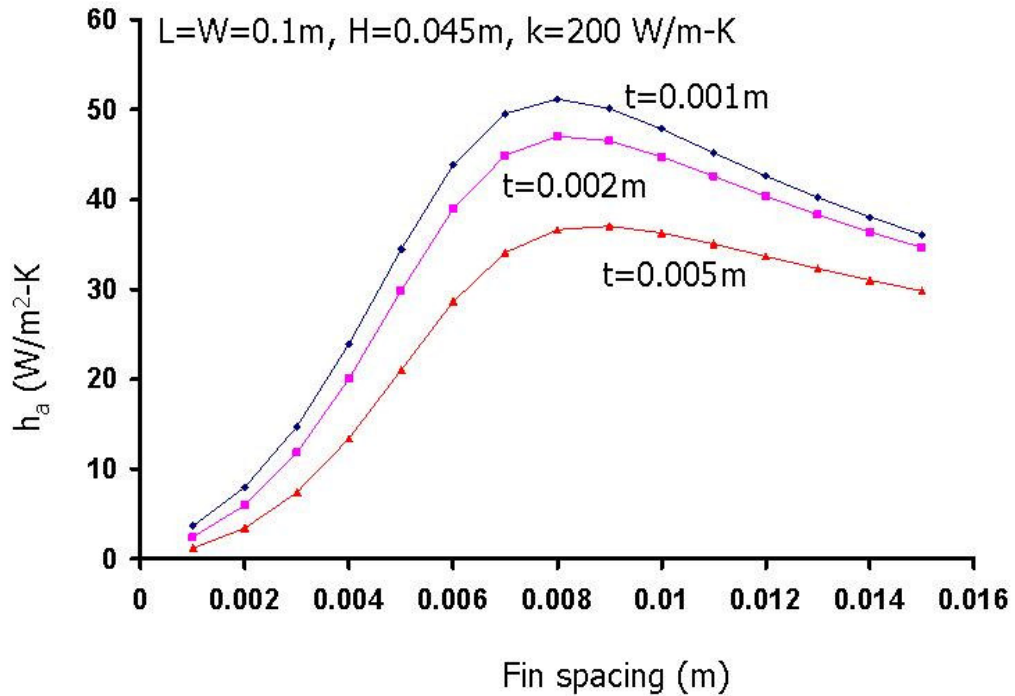
Figure 4.5 Natural Convection Aluminum Array Heat Transfer Coefficients - Variation with Fin Spacing for 45mm Height (θ_b=25K)
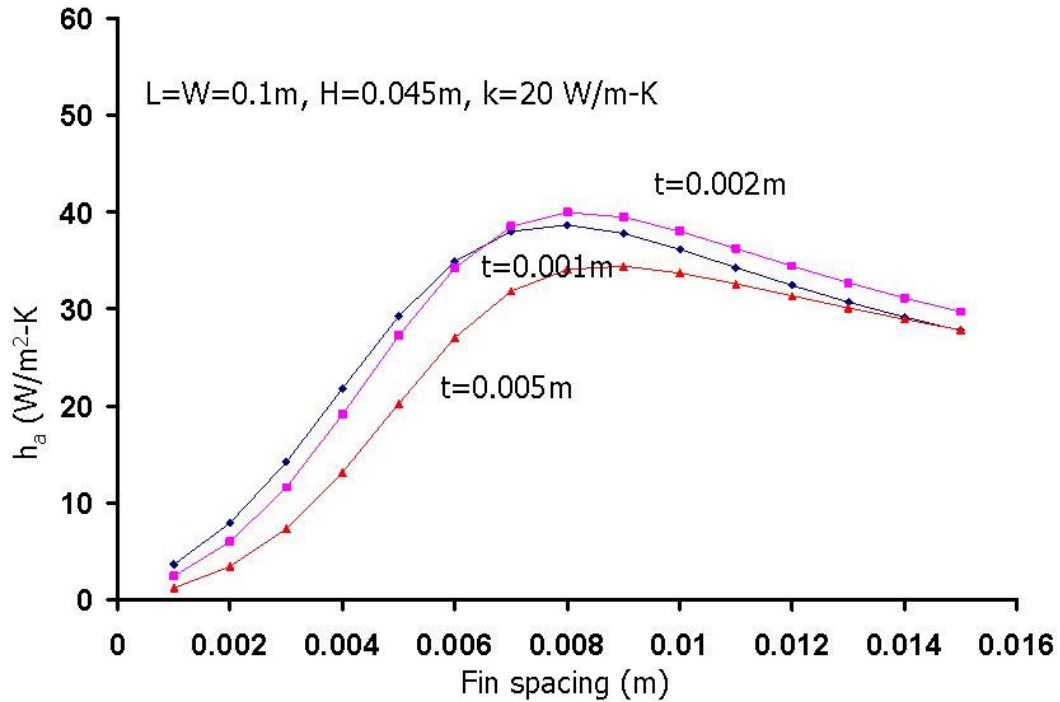
Figure 4.6 Natural Convection PPS Array Heat Transfer Coefficients - Variation with Fin Spacing for 45mm Height (θ_b=25K).

4.4.3 Least-Material "Double Optimum" Design

In keeping with the aims of "design for sustainability" and consideration of the significant energy investment in the formation of plate fins, it is appropriate to examine the design of natural convection arrays using optimally-spaced, least material fins. Prior work has revealed that heat sinks based on such a "doubly optimum" designs are not only best in transferring heat per unit mass, but also consistently provide the highest natural convection heat transfer rates within the least material design domain.

This approach, using the earlier heat sink constraints but relaxing the height restriction, is illustrated in, Fig. 4.7, Fig. 4.8 and Fig. 4.9 for copper, aluminum and PPS, respectively, where the variation of the array heat transfer coefficient, h_a, with fin aspect ratio and fin lateral spacing, is plotted for the least material designs. For a

fixed fin spacing, the array heat transfer coefficient increases with the thickness until it reaches a maximum value and then drops down. For an optimum spacing of 0.8cm the maximum value is 276 W/m^2-K for copper and occurs when the fin thickness is equal to the "optimum spacing" of 0.8cm and the fin height is 94cm. For aluminum the maximum h_a of 196 W/m^2-K is found at the optimum spacing of 0.8cm and an equal fin thickness (of 0.8cm), yielding a fin height of 66 cm, and for a heat sink made of PPS, the maximum h_a value is 64 W/m^2-K at an optimum spacing and fin thickness of 0.8cm and a fin height of 21cm. At this "doubly optimum" point, the maximum h_a values for the plate fin array can be calculated using,

$$h_a = 0.236(k\frac{k_a}{P^2})^{\frac{1}{2}}$$
(4.15)

Where, $P = (Lv^2/g\beta\theta_b Pr)^{1/4}$

The resulting h_a values of 195 W/m^2-K for aluminum, 276 W/m^2-K for copper, and 62 W/m^2-K for enhanced PPS are essentially identical to the values obtained by searching the generated tabulated results of the design space for the peak values of the array heat transfer coefficient.

As previously noted, in referring to Eq. (4.14), the optimum fin spacing is nearly the same for all three materials, as it is a function of geometry and the air properties but depends only weakly on the thermal conductivity of the fin array material through the fin efficiency. Moreover, in keeping with the findings in [60], the "doubly optimum" plate fin array, with fin thickness equal to the optimum spacing, yields the highest heat transfer rates. Fig. 4.10 shows the variation of the least material array heat transfer coefficient with the fin aspect ratio for the PPS material. It may be observed that for each of the fin spacing there is an optimum aspect ratio and that this aspect

71

ratio increases as the fin spacing is reduced. Moreover, even for the wide range of fin aspect ratios considered, Eq. (4.14) properly predicts the spacing (0.8cm) that gives the optimum array heat transfer coefficient.
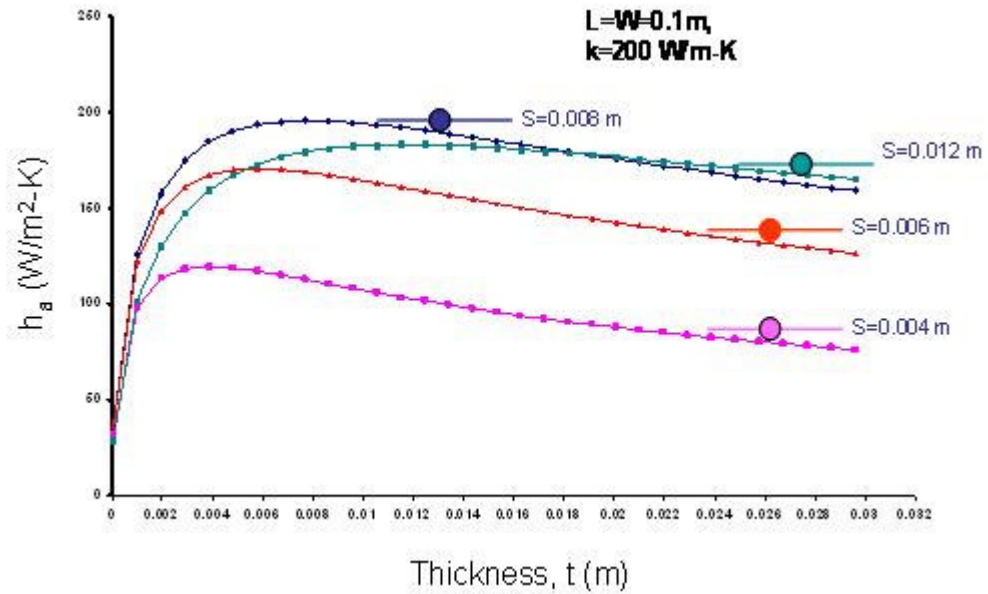
Figure 4.7 Natural Convection Copper Array Heat Transfer Coefficients - Variation with Fin Thickness for Least Material Fins (L= 0.1m, W = 0.1m, θ_b=25K)
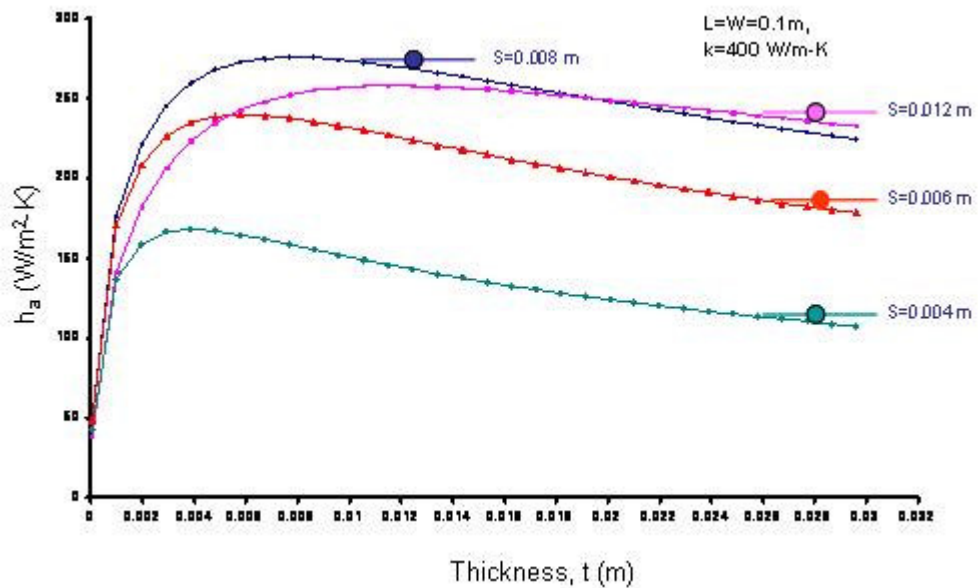
Figure 4.8 Natural Convection Aluminum Array Heat Transfer Coefficients - Variation with Fin Thickness for Least Material Fins (L= 0.1m, W = 0.1m, θ_b=25K)
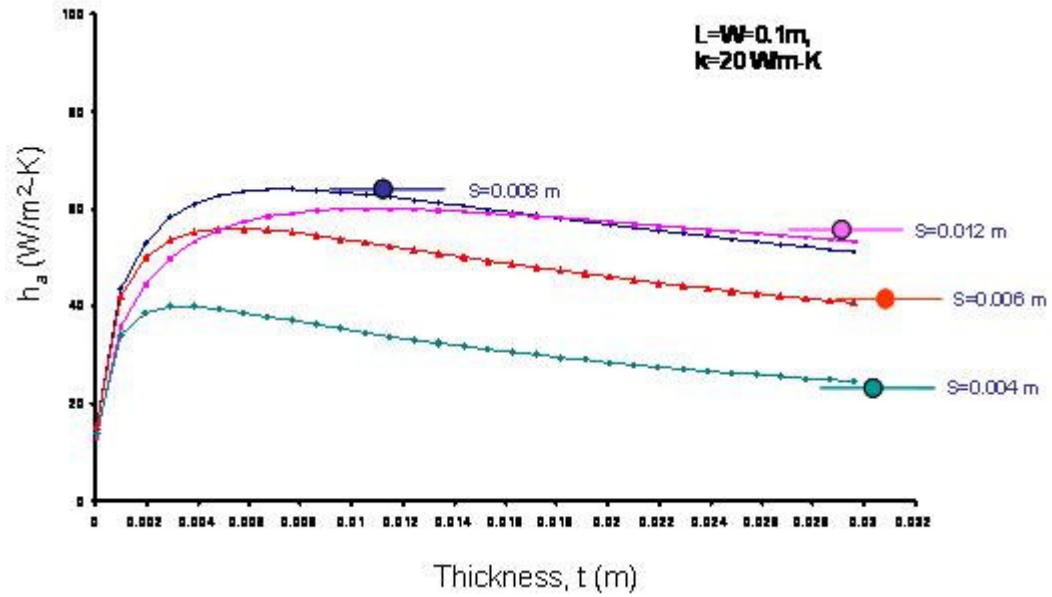
Figure 4.9 Natural Convection PPS Polymer Array Heat Transfer Coefficients - (a) Variation with Fin Spacing for 45mm Height, (b) Variation with Fin Thickness for Least Material Fins (L= 0.1m, W = 0.1m, θ_b=25K)
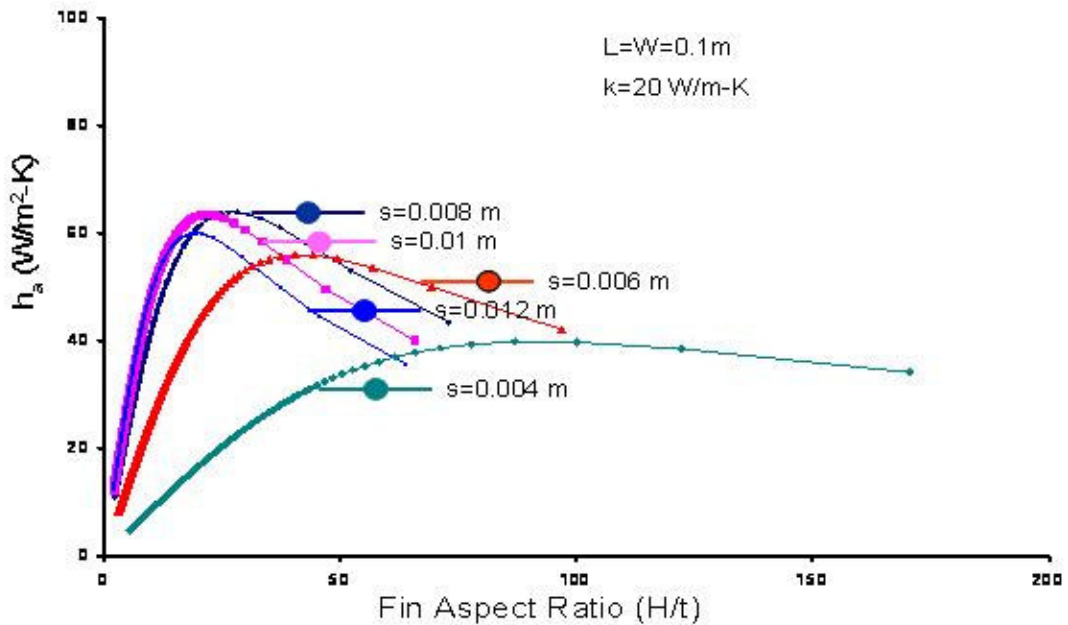
Figure 4.10 Natural Convection Array Heat Transfer Coefficient Variation with Fin Aspect Ratio for PPS Polymer (L= 0.1m, W = 0.1m, θ_b=25K)

In many electronic cooling applications, the fin height is constrained by system considerations. The loci of the maximum array heat transfer coefficients for copper, aluminum, and PPS fins of 4.5cm height are compared in Fig. 4.11 for various fin spacing, while Fig. 4.12 provides a comparison of the h_a values for all 3 materials for optimally-spaced fins with height as a variable, but with the thickness set at 1mm for copper and aluminum and 2mm for the polymer composite. The latter comparison shows that at fin heights below 3.0cm the copper-aluminum-PPS plate fins have identical thermal performance; at fin height of 4.5cm the PPS arrays can provide two thirds of the thermal performance (40 W/m^2-K) of that of the copper and aluminum heat sinks (50 W/m^2-K). However, as the fin height increases further, the higher thermal conductivity provides the copper fin arrays with a greater and greater heat transfer advantage. Thus, the copper heat sinks reach peak values of 180 W/m^2-K at a fin height of 40cm, while the aluminum arrays attains h_a values of 125 W/m^2-K at fin height of 22 cm, and the PPS arrays reach a maximum value of 55 W/m^2-K at fin height of 10cm. Thus, in each case, the peak heat dissipation capability for these optimally-spaced, constant thickness fins is attained at the "least material" fin aspect ratio appropriate to the thermal conductivity of that material. Interestingly, even the low conductivity polymer composite heat sink can thus provide array heat transfer coefficients that are some 11 times greater than could be achieved by natural convection from a bare surface of these dimensions and excess temperature.
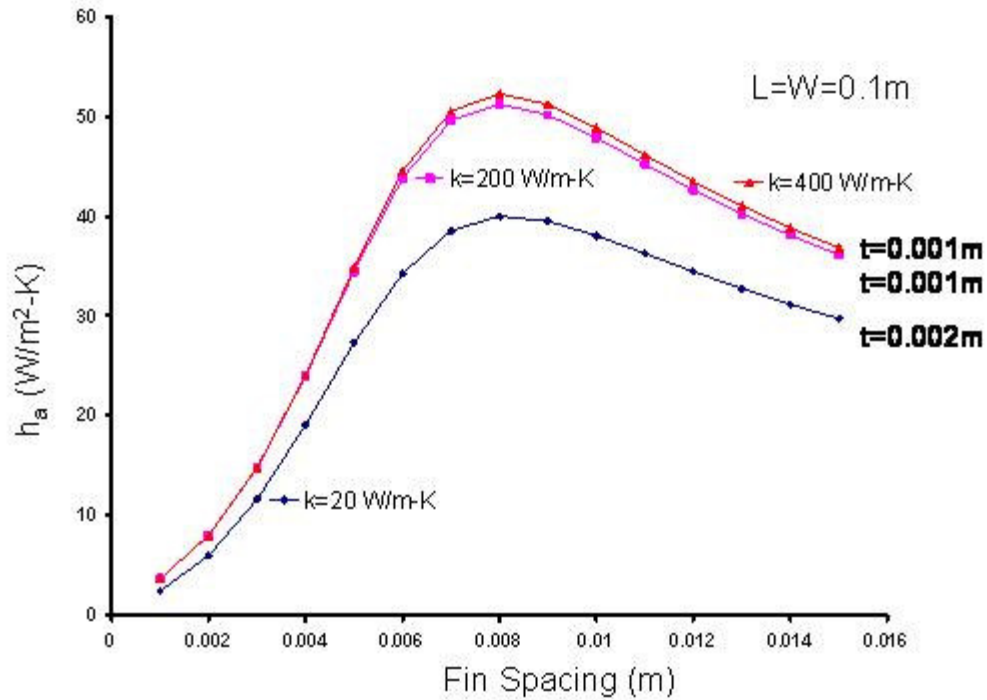
Figure 4.11 Natural Convection Array Heat Transfer Coefficient Variation with Fin Spacing and Thermal Conductivity for 45mm Fin Height (L= 0.1m, W = 0.1m, θ_b=25K)
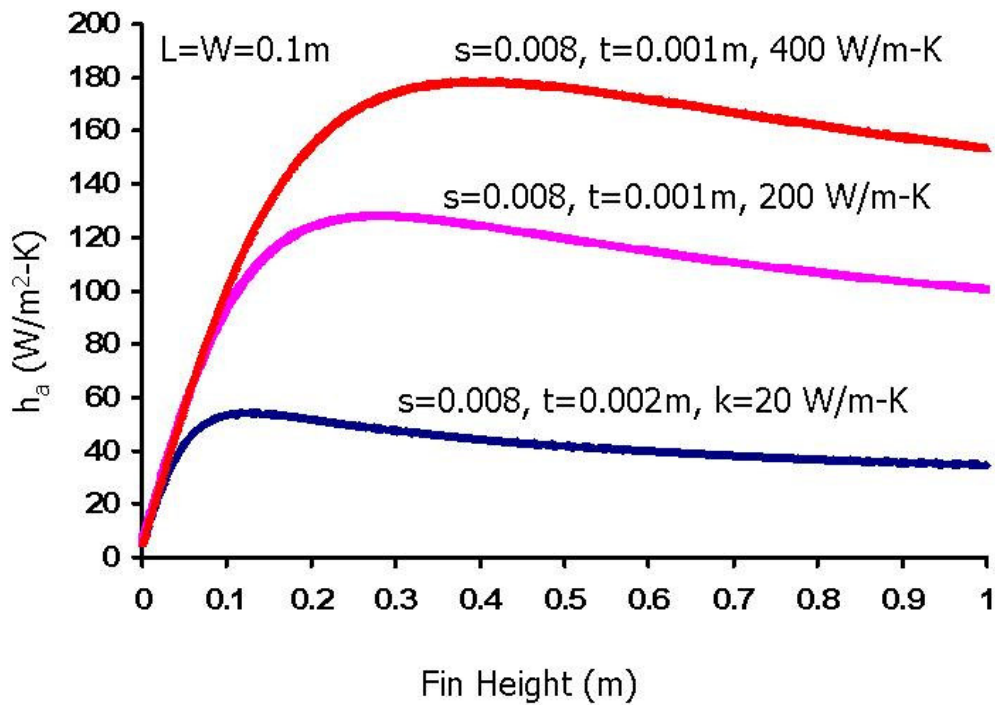
Figure 4.12 Natural Convection Array Heat Transfer Coefficient Variation with Fin Conductivity and Height – Optimally Spaced Fins (L= 0.1m, W = 0.1m, θ_b=25K)

4.5 Forced Convection Plate-Fin Heat Sinks

4.5.1 Analytical Modeling

The analytical methodology developed by Holahan et al. [110] for calculating the thermal performance and pressure drop in fully shrouded, laminar, parallel plate heat sinks has been utilized to characterize the thermofluid performance of the side-inlet-side-exit (SISE) heat sink configurations depicted in Fig. 4.3.

Holahan et al [110] discretized the plate fin into a large number of "patches," and the local heat transfer coefficient was determined from the straight duct flow correlation for developing thermal and hydrodynamic laminar flow between parallel plates with uniform wall temperature, provided in Kakac et al [111] and given by,

$$h_{fin, local} = \frac{k_{air}}{2s}[7.55 + (0.024X^{-1.14}) \frac{0.0179Pr^{0.17} X^{-0.64} - 0.14}{(1 + 0.0358Pr^{0.17} X^{-0.64})^2}] \ (4.16)$$

where, k_{air} is the air thermal conductivity and $Pr = v/\alpha$ is the Prandtl number with v as the mean kinematic viscosity of air and α thermal diffusivity. In Eq. (4.16), X is the dimensionless axial distance, and is given by,

$$X = \frac{xv}{4s^2 U_m Pr} \qquad (4.17)$$

where, x is the distance along the stream tube from the fin entrance to the patch, and U_m is the mean air velocity in the channel. The heat transfer from a patch is determined using the patch fin–to-air temperature difference, θ_b, calculated using the superposition of a kernel function determined from the method of images. For the entire set of points on the fin, θ_b can be written in matrix form:

$$[\theta_b]_{n \times 1} = [C]_{n \times n} [q]_{n \times 1} \qquad (4.18)$$

76

Where the matrix C contains coefficients that represent the combined effect of conduction, convection through the patch, and upstream bulk air heating in the individual channels or "flowtubes," and is given by:

$$C_{i,j} = G_{i,j} + H_{i,j} + B_{i,j}$$ (4.19)

in which $G_{i,j}$ represents the reduction in local fin temperature due to conduction This matrix is found by superposition of coefficients from the method of images. $H_{i,j}$ represent the combined conduction and convection losses local to each patch, and this matrix is found by treating each patch as a circular fin, then applying the Bessel solution and using the convection coefficient from the parallel plate correlation. $B_{i,j}$ represent the decrease in the temperature difference due to bulk heating of the upstream air and it is found from an energy balance applied to the mass of air flowing through each "flowtube.".

Further solving Eq. (4.19) by matrix inversion, the patch heat transfer rate is given by:

$$q_n = (C^T C)^{-1} C^T (\theta_b I)$$ (4.20)

The heat dissipation from the heat sink array, q_T, is then found by the global summation of heat transfer for all the patches, i.e.

$$q = \sum_n q_n$$ (4.21)

The overall pressure drop developed across the heat sink is based on correlations for laminar duct flow and is estimated by again dividing the fin flow field into flow-tubes [110]. The heat sink pressure drop includes all the frictional and dynamic losses, as

$$\Delta P = \Delta P_{fd} + \frac{1}{2}\rho V_{in}^2 K(\infty) + \frac{1}{2}\rho V_{in}^2 K_c + \frac{1}{2}\rho V_{out}^2 K_e$$ (4.22)

Where ΔP_{fd} is the fully developed frictional loss [111]; K_c and K_e are contraction and expansion coefficients, respectively [112], and V_{in} and V_{out} are inlet and outlet velocities. Furthermore, a term $K(\propto)$ is used to account for the hydrodynamic losses associated with developing flow in a parallel plate channel [111] where, $K(\propto)$ is equal:

$$K(\propto) = 0.64 + \frac{38}{R_e} \qquad (4.23)$$

A careful analysis of the resulting heat dissipation rates and pumping power losses, throughout the parametric space of interest, based on Eqs. (4.20) and (4.23) can then be used to guide the designer to the most thermally advantageous combinations of airflow characteristics and fin geometries. Heat dissipation rates obtained with the Holahan et. al. approach were shown to give good agreement with both experimental [110] and CFD results [113].

4.5.2 Candidate Heat Sink Configurations

In the design of a forced convection heat sink, care must be taken to balance the pressure drop of the heat sink with the pressure head available from the selected fan, at the prescribed flow rate. This balance is represented most conveniently on a two-dimensional map, relating the pressure and the volumetric flow rate. In the coordinates of such a map, it is possible to represent both the "fan curve" - shown as several convex lines in Fig. 4.13, and the hydraulic resistance of the heat sink - represented by several concave curves in Fig. 4.13. The fan curve farthest from the origin of this graph represents the highest pumping power choice, while the resistance curve closest to the horizontal axis represents the heat sink most easily traversed by

the airflow. It may thus be seen that, for a given heat sink, as the fan pumping power increases, operation shifts to higher and higher flow rates. Alternatively, for a given fan, progressively higher flow resistances heat sinks will operate at lower and lower volumetric flow rates. The points of intersection between these two sets of curves mark the possible operating points of the heat sink - fan "systems" considered. In pursuing the design of a "sustainable" heat sink, it is important to identify the fan-heat sink combination that yields the maximum heat transfer rate within a specific design domain, subject to the imposed design and operating constraints. It must also be recognized that the operational parameters and array geometries that result from this optimization procedure may not always be achievable using existing manufacturing technology.
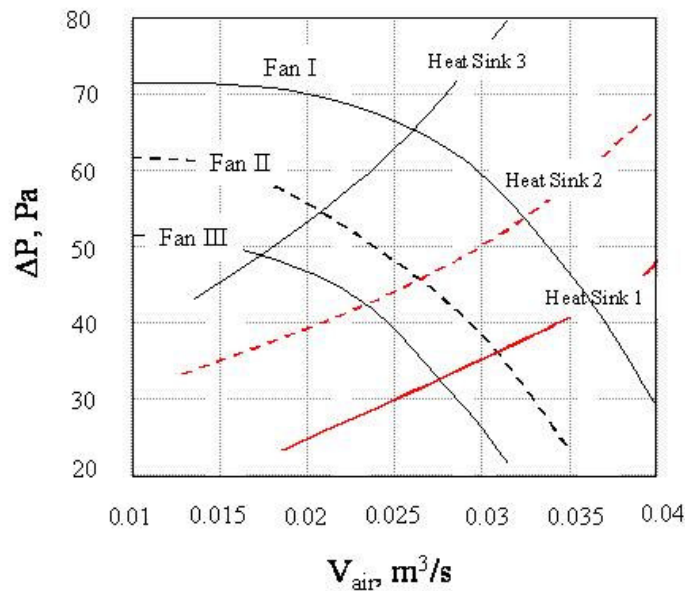
Figure 4.13 Heat sink design space with pressure head – flow rate operating points

An advanced heat sink application, occupying a volume of 500cm^3 [10×10×5cm], with an excess base temperature of 25K, is used to illustrate the "design for

sustainability" methodology. Information gathered from several prominent heat sink manufacturers, and discussed in greater detail in Iyengar and Bar-Cohen [46], serves to establish the geometric constraints which are encountered in today's heat sinks. Volumetric flow rates and pressure heads across the heat sinks were varied from 0.01 to $0.04m^3$/s and 20 to 80Pa, respectively, yielding fluid pumping powers ranging from 0.2W to 3.2W.

4.5.3 Maximum Heat Transfer Design

Fig. 4.14 illustrates the heat transfer rates obtained with the heat sink dimensions described above for two pressure-flow rate conditions at the extremes of the fluid power range: i.e. 80Pa and $0.04m^3$/s (3.2W) and 20Pa and $0.01m^3$/s (0.2W), respectively. With a fixed fin height of 5cm, for each value of fin density (fins/cm), N', there is a corresponding fin-to-fin spacing, s, and fin thickness, t, which meets the pressure drop requirement at the specified flow rate. It may be seen that for a fixed ΔP and V_{air}, designs with very small and very large fin density, N', yield low values of the array heat transfer coefficient, referenced to the heat sink base area, h_a. Low fin densities provide insufficient fin area, A_{fin}, and high fin densities result in a large number of highly inefficient thin fins – both leading to poor heat transfer rates. An intermediate value of fin density can thus be found which maximizes the product of the total fin area, fin efficiency, and local heat transfer coefficient {N' W A_{fin} x η x h_{fin}} and, consequently, yields the highest h_a value for each pressure-flow rate combination.
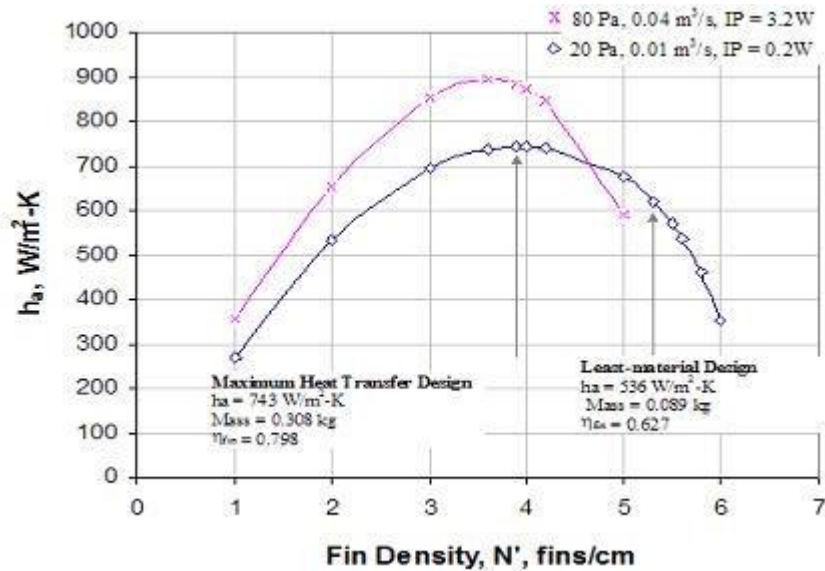
Figure 4.14 Array heat transfer coefficient variation with fin density – High and low fluid power conditions (L= 0.1m, W = 0.1m, θ_b=25K, H = 0.05m, Aluminum)

Examining Fig. 4.14 more closely, it is interesting to observe that, although the locus of h_a values for the higher pumping power condition (80Pa and 0.04m^3/s) is generally above the locus of the lower fluid power combination and peaks at a substantially higher array heat transfer coefficient, these 2 curves cross at 4.5fins/cm. Beyond this value, the need to maintain the pressure drop at 80Pa with the significantly higher volumetric flow rate of 0.04m^3/s, necessitates the use of ever thinner, less effective fins and results in lower overall thermal performance than attained with the 20Pa and 0.01m^3/s flow. This is despite the highly favorable (by a factor of 16) fluid power ratio for the 80Pa and 0.04m^3/s flow. Examining the h_a locus of the 20Pa and 0.01m^3/s flow condition, it is found that the maximum heat transfer rate with an excess base temperature of 25K and a base area of 0.01m^2 is equal to 186W and can be achieved with 4fins/cm, yielding a heat transfer coefficient of 743W/m^{2}K, and a fin mass of 0.308kg, for a mass-specific transfer rate 0.6W/gm or 24.1 W/kg-K. As the fin density increases, the increasing frictional dissipation along the new surface

81

area necessitates a larger fin spacing to maintain the pressure drop, leading to lower

heat transfer coefficients and thinner fins, thus poorer thermal transport rates, and

decreasing values of h_a, despite the obvious increase in fin surface area.

(a) 0.6 W Pumping Power
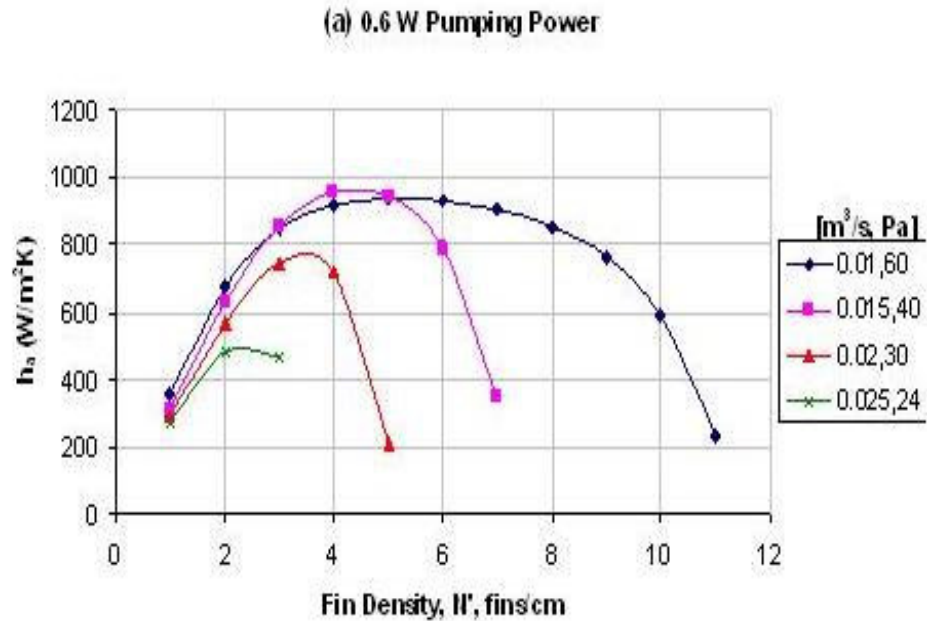
Figure 4.15 Array Heat Transfer Coefficient Variation with Fin Count – Various
Flow Conditions, 0.6W Fluid Power ((L= 0.1m, W = 0.1m, θ_b=25K, H = 0.05m,
Aluminum)

Fig. 4.15 displaying the variation of h_a with the number of fins across a 10cm x 10cm

aluminum heat sink and using 0.6W of operating fluid power – reveals that the

particular choice of the flow rate and pressure head combination directly affects the

breadth and height of the h_a locus. For the conditions examined, the flow rate –

pressure head combination with the highest pressure appears to nearly always yield

the best cooling capability. Plotting the highest array heat transfer coefficients for

three fluid power values – 0.6W, 1.6W and 2.1W - against the fin count, it may be

seen in Fig. 4.16 that the peak h_a values do increase with fluid power and occur at

progressively higher fin counts (48, 55, and 57) as the power increases, with a

consequent improvement in the heat transfer rate by 22 % and 27 %, respectively, to

h_a values approaching 1400W/m^{2}K. Thus, at the upper-limit of heat sink cooling

capability, there is a benefit to the application of greater pumping power, but

alternatively, it is only at the higher fin counts, above 35 fins, or 3.5fin/cm, that

differentiation among the 3 fluid power values begins to be visible.
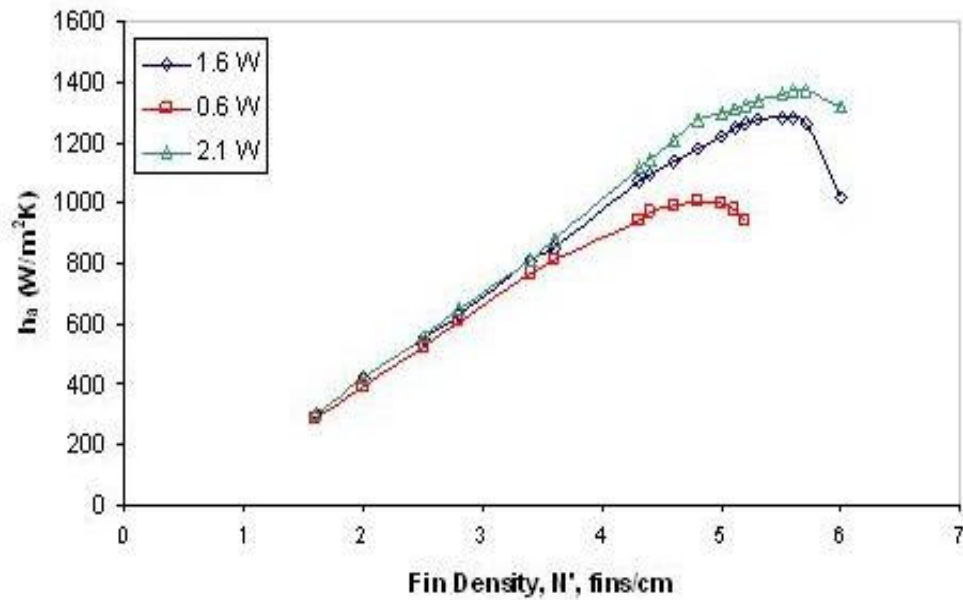
Figure 4.16 Array Heat Transfer Coefficient Variation with Fin Count – Various
Flow Conditions, 0.6W Fluid Power ((L= 0.1m, W = 0.1m, θ_b=25K, H = 0.05m,
Aluminum)

Similar plots for copper and polymer PPS heat sinks are shown in Fig. 4.17 and Fig.

4.18, respectively. As might be expected, use of the high thermal conductivity copper

leads to approximately 20% higher maximum heat transfer rates (peaking at

1600W/m^{2}K) than for aluminum. This peak heat transfer rate occurs at fin counts

approaching 6.5fins/cm, which is some 15% higher than the 5.7fins/cm maximizing

fin density for aluminum.
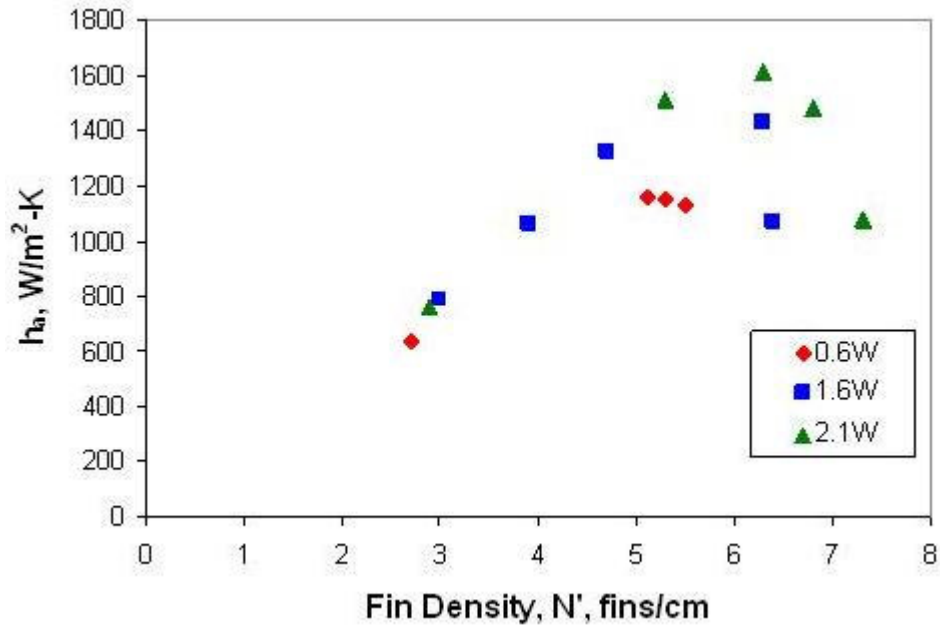
Fig. 4.17 Array Heat Transfer Coefficient Variation with Fin Count and Fluid Power
(L= 0.1m, W = 0.1m, θ_b=25K, H = 0.05m, Copper)
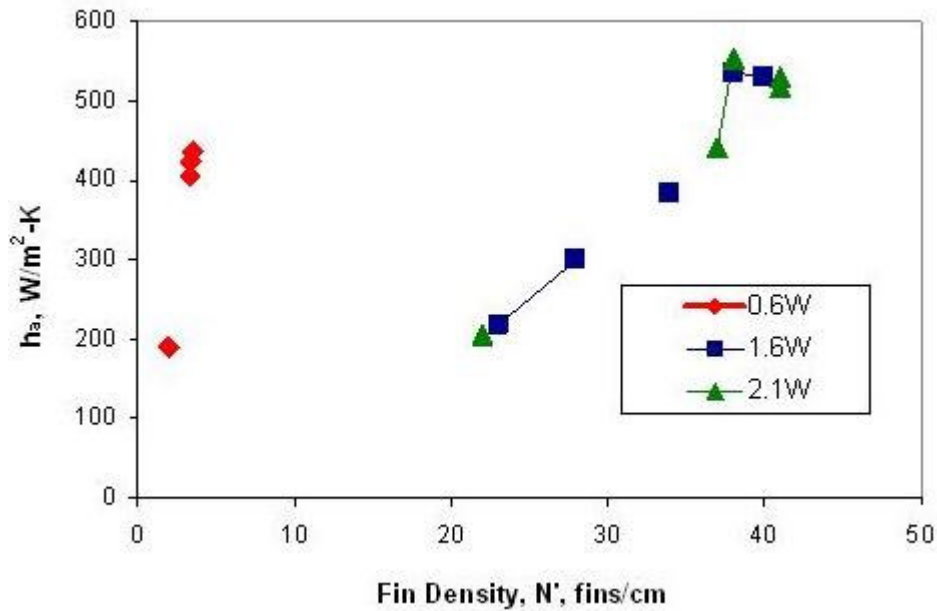
Fig. 4.18 Array Heat Transfer Coefficient Variation with Fin Count and Fluid Power
(L= 0.1m, W = 0.1m, θ_b=25K, H = 0.05m, PPS Polymer)

On the other hand, for the 20W/mK filled PPS material, the maximum heat transfer

coefficients fall to some 40% of those attained with aluminum, peaking at fin density

of 4.0fins/cm and then rapidly decreasing. It is, nevertheless, revealing to observe that

an optimized array of PPS fins [65], with thermal conductivity just 13% and weight only 63% that of aluminum, is capable of providing formidable heat transfer rates and attaining h_a values as high as 550W/m^{2}K.

Chapter 5: Thermal Performance of Natural Convection PPS Composite Pin Fin Heat Sinks

5. 1. Introduction

Pin fin arrays relying on natural convection can be effectively used as heat sinks for various electronic cooling applications. While, aluminum is the current material of choice for heat sinks, the availability of thermally conductive PPS polymers [10] raises the possibility of lighter, more energy efficient, moldable plastic heat sinks with thermal performance in the range needed for commercial applications. The present study involves the application of the Aihara et al [62] correlation, together with the Sonn and Bar-Cohen [55] least-material insulated tip pin fin relation, to the design and optimization of a Polyphenylene sulphide (PPS) polymer, staggered pin fin array on a 10 cm by 10 cm vertical base, operating at 25K above the ambient temperature and cooled by natural convection. This configuration is typical of advanced electronic cooling applications and facilitates a direct comparison between the present results and the reported thermal performance of natural convection heat sinks fabricated of aluminum [65].

While an extensive literature exists on convective heat sinks and fin arrays [42, 60], the available literature devoted specifically to natural convection from pin fin arrays is relatively limited. Early, experimental results [66] were presented for a set of five staggered, widely spaced cylindrical pin fins (fin density of 0.31-1.17 fins/cm^2) on a vertical base with horizontal fins, horizontal upward facing base/vertical fins, and horizontal downward facing base/vertical fins that exchange heat by both natural convection and radiation. However to the authors knowledge,

there is no available correlation for predicting natural convection pin fin array heat transfer, other than Aihara et al [62], and it is obtained for the average heat transfer coefficient along a vertical surface of staggered pin fins, at a fin density of 2.42-9.90 fins/cm^2, one order of magnitude higher than in [66]. Consequently, this correlation [62], along with the work reported in [55], served as the basis for the current least-material optimization of vertical pin fin heat sinks in natural convection. The presented optimization methodology uses the Aihara et al correlation for predicting cooling rates in a wider fin density ranges than reported in the original work [66]. This work focuses on presenting a design and optimization methodology for, and experimental validation of, the thermal performance of PPS polymer pin fin heat sink. Prior to the commencement of this Thesis, no study had addressed the use of relatively low thermal conductivity polyphenylene sulfide (PPS) polymers, for heat sink applications.
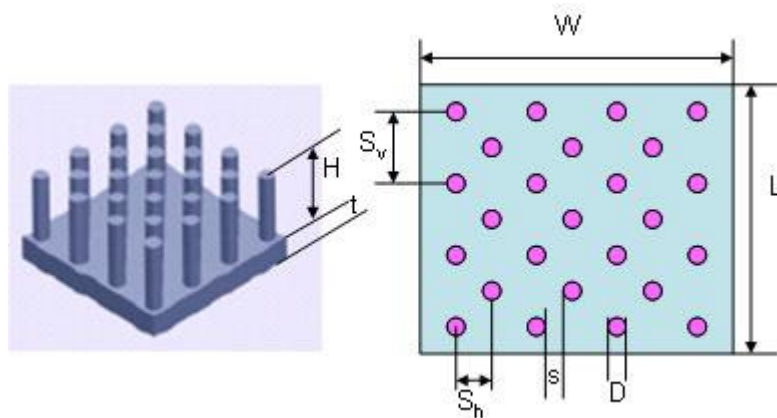
Figure 5.1 Staggered pin fin heat sink

Due to the low heat transfer coefficients encountered in natural convection cooled heat sinks for electronic applications, and the relatively weak dependence of fin performance on the thermal conductivity of the fin [60], and despite their relatively modest thermal conductivity, it may be expected that thermally conductive PPS polymers could be effectively used for commercial heat sinks. For example, the commercially available, thermally-enhanced polyphenylene sulphide (PPS) resin that is reported to possess a thermal conductivity of 20 W/m-K [10], density of 1.7g/cm^3 [10], and a Coefficient of Thermal Expansion (CTE) of 4-7ppm/K [10], could constitute a lightweight, low interfacial stress alternative heat sink material. Moreover, the moldability and ease of fabrication of a PPS polymer heat sink may yield significant cost savings in the development of future commercial heat sinks. Interestingly, the energy required to produce a unit mass of this PPS polymer, at some 115 MJ/kg as described in section 1.3, is about half of the energy required to form the comparable mass of aluminum in section 1.2, making this a most attractive choice for sustainable development.

5.2 Pin Fin Equations

Heat transfer from an array of cylindrical fins is the sum of heat dissipation from the fins and the array base, and can be calculated as,

$$q_T = \theta_b (h_p A_p \eta_p + h_b A_b) \tag{5.1}$$

Where A_b, A_p are the base area and pin fin area (with the fin tip contribution assumed to be negligible) available for heat transfer, respectively, and are given by

$$A_b = n_T (S_v S_h - \pi d^2 / 4) \tag{5.2}$$

$$A_p = n_T \pi d H \tag{5.3}$$

The array dimensions L, W, and H, and the pin configuration d, S_v, and S_h affect the number of pins in the vertical and horizontal direction, as described in the equations below,

$$n_v = (L-d)/S_v + 1 \tag{5.4}$$

$$n_h = (W/2-d)/S_h + 1 \tag{5.5}$$

$$n_T = n_v n_h + (n_v - 1)(n_h - 1) \tag{5.6}$$

Following the form of the Elenbass correlation [61], the Aihara et al correlation [62] predicts pin heat transfer coefficients to within ±10%, in the range d = 0.123 cm, W=10 cm, L=5-20 cm. H=3.2-6 cm, S_v=0.209-0.429cm, S_h=0.212-1.37cm, N=2.25-10.58 fins/cm^2.

$$Nu_{Sh} = h_p S_h / k_b = [2S_v / \pi d][(1/20)(\eta_p Ra_{Sh}^{3/4})$$
$$(1 - 1/e^{120/\eta_p Ra_{Sh}})^{1/2} + (1/200)\eta_p Ra_{Sh}^{1/4}] \tag{5.7}$$

The parametric range of the Aihara et al data falls within the following values [62]: In the test data reported by Aihara et al [62], the vertical separation distance was set to 1.7 or 3.5 times the fin diameter. Heat transfer from the base of the array, using the classical correlation for laminar flow over a vertical flat plate [61, 57], is used for base plate heat loss

$$Nu_b = h_b L / k_b = 0.59 Ra_L^{1/4} \tag{5.8}$$

Following Sonn and Bar-Cohen [55], the relation between pin diameter and height, for a "least-material" fin, which maximizes heat transfer for a specified fin volume (or mass), is given by

$$d_{lm} = 4.73 h_p H^2 / k_b \tag{5.9}$$

The fin efficiency for a cylindrical pin fin is given by Eq. (5.10),

$$\eta_p = \tanh(2Hd^2\,(h_p\big/(k_b d^5))^{1/2})\big/(2Hd^2\,(h_p\big/(k_b d^5))^{1/2}) \qquad (5.10)$$

Using Eq. (5.9) and (5.10), the efficiency of the optimal pin fin is obtained as 0.789.

The heat dissipation from this least material fin was then found to equal [56]

$$q_{fin} = 11.736\theta_b\,h_{pin}{}^2 H^3/k \qquad (5.11)$$

5.3 Pin Fin Heat Sink Thermal Performance

5.3.1 Array Heat Transfer Coefficients

Using the approach outlined above, it is possible to determine the array heat transfer coefficient for a range of pin fin geometries. Fig. 5.2 shows the variation of the array heat transfer coefficient, h_a, with fin height for a subset of PPS, aluminum, and copper heat sink configurations. Focusing first on the PPS fins, it may be seen that an "optimum" fin height exists for each fin diameter-fin spacing configuration. The array heat transfer coefficient appears to increase steeply, as this fin height is approached, and to decrease in a gradual fashion, as this value of H is exceeded. While the enlargement in fin area with height is responsible for the initial increase in h_a, the consequent deterioration in fin efficiency (Fig. 5.3) leads to a reduction in the array heat transfer coefficient for fins of progressively greater height. Fig. 5.2 suggests that for PPS polymer pin fins, with a thermal conductivity of 20W/mK, this transition occurs around fin heights of 15cm. and – that for the conditions stated – h_a values approaching 73W/m^{2}K, or some 15 times greater than natural convection from a bare surface, can be achieved.

Alternatively, the h_a values for the aluminum (k=200W/mK) and copper (k=400W/mK) array can be seen in Fig. 5.2 to reach and exceed 230W/m^{2}K and

320W/m^{2}K respectively, or some 46 and 64 times the natural convection rates on a bare surface, at fin heights of some 45cm and 70cm for aluminum and copper, respectively. At this height the array heat transfer coefficient for the heat sink is still increasing, although at a slower rate for aluminum than for copper. This difference in thermal performance is associated with the much higher thermal conductivity of the copper fins than aluminum and enhanced PPS.
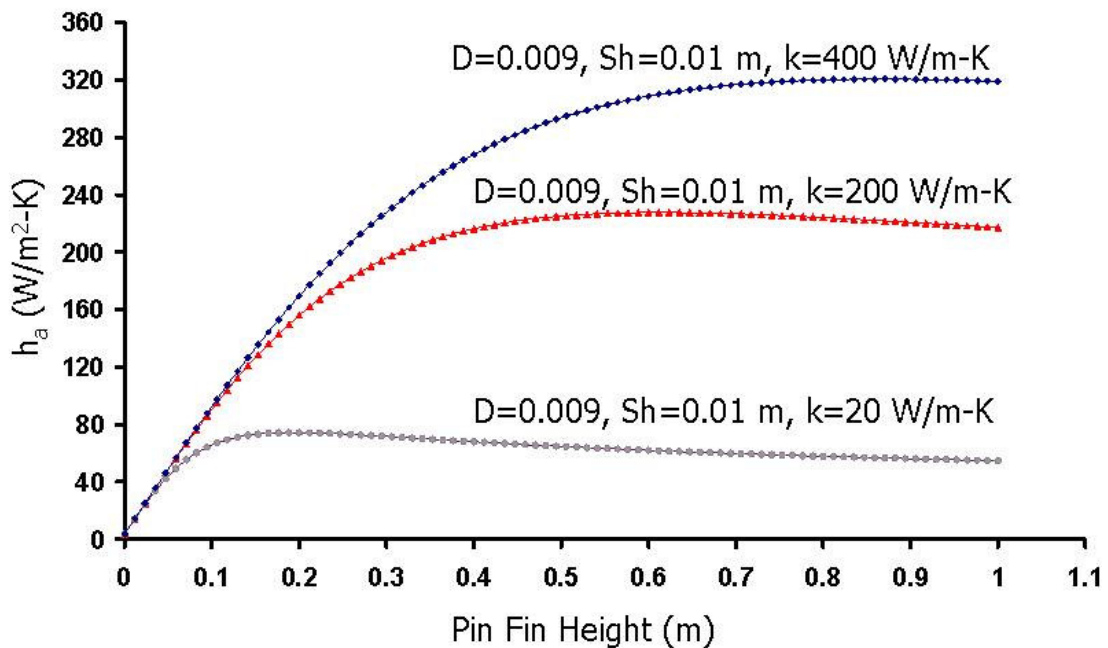
Figure 5.2 Natural Convection Array Heat Transfer Coefficient Variation with Fin Conductivity and Height – Optimally Spaced Fins (L= 0.1m, W = 0.1m, θ_b=25K)

It may also be noted that in the most common range of fin heights, up to 5cm, Fig. 5.2 shows that there is essentially no difference in the array heat transfer coefficients for these three materials and only relatively modest differences up to 10cm fin heights. After this fin height is exceeded, the thermal performance of the PPS pin fin array attains a peak value of 73 W/m^2-K and then flattens out. However the aluminum heat sink thermal performance remains comparable to copper up to fin heights of

15cm. Owing to the relatively high thermal conductivity of copper and the resulting high fin efficiency for relatively tall fins, Fig. 5.2 displays a steady increase in the thermal performance of the copper pin fin array up to fin heights of 75cm and heat transfer coefficients of 320W/m^{2}K, while the aluminum pin fin array peaks at a value of 230 W/m^2-K. Despite the differences in thermal conductivity and fin efficiency (Fig. 5.3), the optimum fin geometry in natural convection for all three materials is attained with a fin diameter of 0.9cm and S_h value of 1.0cm, or a clear inter-fin spacing of just 0.1cm. Detailed analytical-numerical-experimental validation [45] of this performance by a relatively high thermal conductivity the polymer pin fin array is has been discussed in current and Chapter 6.
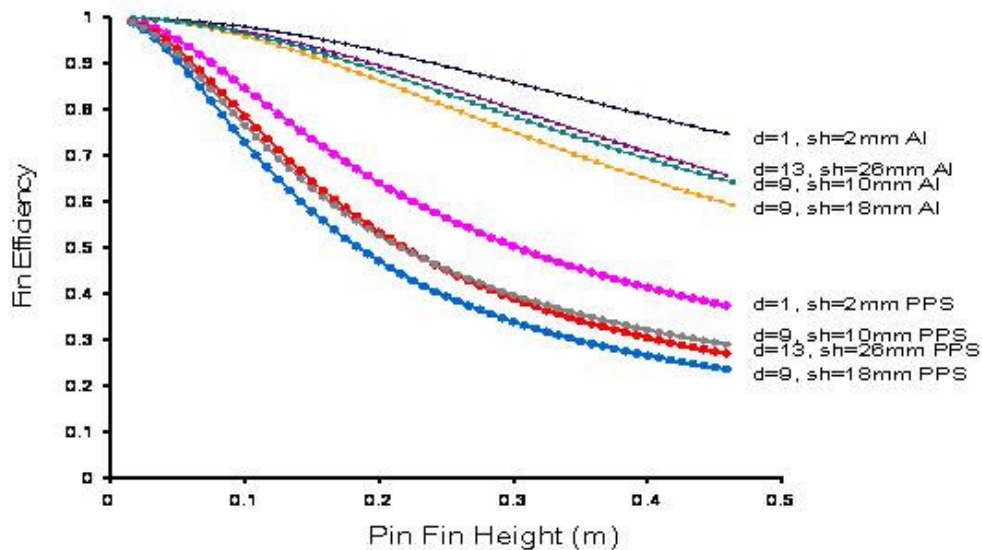
Figure 5.3 Pin fin efficiency for enhanced PPS and aluminum

5.3.2. Optimal Pin Fin Lateral Spacing

Fig. 5.4, obtained by an exhaustive search through the enhanced PPS heat sink solution space, provides the surface of the array heat transfer coefficients for fin spacing varying from 1cm to 2.5cm and the fin diameter from 0.1cm to 1.5cm, for an

92

air cooled, pin fin array operating 25 K above the ambient temperature of 45 $^\circ$C and across a base area of 10 by 10 cm. The 'h$_a$' values are seen to span the range from approximately 30W/m^{2}K to 73W/m^{2}K and to identify the optimum "horizontal" spacing as a S$_h$ value of 1.0cm (diameter = 0.9cm and the clear spacing = 0.1cm), yielding h$_a$ value of 64W/m^2-K. Using, Eqs. (5.1), (5.7), & (5.8), Iyengar and Bar-Cohen [44] determined that the optimum center-to-center spacing between staggered pin fins, i.e. the value that maximizes the array heat dissipation rate, could be expressed in the form used for parallel plate heat sinks [64, 59, and 60], as in Eq. (5.12) below,

$$S_{h, opt} = 3.18 \; P \tag{5.12}$$

Where the parameter P, characterizing the thermal environment, is set equal

$$P = [Lv^2/g\beta\eta_{fin}\theta_b \; Pr_b]^{1/4} \tag{5.13}$$
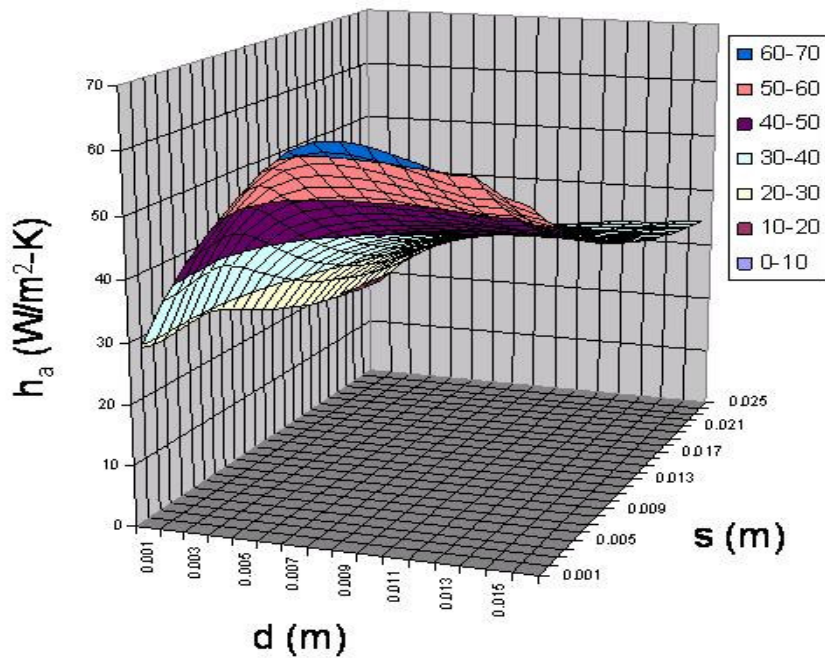
Figure 5.4 Natural Convection PPS Pin Fin Array Heat Transfer Coefficient Variation with Fin Diameter and Spacing (L= 0.1m, W = 0.1m, θ$_b$=25K)

This relation yields an optimum horizontal spacing of 1.0cm for this staggered array of pin fins , identical to that obtained by the elaborate search of the design space and somewhat larger than earlier obtained for parallel plate arrays (0.8 cm). It is to be noted that the optimum spacing for a staggered array of pin fins is, thus, somewhat larger (by approximately 25%) than obtained for parallel plate arrays [65].

5.3.3 Mass Based Heat Transfer Coefficient and COP_T

The heat transfer rate per unit mass of the aluminum and the polymer composite polyphenylene sulphide heat sinks is depicted in Fig. 5.5. The figure indicates that for both materials and for each configuration, the h_m decreases monotonically with fin height, due to the incremental deterioration in the thermal transport capability of fin sections far removed from the base. However, the PPS polymer's reduced density ($1700kg/m^3$, [10]) relative to aluminum (2700 kg/m^3) does provide these polyphenylene sulphide fins with superior mass-based performance, up to fin heights of approximately 10cm.
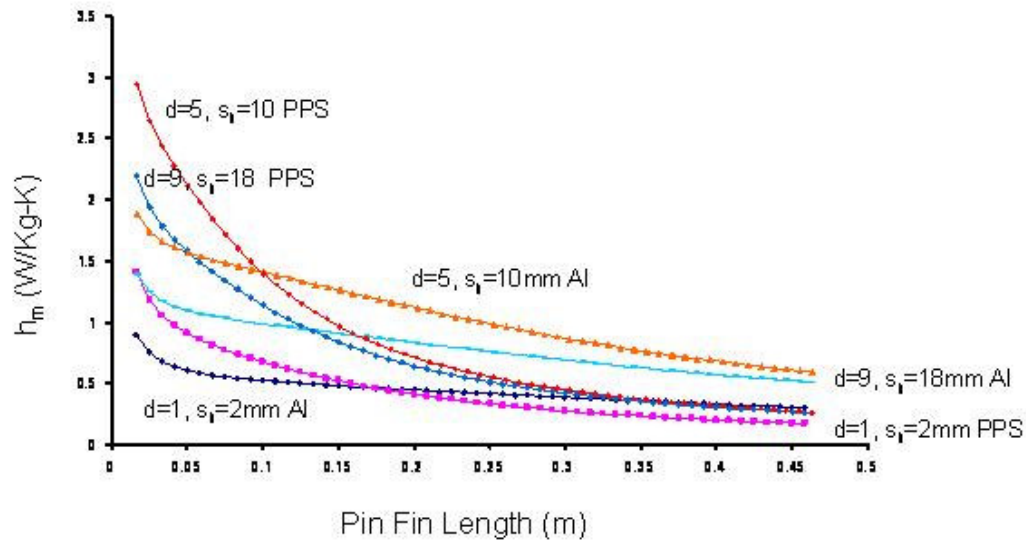
Figure 5.5 Mass-specific Heat Transfer Coefficient Variation with Pin Fin Height, Thermal Conductivity and Diameter for Aluminum and PPS heat sinks.

As the fin height is increased beyond 10cm, the rapid decrease in fin efficiency (Fig. 5.3) of the low thermal conductivity PPS results in nearly constant heat transfer rates, despite the increase in physical surface area, and to a decrease in the mass-based heat transfer coefficient. However, the high thermal conductivity aluminum heat sink experiences a more modest decrease in fin efficiency, resulting in slowly falling values of the mass-based heat transfer coefficient and h_m's that are higher than the PPS fins for heights greater than 15cm.

5.3.4 Space-Claim Heat Transfer Coefficient
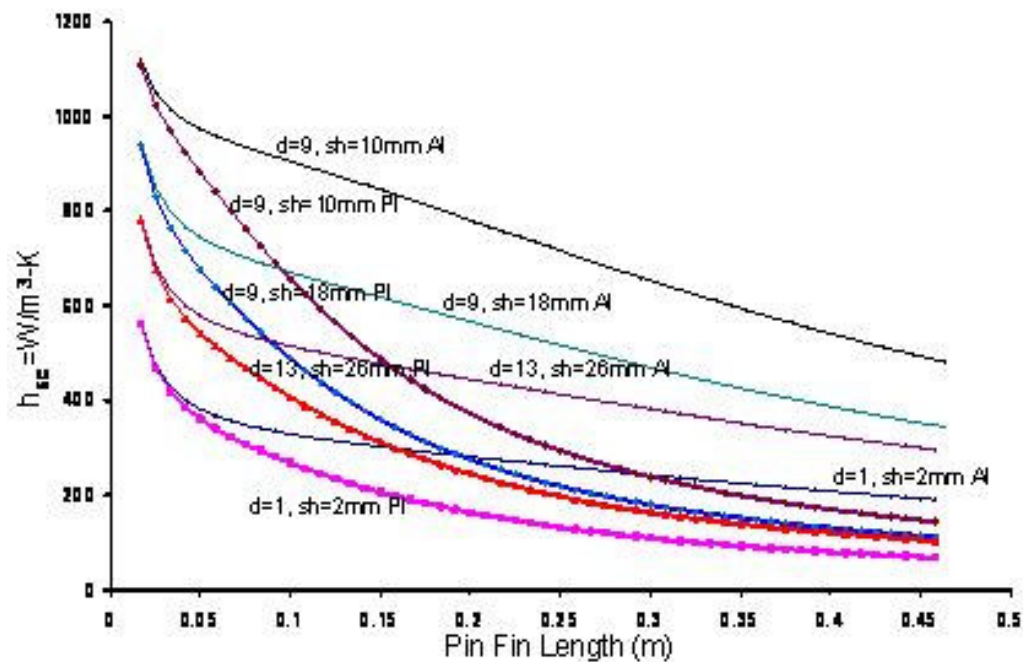
Figure 5.6 Pin fin h_{sc} for enhanced PPS and aluminum in natural convection

The "space claim" heat transfer coefficients, h_{sc}, are displayed in Fig. 5.6 for the polyphenylene sulfide and aluminum least material heat sinks. As previously noted for the mass-based heat transfer coefficients and due, again, to the deleterious effect

of height on the fin efficiency (Fig. 5.3), the h_{sc} values are seen to fall monotonically for both materials and all heat sink configurations. However, as a direct consequence of the higher thermal efficiency of the aluminum fins, these heat sinks experience a less steep descent than the PPS heat sinks and provide significantly higher "space claim" heat transfer coefficient for fin heights greater than 10-15cm. As may be observed in Fig. 5.6, for low fin height the PPS pin fins have comparable "space claim" thermal performance to the aluminum fins.

5.3.5 Energy Efficiency Analysis

Since the invested energy in natural convection arrays, in the absence of fan pumping power, depends exclusively on the required mass, the highest mass based heat transfer coefficient array – for a specified material - will also be the highest COP_T design. As previously discussed in sections 1.2 and 1.3, the fabrication energy requirements for the enhanced PPS (115 MJ/kg, Appendix G) is lower than copper (71MJ/kg) and aluminum (200MJ/kg) and also because of lower mass requirements for PPS due to relatively lower density.

The COP_T value using PPS pin finned heat sink in natural convection is as high as 82 (Fig. 5.7) some 3.3 times higher than the peak copper value of 25 as shown in Fig. 5.8 and 6 times higher than aluminum in Fig. 5.9 for the complete range of parameters in the design space. This clear advantage in the COP_T , or sustainability metric, particularly in the domain of short fins, for the polymer matrix composite derives from the factor of 2 lower fabrication energy requirement than aluminum and the far lower density (by a factor greater than 5) than copper.
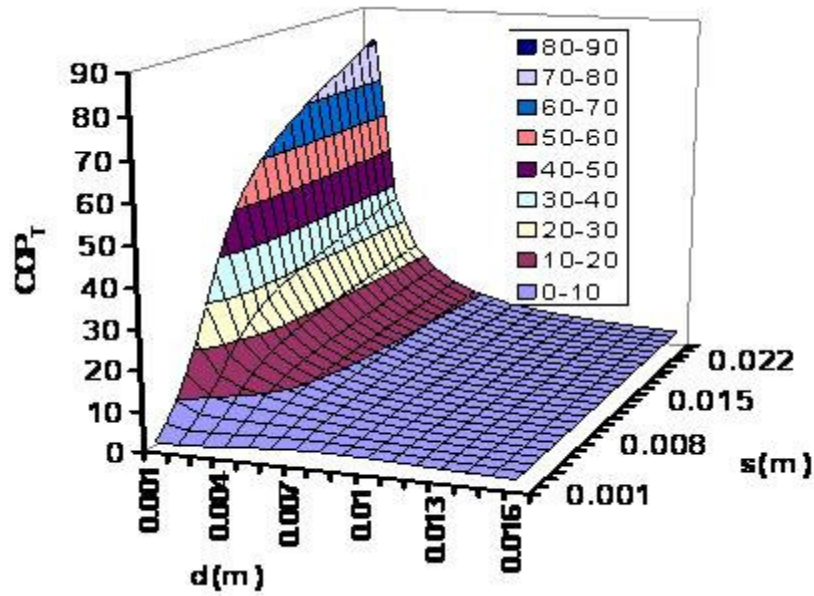
Figure 5.7 COP$_T$ for the PPS pin fin array in natural convection (L= 0.1m, W = 0.1m, θ_b=25K)
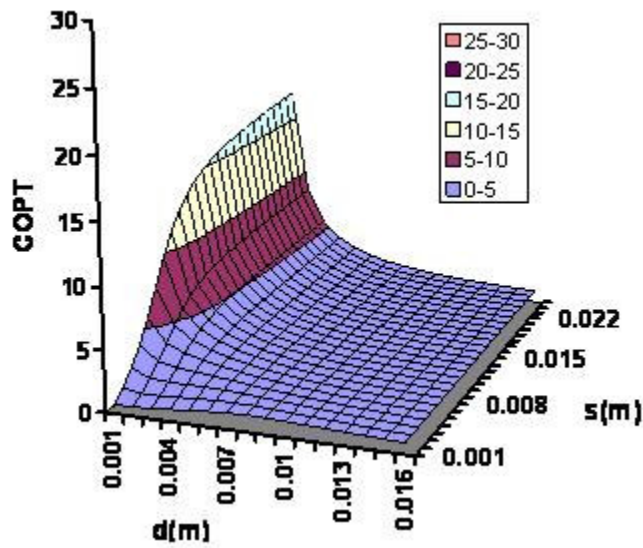
Figure 5.8 COP$_T$ for the copper pin fin array in natural convection (L= 0.1m, W = 0.1m, θ_b=25K)
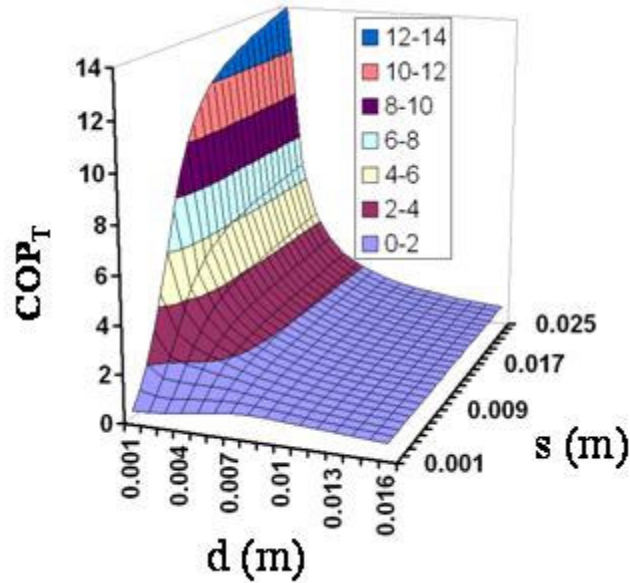
Figure 5.9 COP$_T$ for the aluminum pin fin array in natural convection (L= 0.1m, W = 0.1m, θ_b=25K)

5.4 Least Material Pin Fin Array Analysis

Using the horizontal spacing obtained from Eq. (5.12) to determine the optimum fin heat transfer coefficient from Eq. (5.7) and inserting the result in Eq. (5.9), with an assumed fin diameter of 0.9cm, the "least material" fin height is found to equal 9.3 cm (Fig. 5.10) and to yield an array heat transfer coefficient of ~64 W/m^2-K. From Fig. 5.2 it may be seen that increasing the height of these pin fins to 15 cm increases the array heat transfer coefficient to ~73 W/m^2-K. However, this suggested 15% increase in heat transfer coefficient requires an increase in fin height and fin weight by some 67%, thus substantially lowering the mass-based heat transfer coefficient for this fin array. It may, thus, be argued that – as noted in [65] - an array consisting of such individually optimum, pin fins, placed at the optimum distance from each other, can closely approximate the optimum heat sink configuration.
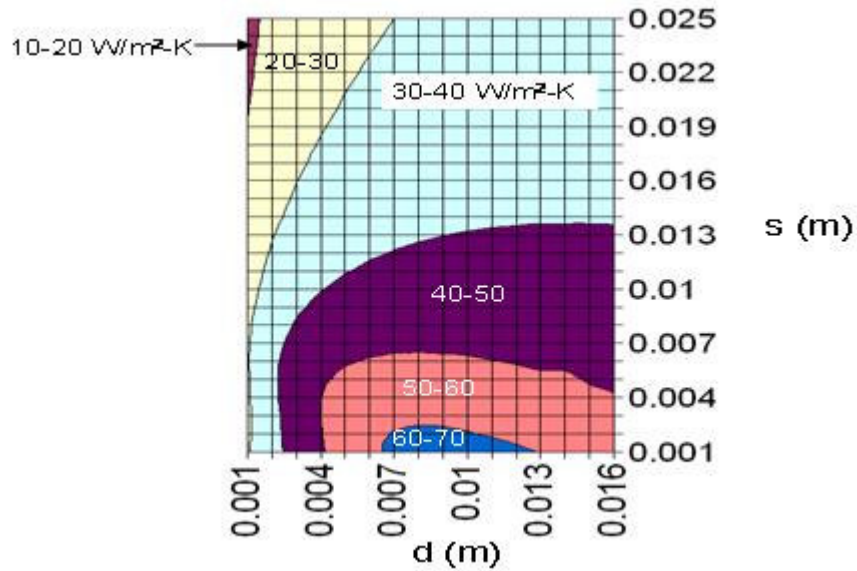
Figure 5.10 Least material h_a for enhanced PPS fins in natural convection
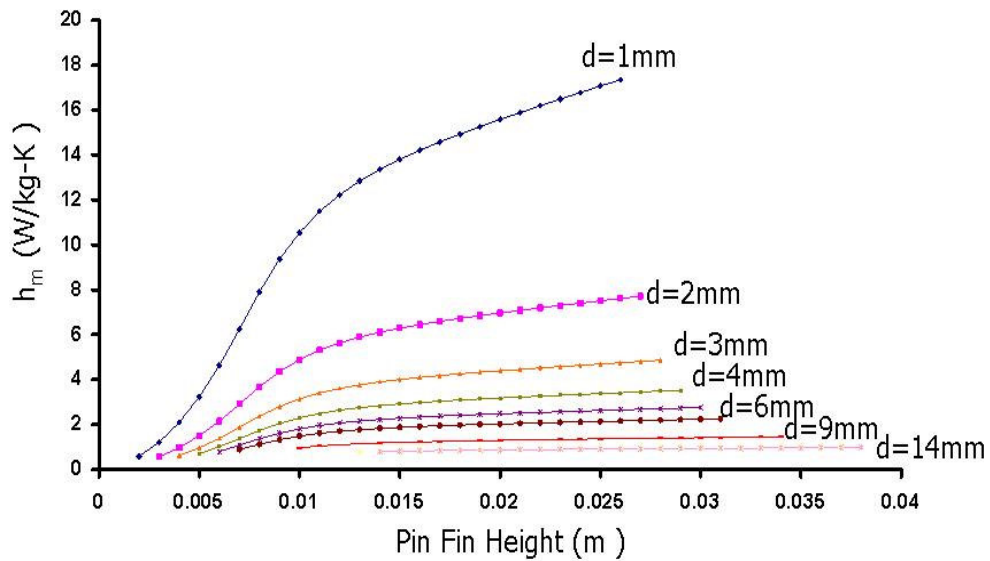
Figure 5.11 Least material h_m for enhanced PPS in natural convection

The mass based heat transfer coefficient of least-material fins increases with decreasing diameter and increasing horizontal spacing, as depicted in Fig. 5.11. The highest observed mass heat transfer coefficient of the PPS polymer heat sink is obtained for an array that has the smallest considered pin fin diameter of 0.1cm and

99

center-to-center horizontal spacing of 2.6cm yielding a value of 17 W/kg-K, nearly 18 times that for the optimum thermal performance array. However, the array heat transfer coefficient for this configuration is just 18 W/m^2-K, or 28% of the optimum PPS polymer pin fin array value of 64 W/m^2-K.

5.5 Pin Fin Array Analysis with Fin Density

The maximum thermal performance for the specified PPS heat sink parameters, yields an h_a value of approximately 73 W/m^{2}K, for 0.9cm fins, spaced 1cm apart, while the highest mass based heat transfer coefficient of the PPS polymer material, at 17W/kgK, is obtained for least-material fins of the smallest considered diameter (0.1cm) and at a center-to-center horizontal spacing of 2.6cm. Thus, the highest h_a configuration and highest h_m configuration, occur at substantially different fin dimensions. Depending on the requirements associated with specific applications, the "best" pin fin array arrangement can be expected to fall between the maxima of the array heat transfer coefficient (W/m^2-K) and the mass based heat transfer coefficient (W/Kg-K). However it is to be noted that an array consisting of individually optimum, pin fins, placed at the optimum distance from each other, can closely approximate the optimum heat sink configuration, providing a balance between achieving the maximum thermal performance and minimizing the mass of a pin fin array.

5.5.1 Parametric Range

In basing the design and optimization of pin fin arrays on the Aihara et al correlation, Eq. (5.7), some attention must be devoted to the parametric range of the

data gathered and correlated in that pioneering study [62], particularly the fin density which reflects the combined impact of both pin fin diameter and fin spacing and varied from approximately 2.25 to 10.5 fin/cm^2. The fin density for the optimized pin fin array, with a pin diameter of 0.9cm and spacing of 1cm, achieves a value of 0.65fins/cm$^{2.}$, which is unfortunately below the range of the Aihara et al correlation. Thus, it must be considered that, in certain of the situations described above, the heat transfer coefficients calculated using the Aihara et al correlation may not be within the stated ±10% accuracy range To aid the reader, the array heat transfer coefficients have been re-plotted as a function of fin density in Fig 5.12 with the domain of the Aihara et al correlation clearly delineated in each figure.

In Fig. 5.12 array heat transfer coefficient as high as 50 W/m^2-K is achievable for a fin density of 2.3fins/cm^2 within the Aihara et al range using pin fin diameter of 4mm. The least material optimized geometry suggests that an h_a as high as ~63 W/m^2-K can be achieved using thicker pin fin of 9mm at much lower pin fin density of 0.65 fins/cm^2 but well outside Aihara et al range.

These predicted values are subject to the accuracy of the Aihara et al correlation used to determine the thermal performance. It is to be expected that within the Aihara et al data range the predictions will be more accurate than outside this domain. Nevertheless, in the absence of other natural convection pin fin correlations, the described optimization methodology provides the best initial design for an optimum fin array and can generally be expected to yield an accuracy of ±10% for configurations that fall within the Aihara fin density range.
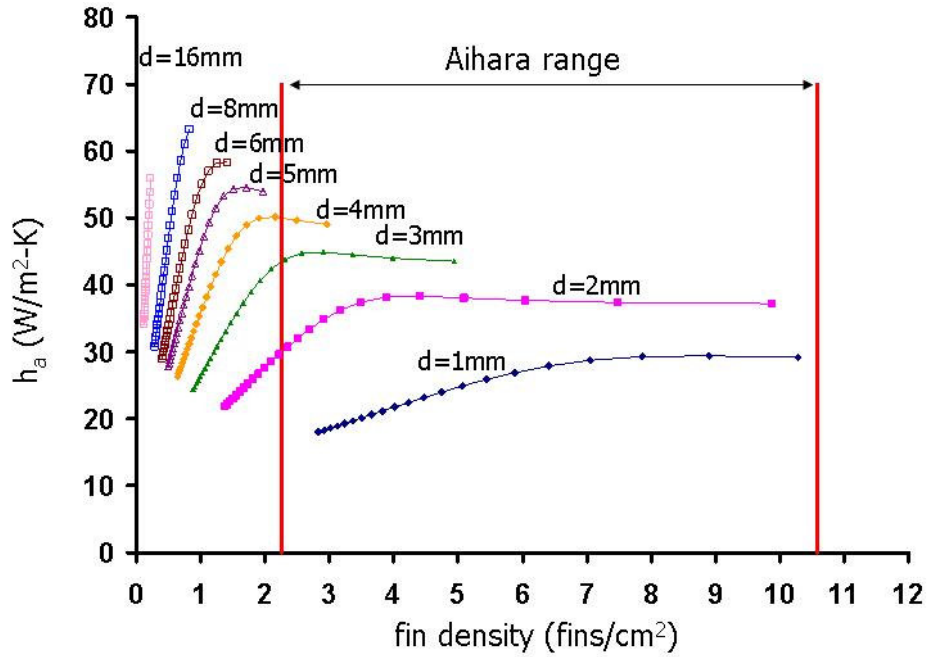
Figure 5.12 Enhanced PPS pin fin h_a variation with fin density in natural convection

The thin, widely spaced PPS pin fins seem to provide the highest mass based heat transfer coefficients in Fig. 5.13, with a value of 17 W/kg-K achieved using a 1mm diameter fin at a fin density of 3fins/cm^2.
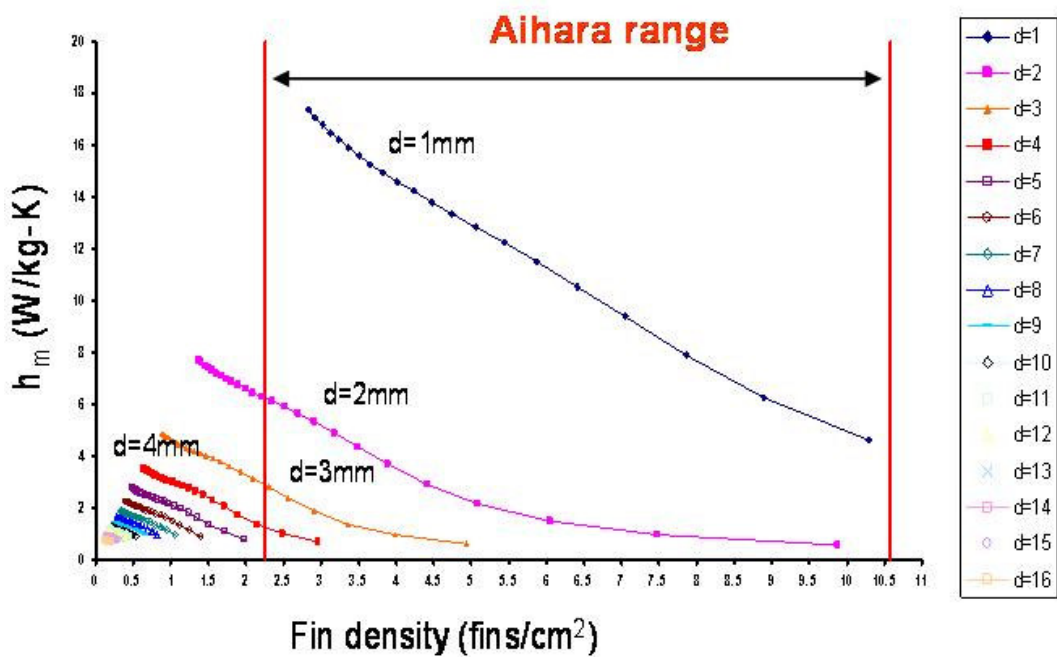
Figure 5.13 Enhanced PPS h_m variation with fin density in natural convection

This is well within the Aihara range, but provides an array heat transfer coefficient of just 18 W/m^2-K. Least material optimized diameter of 9mm and spacing 1mm provides mass based heat transfer coefficient of ~1W/kg-K and array heat transfer coefficient as high as ~64 W/m^2-K.

5.6 Experimental Study

5.6.1 Test Apparatus

Experimental verification of the thermal performance capability of the commercially available, thermally enhanced PPS polymer heat sinks [10] was performed. A 2m x 2m x 2m wooden enclosure (Fig 5.14) was used to isolate the experimental setup from the laboratory environment. The inside walls of the wooden enclosure were painted black to establish a measured surface emissivity of 0.8 using infrared camera for the determination of the radiative heat transfer from the tested heat sinks. The room temperature (~25 ^{o}C) was used as a reference temperature. Commercial E type thermocouples, having an accuracy of ± 0.5 ^{o}C, were used with a copper thermocouple junction box kept at room temperature serving as a reference block. For data acquisition, a switching unit (Agilent 3499 A) and digital multimeter (Agilent 34401 A) with Windows 2000-installed desktop computer were used. A Minco HR5590R11L12B thin film heater, having Nickel wire element of electrical resistance (11 ohms) with a silicone rubber covering, was used as the heat source in the experiments. An identical guard heater to minimize heat loss from the back of the heat sink was also used. The resistance heaters covered about 51% of the heat sink base cross-sectional area.
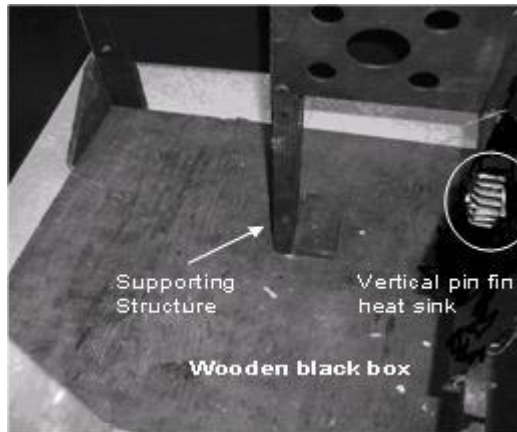
Figure 5.14 Apparatus for natural convection heat sink experiments

The experimental plan was to test and verify the performance of the thermally conductive PPS heat sinks available from CoolPolymer [10]. For this purpose, use was made of a heat sink configuration, which was relatively close to the optimum pin fin array configuration for base plate dimensions of 5.6 cm by 5.6 cm. The pin fin height is 18 mm and the diameter of this tapered fin is 0.398 cm at the base and 0.29 cm at the tip. It is to be noted that at 1.39fins/cm^2, this heat sink falls significantly below the parametric range of the Aihara et al (Eq. 5.7) correlation. Three distinct heat sinks of identical geometry, labeled A, B, C for identification and convenience, were individually tested inside the test chamber at different power levels ranging from 1.2-7.2 W.

After completion of these heat transfer experiments, an extensive effort, detailed in Chapter 3, was devoted to determining the actual thermal conductivity of the material used in these commercial heat sinks. From these characterization experiments and the supporting theory of composite materials, it was determined that the PPS composite thermal conductivity was approximately k_z=15 and k_r=4 W/m-K. As shown in Fig. 5.20, the radial conductivity effects are negligible in natural convection.

5.6.2 Experimental Results:

 The results for 3 distinct heat sink samples of the CSH 043 021 [Coolshield, 10], expressed in terms of the array heat transfer coefficient, are shown and compared in Fig. 5.15. Heat transfer coefficient values ranging from 32W/m^{2}K to 46 W/m^2-K were obtained using the tested heat sinks in natural convection and radiation heat transfer modes, with very good repeatability across the three samples. The overall average uncertainty for all experiments was calculated to be within 3%, as shown in Table 5.1.
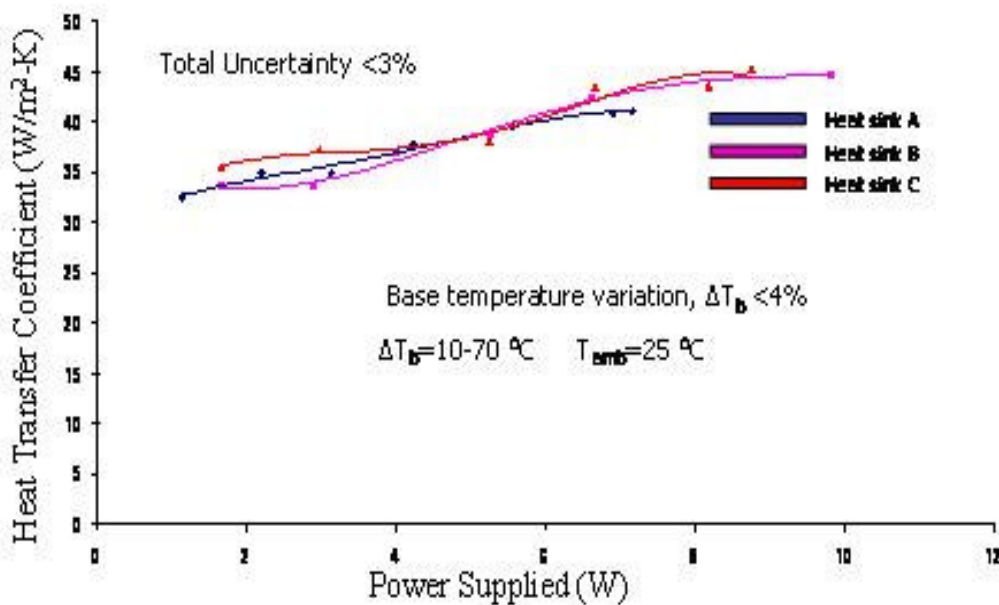
Figure 5.15 Experimental h$_a$ for enhanced PPS heat sink in natural convection

  Fig. 5.16 shows the experimental convection-only heat transfer coefficient values obtained after removing the radiation contribution (~32%) obtained using numerical modeling (section 5.7.3). The experimental convection only results were found to follow the trend of the Aihara et al correlation but, as shown in Fig 5.16, to reach on an average only ~85% of the analytically predicted values for 15 W/m-K thermal

conductivity heat sink with power dissipation from 1 to 7W and base excess temperatures of 10K to 60K above the 25°C ambient. It is believed that this discrepancy is associated with the tested hest sink configuration falling well outside the fin density range of the Aihara et al. correlation described in Eq. (5.7).

Table 5.1: Experimental h_a for enhanced PPS heat sink – values and uncertainty

Power (W)	h_a (W/m^2-K)	Deviation (± W/m^2-K)	Bias error (± W/m^2-K)	Total uncertainty (± W/m^2-K)	% uncertainty
1.12	32.57	0.357	0.120	0.38	1.2
2.19	34.94	0.428	0.089	0.44	1.25
3.12	34.88	0.099	0.071	0.12	0.35
4.21	37.79	0.658	0.066	0.66	1.75
5.55	39.45	0.998	0.060	0.10	2.53
6.89	40.75	0.750	0.058	0.75	1.85
7.16	41.13	0.555	0.057	0.56	1.36
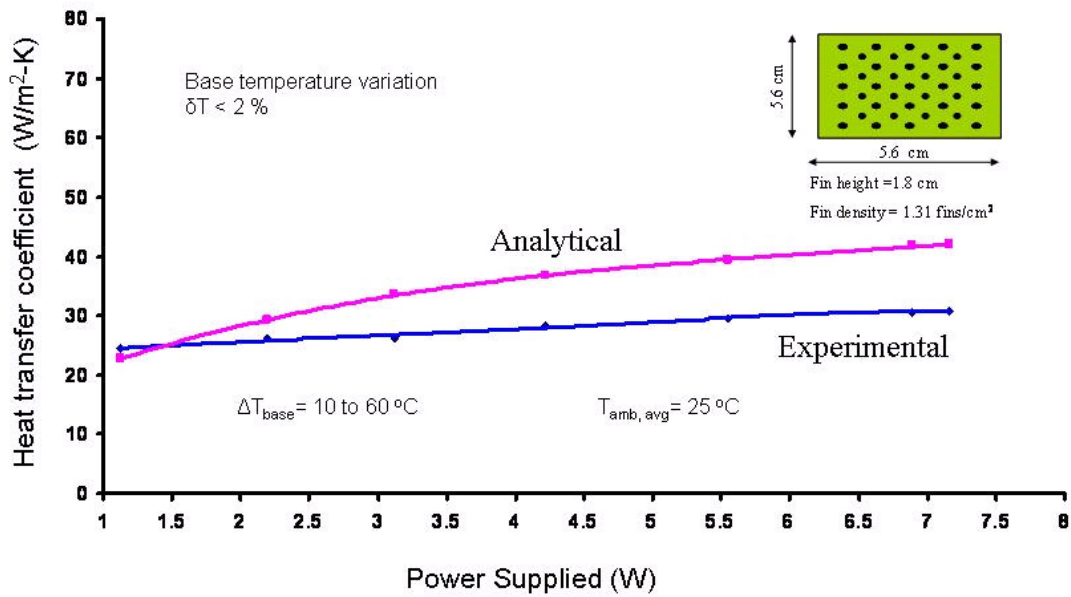
Figure 5.16 Enhanced PPS h_a (convection only) – Experimental/Analytical

106

5.7 Numerical Study

5.7.1 Geometry

The three dimensional geometry of the tested heat sink samples, and the surrounding space (approximately 5 times the volume of the heat sink) was captured using commercial CFD software IcePak as shown in Fig. 5.17. The heater attached to the heat sink was modeled as a constant power source and the insulation layer on the back of the heater with its associated guard heater was represented by a symmetry (or insulation) boundary condition. For the computation of thermal radiation, the emissivity of the PPS polymer heat sink material was set equal to 0.8, as had been experimentally determined with an infrared camera in the laboratory. The built IcePak 7.1, 3D model was run in a UNIX machine having 1.2 GHz processor.

5.7.2 Numerical Mesh Independence
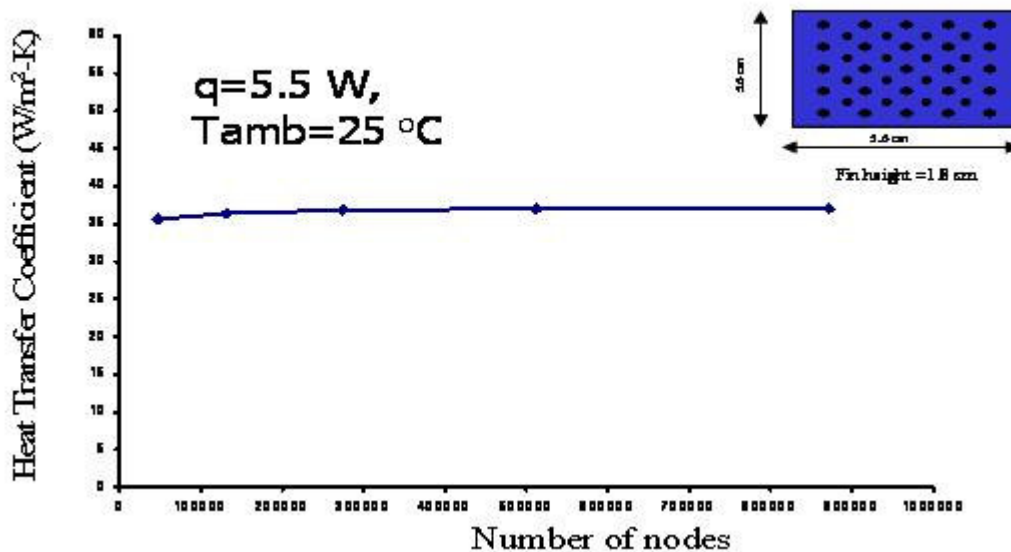
Figure 5.17 Numerical mesh sensitivity of h_a for enhanced PPS heat sink

The mesh independence criteria for the numerical solution of the array heat transfer coefficient for the pin fin heat sink was set to be within 0.1% for two consecutive results during mesh refinement. The resulting plot, in a combined convection and radiation heat transfer mode, is shown in Fig. 5.17 for an intermediate power value of 5.5 W. The plot indicates that about 500,000 nodes were needed to obtain the desired accuracy. The default convergence criteria in IcePak were used to judge convergence for mass, momentum and energy equations.

5.7.3 Numerical Results

The converged computed temperature distribution is shown in Fig. 5.18 and reveals the expected symmetry along the vertical center line of the base plate. Since the heater occupies just 50% of the heat sink base, the temperature field displays a hot zone in the center. Due to the progressively warmer air rising through the heat sink and the decreasing heat transfer coefficient in the vertical direction, as expected for buoyancy driven natural convection flow, this hot zone is shifted upwards from the geometric center of the base, with a maximum excess temperature of 56K occurring 3.3 cm from the leading edge (0.5 cm above the center as shown in Fig. 5.19). Due to these same considerations, the upper fins are hotter than the bottom fins protruding from the heat sink base. The computed air velocity between the fins in the heat sink reached a maximum of 39.8 cm/s for an excess temperature of 56K.

The numerical CFD models were used to simulate heat transfer from the heat sink in the specified test chamber, both with and without thermal radiation. As may be seen in Table 5.2, the numerical simulation of the heat sink performance indicated that thermal radiation contributed about ~32% of the total heat transfer.

108
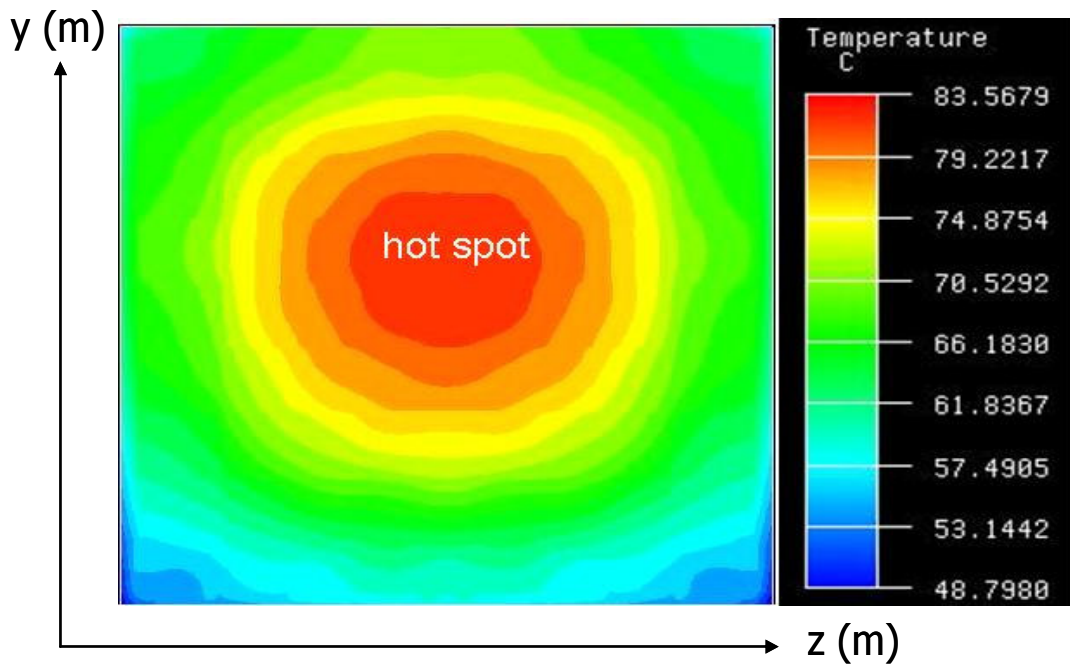
Fig. 5.18 Enhanced PPS heat sink base temperature distribution for 5.5 W
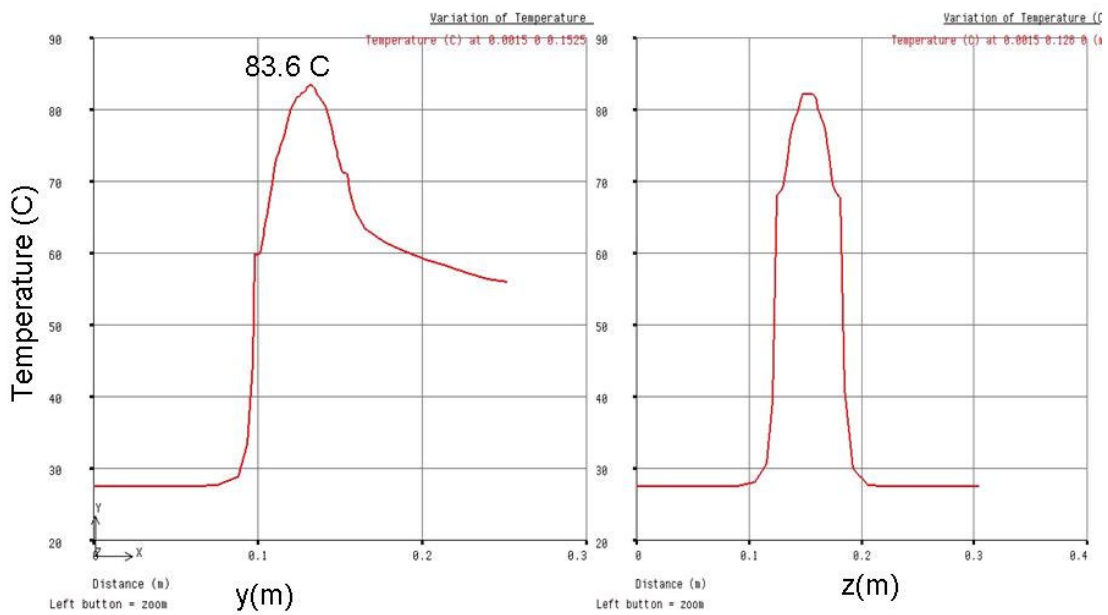
Fig. 5.19 Enhanced PPS heat sink hot spot location for 5.5 W

Table 5.2 Numerical h_a values for enhanced PPS heat sink

Power (W)	h_a (radiation and convection)	h_a (convection only)	% radiation loss
4.03	33.9	23.1	31.8
5.50	37	25.2	31.8
7.16	39.3	26.7	32.1
9.82	42.1	28.9	31.4
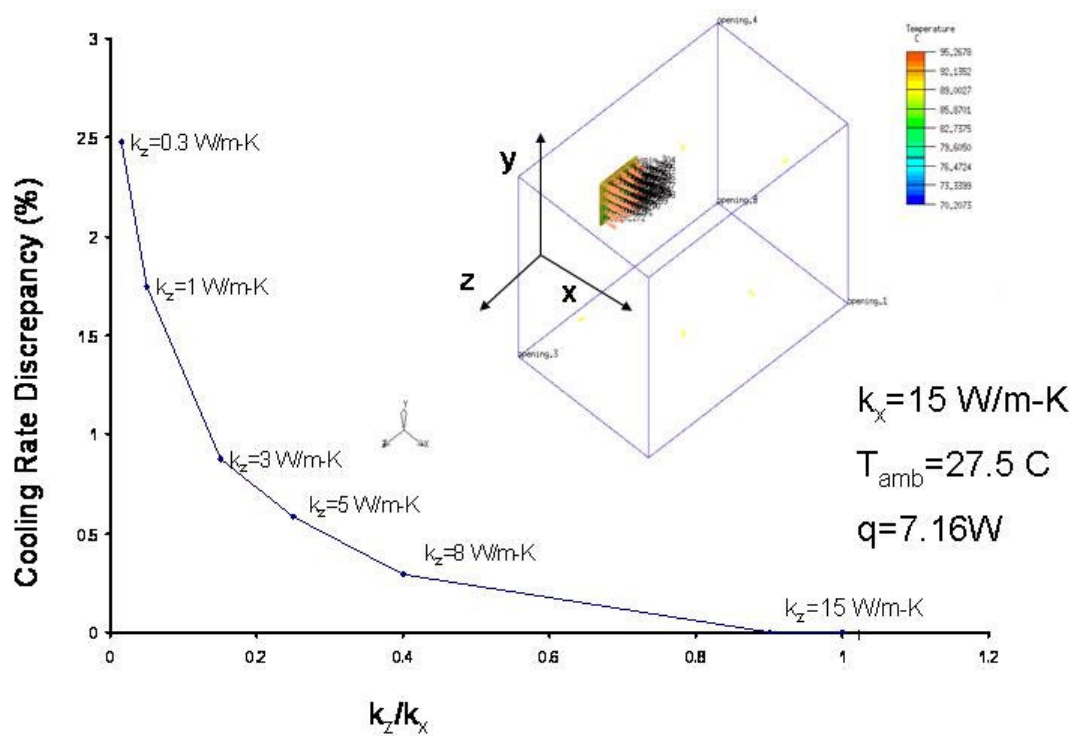
Fig. 5.20 Enhanced PPS heat sink orthotropic conductivity effect

In order to establish the effect of radial thermal conductivity effects on overall pin fin

heat flow rates several numerical runs were made. The axial thermal conductivity

value was fixed at 15 W/m-K and the radial thermal conductivity value varies as, 0.3, 1, 3, 5, 8, 15 W/m-K respectively. The highest cooling rate prediction discrepancy in Fig. 5.20 is less than 3% in case of radial thermal conductivity value of 0.3 W/m-K compared to the case when isotropic thermal conductivity value of 15 W/m-K is assumed.

5.7.4 Numerical – Experimental Result Comparison

Comparison of the experimental values in Fig. 5.21 with the numerical results for the combined three-dimensional convection and radiation heat transfer rates (using default surface to surface radiation model) indicates that the CFD simulation provides very close agreement (4%) with the measured values.
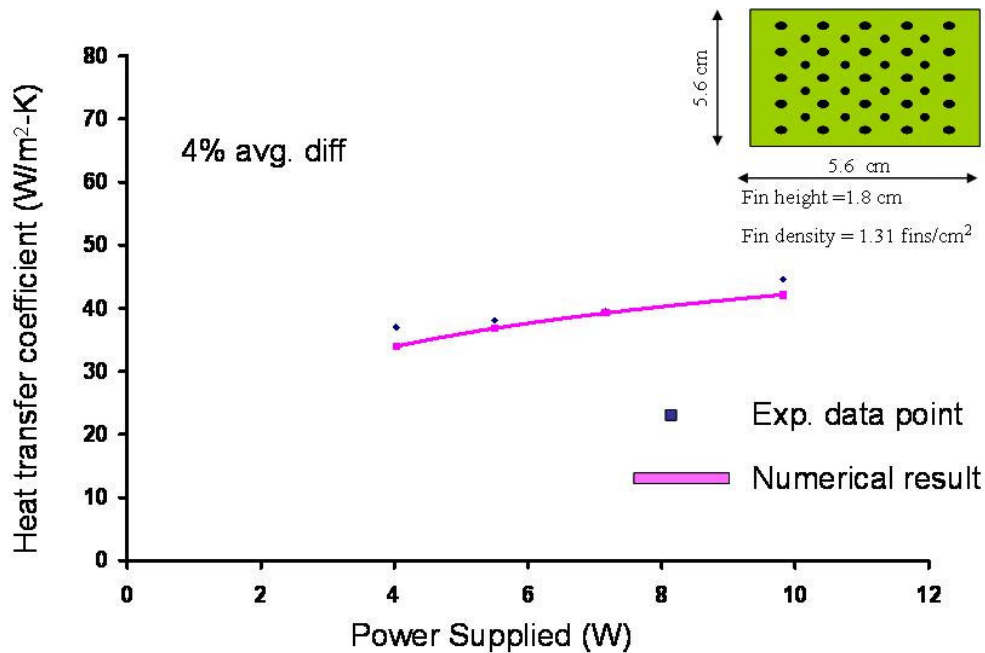
Figure 5.21 Pin fin enhanced PPS heat sink h_a numerical/experimental results

The agreement of the CFD combined convection and radiation numerical simulation with experimental data serves to establish the accuracy of the experimental results obtained in this apparatus.

5.7.5 Numerical – Analytical Result Comparison

An additional model 3D CFD model was built in IcePak to verify the analytical modeling (convection only) results obtained using the Aihara et al pin fin array correlation (Eq. (5.7)). Mesh refinement was performed to ensure a mesh independent solution. As shown in Fig. 5.22, close agreement (analytical values just 1.2% higher than the numerical) between the CFD modeling results and the analytical modeling results was achieved for a pin fin density of 8.62fins/cm^2 which is within the Aihara correlation range (2.25-10.58 fins/cm^2).
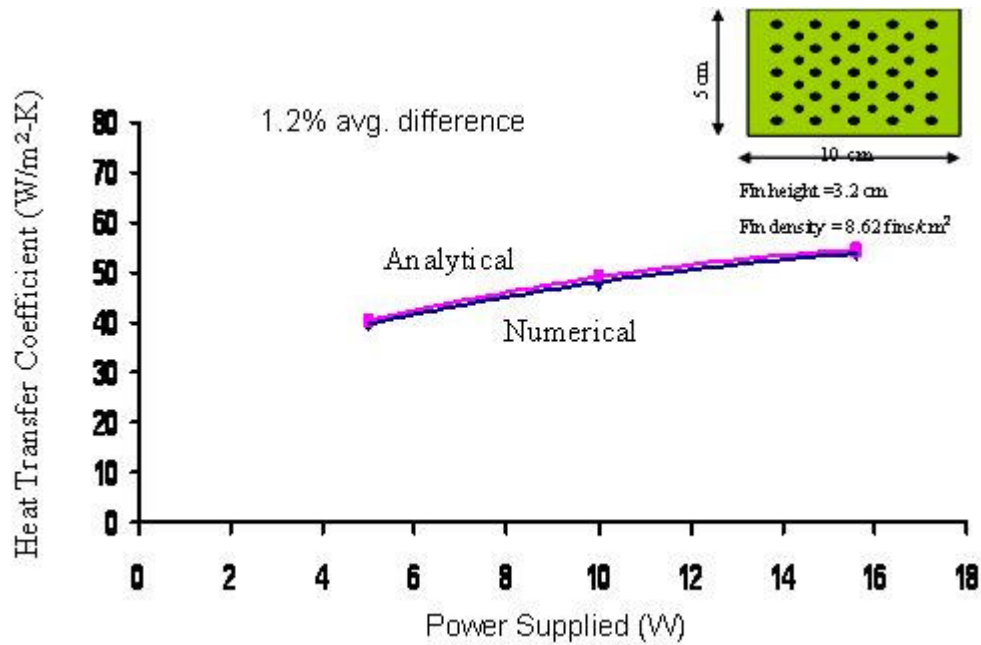
Figure 5.22 Pin fin enhanced PPS heat sink h$_a$ in Aihara domain

The agreement of the analytical predictions with the CFD convection-only simulations, performed within the Aihara et al domain, lends credibility to the use of the previously described analytical modeling methodology for the design and optimization of natural convection polymer pin fin heat sinks. However for PPS pin fin heat sinks with fin densities well below the Aihara et al range, as was seen for a

pin fin array with a fin density of 1.39fins/cm^2, the analytical prediction may over predict the performance by as much as 25% and on average by about 15%.

Chapter 6: Thermal Performance of Forced Convection PPS Pin Fin Heat Sinks

6.1. Introduction

The thermal performance of forced convection air cooled heat sinks made up of a polyphenylene sulphide composite (PPS, 20W/m-K), are predicted and compared to aluminum and copper pin fin heat sinks, using a defined heat sink volume and a range of pumping powers. The thermal performance is analytically predicted across an extensive parametric space in terms of the primary thermal metrics and identifies the thermal performance limits. PPS heat sinks are seen to constitute a viable alternative material for energy efficient heat sink design and show comparable thermal performance to aluminum and copper heat sinks at low fin densities and pumping power. The analytical models used to predict the heat sink thermal performance are seen to provide good agreement with typical aluminum pin fin heat sink experimental and CFD modeling results. The present Chapter focuses on the use of PPS polymer matrix pin fin heat sinks for forced convection cooling.

6.2. Theory and Formulation

Heat transfer from an array of cylindrical fins is the sum of heat dissipation from the fins and the array base, and can be calculated as,

$$Q = \theta_b (h_f A_f + h_b A_b) \tag{6.1}$$

Where A_b, A_f are the base area and fin area available for heat transfer, respectively and are given by

$$A_b = LW - n\pi D^2/4 \tag{6.2}$$

$$A_f = n\pi D(H + D/4)$$ (6.3)

Forced convection heat transfer from the base of the array, using the classical correlation for laminar flow over a flat plate [63], given by,

$$Nu_b = \frac{h_b L}{k_{air}} = 0.664 \, \mathrm{Re}_L{}^{\frac{1}{2}} \, \mathrm{Pr}^{\frac{1}{3}}$$ (6.4)

The array dimensions L, W, and H, and the pin configuration d, S_L, and S_W, affect the number of pins in the vertical and horizontal direction.

$$n_L = (L - D)/S_L + 1$$ (6.5)

$$n_W = (W - D)/S_W + 1$$ (6.6)

$$n_i = n_W n_L$$ (6.7)

6.2.1 Inline Pin Fin Heat Sinks

Following the approach for fully shrouded flow across a bank of tubes [63] and using analytical equations developed for inline pin fin arrays [68], it is possible to determine the heat transfer rate from a heat sink with in line pin fins.

The pin fin array Nusselt analytical correlation is given as,

$$Nu_f = \frac{h_f D}{k_{air}} = C_i \, \mathrm{Re}_D{}^{\frac{1}{2}} \, \mathrm{Pr}^{\frac{1}{3}}$$ (6.8)

Where, C_i is a constant that depends upon the longitudinal and transverse pitches, arrangement of the pins, and thermal boundary conditions. For isothermal boundary condition at the inlet, C is given by:

$$C_i = \frac{0.65[0.2 + \exp(-0.55S*_W)]S*_W{}^{0.785} \, S*_L{}^{0.212}}{(S*_W - 1)^{0.5}}$$ (6.9)
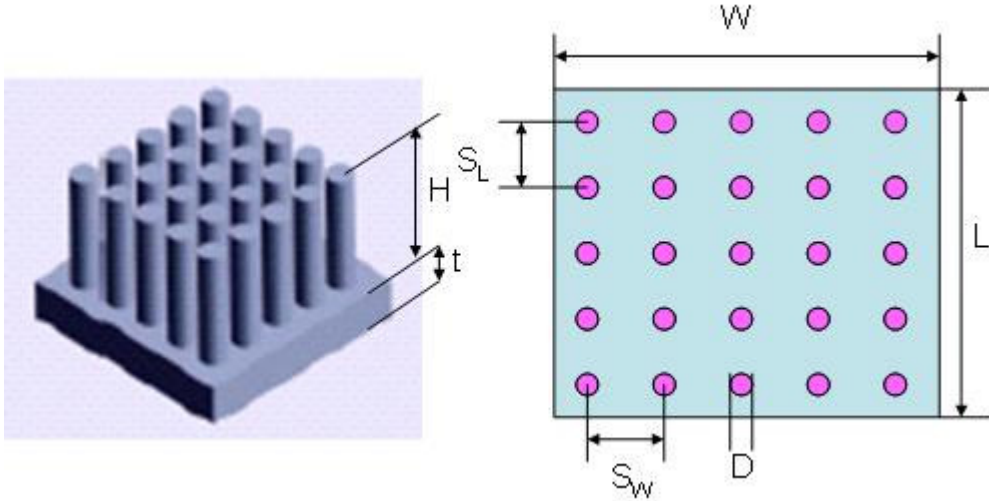
Figure 6.1 Inline pin fin heat sink

The pressure drop for flow through an array of such fins can be determined from,

$$\Delta P_i = \frac{f_i \rho (v_{max}{}^2) n_L}{2} \tag{6.10}$$

$$v_{max,i} = S *_W v_{in} / (S *_W - 1) \tag{6.11}$$

$$f_i = K_i (0.233 + 45.78 / ((S *_W - 1)^{1.1} \operatorname{Re}_D)) \tag{6.12}$$

$$K_i = 1.009 \left(\frac{S *_W - 1}{S *_L - 1} \right)^{(1.09 / \operatorname{Re}_D{}^{0.0553})} \tag{6.13}$$

6.2.2 Staggered Pin Fin Heat Sinks

Following an approach similar to the above for fully shrouded flow across a bank of tubes [63] and using analytical equations developed for staggered pin fin arrays [68] under identical assumptions and boundary conditions at the inlet , we have

$$n_s = n_L (n_W - 1) + 1 \tag{6.14}$$

$$Nu_f = \frac{h_f D}{k_{air}} = C_s \operatorname{Re}_D^{1/2} \operatorname{Pr}^{1/3} \qquad (6.15)$$

$$C_s = \frac{0.28[S*_W^{0.591} S*_L^{0.053}]}{(S*_W - 1)^{0.5}[1 - 2\exp(-1.09S*_W)]} \qquad (6.16)$$

$$\Delta P_s = \frac{f\rho(v_{max}^2)n_L}{2} \qquad (6.17)$$
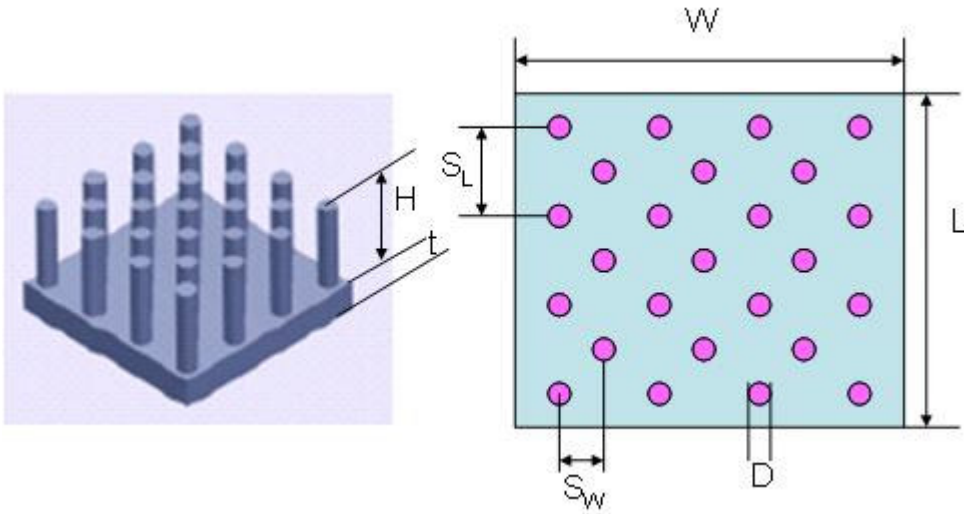
Figure 6.2 Staggered pin fin heat sink

$$v_{max} = \max[S*_W \, v_{in}/(S*_W - 1), S*_W \, v_{in}/(S*_D - 1)] \qquad (6.18)$$

$$S*_D = \{S*_L^2 + (S*_W/2)^2\}^{1/2} \qquad (6.19)$$

$$f_s = K_s(378.6/S*_W^{(13.1/S*_W)})/\operatorname{Re}_D^{(0.68/S*_W^{1.29})} \qquad (6.20)$$

$$K_s = 1.175[S*_L/(S*_W \operatorname{Re}_D^{0.3124})] + 0.5\operatorname{Re}_D^{0.0807} \qquad (6.21)$$

6.3. Forced Convection Inline Pin Fin Heat Sinks

6.3.1 Typical Pin Fin Geometry Results

Numerical modeling: Exact same pin fin heat sink geometry as used in the experiments (Fig. 6.3) is modeled in Commercial CFD software IcePak. The pin fins were shrouded completely and no by pass was allowed. The air came in from the side of the heat sink and exits from the other end. The total length of the flow modeled was x3 times the side of the heat sink base. The Reynolds number indicated laminar flow. The default laminar flow model in IcePak is used to obtain forced convection results.
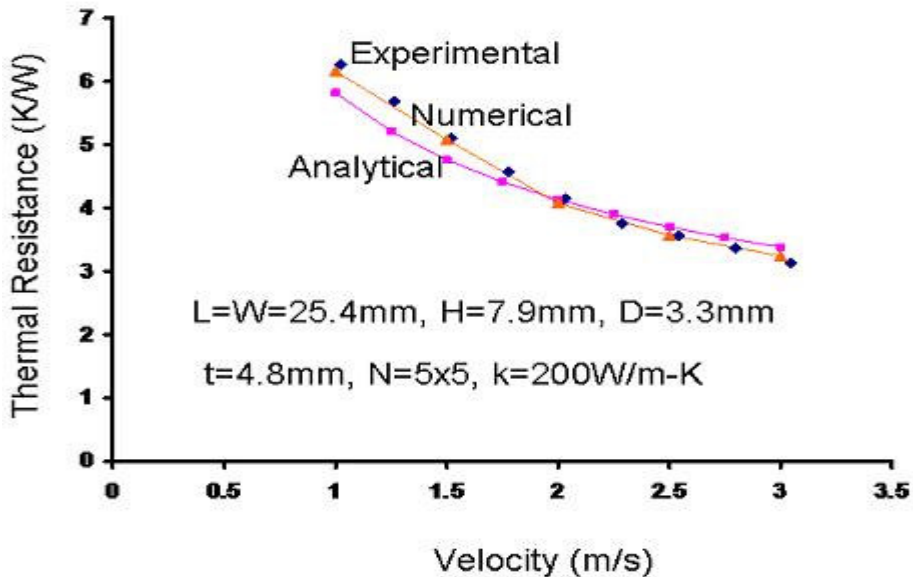
Figure 6.3 Inline pin fin heat sink thermal resistance in forced convection (θ_b=25K)

Experimental verification: Experimental thermal resistance values for various inlet air velocities ranging from 1-3 m/s are compared with numerical and analytical results in Fig. 6.3 for a typical commercial inline 5x5 aluminum pin fin heat sink (Fig. 6.1) used for cooling surface mount components [69]. An average standard deviation

value of about 1% was found between experimental and numerical results. Analytical-experimental average standard deviation was less than 2% (1.7%). This comparison serves to validate the analytical modeling methodology used in this study to carry out the detailed parametric study and optimization of inline pin finned heat sinks.

The analytical modeling results are further used to carry out the least material optimization of inline pin fin heat sinks in order to achieve low mass optimum thermal performance heat sink configuration. A fixed available heat sink volume of 0.1x0.1x0.02 m was selected in order to carry out the least material optimization. The diameter of the least material pin fin is obtained using Eq. (5.9). No air bypass is allowed in the present analysis. A uniform temperature distribution is assumed across the base of the heat sink. Geometric optimization of the heat sink base is not included in the present analysis.

Cooling Rate: The analysis of PPS heat sink capability starts with a typical easily fabricated pin fin diameter of 5mm for PPS, aluminum, and copper inline pin fin heat sinks and a given heat sink volume of 0.1x0.1x0.02 m, supplied with a fixed fluidic power of 0.04W. A PPS pin fin heat sink cooling rate, as high as 75 W for a base temperature rise of 25 K, is achievable with fin density of 1.75fins/cm^2 for a total heat sink mass of 0.154 kg, as shown in Fig. 6.4. Using aluminum and copper, heat sink cooling rates as high as 84W and 86 W, respectively, are achieved for the fin density of 1.5fins/cm^2 with a total heat sink mass of 0.22 and 0.716 kg, respectively. It is to be noted, however, that "least-mass" optimization of these pin fin arrays, as described above, could be expected to result in a considerable reduction in the mass of the

119

copper and aluminum heat sinks, without a significant loss in cooling capability. The consequences of such a least material fin optimization will be discussed in subsequent sections.
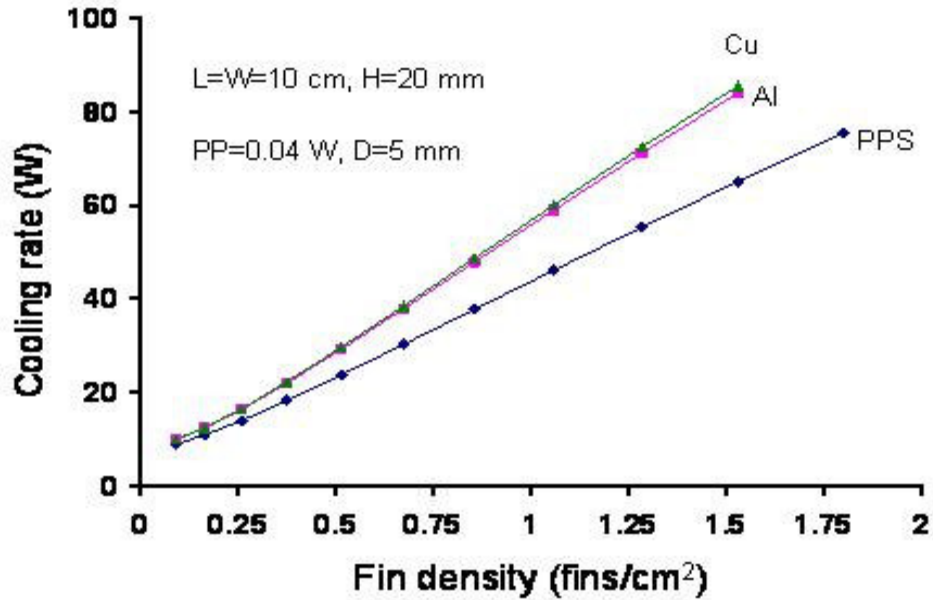
Figure 6.4 Inline pin fin heat sink cooling rate in forced convection (θ_b=25K)
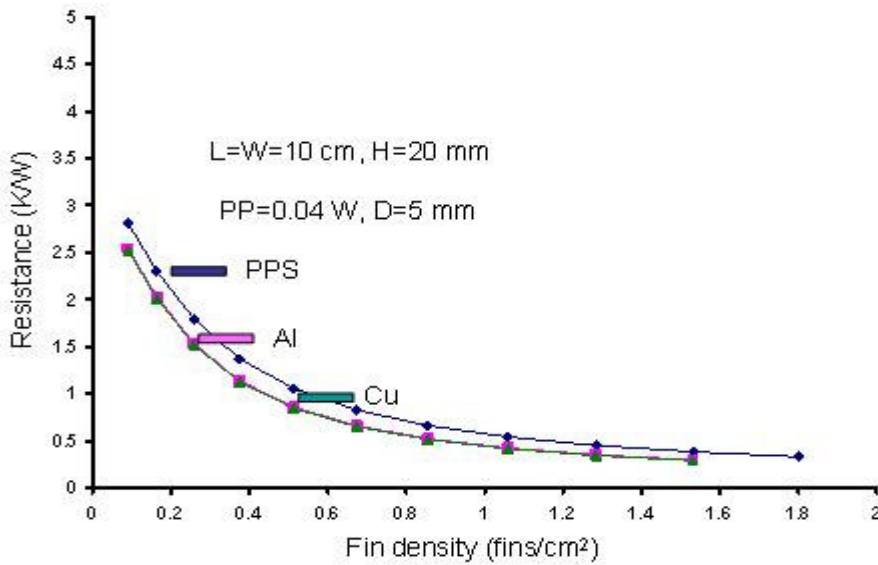
Figure 6.5 Typical inline heat sink thermal resistance in forced convection (θ_b=25K)

The heat sink to ambient thermal resistance value as low as 0.33 K/W is achieved using PPS (20 W/m-K) fin density of 1.8 fins/cm^2 comparable to 0.3 K/W achieved using copper and aluminum heat sinks for fin density of 1.53 fins/cm^2 as shown in Fig. 6.5. The heat sink thermal resistance value decreases steeply at first as the pin fin density increases, but starts to decreases asymptotically at 1.5fins/cm^2.

Mass-Based Heat Transfer Coefficient: The mass-based heat transfer coefficient captures the effectiveness of mass utilization in achieving a desired cooling rate. As shown in Fig. 6.6, reflecting the large variation in density across the three fin materials, the highest value of 19.6W/kg-K is achieved at fin density of 1.8fins/cm^2 by the PPS heat sink, followed by aluminum at 15.6, and the copper heat sink at 4.8 W/kg-K for a fin density of 1.6fins/cm^2. The mass based heat transfer coefficient rises asymptotically for all three materials and plateaus beyond a fin density of 1.6fins/cm^2.
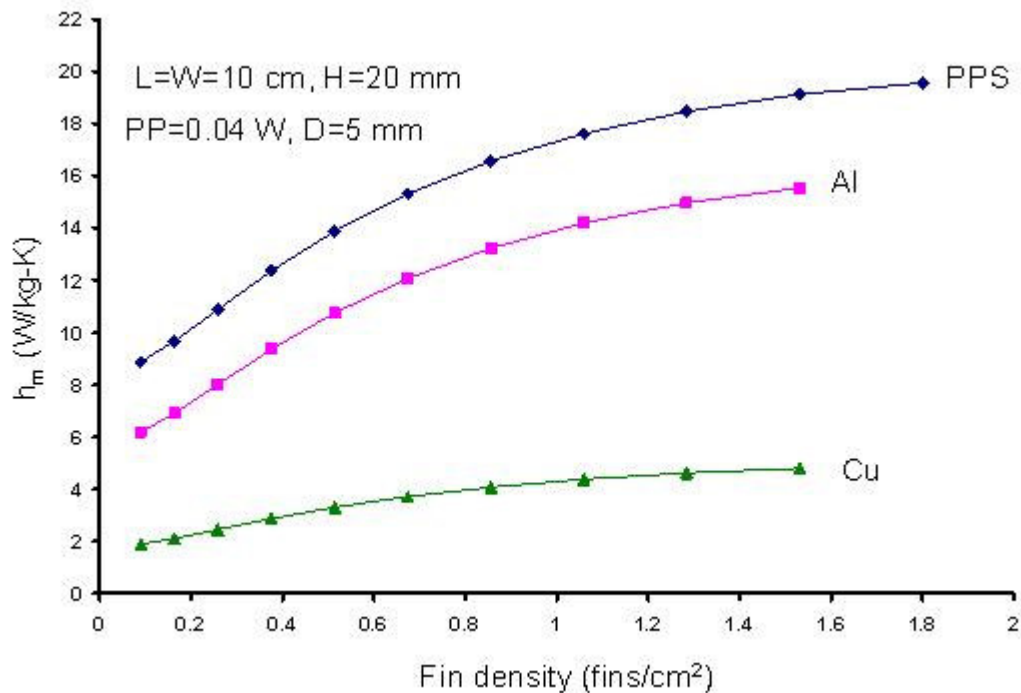
Figure 6.6 Mass based heat transfer coefficient in forced convection (θ_b=25K)

Coefficients of Performance: Fig. 6.7 displays the variation of the coefficient of performance with fin density, for a fixed pumping power of 0.04W and reveals that the maximal PPS values are approximately 20% lower than those achieved by aluminum and copper, with a peak PPS value of 2000, despite PPS having a fin thermal conductivity at 20 W/m-K, only 1/20th and material density at 1700 kg/m^3 [10] just 1/5th that of copper.
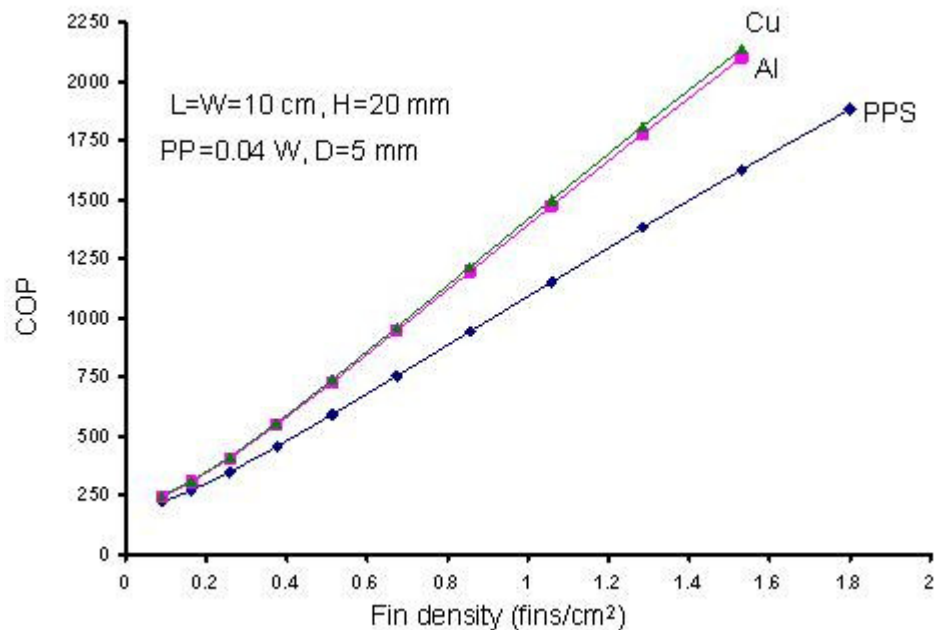
Figure 6.7 Coefficient of performance for heat sink in forced convection (θ_b=25K)

The COP_T values plotted in Fig 6.8, clearly displays the superior energy efficiency of the PPS pin fin heat sinks compared to aluminum and copper, over a wide pin fin density range, for a fixed (and typical) fin diameter of 5mm. However, the high thermal conductivity of the two metals does allow for far slimmer pin fins than PPS and a more complete comparison would require the "least-material" optimization of each array of fins.
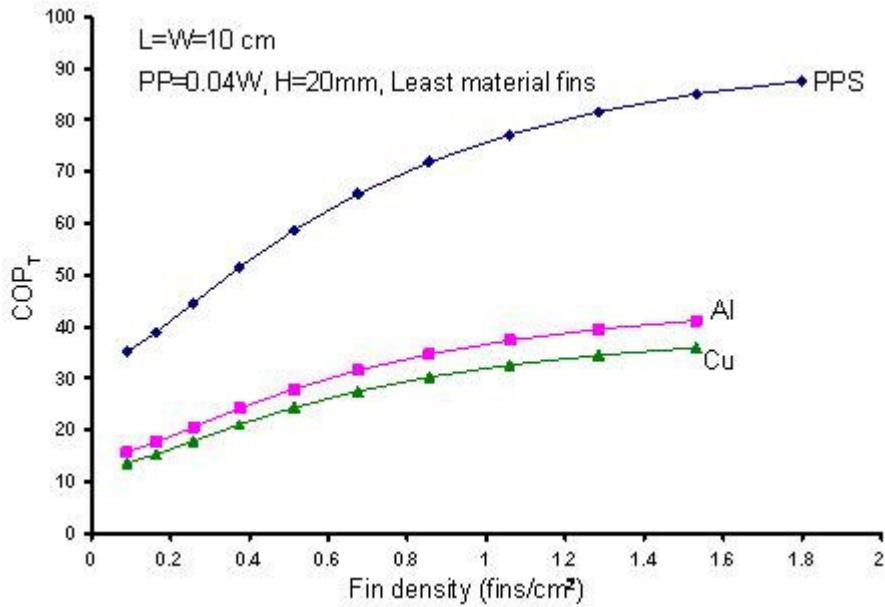
Figure 6.8 Total coefficient of performance of heat sink in forced convection (θ_b=25K)

Increasing pumping power can lead to far higher cooling rates for PPS heat sinks, as shown in Fig. 6.9, starting from cooling rate of 75W at 0.04W of pumping power up to as high as 200 W at a high pumping power of 2.1 W.
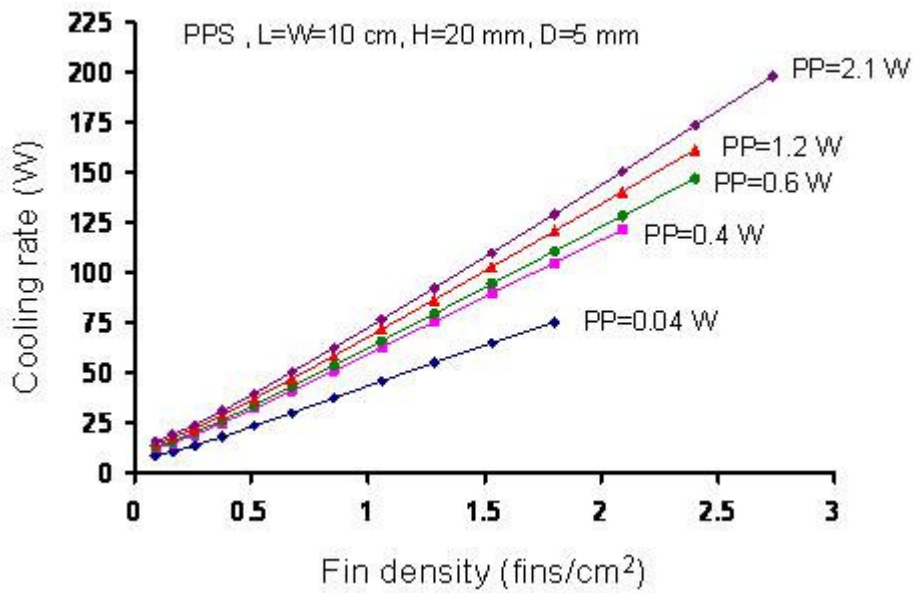
Figure 6.9 PPS inline heat sink cooling rate in forced convection (θ_b=25K)

A cooling rate as high as 120W at 2.1fins/cm^2 is achievable using a still reasonable fluid power of 0.4W. Thus, higher cooling rates can be obtained with increasing fin densities but at the expense of ever higher pumping power to overcome the resistance of the fins (ΔP) and avoid excessive sensible temperature rise in the cooling air (flow rate). Earlier published results [65] for plate fins predicted cooling rates as high as 150 W using pumping power of 0.6 W; compared to a cooling rate of 147 W using an inline pin fin density value of 2.4fins/cm^2, as shown in Fig. 6.9. However, as may be seen in Fig. 6.10, increasing pumping power to achieve higher cooling rates requires higher total energy investments, resulting in reduced COP$_T$'s for the PPS heat sinks.
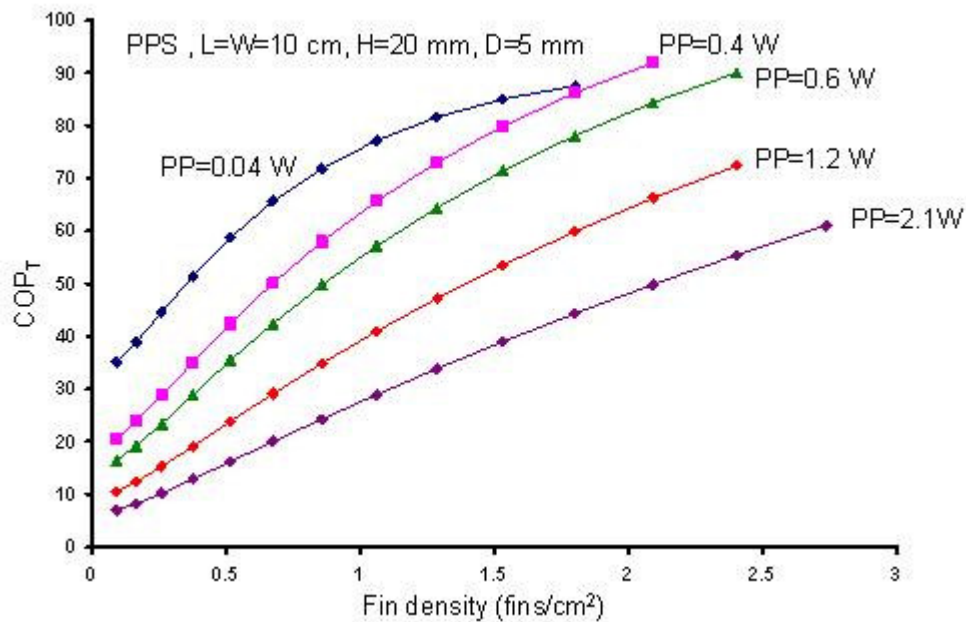
Figure 6.10 PPS inline pin fin heat sink COP$_T$ in forced convection (θ_b=25K)

The highest COP$_T$ value of 92 is achieved for a pumping power of 0.4 W at a fin density of 2.1fins/cm^2 using a PPS heat sink that provides a cooling rate of 121 W.

124

6.3.2 Inline Least Material Pin Fin Results

Fin Diameter: As previously discussed, the least-material pin fin has been found to achieve a fin efficiency of 0.789 and to follow the aspect ratio defined by Eq. (5.9). The "least-material" fin diameters for copper and aluminum pin fins, placed into the specified 20mm high pin fin array, are shown in Fig 6.11 and found to be in the range of 1mm for fin densities above 1 fin/cm^2, while optimum PPS fins reach a diameter of nearly 9.7 mm as the fin density increases to the highest "packing" fin density of 0.86 fins/cm^2
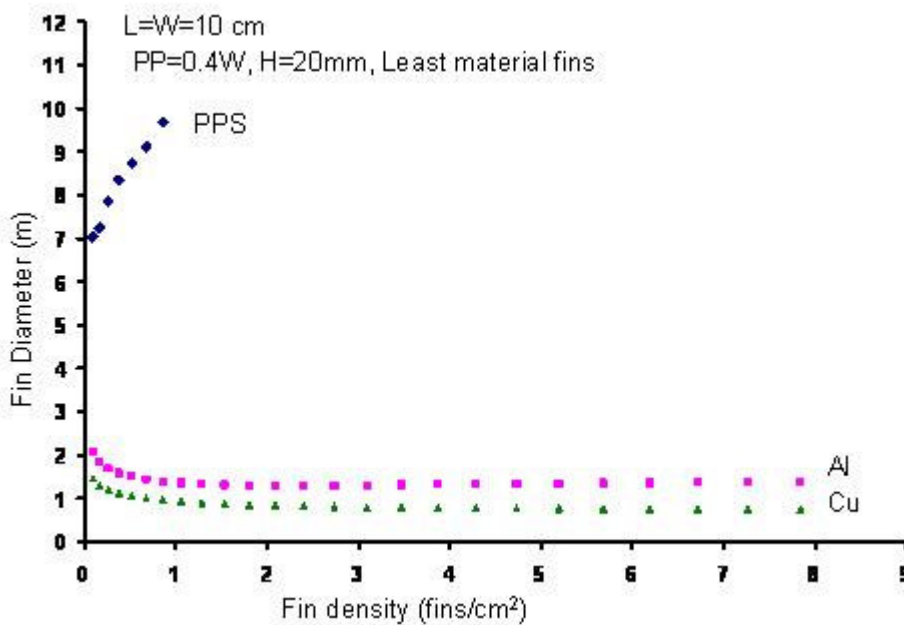
Figure 6.11 Least material pin fin diameter with fin density (θ_b=25K)

Cooling Rate: Using these least-material relations to configure heat sinks, within the specified geometric and pumping power constraints, the maximum PPS cooling rate is seen, in Fig 6.12, to reach 107 W, achieved with 9.7mm diameter fins, 0.86 fins/cm^2, and an array mass of 0.25 kg. The aluminum heat sink provides maximum cooling rate of 202 W (with 1.39mm diameter, at 7.8fins/cm^2 and a mass of 0.12kg),

while a copper heat sink would yield 125 W (with 0.8mm fins, at the same 7.8 fins/cm^2 and a mass of 0.24 kg). The indicated fin dimensions assure that – for each fin material – the mass is best utilized for heat transfer. It is to be noted that the small diameter of the aluminum and copper fins makes it possible to substantially increase the fin density, without unduly raising the pressure drop of the pin fin array. However, such fine metal "wires" may pose some manufacturing challenges and require structural reinforcement to withstand handling and blower-induced pressure transients.
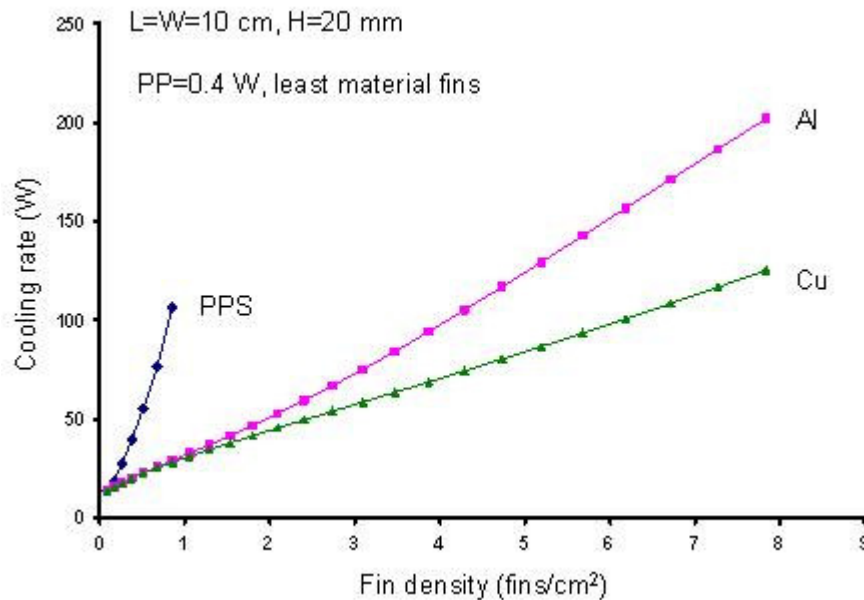
Figure 6.12 Inline least material pin fin cooling rate in forced convection (θ_b=25K)

The least material results, shown in Fig 6.13, indicate that thermal resistance values as low as 0.23 K/W at 0.85fins/cm^2 can be achieved using a least material PPS fin diameter of 9.7 mm. However, aluminum provides thermal resistance value of 0.12 K/W at a fin density of 7.8fins/cm^2 for a 1.4mm diameter pin fin, while copper provides a resistance of 0.2 K/W at 7.8fins/cm^2 for a diameter of 0.76 mm. Most

interestingly, the least material PPS pin fins provide low thermal resistance values and high cooling rates using relatively thick fins at the lowest pin fin density values.
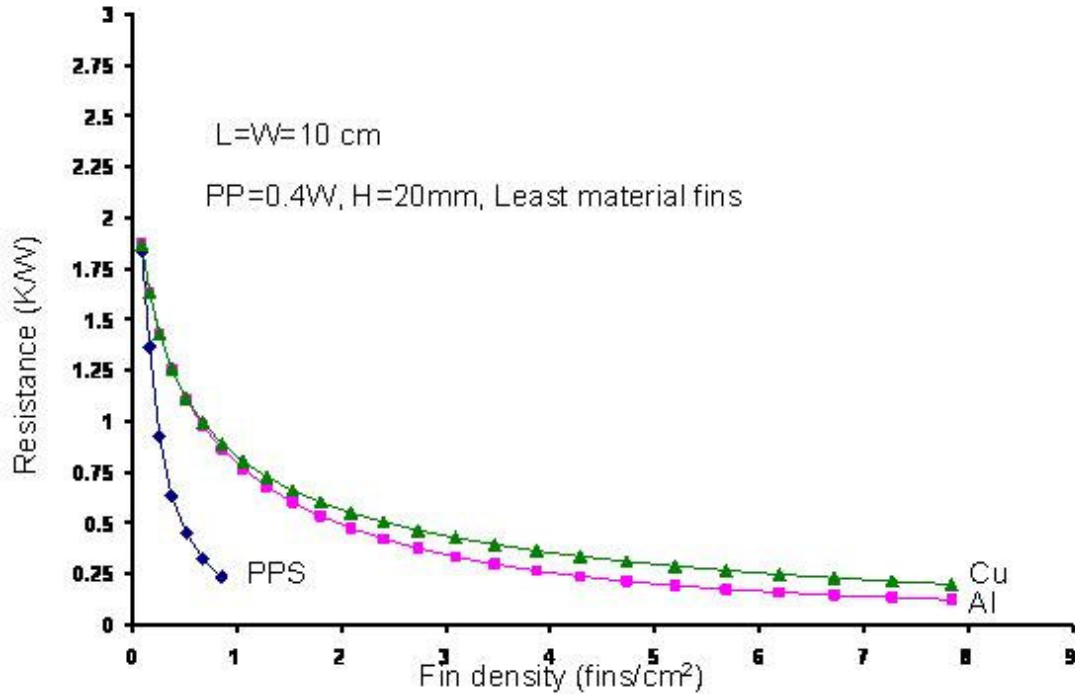
Figure 6.13 Thermal resistances for least material fins in forced convection (θ_b=25K)

Coefficients of Performance: At lower pumping power, the PPS COP, achieved at lower fin densities, is far superior to that of the two metals. However, as shown in Fig. 6.14, for a fixed pumping power of 0.4 W, the coefficients of performance for aluminum and copper continue to rise and exceed the PPS COP (266 at 0.86 fins/cm^2) value at 5 fins/cm^2 and 7 fins/cm^2, respectively. This is because the least material pin fin diameter for enhanced PPS composite tends to be thicker providing higher effective surface area than aluminum and copper at that fin density value. However it is not possible to achieve greater than 0.86 fins/cm^2 using enhanced PPS. The high conductivity aluminum and copper allows much higher fin density values and therefore results in higher COP values.
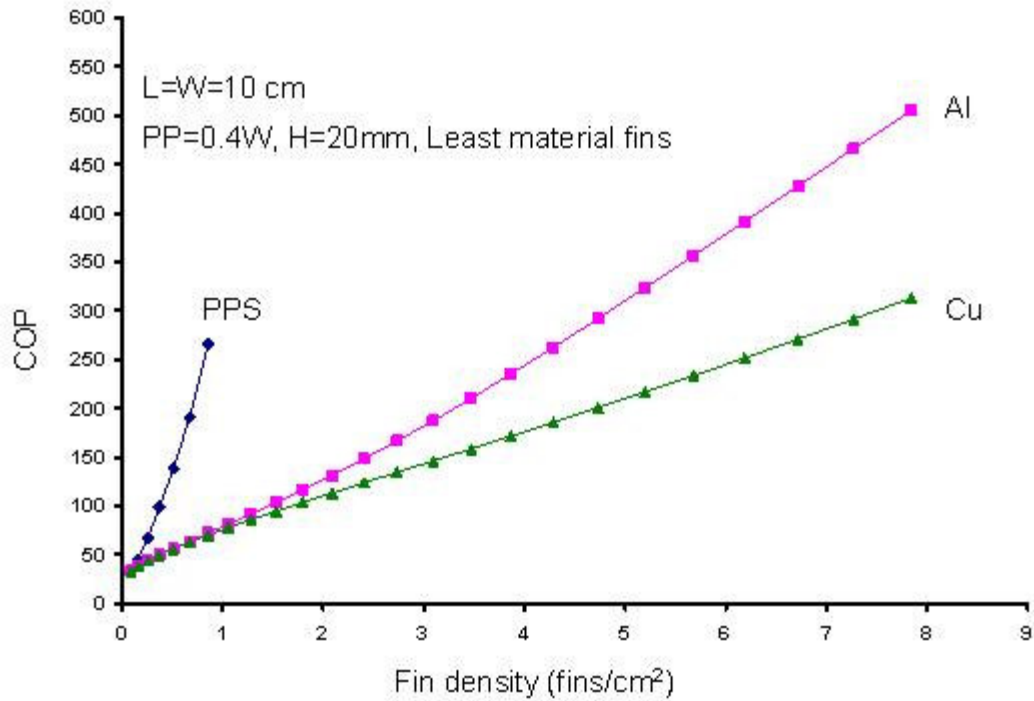
Figure 6.14 Coefficient of performance for least material in forced convection (θ_b=25K)

The total coefficient of performance is highest for PPS heat sinks up to a fin density of 0.87fins/cm^2, providing a COP$_T$ approaching 62 and a cooling rate as high as 107 W. The lower fabrication energy requirements associated with PPS material are responsible for these higher total coefficients of performance. However, the ability to design thermally efficient, yet thinner fins using the higher thermal conductivity aluminum and copper enables the use of increased fin densities which attain values as high as 7.8fins/cm^2 with a pumping power of 0.4W. At these values,, significantly higher cooling rates of 102 (?) W and 125 W, respectively, can be achieved by copper and aluminum heat sinks. Therefore, the COP$_T$ for aluminum and copper exceeds the best PPS heat sink value at a fin density of 2.7 and 3.9fins/cm^2 respectively.

128

Nevertheless, PPS pin fin heat sinks do provide cooling rates up to approximately 100

W, with greater energy efficiency, for low fin densities of up to 0.87fins/cm^2.
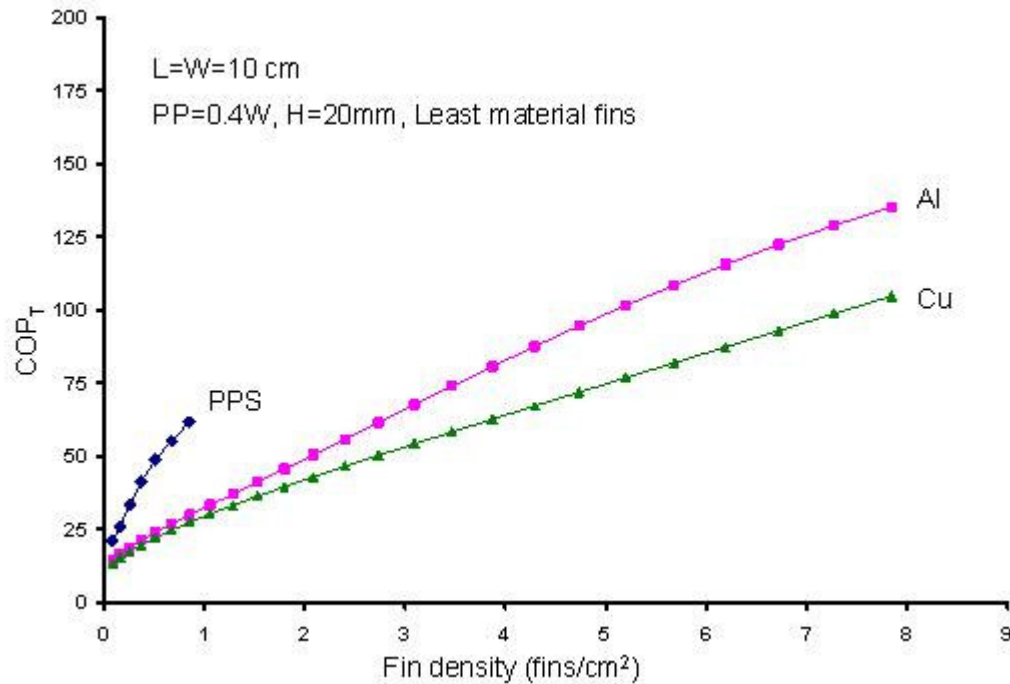
Figure 6.15 Coefficient of total performance for least material fins (θ_b=25K)

6.4. Forced Convection Staggered Pin Fin Heat Sinks

6.4.1 Typical Staggered Pin Fin Heat Sink Result

   Experimental Verification: Experimental thermal resistance values for various air

velocities ranging from 1-3 m/s are compared with numerical and analytical results in

Fig. 6.16. For a typical commercial staggered 7x4 aluminum pin fin heat sink (Fig.

6.2) used for cooling surface-mount components, heat sink thermal resistance is seen

to be lower than those achieved in the inline fin array, but at a (x4) higher pressure

drop. The average standard deviation between numerical (Section 6.3.1) and

experimental results [69] is 0.21% and 1.2% between the experimental and analytical

results, based on the use of Eq. (6.14) to Eq. (6.21).
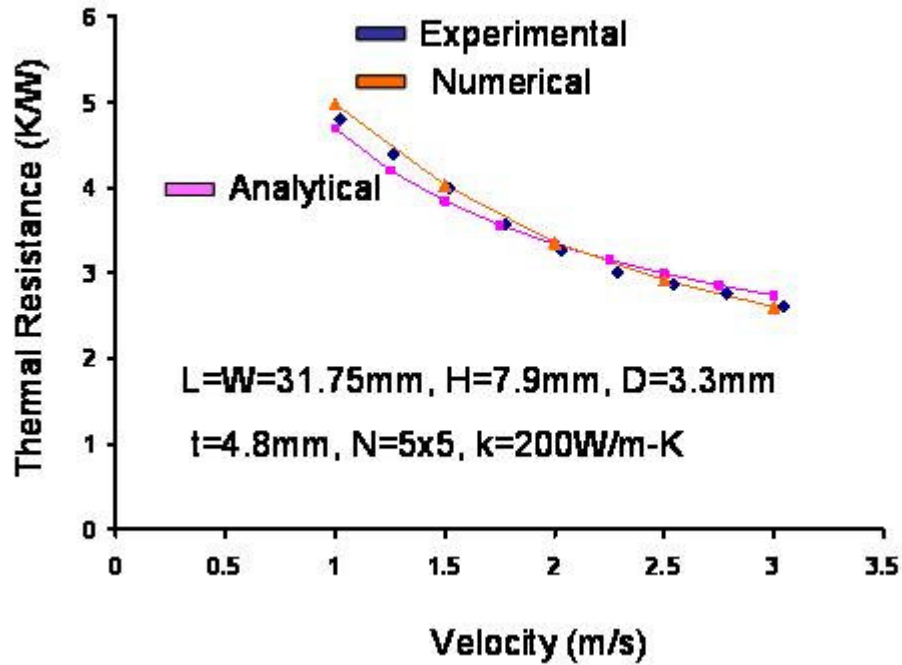
Figure 6.16 Staggered pin fin heat sink thermal performance

Succeeding sections will explore the performance characteristics of staggered pin

fin arrays occupying the previously defined heat sink volume of 0.1x0.1x0.02 m, and

operating with a 25K base excess temperature and pumping power of 0.4W across a

wide range of fin densities. It is to be noted that in these calculations, the maximum

allowable fin density is artificially restricted by the limitation of the Nu correlation in

Eq. (6.1) - Eq. (6.16) to fin center-to-center spacing greater than the fin diameter.

6.4.2 Least Material Pin Fin Staggered Heat Sink Result
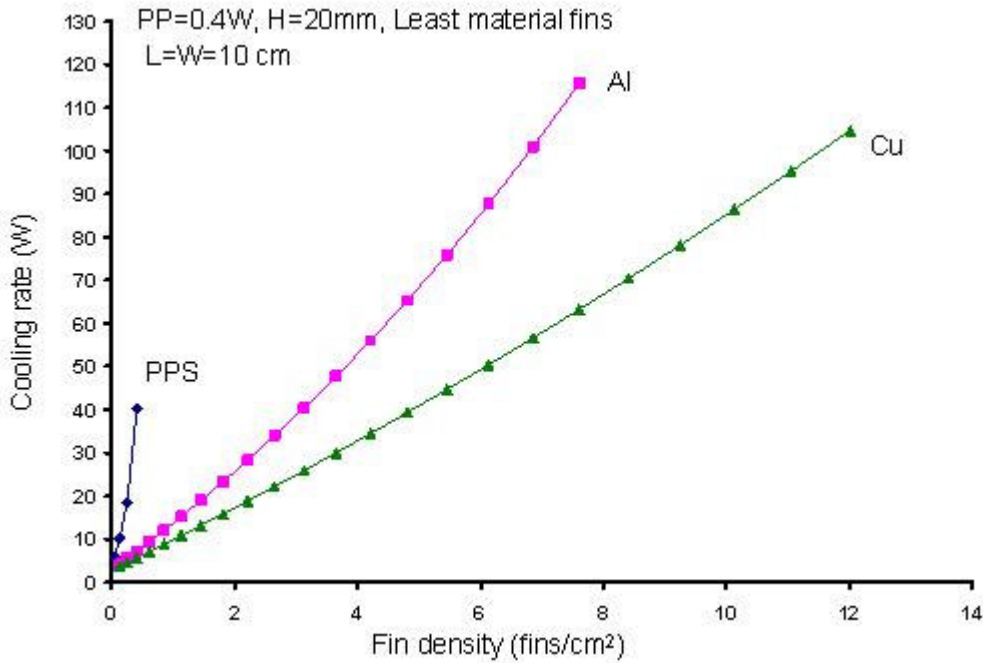
Figure 6.17 Staggered least material fins cooling rate in forced convection (θ_b=25K)

The staggered pin fin configuration in the PPS array is optimized for a pumping power of 0.4W at a much lower fin density of 0.41fins/cm^2 than considered in the inline array, and a least-material pin fin diameter of 8.3 mm. The resulting cooling rate peaks at a value of 40W, as shown in Fig. 6.17. However, for copper (12 fins/cm^2) and aluminum (7.6fins/cm^2) pin fin heat sinks, a much higher cooling rate of 105 W and 116 W is obtained at a pin fin diameter of 0.57 and 1.1 mm, respectively. Comparatively, inline configurations using least material PPS, Al, and Cu provide cooling rates of 42W at 0.38fins/cm^2, 105W at 7.8fins/cm^2, and 135W at 7.8fins/cm^2, respectively. In the staggered configurations, it is possible to have center-to-center clear spacing far lower than the pin fin diameter, resulting in higher pin fin density values and staggered fin distributions that can provide comparable cooling rates to inline configurations.

Fig. 6.18 shows the lowest PPS thermal resistance to equal 0.41 K/W, while a resistance as low as 0.22 K/W is achievable using aluminum at 7.61fins/cm^2. Use of copper least material pin fins, provides a thermal resistance value of 0.24K/W at fin density of 12fins/cm^2.
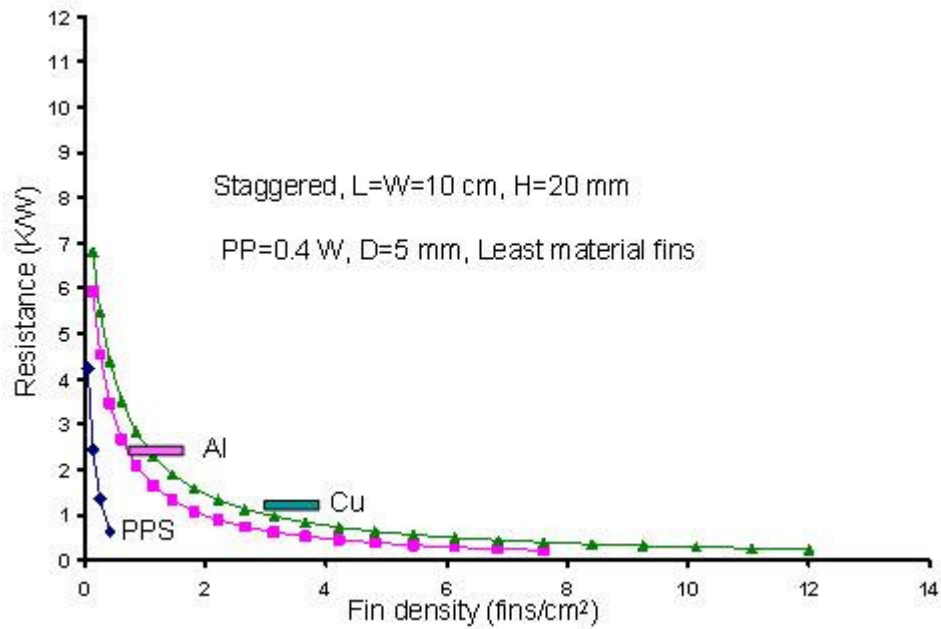
Figure 6.18 Staggered least material fins thermal resistance in forced convection (θ_b=25K)

Figs. 6.19 and 6.20 depict the fin density variation of the staggered array COP and COP$_T$. At the lowest fin densities, the PPS values exceed substantially those of the two metal arrays, but for the larger fin densities - made possible by the small, least-material diameters of the copper and aluminum fins - dramatically higher COP and COP$_T$ values are achieved by the aluminum and, to a lesser extent, the copper heat sinks.
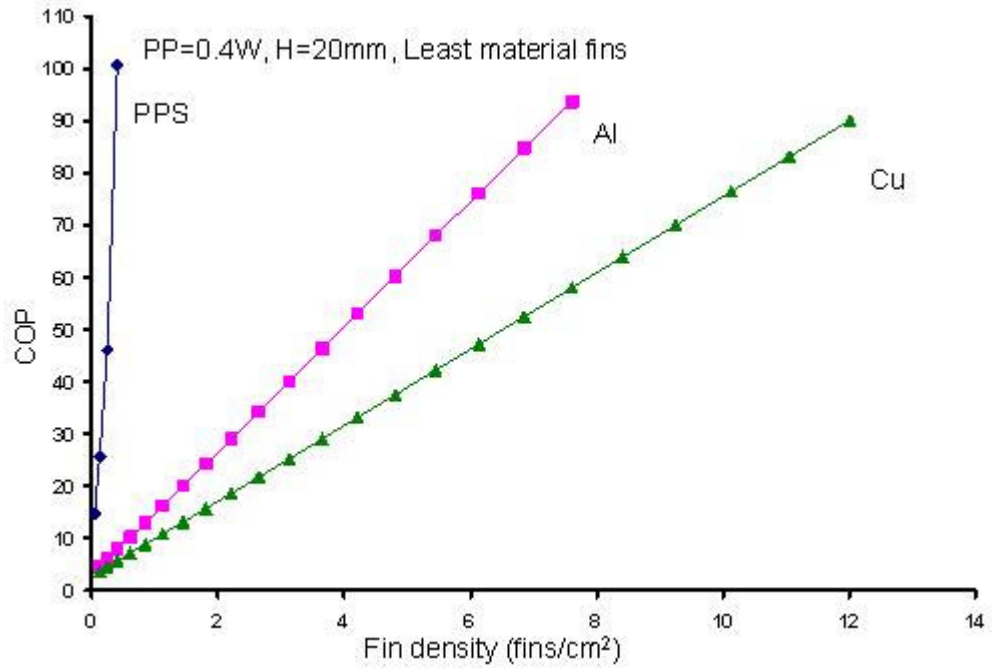
Figure 6.19 COP values for least material staggered heat sinks (θ_b=25K)
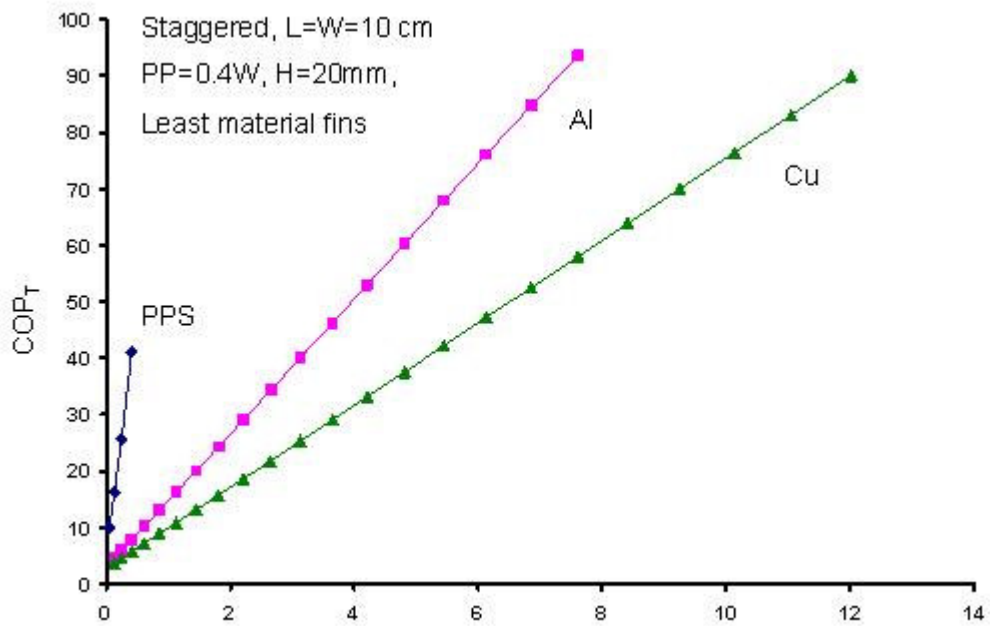
Fig. 6.20 COP$_T$ values for least material staggered heat sinks (θ_b=25K)

6.5 Inline and Staggered Pin Fin Forced Convection Results

Fig. 6.21 displays the effect of varying pumping power on staggered (solid lines) and inline (dashed lines) PPS least material pin finned heat sinks. It is to be noted that progressively higher pumping powers produces only marginal increases in thermal performance at fixed fin densities. Moreover, due to the increased diameter needed at the higher air velocities associated with higher input powers, the best results are obtained at pumping power of 0.4 W. Due to the higher pressure drop associated with the staggered arrangement, the inline configuration provides higher cooling rates, across the indicated range of fin density values, for any fixed pumping power curve. The reader is reminded that the upper limit on staggered pin fin heat sink performance is related to the limitation of Eq. (6.16).
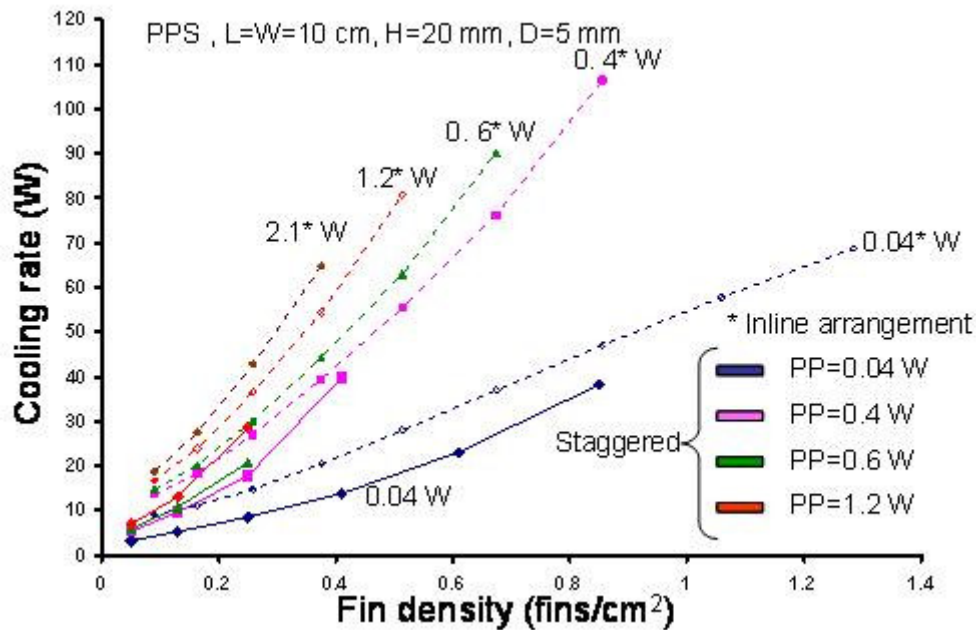
Figure 6.21 Least material PPS pin fins cooling rate in forced convection (θ_b=25K)

Since, there is not a significant increase in the cooling rate achieved by increasing pumping powers, the COP_T values shown in Fig. 6.22, decrease as the pumping power increases. For staggered pin fin arrangement, the highest COP_T value of 62 at pumping power of 0.04W and 0.85fins/cm^2 provides a cooling rate of 37W. For an inline pin fin arrangement, the highest COP_T value of 73 is obtained along with cooling rate of 70W at a pumping power of 0.04W and fin density of 1.3fins/cm^2.
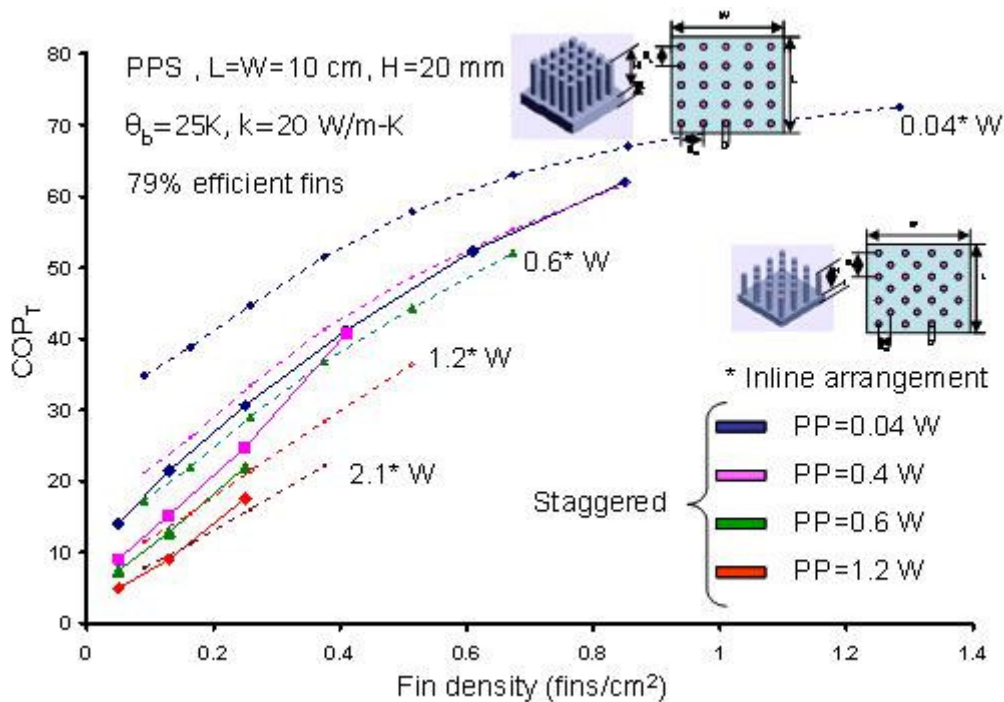
Figure 6.22 Least material PPS pin fins COP_T in forced convection (θ_b=25K)

6.6 Summary

Cooling rates as high as 200 W appear to be achievable using inline PPS (20 W/m-K) heat sink 0.1x0.1x0.02m in size with a total mass of 0.22 kg using typical fin diameter of 5 mm and fin density of 2.8 fins/cm^2. The base temperature rise is

maintained at 25K above 45°C using high fluid power of 2.1W, for a low COP of nearly 95. Using, reasonable fluid power value of 0.4 W cooling rates as high as 120W is achievable using fin density of 2.1fins/cm^2. This is about x 20 time's cooling rate enhancement over bare surface in free convection.

At low pin fin densities and fixed pin fin diameters PPS has comparable thermal performance to aluminum/copper heat sinks up to 0.3fin/cm^2 but lower in mass and fabrication energy expenditures. The lower mass and fabrication energy requirements achieved using lower material density PPS arrays provide significant energy and material savings for heat sinks fabricated of this material.

Application of a least-material optimization methodology reveals that there is an optimum "least material" pin fin diameter for each of these, a given material, pin fin density, and pumping power. Least material optimized PPS pin fins are an order of magnitude thicker than aluminum and copper pin fins, resulting in relatively lower maximum achievable pin fin densities. However, at lower pin fin densities using thicker PPS pin fin heat sinks, higher cooling rate, W/kg, COP, and COP$_T$ is achievable than aluminum and copper heat sink.

Chapter 7: Orthotropic Thermal Conductivity Pin Fin Heat Transfer

An analytical equation for heat transfer from a cylindrical pin fin with orthotropic thermal conductivity, encountered in the use of thermally enhanced polymer composites, is derived and validated using detailed finite-element results. The thermal performance of such fins was found to be dominated by the axial thermal conductivity, but to depart from the classical fin solution with increasing values of a radius- and radial conductivity-based Biot number. Using these relations, it is determined that fin orthotropy does not materially affect the behavior of typical air-cooled fins. Alternatively, for heat transfer coefficients achievable with water cooling and conductivity ratios below 0.1, the fin heat transfer rate can fall more than 25% below the "classical" heat transfer rates. Detailed orthotropic fin temperature distributions are used to explain this discrepancy. Insulated tip orthotropic pin fin heat transfer equations is derived, modified fin height correction to account for fin tip heat loss is validated over a wide range of orthotropic conditions.

7.1 introduction

Recent advances in polymer composites, using carbon fiber [6], and graphite fillers [7] to increase the thermal conductivity, have made such materials viable alternatives to conventional metals in the design and fabrication of heat sinks and heat exchangers [see in Table 7.1]. Ongoing research into the use of carbon nano tubes (CNT's) [8] in epoxy matrixes may yield further improvements in such polymer composites. In

addition to the manufacturing advantages offered by such moldable, high thermal conductivity composites, their relatively low density can provide a significant weight reduction and require less energy [45] for formation and fabrication than copper and aluminum, yielding an important contribution to sustainability.

Conventional polymers can be expected to display thermal conductivities in the range of 0.15-0.5W/mK, but with the addition of high thermal conductivity continuous carbon fibers these composites can reach thermal conductivities of 300W/mK in the fiber axis direction, as shown in Table 7.1. They display far lower thermal conductivities in the orthogonal (perpendicular to fiber axis) direction, with values that are as much as 2 orders of magnitude lower at 3 W/m-K. Use of pitch based discontinuous fibers results in axial conductivity up to 100 W/m-K and radial conductivity as low as the polymer conductivity of 0.4 W/m-K.

Although numerous pin fin analyses exist in the literature [70]-[80], including the derivation of temperature and heat flow equations for two-dimensional isotropic pin fins [42, 75], the impact of orthotropic thermal conductivity on the thermal performance of polymer composite fins has yet to be established. Failure to properly account for the role of orthotropy could limit the thermal designer's ability to predict and optimize the thermal performance of such polymer composite fins and heat sinks.

Table 7.1 Polymer composite properties

Filler	Matrix	Parallel to fibers (W/m-K)	Normal to fibers (W/m-K)	Density (g/cc)	Wt (%) filler
Continuous carbon fiber	Polymer	330 [1]	3-10	1.8	NA
Discontinuous carbon fiber	Polymer	10-100 [1]	3-10	1.7	NA
Graphite	Epoxy	370 [2]	6.5	1.94	NA
Single walled nanotubes	Epoxy	0.5 [3]	NA	NA	1
Thermal graph DKD X	Lexan HF 1110-11N	8.0 [20]	0.6	1.38	30
Thermal graph DKD X	Lexan HF 1110-11N	11.4 [20]	0.74	1.46	40
Thermocarb CF-300	Zytel 101 NC010	1.1[20]	0.4	1.17	5
Thermocarb CF-300	Zytel 101 NC010	4.4 [20]	0.8	1.33	30

7.2 Isotropic Conductivity Pin Fin Heat Transfer

7.2.1 Literature Review

Classical fin, or extended surface, thermal analysis is based on the Murray-Gardener [70] assumptions, which – along with other assumptions – neglect the presence of radial temperature gradients in the fin and anisotropy in the fin material. It might be anticipated that for low Biot Number fins, signifying fins that are nearly isothermal in the radial direction, the classical relations would apply. Alternately, for large Bi fins with significant radial gradients, fin thermal performance can be

expected to depart from the classical relations. This behavior may be observed in Figure 7.1, showing a comparison between fin heat transfer rates obtained with an analytical two-dimensional isotropic solution [42, 75] and values predicted by the classical and modified classical [72] relations. It may be seen that isotropic pin fin heat transfer rates can be determined using the classical pin fin equations [54], [71] only up to Biot numbers of approximately 0.9 with less than a 10% discrepancy compared to two-dimensional isotropic solution. The Aparecido and Cotta modified 1D relation [72] extends this agreement up to Biot numbers of 4 or 5 with a 10% to 15% discrepancy. However, beyond these Biot values the classical 1D formulation over-predicts and the modified 1D equation under-predicts the two-dimensional pin fin cooling rate.

In order to provide a context for the wide range of Biot numbers, consider a 2.2 x $10^{-6} m^3$ (2.2 cm^3) polymer pin fin operating at 80% efficiency. When subjected to a typical forced convection heat transfer coefficient of 25W/m^{2}K, an unenhanced polymer [81], [82] pin fin with a thermal conductivity of 0.3 W/m-K will have a 10 mm radius and 7 mm height, yielding a Bi of 0.83. This same volume and material fin cooled by water, with an 'h' of 1000 W/m^2-K, results in (80% efficiency) fin radius of 22 mm and 1.45 cm height and display a Biot number of 73. Alternatively, the Bi of a 2.2cm^3 fin made of enhanced polymer with a conductivity of 3 W/m-K and cooled by a 25W/m^{2}K heat transfer coefficient has 6.25 mm radius and 1.8 cm height, yielding Bi of 0.052. It may, therefore, be expected that the performance of unenhanced, isotropic air cooled fins and enhanced water-cooled fins will display some significant departures from the classical predictions. On the other hand, for

enhanced polymer fins used in air-cooled applications, it would appear that reasonably accurate results can be obtained using the classical 1D solution for all but the highest heat transfer coefficients.
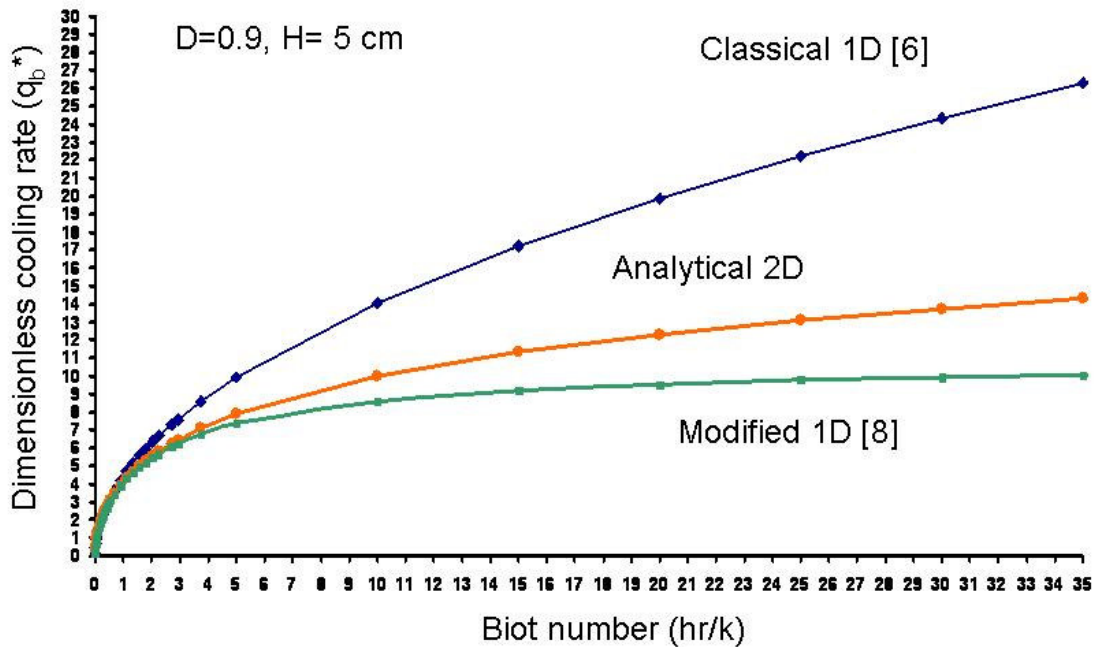
Figure 7.1 Variation of non-dimensional isotropic pin fin cooling rate with radial Biot number (H=50mm, D=9mm) (θ_b=50K)

7.2.2 Temperature Profiles

The observed discrepancies at progressively larger Bi derive from the inability of the 1D formulation to accurately capture the radial temperature gradients that occur even in an isotropic pin fin. These gradients are accentuated by low thermal conductivity, large radius, and high heat transfer coefficients. This behavior can be seen in Fig. 7.2a and Fig. 7.2b that display, side by side, the one dimensional [54] and two dimensional [75] isotropic temperature distributions for a 9mm radius and 50 mm

high polymer fin with a thermal conductivity of 1 W/m-K and a radial Biot number of 4.5. The fin has a constant base temperature of 95 ^{o}C and is exposed to an air convective heat transfer coefficient of 500 W/m^2-K in a 45 ^{o}C ambient temperature. The classical 1D solution by assumption produces isotherms that are parallel to the pin fin base and display no radial temperature variation (Fig 7.2a). However, the more rigorous 2D solution, results in isotherms that, at Bi number of 4.5, are radially parabolic (Fig 7.2b).
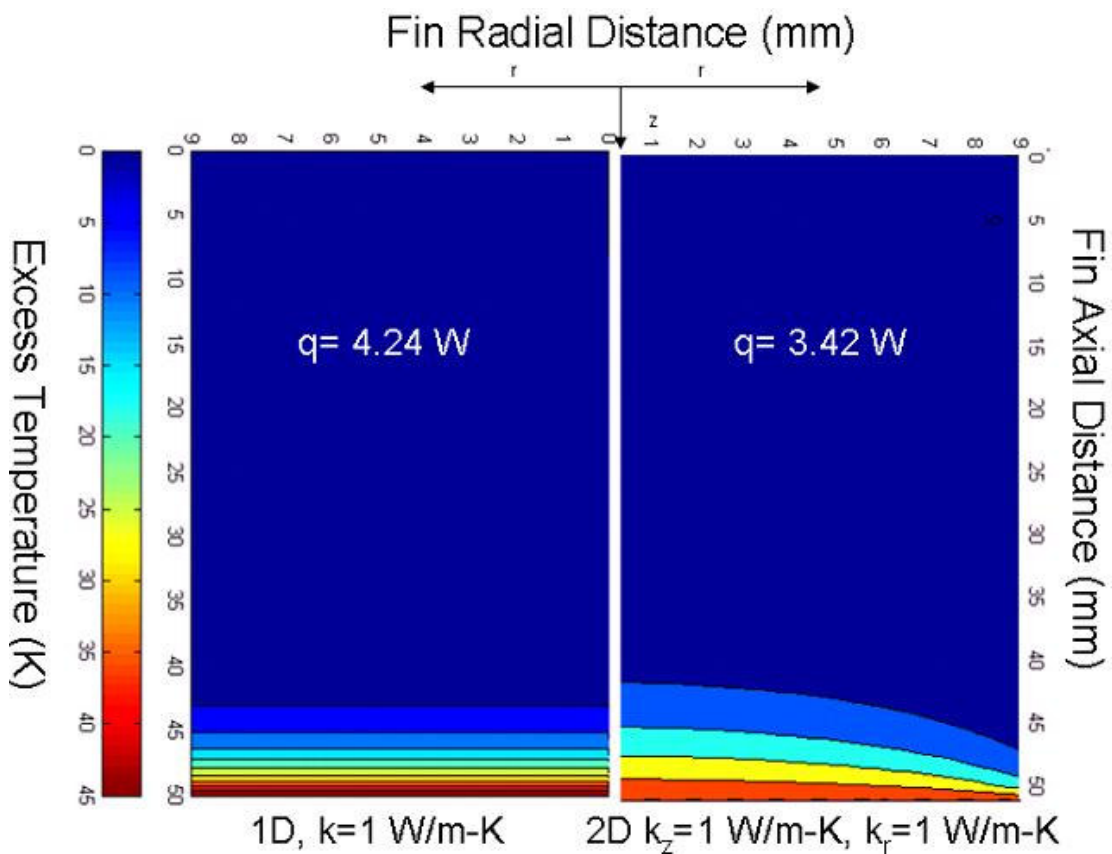
Figure 7.2 Analytical excess temperature profile for an isotropic low conductivity pin fin (a) 1D temperature field (b) 2D temperature field (θ_b=50K)

As a consequence of these different temperature profiles, the 1D solution for the specified pin fin configuration overpredicts the cooling rate (4.24 W) by 24% compared to the value predicted by the more rigorous 2D relation (3.42 W). The use

of orthotropic polymer composite pin fins, with lower radial thermal conductivity than axial thermal conductivity, can be expected to lead to much larger radial temperature gradients than experienced in isotropic fins and, consequently, to greater deviations from the classical 1D fin solutions than seen in this example. If these newly available composite materials are to be successfully used for fins and heat sinks it is, thus, imperative that the effect of thermal orthotropy be incorporated into the thermal analysis and design of such orthotropic pin fins.

7.3 Orthotropic Pin Fin -Detailed Model

7.3.1 Analytical Model
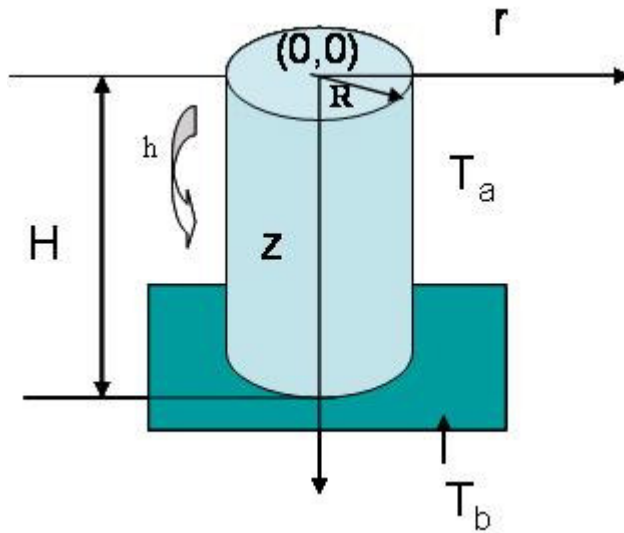
Figure 7.3 Pin fin coordinates

For steady state heat conduction in a radially symmetric, orthotropic fin with no internal heat generation and with θ defined as the fin excess temperature, i.e. $\theta = T - T_a$, the energy equation can be expressed in cylindrical coordinates, as

$$k_r \frac{\partial^2 \theta}{\partial r^2} + k_r \frac{1}{r} \frac{\partial \theta}{\partial r} + k_z \frac{\partial^2 \theta}{\partial z^2} = 0 \tag{7.1}$$

Solution of this equation is sought under the following boundary conditions (referring to Figure 7.3):

a. Symmetry boundary condition at the fin center line:

$$r = 0 \qquad \frac{\partial \theta}{\partial r} = 0 \tag{7.2}$$

b. Uniform and non-zero heat transfer coefficient at the fin tip

$$z=0 \qquad k_z \frac{\partial \theta}{\partial z} = h\theta \tag{7.3}$$

c. Uniform heat transfer coefficient at fin surface

$$r = R \qquad -k_r \frac{\partial \theta}{\partial r} = h\theta \tag{7.4}$$

d. Fixed fin base excess temperature

$$z=H \qquad \theta = \theta_b \tag{7.5}$$

The governing equation for the fin excess temperature, Eq. (7.1), is homogeneous and the method of separation of variables can be applied to its solution. Carrying out the separation of variables and obtaining the needed coefficients using orthogonality of the Bessel functions and utilizing the stated boundary conditions in Eqs. (7.2-7.3), the radial and axial variation of the pin fin excess temperature, $\theta(r, z)$ is found as,

$$\theta(r,z) = 2\theta_b \sum_{n=1}^{\infty} \frac{\lambda_n J_1(\lambda_n) J_o(\lambda_n \frac{r}{R})}{J_o^2(\lambda_n)[\lambda_n^2 + Bi_r^2]} x \frac{[1+\exp(2\lambda_n(k^*)^{1/2} z/R + \tanh^{-1}(\frac{Bi_{gm}}{\lambda_n})])]}{[1+\exp(2\lambda_n(k^*)^{1/2}\gamma + \tanh^{-1}(\frac{Bi_{gm}}{\lambda_n})])]} \exp(\lambda_n(k^*)^{1/2}(H-z)/R) \tag{7.6}$$

Heat flow in such an orthotropic fin can be determined by applying Fourier's Law at the base of the fin. Thus, differentiation of Eq. (7.6) and evaluation of the temperature gradient at z=H, yields the relation for a fin heat flow, q_b, as,

$$q_b = 4\pi k_z \theta_b R(k^*)^{1/2} \, x \sum_{n=1}^{\infty} \frac{Bi_r^2}{\lambda_n[\lambda_n^2 + Bi_r^2]} \frac{[1-\exp(-2[\lambda_n \gamma(k^*)^{1/2} + \tanh^{-1}(\frac{Bi_{gm}}{\lambda_n})])]}{[1+\exp(-2[\lambda_n \gamma(k^*)^{1/2} + \tanh^{-1}(\frac{Bi_{gm}}{\lambda_n})])]} \qquad (7.7)$$

The eigen values for both Eqs. (7.6) and (7.7) are found by using the boundary condition expressed by Eq. (7.3) to obtain the following eigen value equation,

$$J_1(\lambda_n) = \frac{Bi_r}{\lambda_n} Jo(\lambda_n) \qquad (7.8)$$

In order to conform to classical form, the exponential terms in Eq. (7.7) can be converted to hyperbolic tangents, yielding,

$$q_b = 4\pi k_z \theta_b R(k^*)^{1/2} \sum_{n=1}^{\infty} \frac{Bi_r^2}{\lambda_n[\lambda_n^2 + Bi_r^2]} \tanh[\lambda_n \gamma(\frac{k_r}{k_z})^{1/2} + \tanh^{-1}(\frac{Bi_{gm}}{\lambda_n})] \qquad (7.9)$$

It is to be noted that eliminating the orthotropy contained in Eq. (7.7) by setting, $k_r = k_z = k$ and, hence $Bi_r = Bi_{gm} = Bi$, and k*=1 yields the 2D isotropic pin fin Eq. (7.10).

$$q_b = 4\pi k \theta_b R \, x \sum_{n=1}^{\infty} \frac{Bi_r^2}{\lambda_n[\lambda_n^2 + Bi_r^2]} \frac{[1-\exp(-2[\lambda_n \gamma + \tanh^{-1}(\frac{Bi}{\lambda_n})])]}{[1+\exp(-2[\lambda_n \gamma + \tanh^{-1}(\frac{Bi}{\lambda_n})])]} \qquad (7.10)$$

Eq. (7.10) can be further rearranged, using Eq. (7.8), to take on the form of the two dimensional isotropic relation appearing in the literature [42], i.e.

145

$$q_b = 4\pi k \; \theta_b R \; x \sum_{n=1}^{\infty} \; \frac{\lambda_n [J_1(\lambda_n)]^2}{[\lambda_n^{\;2} + Bi^2][J_o(\lambda_n)]^2} \frac{\lambda_n \sinh\lambda_n\gamma + Bi\cosh\lambda_n\gamma}{\lambda_n \cosh\lambda_n\gamma + Bi\sinh\lambda_n\lambda} \tag{7.11}$$

7.3.1.1 Analytical Convergence
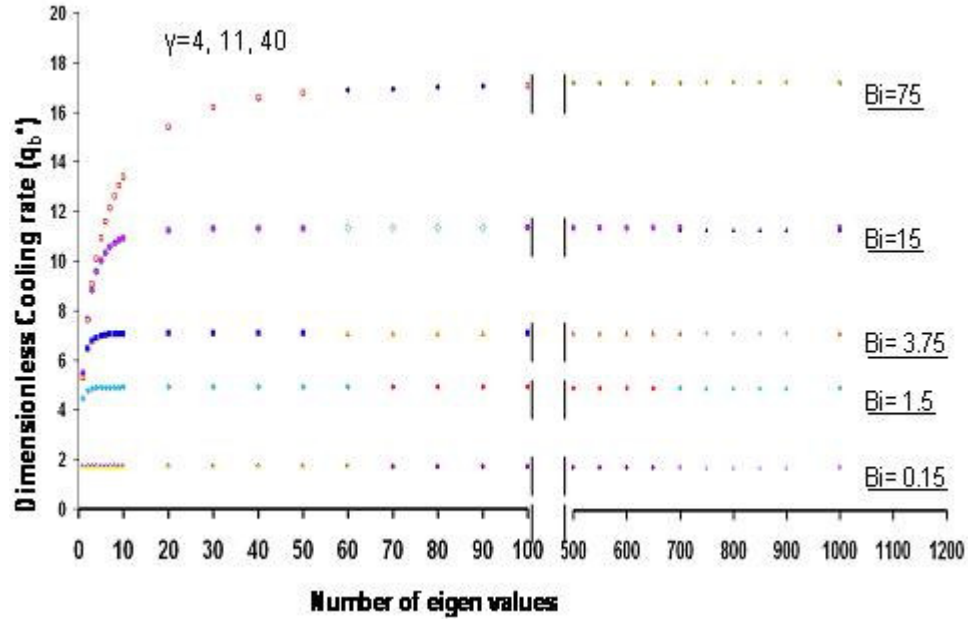
Figure 7.4 Dependence of non-dimensional isotropic pin fin cooling rate on number of eigen values (red: γ=4, blue: γ=11, green: γ=40)

As may be seen in Fig 7.4, the number of eigen values required for first decimal convergence of the analytical solution increases from a single term for Bi of 0.15, through 10 for Bi of 15, and to as many as 100 eigen values for Bi of 75, the highest radial Biot number studied. It may also be noted that the convergence of q* is independent of the aspect ratio for a range of γ from 4 to 40.

7.3.2 Numerical FEM 3D Modeling

  To further quantify the impact of two-dimensional heat flow in pin fins and establish a valid baseline for understanding the role played by orthotropy in this configuration, a FEM model, using ANSYS 7.1, was developed using solid 70 elements. The convergence of the FEM-derived pin fin heat transfer rate with the node count is shown in Figure 7.5 and it reveals that some 30,000 nodes were needed to achieve a "mesh-refined" solution to a first decimal place accuracy for Bi=15 and about 125,000 for a Bi=75, for which the larger temperature gradients necessitate a larger number of nodes to properly capture the temperature field. A comparison of Figs 7.5 and 7.6 reveals the fully-converged analytical and FEM results to be in close agreement (0.4%) with each other.
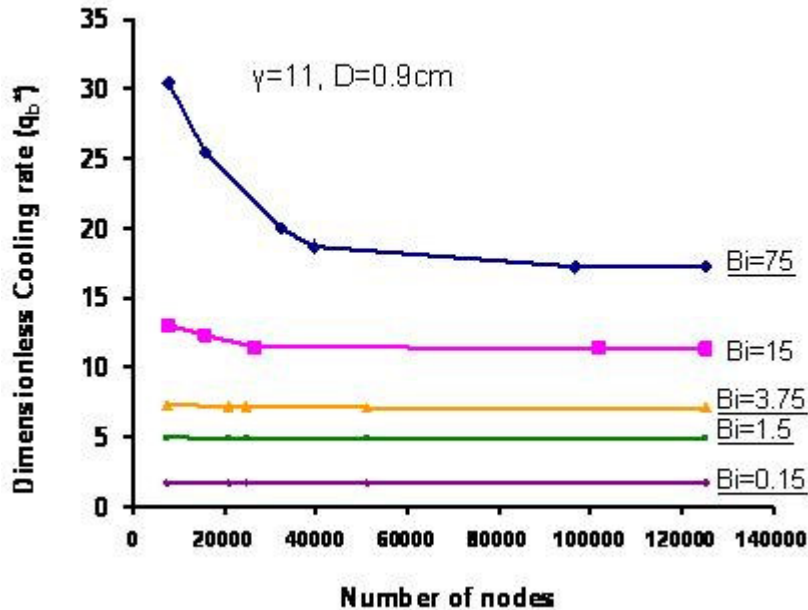
Figure 7.5 Non-dimensional isotropic pin fin cooling rate – FEM mesh refinement effect

To more clearly display the effect of the radial Biot number on isotropic fin heat transfer, the analytical and numerical results for heat flow in an "extreme" 9mm diameter, 50mm long, pin fin are shown in Figure 7.6. It is to be noted that the smaller Bi values are obtained with a fin thermal conductivity of 20W/mK and heat transfer coefficients ranging from $10W/m^2K$ (Bi=0.0022) to 5000 W/m^2K (Bi= 1.125), while Bi values approaching 75 were obtained with a thermal conductivity of 0.3W/mK, typical of an un-enhanced polymer, and a heat transfer coefficient of 5000 W/m^2K, as might be encountered in compact water-cooled heat exchangers [81, 82].
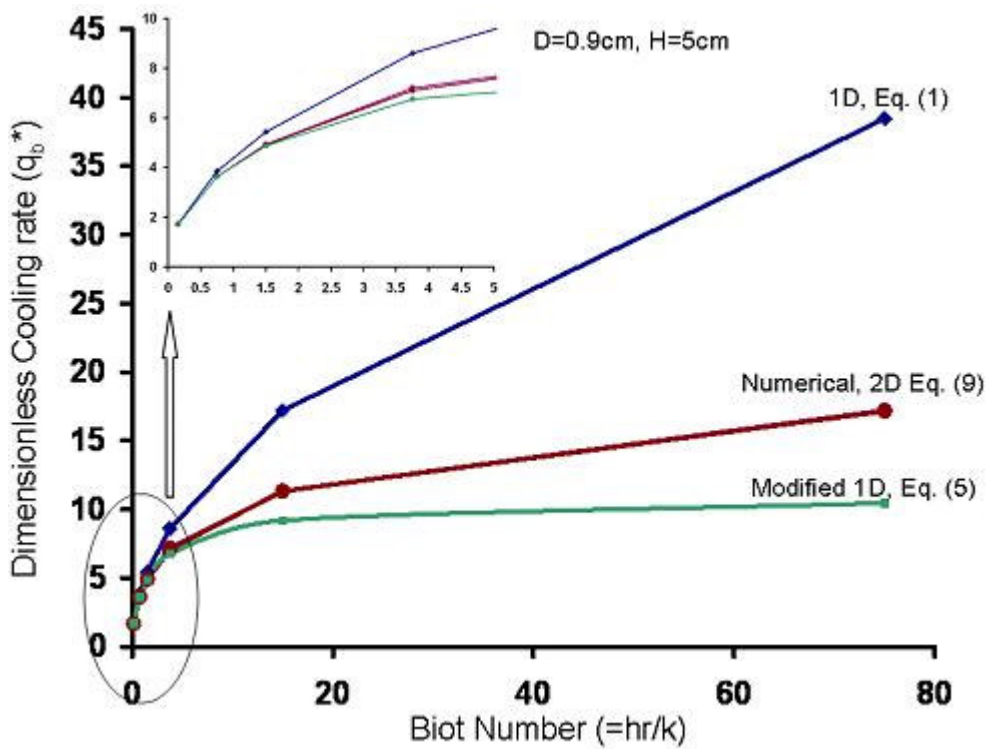
Figure 7.6 Variation of non-dimensional isotropic pin fin cooling rate with radial Biot number (H=50mm, D=9mm)

Figure 7.6 makes it clear that while the heat transfer rate from a pin fin can be determined using the classical pin fin equations up to Biot numbers of 0.5 (with less

than a 4% discrepancy), the Aparecido and Cotta modified 1D relations [72] extend this agreement up to Biot numbers of 5 (15% accuracy). However, beyond these Biot values the classical 1D formulation over- predicts and the Aparecido and Cotta modified 1D equation under-predicts the pin fin cooling rate. The values obtained from the rigorously-derived 2D, isotropic pin fin equation agree very closely ($\leq 0.2\%$) with the FEM results up to radial Biot Numbers close to 75.

7.4 Orthotropic Pin Fin Results

7.4.1 Analytical/Numerical Comparison

Figure 7.7a displays a comparison of the analytical and numerical converged results obtained using ANSYS 7.1 for the heat flow from an orthotropic pin fin 5cm in length and 0.9cm in diameter, with an axial thermal conductivity of 20W/mK, subjected to a heat transfer coefficient variation from 10 to 5000 W/m^{2}K and a base excess temperature of 40K. A total of 99 distinct data points are shown for three different thermal conductivity ratios, k*=0.015, 0.25, and 1, and radial Biot numbers varying from 0.01-15. The plot clearly indicates very strong agreement (standard deviation, σ, =0.073) between the analytical results obtained with Eq. (7.7) and the FEM simulation results. The FEM simulation was first performed with a free mesh of upto 100,000 solid70 3D elements for various described boundary conditions. In order to better utilize available node limit the results were then also verified using ANSYS 8.0 2D axisymmetric modeling using plane 75 elements in Fig. 7.7. The pin fin has 9mm radius and 5 cm fin height. The axial thermal conductivity value is 11.4 W/m-K and radial thermal conductivity is 0.74 W/m-K (Table 7.1). The temperature contour plot

depicts two complementary parts for each half of the fin, left half is produced from analytical Eq. (7.6) and right half is obtained using numerical numerically converged solution at 11121 nodes. The plot indicates agreement within 0.4% on temperature distribution resulting in 0.4% agreement on pin fin heat flow rate.
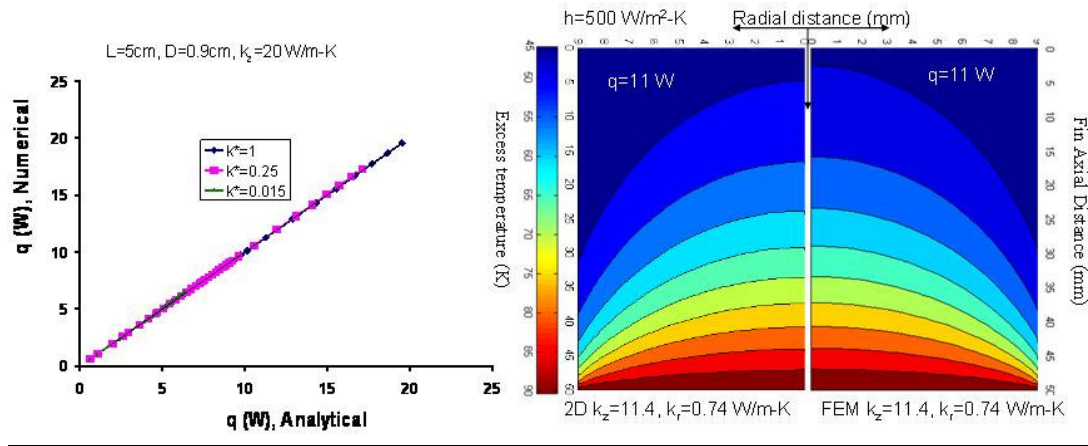
Figure 7.7 Comparison of analytical and numerical orthotropic ratios (a) heat flow rate (b) temperature distribution for various conductivity ratios (θ_b=50K)

7.4.1.1 Temperature Profile:

The impact of thermal orthotropy can be clearly seen in Figure 7.8, showing a comparison of the temperature profile for an isotropic and orthotropic fin, respectively. The temperature distribution for a pin fin with an isotropic thermal conductivity of 11.4W/mK obtained via the 2D isotropic relation, Eq. (7.10), is shown in Fig 7.8a. Fig 7.8b displays the temperature field for a thermally enhanced, orthotropic polymer pin fin case depicted in Table 7.1 with an axial thermal conductivity 11.4W/m-K and 0.74W/mK radial thermal conductivity, obtained via Eq. (7.7). The pin fin in both cases has a 9mm diameter and a 50mm height; the fin

base temperature is fixed at 95 °C in an ambient temperature of 45 °C, and is exposed to a uniform convective heat transfer coefficient of 500 W/m²-K.

Figure 7.8b clearly displays the two-dimensional character of the temperature distribution in an orthotropic pin fin, reflected in the far strong radial curvature of the isotherms throughout the fin volume than seen in the 2D isotropic temperature distribution Ignoring these increased radial temperature gradients by assuming isotropic axial conductivity leads to a 25% over prediction in the fin heat transfer rate (11W vs. 13.8W). It is to be noted that application of the classical isotropic 1D fin analysis results in a further over prediction by some 5% and an erroneous heat transfer rate of 14.3W for this geometry and operating conditions.
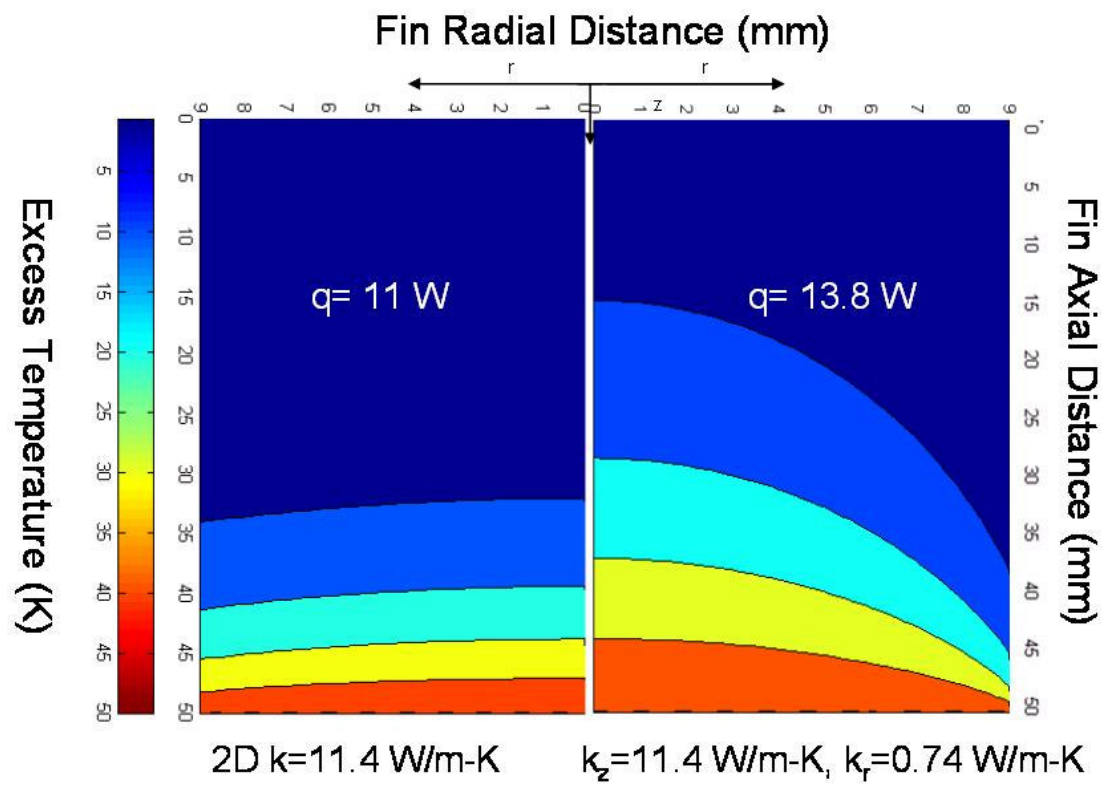
Figure 7.8 Analytical excess temperature profile for a pin fin (a) Isotropic 2D - Eq. (7.10) (b) Orthotropic 2D – Eq. (7.7) (H=50mm, D=9mm, h=500W/m²K)) (θ_b=50K)

7.4.1.2 Thermal Conductivity
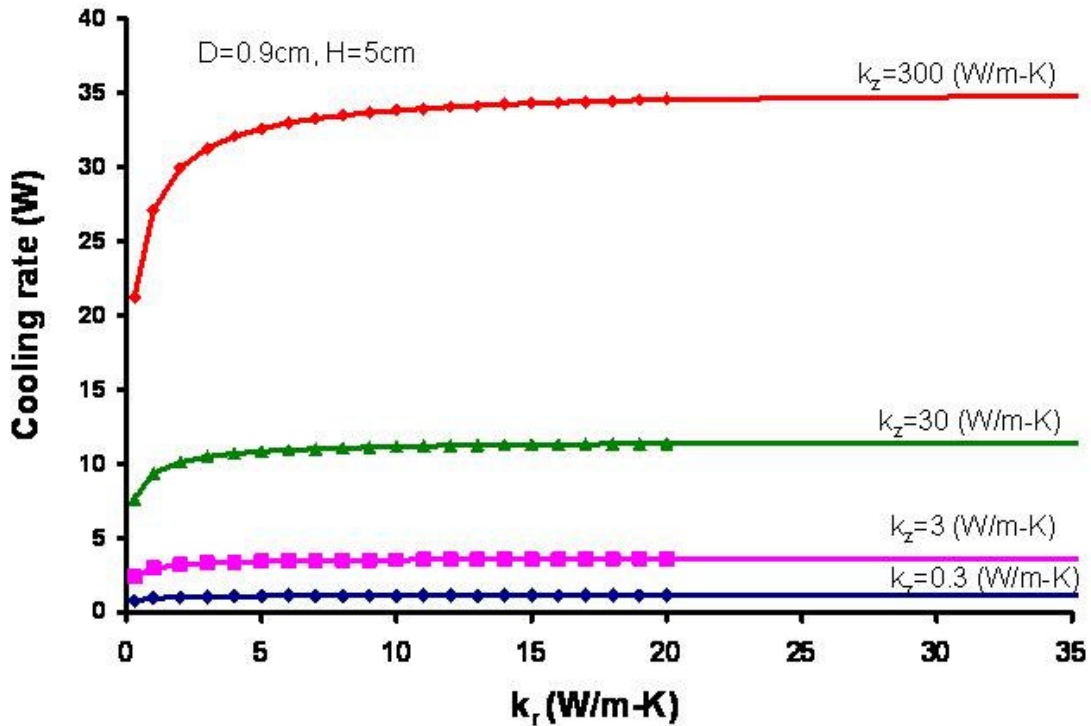
Figure 7.9 Orthotropic pin fin cooling rate variation with radial and axial thermal conductivity - Eq. (7.9) (θ_b=50K)

Figure 7.9 depicts the relatively weak, though complex, cooling rate dependence on the radial thermal conductivity, showing the cooling rate to increase linearly at relatively small values of k_r, followed by a gentle asymptotic rise over a large range of k_r values, for each value of k_z. Despite the complex functional dependence of q_b on k_r in Eq. (7.9), this behavior may well reflect the presence of k_r in the argument of the hyperbolic tangent function in the summation of eigen valued terms. For the conditions studied numerically, the asymptotic domain appears to begin at progressively higher k_r values as the axial thermal conductivity value increases, transitioning to the asymptotic plateau at a radial thermal conductivity approximately

one tenth of the axial thermal conductivity value. Thus for $k_z=300W/m$-K the asymptotic transition occurs in the vicinity of $k_r=30W/m$-K, while for an axial thermal conductivity of 30 W/m-K, the asymptotic zone begins at $k_r=3W/m$-K. The fin heat transfer rate follows an approximately square root dependence on axial conductivity as it increases from 0.3 to 300W/mK.

7.4.1.3 Conductivity Ratios

The effect of the thermal conductivity ratio on the pin fin cooling rate is depicted in Figure 7.10 for the previously described case. In general the fin heat transfer rate increases with k* and asymptotically approaches the limit associated with the classical 1D relation. For the lowest heat transfer coefficient studied ($10W/m^2$-K), the improvement is nearly zero, while for the highest heat transfer coefficient ($5000W/m^2$-K), a four-fold improvement is attained. The asymptotic limit is reached at k* values of approximately unity, though for the high heat transfer coefficients that the fin could experience in water cooled heat exchangers [81] (h=$5000W/m^2$-K) the cooling rate continue to improve up to k* values of 4.

The results shown in Fig. 7.11 for variable fin height and for a fixed heat transfer coefficient of $100W/m^2$-K, displaying the strong effect on the cooling rate of k* values below unity and a progressively weaker effect for larger values of k*, reinforces this conclusion. As the conductivity ratio increases, the radial temperature gradients diminish and at k* of unity or greater the heat transfer rate of this nearly radially-isothermal fin indeed should approach the heat transfer rates obtained from the classical 1D relation.
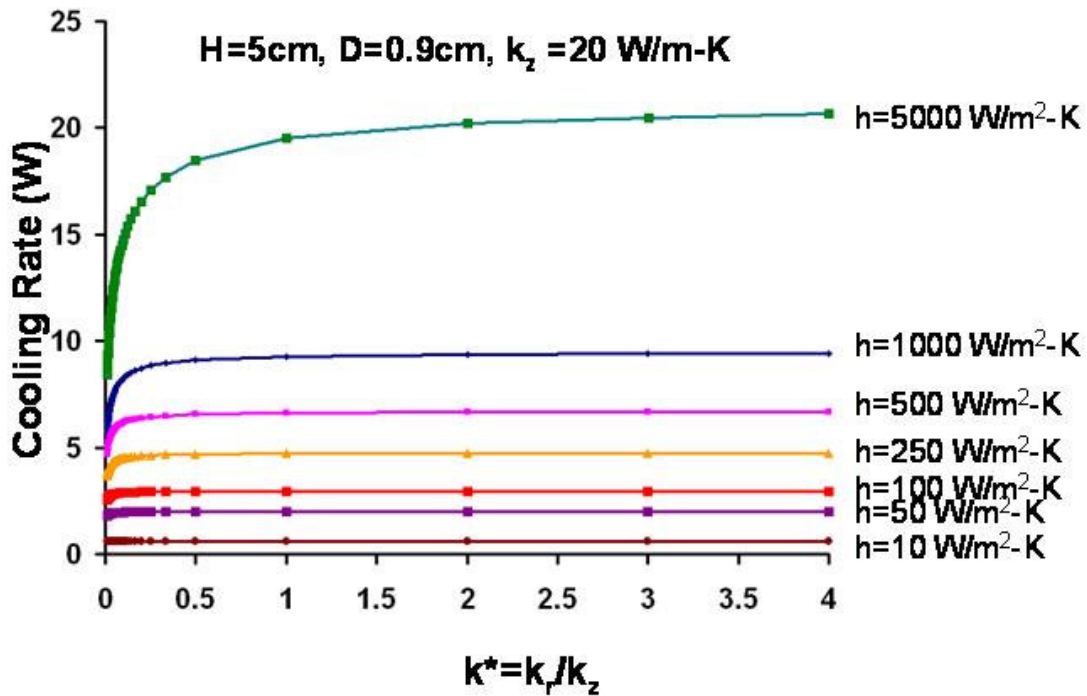
Figure 7.10: Orthotropic pin fin cooling rate variation with thermal orthotropy - Eq. (7.9) (θ_b=50K)

7.4.1.4 Fin Height

The variation of the pin fin cooling rate with fin height, for a fixed axial thermal conductivity of 20 W/m-K in an isothermal medium with a fixed heat transfer coefficient of 1000W/m^2-K, is shown in Figure 7.11. Interestingly, the variation with height - at conductivity ratios of unity as well as higher and lower values – mimics the asymptotic approach (typically hyperbolic tangent variation) to the maximum fin heat transfer rate found in the classical 1-D pin fin solution. This behavior reflects the appearance of the fin height in the argument of the hyperbolic tangent inside the eigen valued summation in Eq. (7.9). For a pin fin with fixed axial 20 W/m-K and diameter of 9mm, this optimum fin height is relatively constant at 0.015 m for a fixed heat transfer coefficient 1000 W/m^2-K over a broad conductivity ratio range obtained by

varying radial thermal conductivity. The relatively weak dependence of the optimum

pin fin height on the conductivity ratio has been further verified for heat transfer

coefficients of 10 and 100 W/m^2-K, as shown in Fig. 7.11.
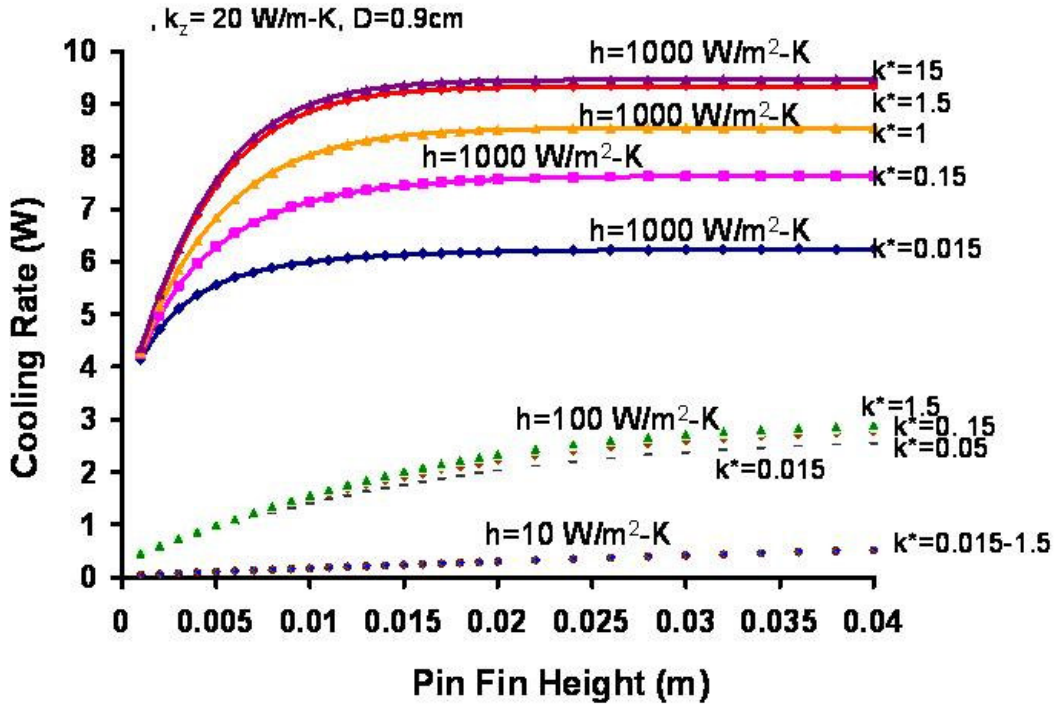
Figure 7.11 Orthotropic pin fin cooling rate variation with fin height - Eq. (7.9)
(θ_b=50K)

7.4.1.5 Effective Conductivity

In the interest of streamlined thermal design, it is tempting to explore the potential for

capturing the orthotropic effect through the use of an "effective" thermal conductivity

in the classical 1D relation. Figure 9 displays the cooling rates obtained using Eq.

(7.7) for a single orthotropic pin fin of diameter 9mm, fin height 50mm, and a

conductivity ratio of 60, subjected to a range of heat transfer coefficients and using

several alternative definitions of "effective" thermal conductivity .
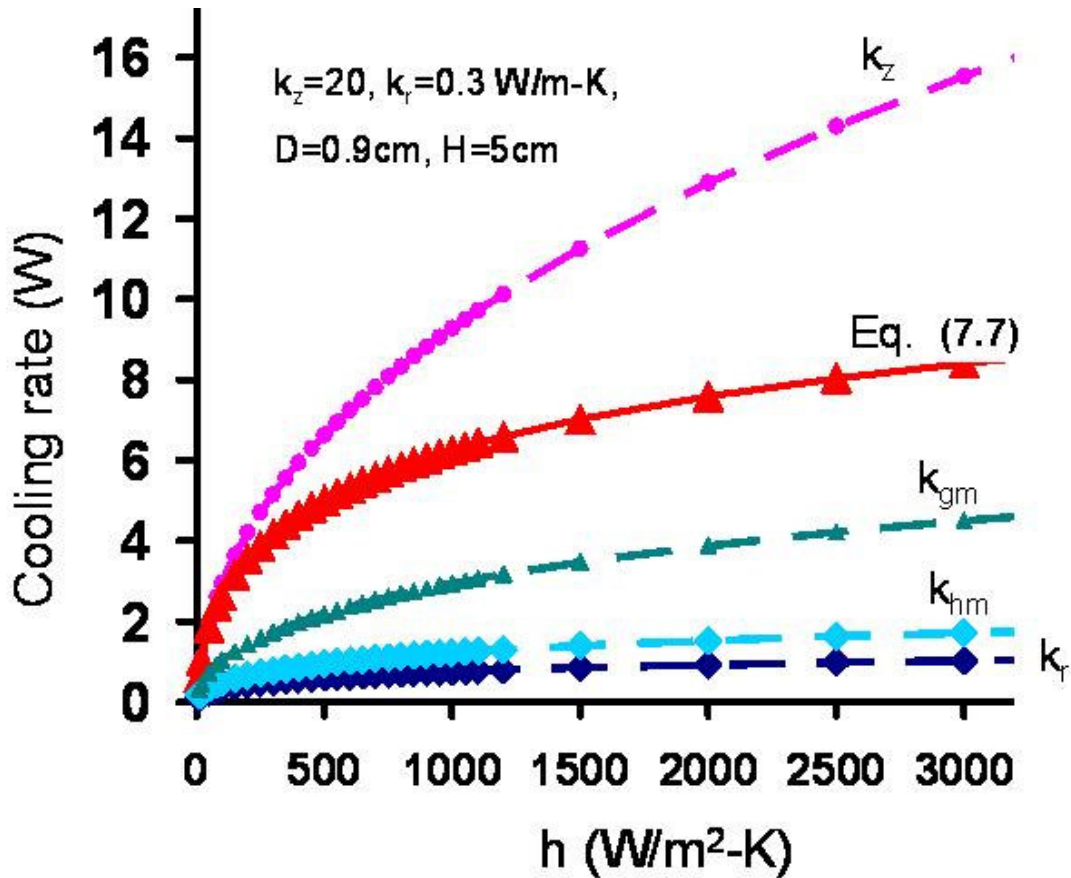
Figure 7.12: Orthotropic pin fin cooling rate based on 1D model with effective thermal conductivities (θ_b=50K)

Examining Fig. 7.12, it is to be noted that the use of an effective thermal conductivity value based on the axial conductivity alone, as well as on the harmonic mean (0.6 W/m-K) or geometric mean (2.45 W/m-K) of k_r and k_z, or the radial conductivity alone, is incapable of predicting – even approximately – the cooling rate of the orthotropic fin over the broad range of heat transfer coefficients studied. However, for air-cooling heat transfer coefficients up to approximately 70 W/m²-K, use of the axial thermal conductivity does provide a predictive accuracy to within 8%.

Moreover, even when the two-dimensional isotropic relation is used (Eq. 7.10), Figure 7.13 reveals that none of the effective single thermal conductivity values can be used to accurately predicts the orthotropic pin fin cooling rate, for heat transfer

156

coefficients above 70 W/m^2-K. For h values of about 80W/m^2-K the 2D isotropic prediction shows an approximately 10% discrepancy, which grows to 110% at 1500 W/m^2-K, relative to the 2D orthotropic results using Eq. (7.9).
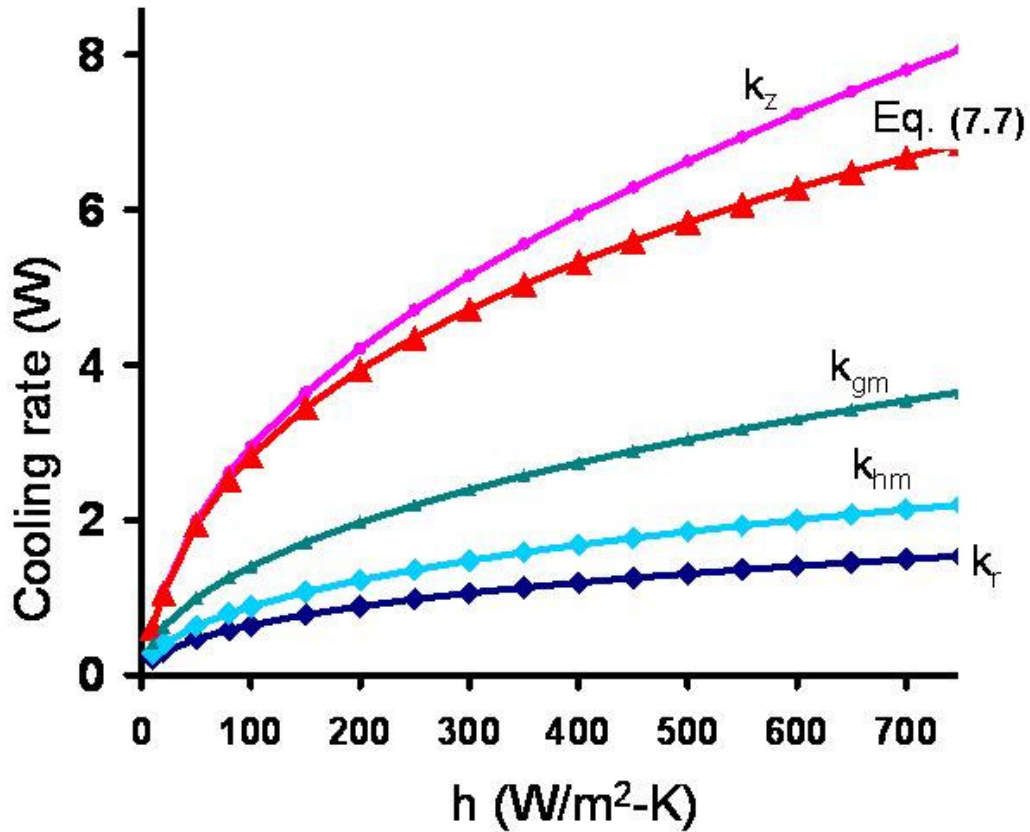
Figure 7.13: Orthotropic pin fin cooling rate based on isotropic 2D relation with effective thermal conductivities (θ_b=50K)

7.5 Approximate Orthotropic Pin Fin Relations

For typical pin fin geometries, fin tip area is a small fraction of the total wetted area. Therefore it is possible to approximate fin heat transfer by assuming negligible heat transfer from the pin fin tip. Setting $\partial\theta/\partial z$ to zero in Eq. (7.3) at the fin tip, and repeating the analysis described above, the total heat transfer rate from the lateral surface area of a tip-insulated pin fin is found to be expressible as,

157

$$q_b = -4\pi k_z \theta_b R(k^*)^{\frac{1}{2}} \sum_{n=1}^{100} \frac{Bi_r^2}{\lambda_n [\lambda_n^2 + Bi_r^2]} \tanh(\lambda_n (\frac{k_r}{k_z})^{\frac{1}{2}} \gamma') \qquad (7.12)$$

Using a modified fin height which includes the tip area, i.e. adding one quarter of the pin diameter to pin fin height [71], in Eq. (7.12) increases the accuracy of this relation.
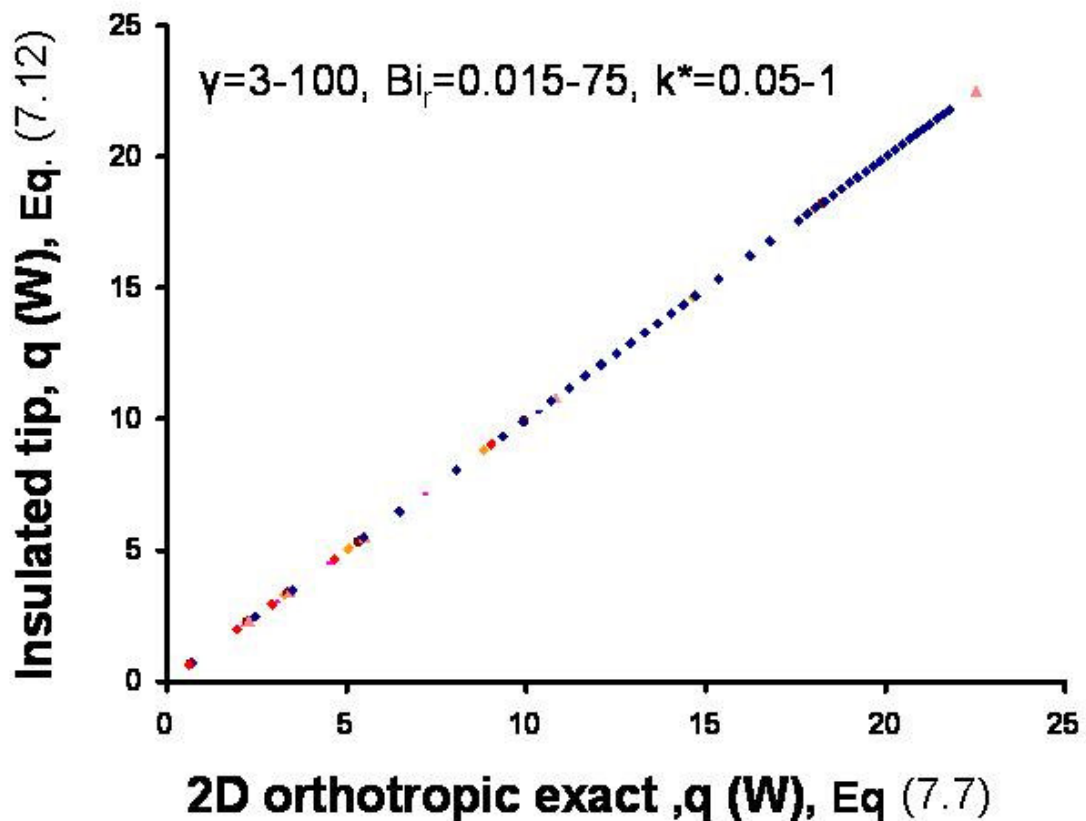
Figure 7.14 Comparison of orthotropic cooling rates using insulated tip pin fin equation (Eq. (7.12)) (θ_b=50K)

Fig 7.14 displays a comparison between the orthotropic pin fin cooling rates, calculated using Eq. (7.12) with modified pin fin height, spanning aspect ratios (H/R) of 3-100, thermal conductivity ratios (k*) from 0.015-1, and heat transfer coefficients

ranging from 10W/m²-K to 5000 W/m²-K, for a total of 547 different cases. The largest discrepancy observed was 3.7%, for the lowest fin aspect ratio of 3, the thermal conductivity ratio of 0.05, and the highest considered heat transfer coefficient of 5000 W/m²-K. As anticipated, the error associated with the simplified formulation of Eq. (7.12) decreases monotonically with increasing aspect ratio and conductivity ratio. This is because the fin tip heat loss becomes smaller in both the cases.

7.6 Summary

A closed form analytical solution for heat transfer from a cylindrical pin fin with orthotropic thermal conductivity is proposed. The resulting relation was numerically validated over a broad parametric range, including fin thermal conductivity ratios of 0.015-15, aspect ratios of 4-100, and radial Biot numbers of 0.0056-75. A tip-insulated approximation, yielding agreement to within 3.7% of the exact closed form equation for fin aspect ratios greater than 3, was also found.

For the parametric range studied, the impact of orthotropy on the pin fin heat transfer rate is found to increase with the radial Biot number and to decrease with increasing thermal conductivity ratio (radial/axial). Using these relations, it is determined that fin orthotropy does not materially affect the behavior of typical air-cooled fins. Alternatively, for heat transfer coefficients achievable with water cooling and conductivity ratios below 0.1, the fin heat transfer rate can fall more than 25% below the "classical" heat transfer rates.

Chapter 8: Orthotropic Pin Fin Design and Optimization

The eigen-value heat transfer equations derived and discussed in Chapter 7 can be used to predict the heat transfer rate and temperature distribution for a thermally-orthotropic pin fin, they are cumbersome and awkward to use for parametric design and optimization. In particular, since earlier chapters have identified the value of the least-material and least-energy optimizations in addressing "design for sustainability" issues, it would be most beneficial if simplified versions of Eqs, (8.1) and (8.4) could be derived and applied to the design and optimization of polymer composite pin fins. The current chapter provides such simplified 2D orthotropic pin fin governing equations for the Biot number range where classical 1D pin fin analysis significantly over predicts the fin heat transfer rate. Two simplified equations, each providing values that are within 7% of the rigorous analytical solutions, are proposed for the intermediate radial Biot number range (0.4-2) and the high radial Biot number range (2-40), respectively. Use of these relations, together with the least-material pin fin aspect ratio, derived from the 1D equation using the axial thermal conductivity, is seen to offer a fin geometry and heat transfer rate that is very close to that obtained from a rigorous 2D orthotropic analysis.

8.1 Introduction

Chapter 7 provided a comprehensive analysis of the effects of thermal orthotropy on the temperature distribution and heat transfer rate of a convectively-cooled cylindrical fin. The classical 1D pin fin heat rate Eq. (8.7) was found to provide satisfactory accuracy up to radial Biot numbers of 0.4. However, at higher radial Biot numbers, the classical 1D pin fin Eq. (8.7) significantly over predicts the heat flow

rate and use must be made of a 2D, orthotropic relation of the form of Eq. (7.9) (repeated here as Eq. (8.1)) to capture the radially non-uniform temperature distribution and it consequences for a broad parametric range.

$$q_b = -4\pi\theta_b R(k_z)^{\frac{1}{2}} \sum_{n=1}^{\infty} \frac{Bi_r^2}{\lambda_n[\lambda_n^2 + Bi_r^2]} \tanh[\lambda_n\gamma(\frac{k_r}{k_z})^{\frac{1}{2}} + \tanh^{-1}(\frac{Bi_{gm}}{\lambda_n})] \qquad (8.1)$$

$$\text{where,} \quad Bi_r = \frac{hR}{k_r} \qquad Bi_{gm} = \frac{hR}{(k_r k_z)^{\frac{1}{2}}} \qquad \gamma = \frac{H}{R} \qquad k* = \frac{k_r}{k_z} \qquad (8.2)$$

$$J_1(\lambda_n) = \frac{Bi_r}{\lambda_n} Jo(\lambda_n) \qquad (8.3)$$

For pin fins having aspect ratio greater than 10, the second (right) hyperbolic tangent term in the summation can be eliminated by assuming the fin tip to be insulated and extending the fin height to account for the tip heat loss, yielding a simplified heat flow relation as shown in Eq. (8.4).

$$q = -4\pi k_z \theta_b R(\frac{k_r}{k_z})^{\frac{1}{2}} \sum_{n=1}^{100} \frac{Bi_r^2}{\lambda_n[\lambda_n^2 + Bi_r^2]} \tanh(\lambda_n\gamma'(\frac{k_r}{k_z})^{\frac{1}{2}}) \qquad (8.4)$$

One major limitation of these orthotropic pin fin equations is the need to determine a large number of eigen values and to perform an exhaustive multi-variable summation for each geometry and conductivity ratio of interest. Thus, while the eigen-value heat transfer equations derived and discussed in Chapter 7 can be used to accurately predict the heat transfer rate and temperature distribution for a thermally-orthotropic pin fin, they are cumbersome and awkward to use for parametric design and optimization. In particular, since earlier chapters have identified the value of the least-material and least-energy optimizations in addressing "design for sustainability" issues, it would be most beneficial if simplified, closed-form versions of Eq (8.1)

could be derived and applied to the design and optimization of polymer composite pin fins. The current chapter provides such simplified 2D orthotropic pin fin governing equations for the Biot number range where classical 1D pin fin analysis significantly over predicts the fin heat transfer rate.

8.2 Low Radial Biot Range Orthotropic Pin Fin Analysis

In determining the least-material orthotropic pin fin parameters, the fin heat transfer rate is calculated with the rigorous 2D orthotropic fin equation (Eq. (8.1)) across a range of geometric and operational conditions and an effort is made to identify the configuration that yields the highest cooling rate for a fixed fin volume (and hence mass). Fig 8.1 displays the results for a highly orthotropic pin fin having a radial thermal conductivity of 0.3 W/m-K, typical of pure polymer resin, while the axial thermal conductivity is 20 W/m-K, obtained using uniaxially oriented carbon fiber in the axial direction. For a heat transfer coefficient of 10 W/m^2-K the least material pin fin radius is 4.2 mm. At a higher heat transfer coefficient value of 20 W/m^2-K the least material radius increases to 4.7 mm and for still higher heat transfer coefficients the optimum value appears to be beyond the specified parametric range.

Increasing the radial thermal conductivity to 3 W/m-K decreases the value of the Biot numbers but results in an increase in the cooling rate, compared to the Fig 8.1 results for a radial thermal conductivity of 0.3 W/m-K. In Fig 8.2 least material radius values of 5.6 mm, 6.6mm, and 7mm are visible for heat transfer coefficient values of 50, 100, 150 W/m^2-K. At the highest heat transfer coefficient of 550W/m^{2}K, the heat transfer rate increases monotonically with the radius (and hence

Bi), while intermediate values reflect the approach to an optimum value somewhere beyond the specified parametric range.

Figure 8.1 Cooling rate with low radial Biot number for (k_r=0.3 W/m-K) fin with various heat transfer coefficient values (Eq. (8.1)) (θ_b=50K)
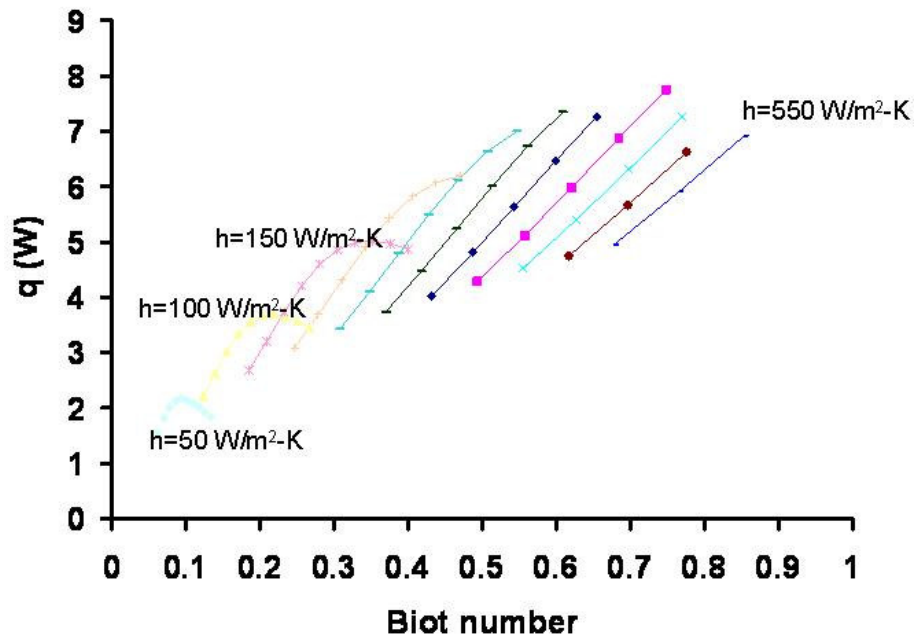
Figure 8.2 Cooling rate with low radial Biot number for (k=3 W/m-K) fin with various heat transfer coefficient values (Eq. (8.1))

8.3 Intermediate Radial Biot Range Orthotropic Pin Fin Analysis

The pin fin volume is fixed at 3.18 cm^3 and axial thermal conductivity at 20 W/m-K. The heat transfer coefficient, radial thermal conductivity and pin fin dimensions were varied in order to obtain least material pin fin dimensions for the described intermediate radial Biot range in Fig. 8.3. As the pin fin radius increases from, 3.7mm to 8mm, for a fixed heat transfer coefficient of 30 W/m^2-K the heat flow rate increases up to the least material pin fin radius of 5.1 mm and then decreases beyond.
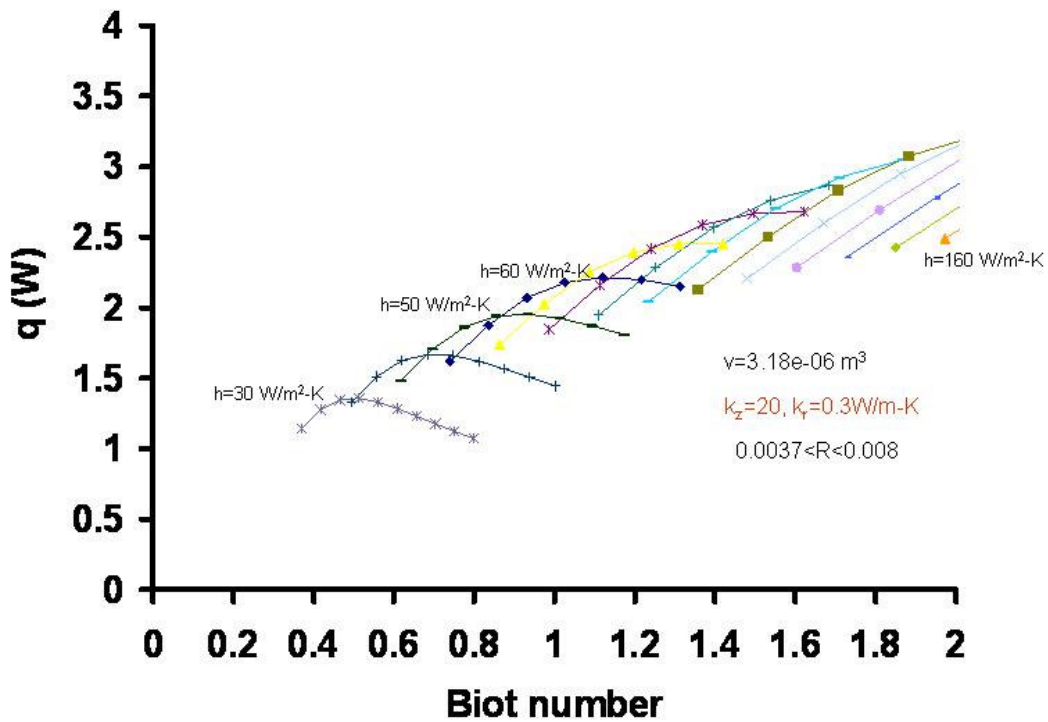
Figure 8.3 Cooling rate with intermediate radial Biot number for (k_r=0.3 W/m-K) fin with various heat transfer coefficient values (Eq. (8.1)) (θ_b=50K)

The effect of radial thermal conductivity 1 W/m-K, axial 20 W/m-K and fixed pin fin volume pin fin is shown in Fig. 8.4. For the fixed heat transfer coefficient value of 75 W/m^2-K curve, the heat flow rate increases up to the least material pin fin radius of 6.1 mm and then decreases. Increasing, the heat transfer coefficient value to 100 W/m^2-K results in least material pin fin radius value of 6.6 mm at radial Biot

number of 0.6564. Similarly at 125 W/m^2-K and 150 W/m^2-K, the least material pin

fin radius value is close to 6.6 mm with a radial Biot number of 0.8 and 1

respectively.
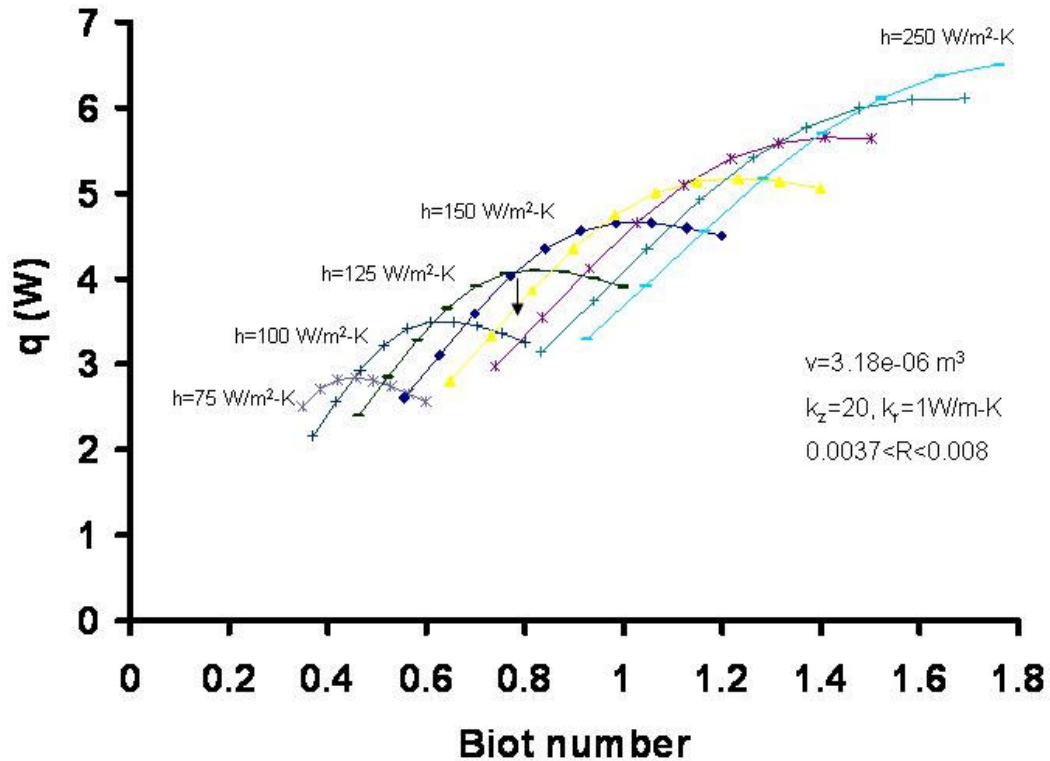
Figure 8.4 Cooling rate with intermediate radial Biot number for (k_r=1 W/m-K) fin
with various heat transfer coefficient values (Eq. (8.1)) (θ_b=50K)

8.3 High Radial Biot Range Orthotropic Pin Fin Analysis

At higher radial Biot numbers, greater than 2, achieved in case of low thermal

conductivity (0.1-0.4 W/m-K) polymer pin fins. The pin fin volume is fixed at

3.18cm^3 and the axial thermal conductivity at 20 W/m-K. The heat transfer

coefficient, radial thermal conductivity and pin fin dimensions were varied in order to

obtain the least material pin fin dimensions for the described high radial Biot range. It

was found that the heat flow rate increases continually for the range of practical pin fin dimensions considered for the higher radial Biot cases.

In Fig. 8.5 the solid lines indicate the rigorous 2D Eq. (8.1) results for a polymer composite pin fin with thermal conductivity ratio of 0.015. The radial Biot number for fixed heat transfer coefficient curve increases from 2 to 35 as the pin fin radius increases from 3.7 mm to 8 mm. The heat transfer coefficient represented in Fig. 8.5, increases from a value of 200 W/m^2-K to 2000 W/m^2-K, as would be encountered in water cooled convection.
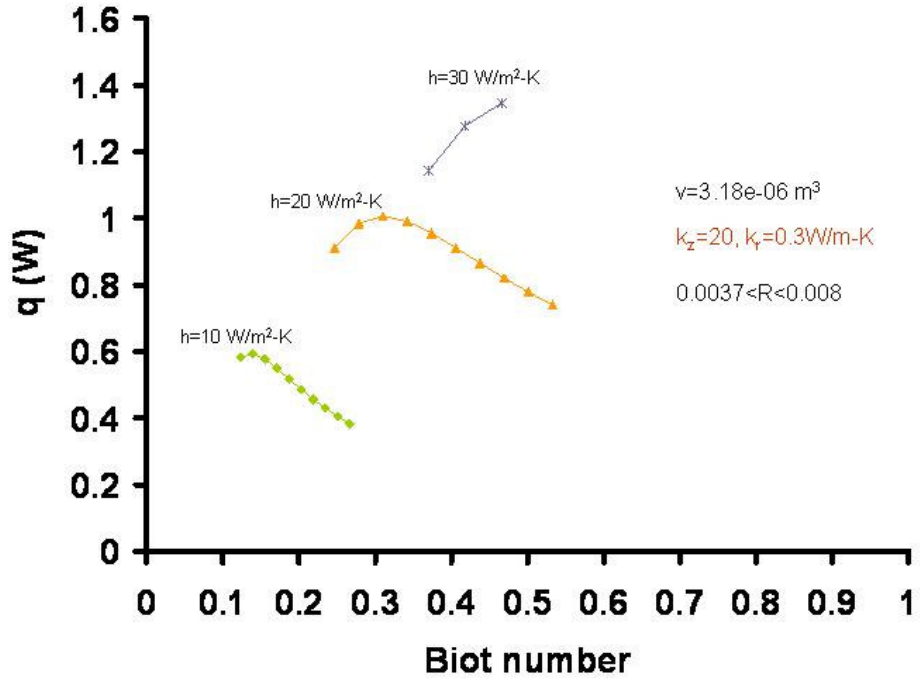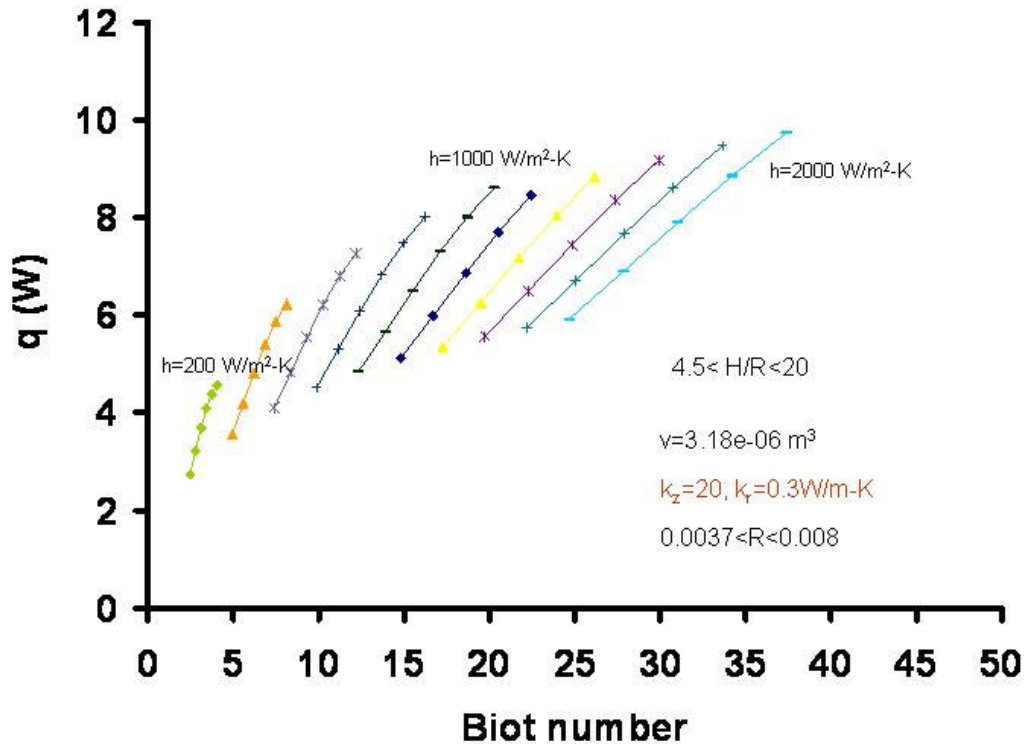

Figure 8.5 Cooling rate with high radial Biot number for (k_r=0.3 W/m-K) fin with various heat transfer coefficient values (Eq. (8.1)) (θ_b=50K)

Figure 8.6 indicates heat flow rate results for a radial thermal conductivity of 1 W/m-K, achieved by increasing the volume fraction of carbon fibers in the polymer

composite. The radial Biot number varies from 2-32 and fin aspect ratio ranges from 3-20. At a highest considered heat transfer coefficient value of 5000 W/m²-K, achieved in forced convection water cooling, the radial Biot number for a pin fin of radius 45mm goes up to 32.
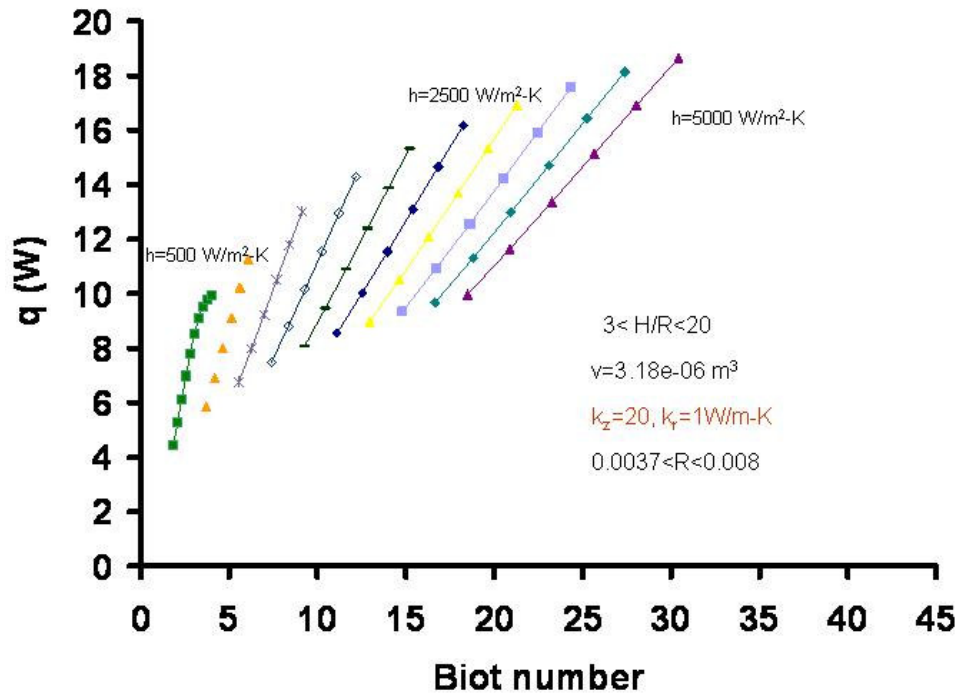
Figure 8.6 Cooling rate with high radial Biot number for (k_r=1 W/m-K) fin with various heat transfer coefficient values (Eq. (8.1)) (θ_b=50K)

8.5 Orthotropic Thermal Conductivity Least Material Pin Fin Analysis

Since the temperature profile for an orthotropic thermal conductivity polymer composite pin fin is significantly different than that of an isotropic pin fin (Fig. 7.8), it is to be expected that the least material orthotropic pin fin would differ in performance, as well as in geometry, from the least-material isotropic pin fin. The least material pin fin equation for a single isotropic fin is given as [55],

$$d_{lm} = 1.503 \left(\frac{hV^2}{k} \right)^{1/5} \tag{8.5}$$

Where, 'h' is the heat transfer coefficient, 'V' is the pin fin volume, and 'k' is the pin fin thermal conductivity value.

Fig. 8.7 displays the relationship implicit in Eq. (8.5) between the least-material fin radius and the heat transfer coefficient for a fixed volume of 3.18 cm^3 and various thermal conductivities. Applying this relation to an orthotropic pin fin having a radial thermal conductivity of 0.3 W/m-K and axial thermal conductivity of 20 W/m-K and noting that the triangular symbols represent the 2-D least material solution obtained by laborious trial and error, it is seen that use of the axial conductivity in Eq. (8.5) appears to yield fin radii essentially identical to the 2D least-material results. The equation obtained for the aspect ratio of the least material, orthotropic fin is,

$$d_{lm} = 1.503 \left(\frac{hV^2}{k_z} \right)^{1/5} \tag{8.6}$$
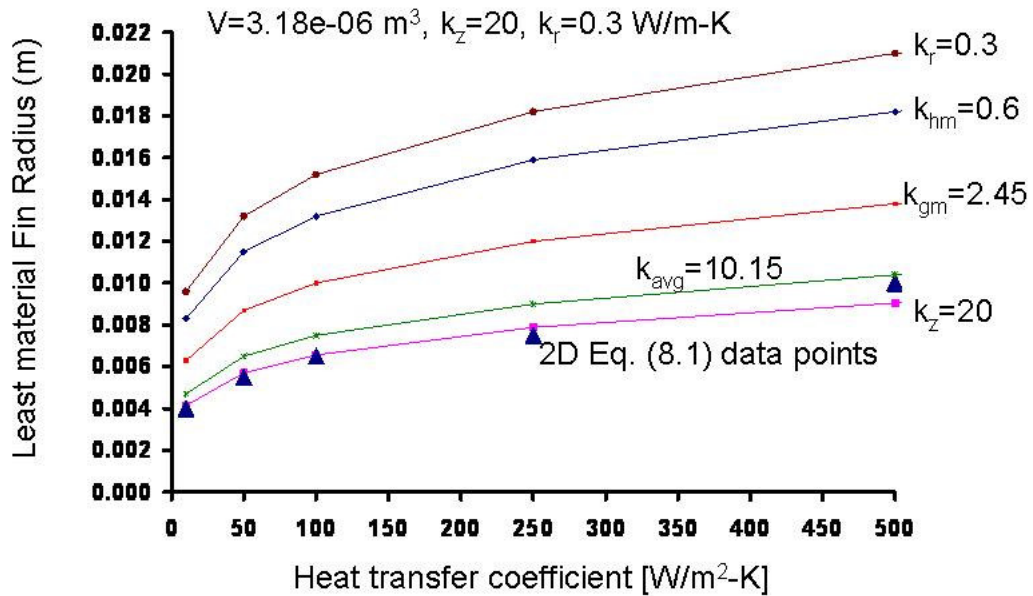
Figure 8.7 Least material orthotropic pin fin radius (Eq. 8.7)

However, as discussed in Chapter 7 and above, at Biot numbers larger than 0.4, use of the classical 1D fin equation over-predicts the heat transfer rate from an orthotropic fin. Therefore, in the following sections, this least material pin fin analysis is extended to orthotropic pin fins by using for predicting pin fin heat transfer in the specified radial Biot number ranges.

8.5.1 Orthotropic Pin Fin Least Material Dimensions

<u>Air cooled natural convection</u>: In order to quantify the effect of low radial thermal conductivity on the least material pin fin, a highly orthotropic fin of axial thermal conductivity 20 W/m-K and radial thermal conductivity of 0.3 W/m-K is considered. The pin fin volume is $3.18cm^3$ and Fig. 8.8 considers air cooled natural convection with a heat transfer coefficient of 10 W/m^2-K. As may be seen in Fig 8.8, the least material pin fin geometry obtained using the orthotropic pin fin Eq. (8.1) is exactly same as that obtained using the classical fin Eq. (8.7). The least material pin fin radius (0.0045 m, $\gamma=15.8$) falls on the vertical line that passes through the least material radius obtained using the least material pin fin relation (Eq. 8.6). Also, the pin fin heat flow rate predictions are exactly same.

The radial Biot number for least material pin fin is 0.15. This reconfirms the earlier conclusion that the orthotropy effects are negligible in air cooled natural convection and that the classical fin design and optimization relations work well – in this range of Biot numbers - even for a highly orthotropic pin fin.
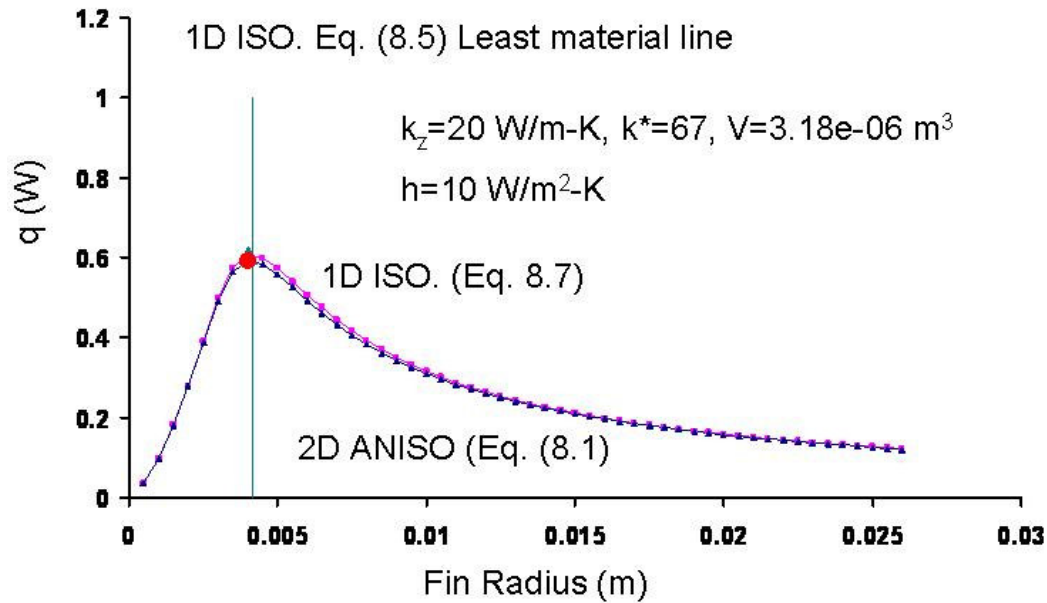
Figure 8.8 Cooling rate with pin fin radius (k_r=0.3 W/m-K) in air cooled natural convection (θ_b=50K)

Air cooled forced convection: Air cooled forced convection in electronics cooling can provide heat transfer coefficients as high as 50 W/m^2-K. In Fig. 8.9 for a highly orthotropic pin fin described earlier, the optimum orthotropic pin fin radius (0.0055m, γ=6.1) is again seen to be nearly identical (to within 0.1%) to that obtained when the radial thermal conductivity is ignored and use is made of the classical 1D Eq. (8.7). However, the cooling rate prediction for the least material fin based on the classical heat flow rate is higher than the actual value, determined by the rigorous 2D relation, by 12.3%. The radial Biot number value for orthotropic least material fin is 0.92. Clearly, it is possible to conclude from these two cases, that in air cooled configurations the proposed Eq. (8.6) gives the correct least material pin fin dimensions even for a highly orthotropic pin fin.

170
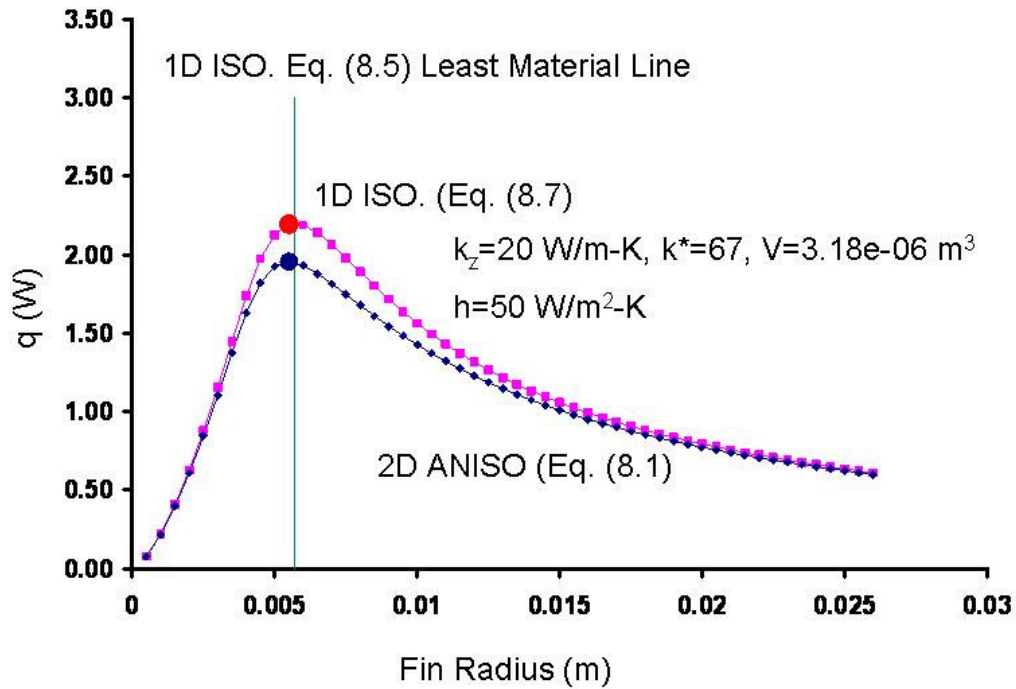
Figure 8.9 Cooling rate with pin fin radius (k_r=0.3 W/m-K) in air cooled forced convection (θ_b=50K)

Water cooled natural convection: The focus is now turned to a water cooled natural convection case. In Fig. 8.10, the heat transfer coefficient value of 500 W/m^2-K is considered. The orthotropic pin fin Eq. (8.1) results in a least material pin fin radius of 0.01m that is thicker than the least material radius (0.0095m) obtained using the classical relation by 5%. The trend is towards larger least material pin fin radii as the heat transfer coefficient increases.
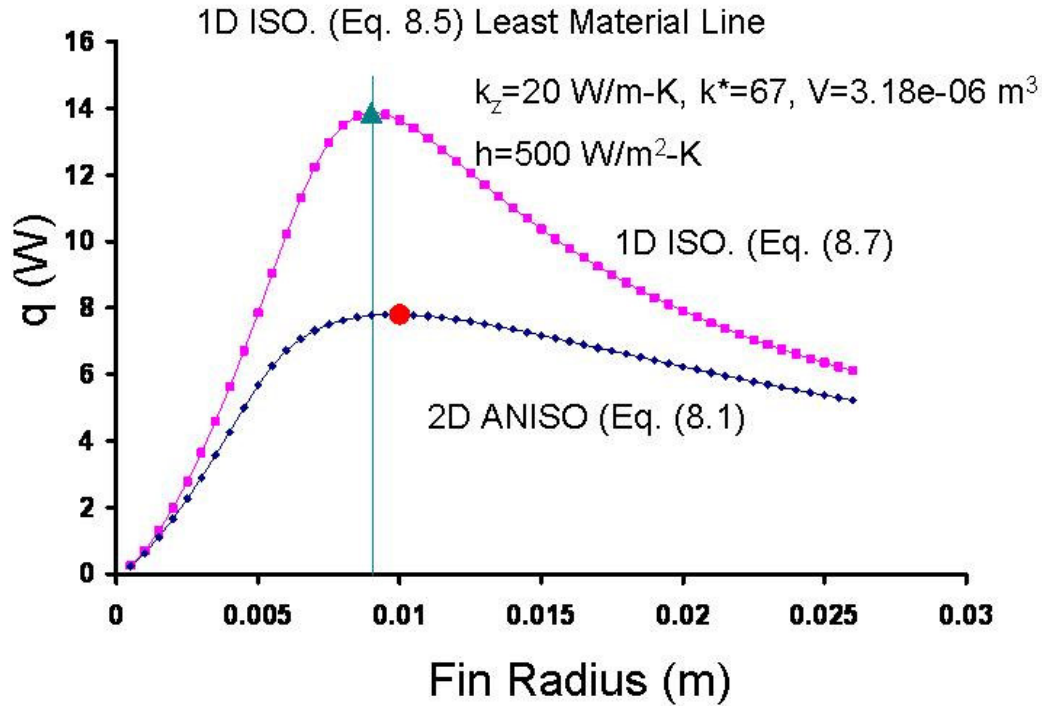
Figure 8.10 Cooling rate with pin fin radius (k_r=0.3 W/m-K) in air cooled forced convection (θ_b=50K)

In Fig. 8.11, the measured thermal conductivity values presented in Chapter 3, of 15 W/m-K along the axis and 4 W/m-K along the radius, are considered, along with a high water-cooled heat transfer coefficient of 5000 W/m²-K. The 2D orthotropic least material pin fin radius is 0.016m and is larger than the pin fin radius of 0.015m obtained using the orthotropic least material Eq. (8.6) by 6.7%. The high heat transfer coefficient results in radial Biot number of 20. At such a high Biot number the classical 1D solution overpredicts the pin fin heat flow rate by nearly 100%.

172
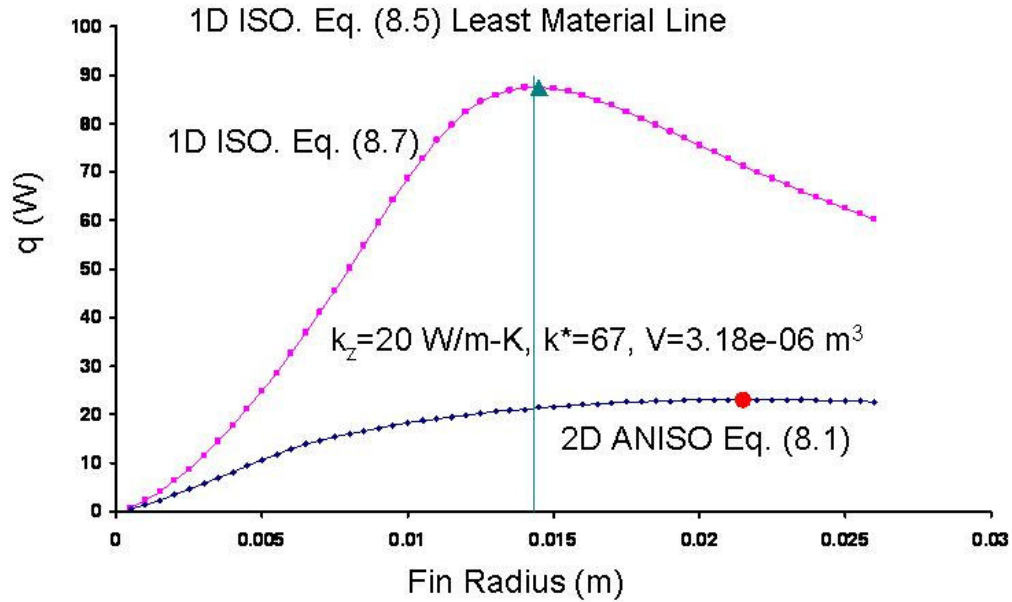
Figure 8.11 Cooling rate with pin fin radius (k_r=0.3 W/m-K) in air cooled forced convection (θ_b=50K)

The performance of a pin fin, with axial and radial thermal conductivities of 15 and 4 W/m-K), respectively, is presented in Fig. 8.12 for a medium with a convection heat transfer coefficient of 1000 W/m^2-K The variation of the heat transfer rate with the pin fin radius is obtained for three different volumes: 1.59cm^3, 3.18cm^3 and 9.54cm^3. The previously observed behavior - of an initial increase in heat flow with radius, peaking at a prescribed value, and then decreasing gently at larger radii - can be seen for each of the three volumes. Moreover, and as suggested by Eq. (8.6), increasing pin fin volume, results in thicker least material fins. Increasing, pin fin volume two times from 1.59e-06 m^3 to 3.18e-06 m^3, results in increase in pin fin radius from 8.25 to 10.9 mm by 32.9%. Whereas, increasing pin fin volume from3.18e-06 m^3 to 9.54e-06 m^3, results in increase in pin fin radius from 10.9 mm to 17 mm by 55.9%.
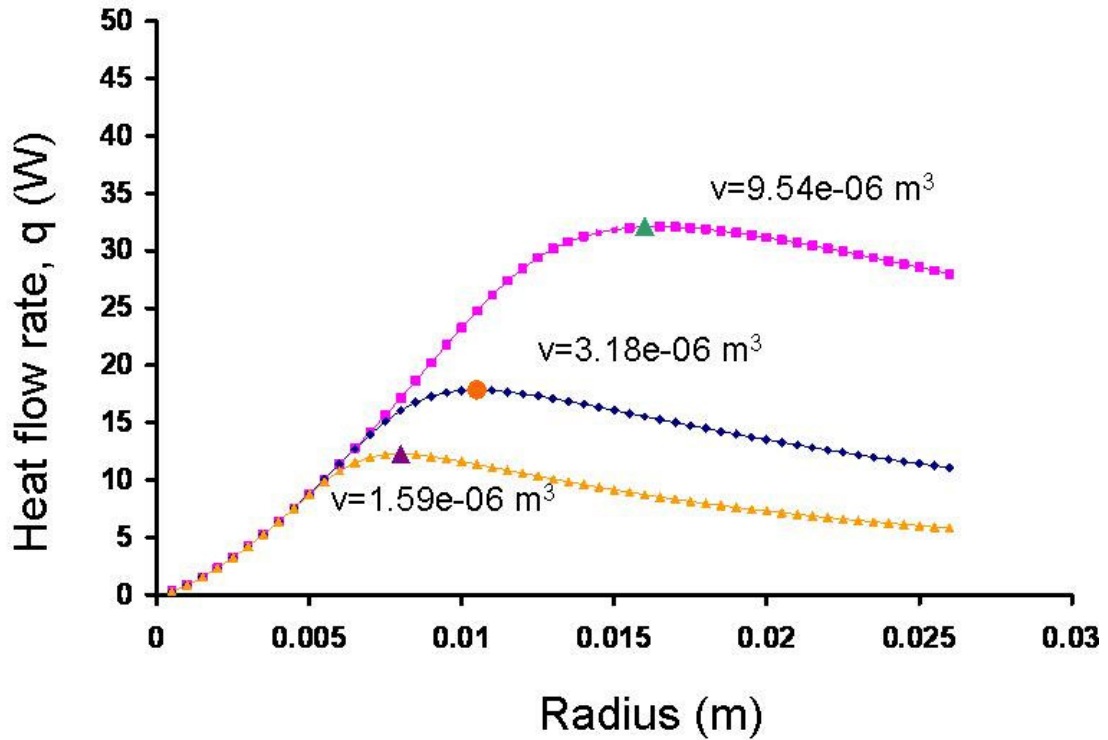
Figure 8.12 Cooling rate with pin fin radius (k_z=15, k_r=4 W/m-K) and h=1000W/m²K for various pin fin volumes (Eq. (8.1)) (θ_b=50K)

8.5.2 Accuracy of Orthotropic Pin Fin Least Material Equation

The orthotropic least material pin fin diameter determined from the heat flow curves for various cases is compared with the value obtained using the proposed orthotropic least material diameter relation (Eq. 8.6) in Fig. 8.13. The results span the range from a highly orthotropic pin fin (20, 0.3 W/m-K) to the measured thermal conductivities (15, 4 W/m-K), volumes from 1.59e-06 m³ to 9.54e-06 m³, and heat transfer coefficients ranging from 10 W/m²-K to 5000 W/m²-K. The results from 23 distinct above mentioned cases indicate excellent agreement between the proposed orthotropic least material Eq. (8.6) and rigorously determining the orthotropic least material dimensions from the plotted results in Fig. 8.13, with a standard deviation of 2%.

174
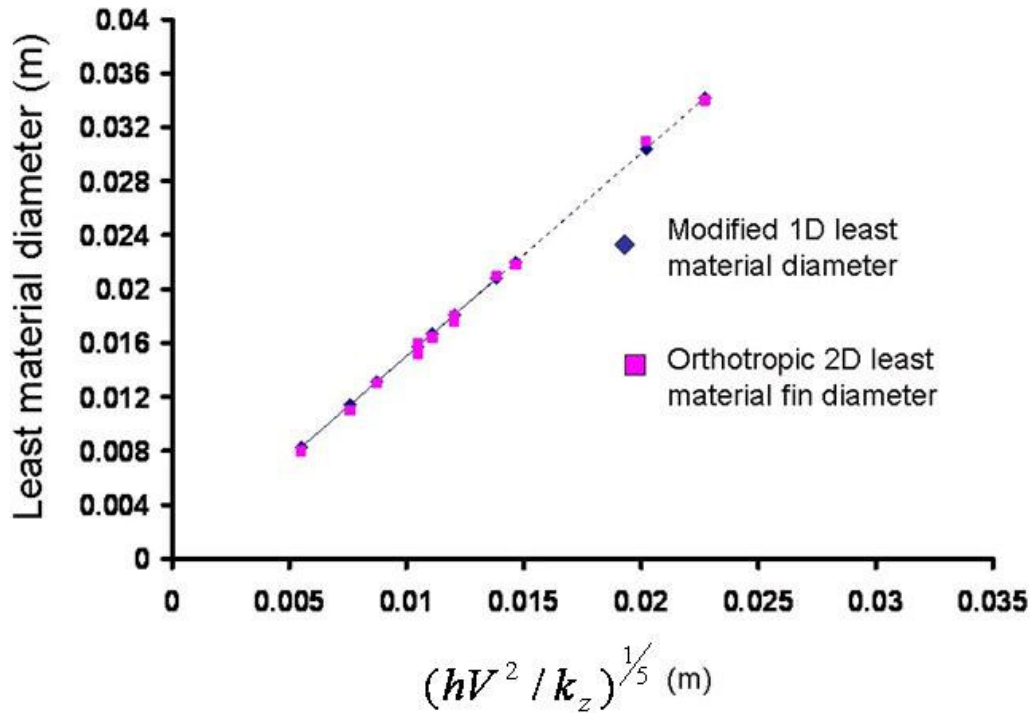
Figure 8.13 Least material pin fin diameter for various cases (Eq. (8.1), Eq. (8.6))

8.4 Simplified Orthotropic Conductivity Pin Fin Heat Transfer Equations

The simplified equations proposed in this thesis are listed below according to the applicable radial Biot number ranges. As was previously noted, at radial Biot numbers up to 0.4, classical 1D pin fin analysis gives accurate heat flow rate predictions for orthotropic fins. For higher Biot numbers, as associated with the low radial thermal conductivity of the polymer composites, low conductivity ratios, and high heat transfer coefficients, the simplified orthotropic heat transfer relations shown below are proposed.

a) Low radial Biot number range (1D classical):

Bi≤0.4

$$q_b = -kA_c \frac{d\theta}{dz}\Big|_{z=H} = \pi k R^2 \theta_b m_{fin} \tanh m_{fin} H \tag{8.7}$$

Where $m_{fin} = (\frac{2h}{kR})^{\frac{1}{2}}$ and the excess temperature θ_b is equal to $T_b - T_a$ (8.8)

b) Intermediate radial Biot number range

0.4≤Bi≤2

$$q = -4\pi k_z \theta_b R(\frac{k_r}{k_z})^{\frac{1}{2}}(0.1333\ln(hR/k_r)+0.3325)\tanh[0.476\ln(hR/k_r)+1.2632(\frac{k_r}{k_z})^{\frac{1}{2}}(\frac{H}{R})] \tag{8.9}$$

Further for fin aspect ratios, H/R> 20, where the tanh approaches unity, we have,

$$q = -4\pi k_z \theta_b R(\frac{k_r}{k_z})^{\frac{1}{2}}(0.1333\ln(hR/k_r)+0.3325) \tag{8.10}$$

c) High radial Biot number range

2≤Bi≤35

$$q = -4\pi k_z \theta_b R(\frac{k_r}{k_z})^{\frac{1}{2}}(0.2473\ln(hR/k_r)+0.2456)\tanh[0.156\ln(hR/k_r)+1.8035(\frac{k_r}{k_z})^{\frac{1}{2}}(\frac{H}{R})] \tag{8.11}$$

Further for fin aspect ratios, H/R> 20, where tanh approaches unity, we have,

$$q = -4\pi k_z \theta_b R(\frac{k_r}{k_z})^{\frac{1}{2}}(0.2473\ln(hR/k_r)+0.2456) \tag{8.12}$$

8.4.1 Low Radial Biot Range Analysis

The governing equation for 1D classical pin fin heat flow rate is given in Eq. (8.7). Typically up to a radial Biot number of unity for isotropic metallic pin fins, the classical 1D equation predict the heat flow rate to within 7% of the exact value. However, for highly orthotropic polymer composite pin fins, having a radial to axial thermal conductivity ratio of 1 to 20 and aspect ratio close to 3, the 7% accuracy is limited to radial Biot numbers of approximately 0.4, as may be seen in Fig. 8.14. In applying Eq. (8.7) to orthotropic fins, it is the axial thermal conductivity that must be

used. In section 7.4.1.5 it has been previously established that no common definition of effective thermal conductivity, such as geometric mean, harmonic mean, and algebraic average of the axial and radial thermal conductivities can be used to obtain accurate heat transfer predictions in the presence of strong orthotropy.

As the radial Biot number increases beyond 0.8, the over prediction in the pin fin cooling capability resulting from the use of Eq. (8.1) with the axial thermal conductivity, grows. Increasing the pin fin aspect ratio, for a fixed diameter of 9mm, by increasing fin height, increases the heat transfer rate up to an aspect ratio of 20, but further increases in pin fin height do not provide a further improvement in the heat transfer rate.
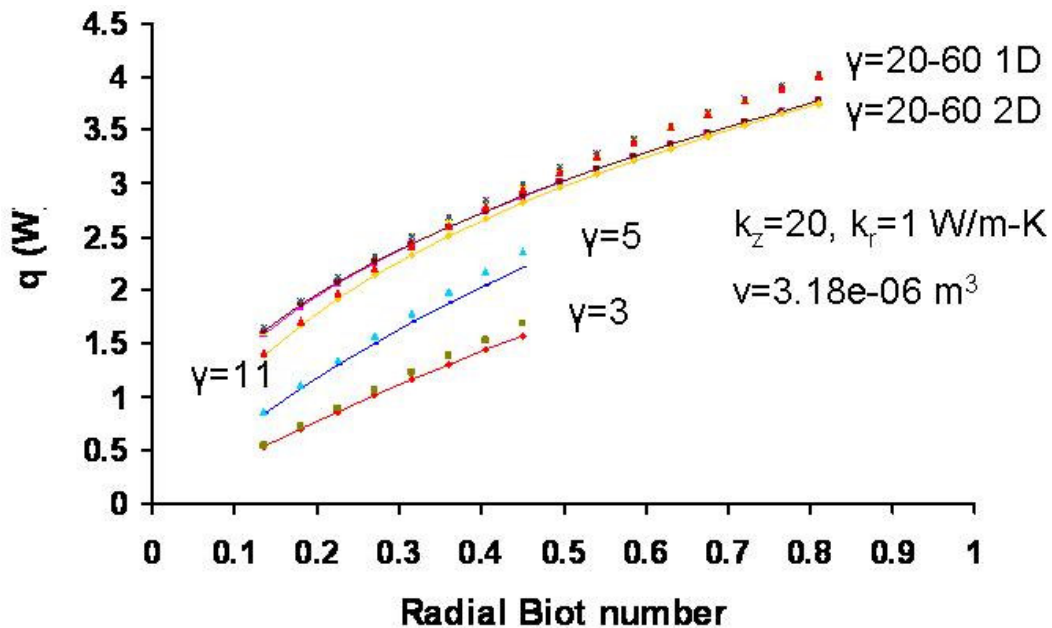
Figure 8.14 Pin fin heat flow rate dependence on low radial Biot numbers (Eq. (8.7))

The effect of increasing the pin fin aspect ratio, achieved by increasing the fin height, on the pin fin cooling rate is more evident in Fig. 8.15 for an orthotropy of 1 to 20, where the heat flow rate first increases and then approaches an asymptotic

177

value at an aspect ratio of approximately 20. The solid lines in the figure indicate the predictions using the 2D exact equation (Eq. (8.1)) and the points indicate the classical 1D prediction using the axial thermal conductivity values. Starting from the smallest indicated radial Biot number of 0.135 in Fig. 8.15, where the points are seen to align with the solid line for aspect ratios as high as 32, the discrepancy grows with increasing aspect ratio and Biot number until it is already more than 7% for aspect ratios of 3 and radial Biot numbers greater than 0.4.
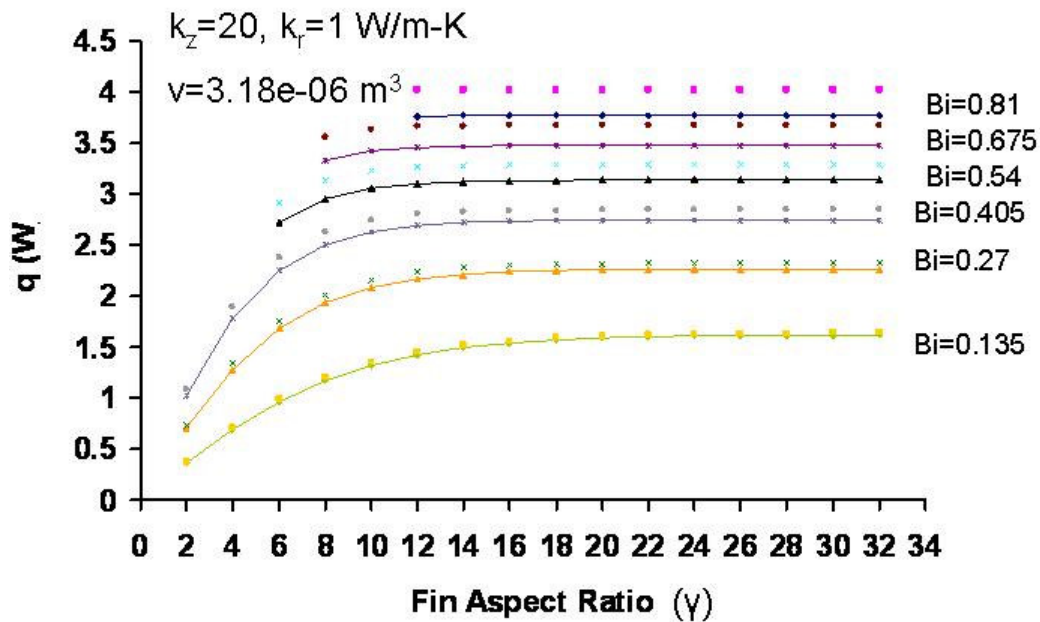
Figure 8.15 Pin fin heat flow rate dependence on fin aspect ratio in low radial Biot numbers (Eq. (8.7)) (θ_b=50K)

  The effect of increasing the radial thermal conductivity   while keeping the axial thermal conductivity value fixed at 20W/m-K on pin fin heat flow is depicted in Fig. 8.16 for a fin with an aspect ratio of 11.1. The agreement between the classical 1D results (points) and the 2D results   (solid line) improves   as the radial thermal conductivity approaches the axial thermal conductivity value from close to 7% at 1 W/m-k to 6.5% at 19 W/m-K.

Figure 8.16 Pin fin heat flow rate dependence on radial thermal conductivity values in low radial Biot numbers (Eq. (8.7)) (θ_b=50K)

8.4.2 Intermediate Radial Biot Range Analysis

The pin fin studied in Figure 8.17 has a fixed diameter of 9mm and a fixed height of 50mm. The increasing radial Biot number is achieved by increasing the heat transfer coefficients from 90 to 467 W/m^2-K. The effect of increasing the radial Biot number from 0.4-2 on overall pin fin heat flow rate is depicted in Fig. 8.17 for an orthotropic pin fin of radial to axial thermal conductivity ratio of 0.05. The solid lines in the plot indicate the 2D exact predictions of Eq. (8.1) and the data points are obtained using the simplified intermediate Biot range relation, Eq. (8.9).

179
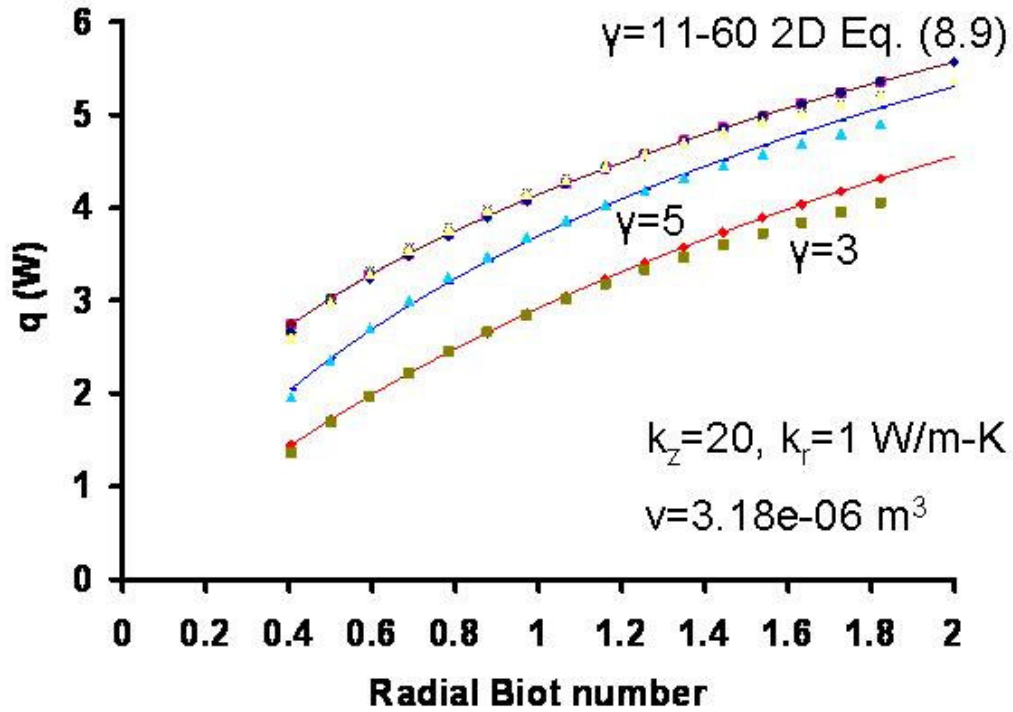
Figure 8.17 Pin fin heat flow rate dependence on intermediate radial Biot numbers (Eq. (8.9)) (θ_b=50K)

The accuracy achieved using the proposed intermediate Biot range equation is within 7% for the prescribed Biot range of 0.4-2. The accuracy is much higher at central radial Biot values within the prescribed range and decreases at both the limits of radial Biot number values.

The heat flow rate in Fig 8.17 is seen to become independent of aspect ratio beyond an aspect ratio of 20. This is explicitly clear in Fig. 8.18 where the effect of aspect ratio on pin fin heat flow rate is depicted. The heat flow rate reaches an asymptote at an aspect ratio of approximately 16 for the Biot range of 0.4-2 in an orthotropic pin with a radial to axial thermal conductivity ratio of 1 to 20.

Figure 8.18 Pin fin heat flow rate dependence on pin fin aspect ratio for intermediate radial Biot numbers (Eq. (8.9)) (θ_b=50K)

Figure 8.19 Pin fin heat flow rate dependence on radial thermal conductivity for intermediate radial Biot numbers (Eq. (8.9)) (θ_b=50K)

The effect of increasing radial thermal conductivity on the fin heat transfer rate for the intermediate radial Biot range is depicted in Fig. 8.19. The accuracy achieved using the simplified relation, Eq. (8.9), is relatively constant at a 2.6% discrepancy with increasing radial thermal conductivity values. However, the agreement is best for the central radial Biot numbers and decreases towards the upper and lower limits of the prescribed radial Biot number range.

8.4.3 High Radial Biot Range Analysis

Fins used in polymer water-cooled heat exchangers have thermal conductivities in the range of 0.15-0.4 W/m-K [81] [82] and experience heat transfer coefficient values that range from 1000-3000 W/m^2-K and beyond, yielding radial Biot numbers as high as 30.. For orthotropic pin fins with radial Biot numbers in the range of 2-35, where the previously described equations do not provide sufficient accuracy, the simplified orthotropic relation, Eq. (8.11), is proposed.
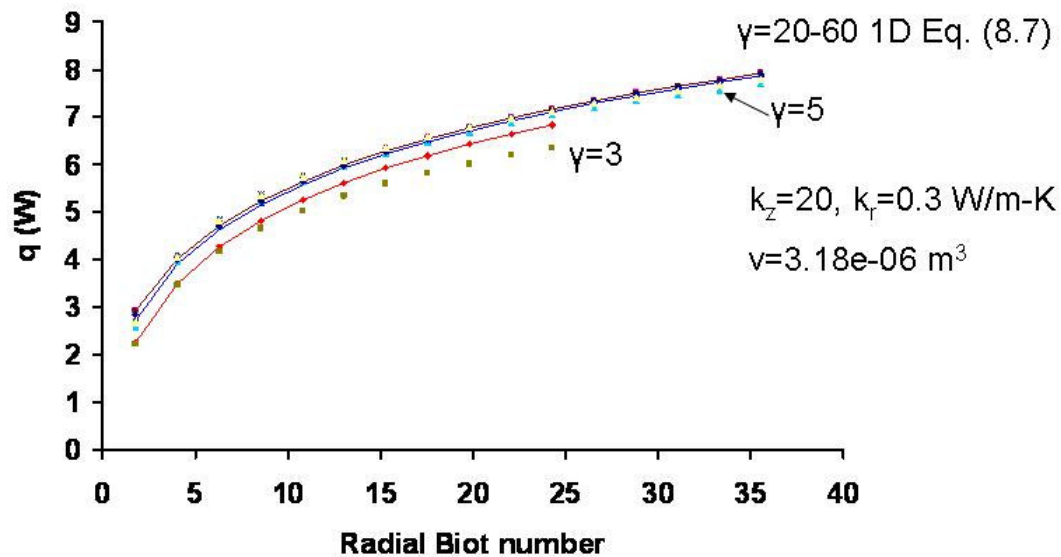
Figure 8.20 Pin fin heat flow rate dependence on high radial Biot numbers (Eq. (8.11)) (θ_b=50K)

Fig 8.20 displays the thermal performance of an orthotropic polymer fin with a conductivity ratio of 1 to 20 and radius of 0.0045 m. The heat flow rate is seen to increases sharply and then more gently as the radial Biot number increases from 2 to 35. The increase in radial Biot number for a fixed aspect ratio is achieved by increasing the heat transfer coefficients. Increasing fin aspect ratio from 3 to 20 will result in increasing the fin cooling rate, due to a larger effective surface area. Further increases in aspect ratio beyond a value of 20 have an insignificant effect.

In Fig. 8.21, as the fin aspect ratio increases from 1-20, the heat flow rate first increases and then approaches an asymptotic value. Further increases in aspect ratio, beyond 20, do not provide any additional increase in the fin heat transfer rate. The agreement between the simplified relation (Eq. (8.11) and the rigorous 2D orthotropic equation (Eq. (8.1)) is well within 7% for the prescribed Biot range of 2 to 35 for a conductivity ratio of 1 to 20, with best results in the central part of this parametric range and poorer results at the extremes.
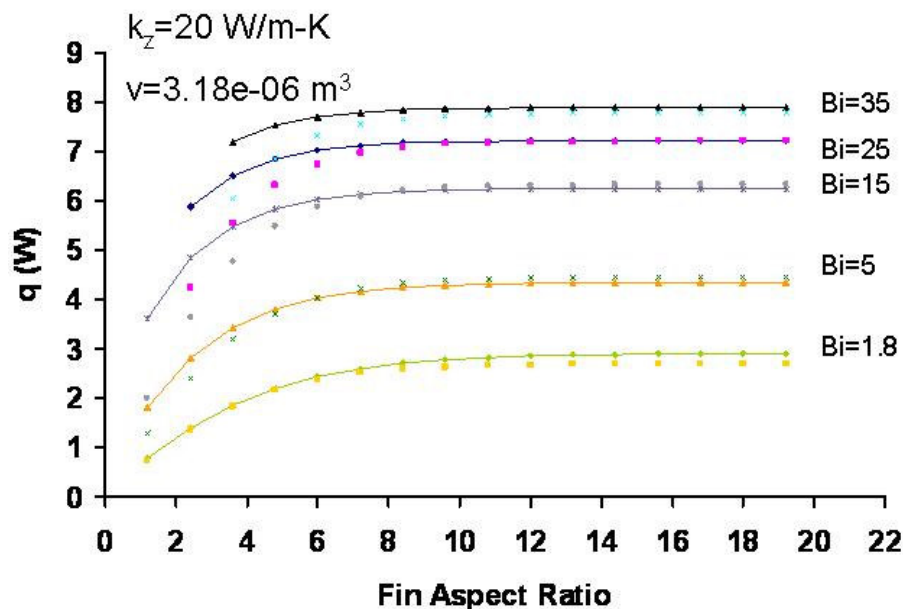
Figure 8.21 Pin fin heat flow rate dependence on pin fin aspect ratio for high radial Biot numbers (Eq. (8.11)) (θ_b=50K)

The effect of changing the radial thermal conductivity and, hence, the conductivity ratio is depicted in Fig. 8.22.
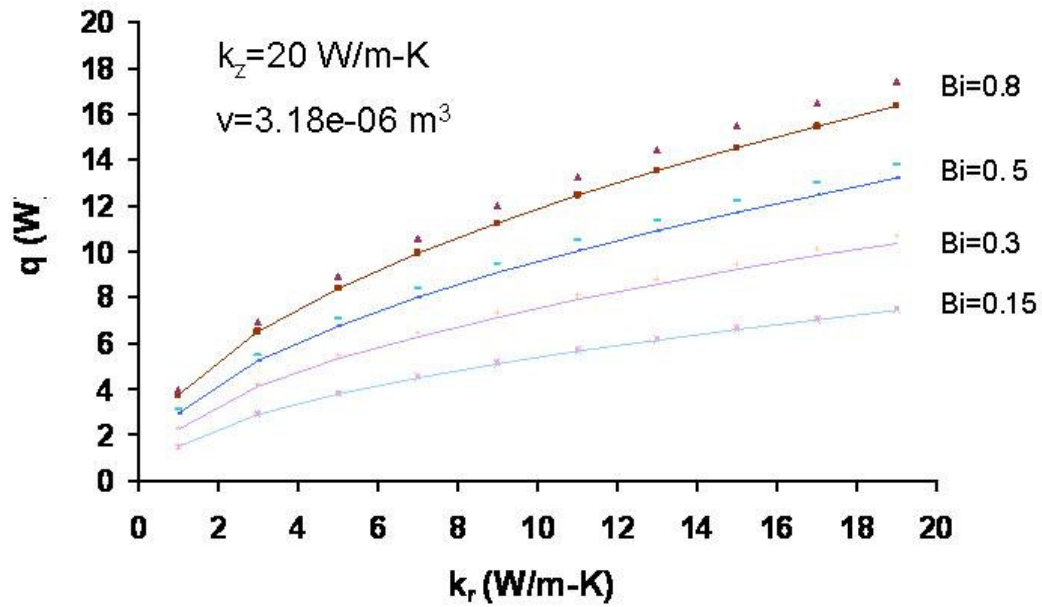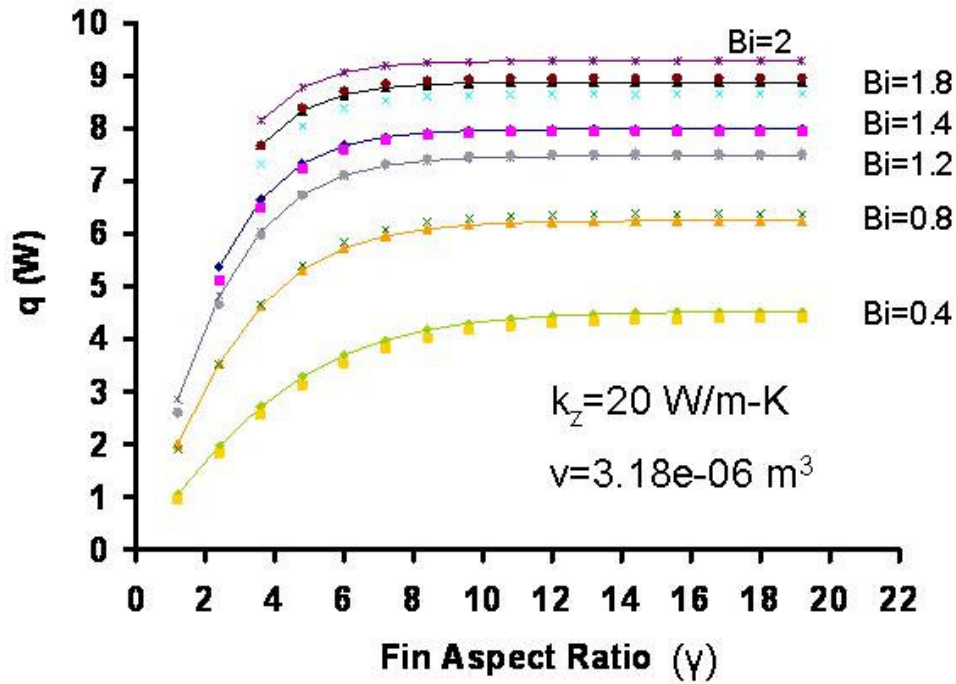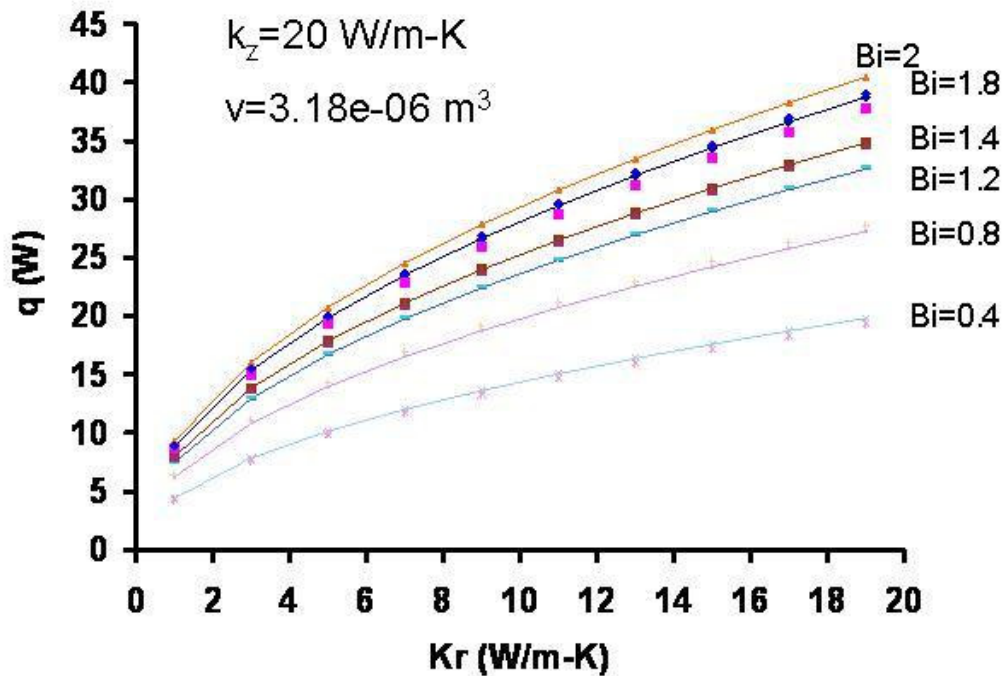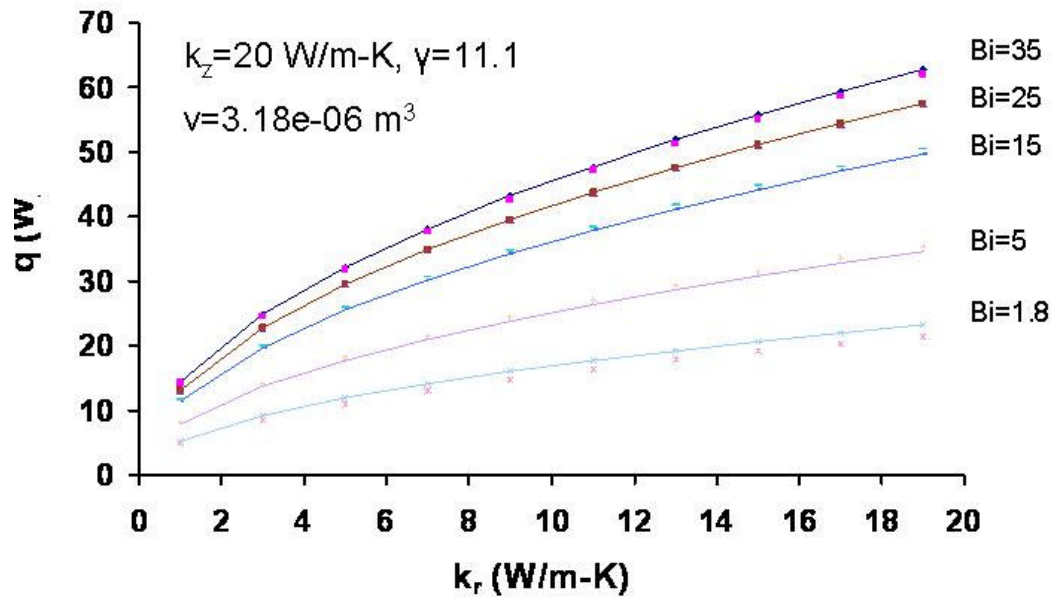

Figure 8.22 Pin fin heat flow rate dependence on radial thermal conductivity for high radial Biot numbers (Eq. (8.11)) (θ_b=50K)

Increasing radial thermal conductivity results in increasing pin fin heat flow rate. The increase in cooling rate is visibly higher for higher radial Biot numbers. Increasing the radial thermal conductivity value from 1 to 20 W/m-K in Fig. 8.22 increases the pin fin cooling rate for each fixed radial Biot number curve.

Fig. 8.23 displays the combined results of the orthotropic least material pin fin Eq. (8.6) and proposed simplified orthotropic heat flow rate Eqs., (8.7) - (8.11). The least material orthotropic pin fin Eq. (8.6) is used to obtain the least material orthotropic pin fin dimensions and the simplified heat flow relations, Eqs., (8.7) - (8.11), are used to obtain the pin fin heat transfer rate shown in Fig. 8.23 for thermal conductivity ratios from 0.015 to 0.5. The solid line in Fig. 8.23 represents the predictions for least material pin fin dimensions obtained using Eq. (8.6) and simplified heat flow rate Eqs., (8.7) - (8.11). The data points are obtained using least

material search from the results obtained using 2D exact orthotropic Eq. (8.1). It was found that 2D orthotropic least material pin fin dimensions are identical to those obtained using least material pin fin Eq. (8.6).
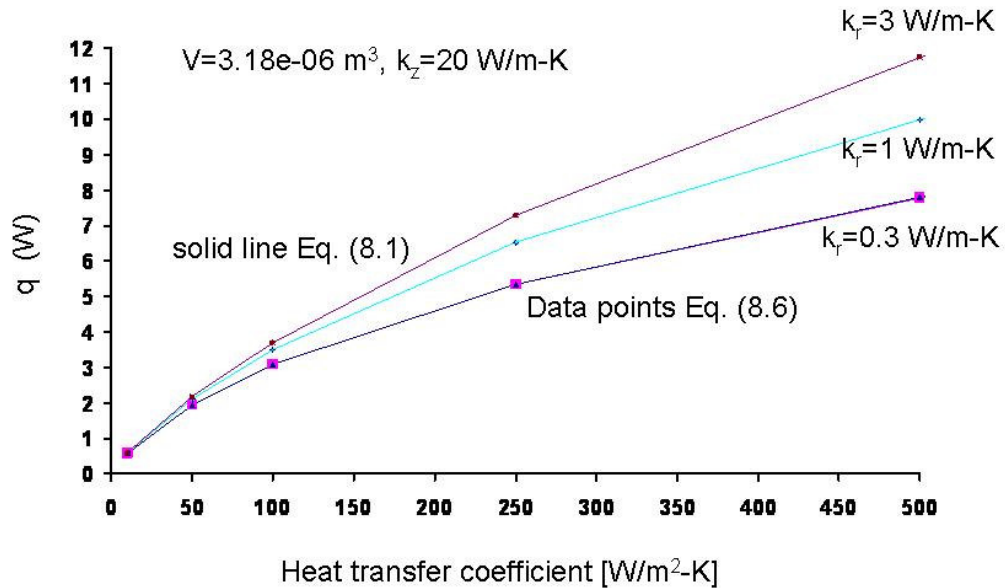
Figure 8.23 Least material pin fin cooling rate with various heat transfer coefficient values (θ_b=50K)

Clearly, the predictions of pin fin heat flow obtained with the simplified equations, Eqs. (8.7) - (8.11), are very close to that obtained using the rigorous 2D orthotropic relation, Eq. (8.1). This validates the accuracy of the proposed simplified Eqs., (8.7) - (8.11) and the use of the proposed least material pin fin relation, Eq. (8.6), to provides accurate orthotropic least material pin fin dimensions.

8.4 Summary

Two new simplified equations are proposed that correctly predict heat flow rate for radial Biot numbers greater than 0.4 and aspect ratios as low as 3. The first equation provides accuracy within 7% for highly orthotropic pin fins having thermal

conductivity ratio of 0.015 and radial Biot number range 0.4 - 2. The accuracy of the equation increases at the central radial Biot number values and decreases at the lower and upper limit values. The second simplified equation proposed provides fin cooling rates within 7% of the rigorously determined values for a radial Biot range from 2 to 35. It has been found possible to predict the dimension of an orthotropic least material pin fin with the relation commonly used for 1D isotropic fin. When this equation is combined with the simplified relations for orthotropic pin fin heat flow, an accurate prediction of the heat transfer from an orthotropic least material pin fin is obtained.

Chapter 9: Experimental Verification of Orthotropic Pin Fin Analysis

9.1 Introduction

To complete this study of orthotropic pin fin heat transfer, the temperature distribution in a polymer composite pin fin immersed in water was experimentally obtained. The dimensions of the fin and natural convection in water combined to produce Biot Numbers in the range of 1.3-4.3, for which anisotropy can be anticipated to affect the pin fin temperature distribution and the overall heat flow rates. A numerical model, using the commercial software ANSYS 8.0, has been used to simulate the experimental runs and to obtain detailed temperature distributions in the pin fin. Experimentally obtained temperatures at several key locations were found to agree with the predicted values. The present chapter discusses the details of the experiments and the numerical (FEM) simulations.

To create a meaningful comparison between the numerical FEM and experimental results it is necessary to accurately determine the convective heat transfer coefficient on the surface of the immersed fin. To minimize the errors in determining this heat transfer coefficient, use was made of a high thermal conductivity copper cylinder with a circumferentially and axially isothermal surface. Temperature measurements in the copper cylinder and the water, along with the heat transferred from the copper cylinder to the water was then used to determine the average heat transfer coefficient along the wetted surface.

The horizontal cylindrical pin fin geometry has been studied extensively and reviewed in the literature [84] for isotropic high conductivity metals. For an isothermal cylinder, the following expression is commonly used to obtain the Nusselt number for a Raleigh number range of 10^4-10^7,

$$\overline{Nu_d} = \overline{h}D/k = CRa_d^{1/4},$$ (9.1)

$$Ra_d = g\,\beta(T_s - T_\infty)H^3/\nu\alpha$$ (9.2)

where, 'C' may vary with the geometry and depends weakly on the Prandtl number of the fluid.

The experimental values obtained with the copper cylinder were correlated in this commonly-used Nusselt-Raleigh form. Using the obtained correlation and the measured temperature rise values, the local heat transfer coefficients at different locations on the PPS pin fin can be obtained. These local heat transfer coefficient values are then used as the boundary condition in the numerical FEM model in order to predict the internal temperature distribution in the orthotropic PPS composite pin fin. The numerically predicted temperature values are then compared with experimentally measured values at several key locations.

9.2 Experimental Apparatus

A clear acrylic tank shown in Fig. 9.1 was used for carrying out the natural convection water cooled tests. The tank dimensions are 0.254x3.05x0.254m and 0.9525 cm wall thickness. The clear acrylic (0.18 W/m-K, [85])) tank was filled with up to 0.254m of clear water. The various components constituting the PPS and copper cylinder assembly are shown in Fig. 9.2. An insulating annular Delrin (or acetal) layer (0.23 W/m-K [85]) of thickness 1.2 cm is used in order to hold the pin fin in the

plexiglass (0.18 W/m-K, [85]) base plate. Four 3.175mm stainless steel screws are inserted via threads made in the Plexiglass base plate to press the Delrin layer onto the pin fin. Another Plexiglass base plate with a blind hole is used to hold the rest of the heater assembly. The various heater assembly layers below the pin fin (or cylinder) include a circular copper (400 W/m-K) spreader plate of diameter 25.4 mm and thickness of 0.4 cm. Heat sink compound, with a thermal conductivity of 2.9 W/m-K [86, RS component, stock no:217-3835], is used to attach the spreader plate to the fin. The Kapton rubber heater of 30 Ω electrical resistances [87, Watlow part no: K05711980-M] is attached below the copper spreader plate using the same thermal grease. The heater terminals and wires were coated with liquid electrical tape [Star brite]. Fiber glass insulation material is used, followed by a Delrin block, to limit heat transfer to the low conductivity insulating clear acrylic wall. Four 3.175mm stainless steel screws at the four corners are used to hold the pin fin assembly plate to the heater assembly plexiglass base plate.

   The completed PPS pin fin assembly was then attached to the opposite wall of the acrylic tank using insulating double-sided tape [3M heavy duty mounting tape], with the pin fin centered on 10"x12" vertical wall (Fig. 9.1). The outside walls and base plate were further insulated using pug duct seal [model DS-110, 114] material. This construction was designed to ensure that the nearly all the heat from the heater conducted into the pin fin and then convected into the surrounding water. The temperature in the clay at the base plate layer and acrylic wall indicated no significant temperature rise even at the highest heat dissipation rates; indicating negligible heat loss from the base plate and plexiglass layers.
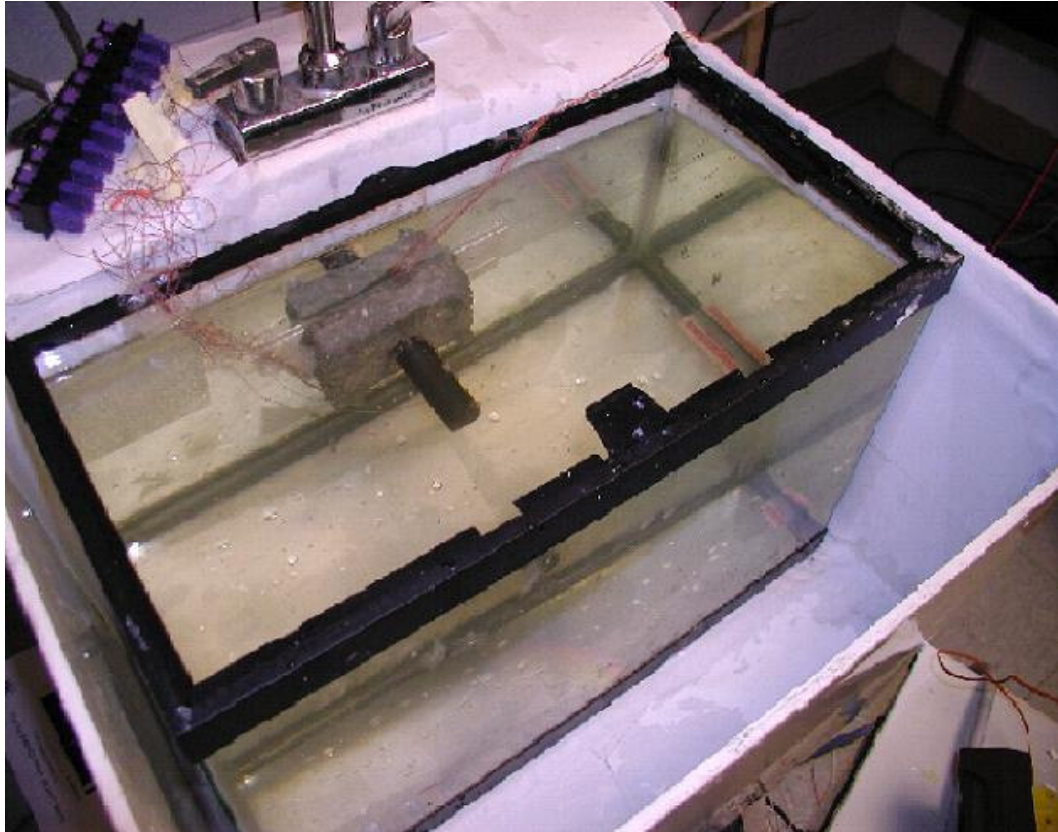
Figure 9.1 Water cooled natural convection test setup

Type 'E' thermocouples (Omega 5TC-TT-E-36-36) of 0.013 mm^2 cross-sectional area are used for measuring pin fin temperatures. The thermocouples were placed inside drilled holes, sealed with epoxy, and coated with liquid electrical tape [Star brite]. A digital multimeter unit (Agilent, 34401A), in combination with a digital switching unit (Agilent, 3499A), was used for measuring various thermocouple voltages. An AC variable power supply unit (Powerstat, 3PN116C) was used as power supply for the heater. A visual basic computer code was implemented to automate the gathering of temperature data; scanning through the thermocouples every 3 minutes. The transient temperature profile, up to thermal steady state, was obtained for each experimental run in order to ensure that steady state temperature data was used in the subsequent analysis.
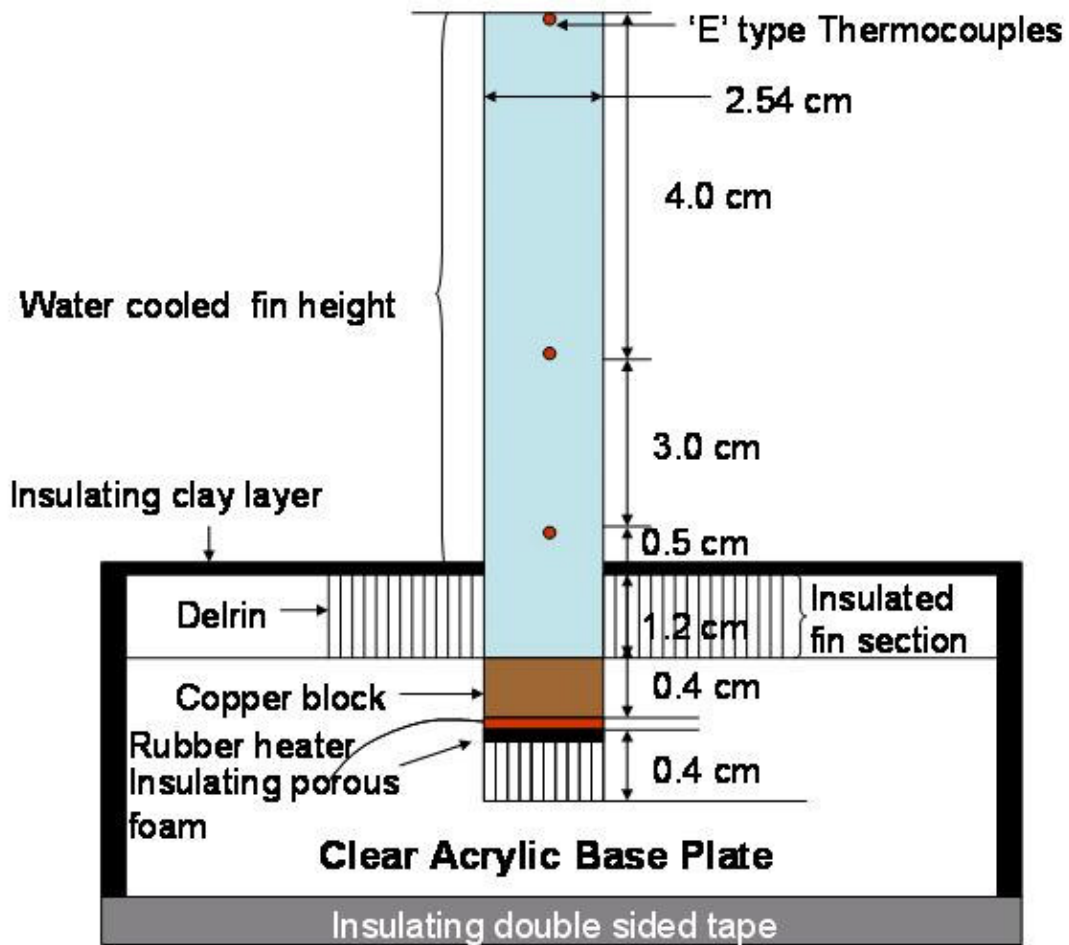
Figure 9.2 Schematic top view of pin fin assembly (not to scale)

9.4 Determining the Convective Heat Transfer Coefficient

A copper cylinder of diameter 2.54cm and submerged length of 7.5 cm was used to determine the empirical convective heat transfer coefficient and to establish the coefficient needed to "calibrate" the Nusselt and Raleigh number correlation for the water cooled natural convection heat transfer in the mentioned test apparatus. The power supplied at the base of the copper pin fin was varied from 18-37 W. The temperature rise at several key locations was measured.

9.4.1 Temperature Measurements

Six thermocouples at three fin height locations were used for the copper pin fin. Two thermocouples each were located at an axial distance of 0.5 cm, 3.5 cm, and 7.5 cm in the immersed copper cylinder. Each of the axial location had one thermocouple at the pin fin center axis and another at a radial distance of 9.5 mm away from the central axis. The six thermocouple holes occupied a total volume of 0.585mm^3, only 0.00016 % of the total pin fin volume.
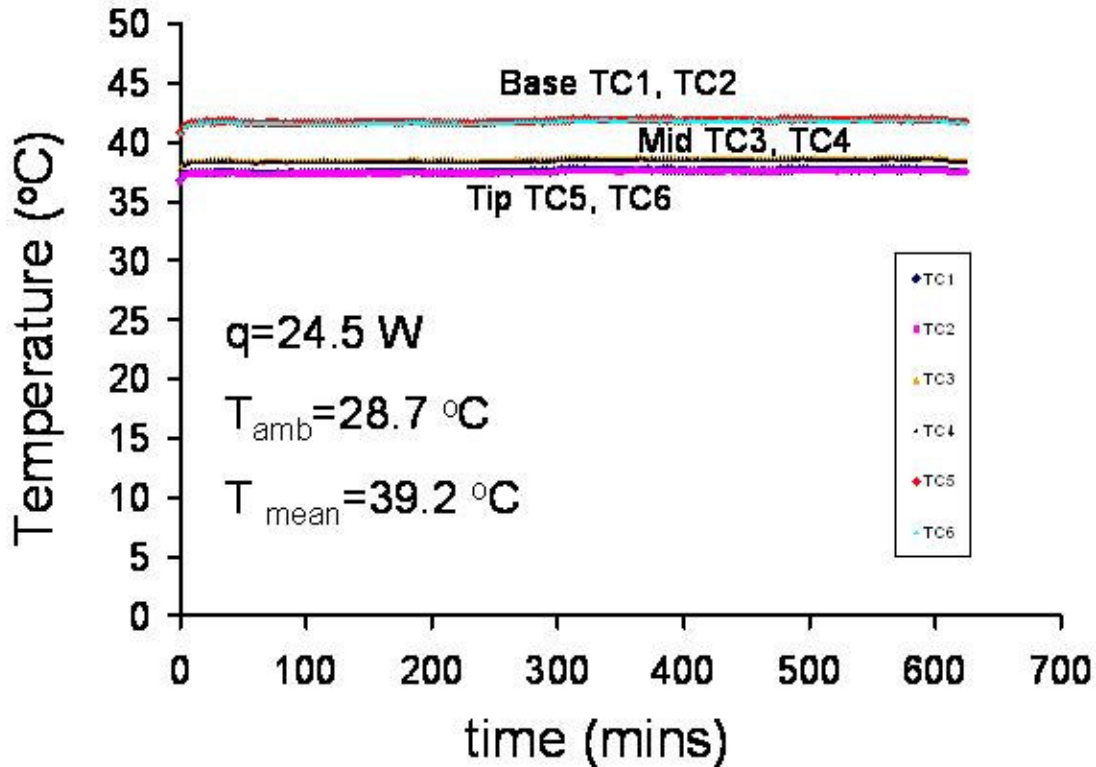
Figure 9.3 Copper pin fin temperature measurement curve

Results from a typical experimental run are shown in Fig. 9.3. This figure reveals that steady-state conditions for copper pin fin were attained after approximately 100 min and where it may be seen that at the three axial distances (base, mid-height and

tip), there is essentially no radial temperature variation in the copper cylinder. This expected result can be related to the very low Biot numbers (~0.03) resulting from the use of the high thermal conductivity copper (400 W/m-K). Fig 9.3 does reveal a temperature variation along the pin fin height of about 5 ^{o}C with 24.5W of heat dissipation. Due to the weak dependence of the heat transfer coefficient on the excess temperature ($\Delta T_{fin-fluid}$), varying with the one quarter power of the excess temperature, the average fin surface temperature was used in the determination of the average convective heat transfer coefficient.
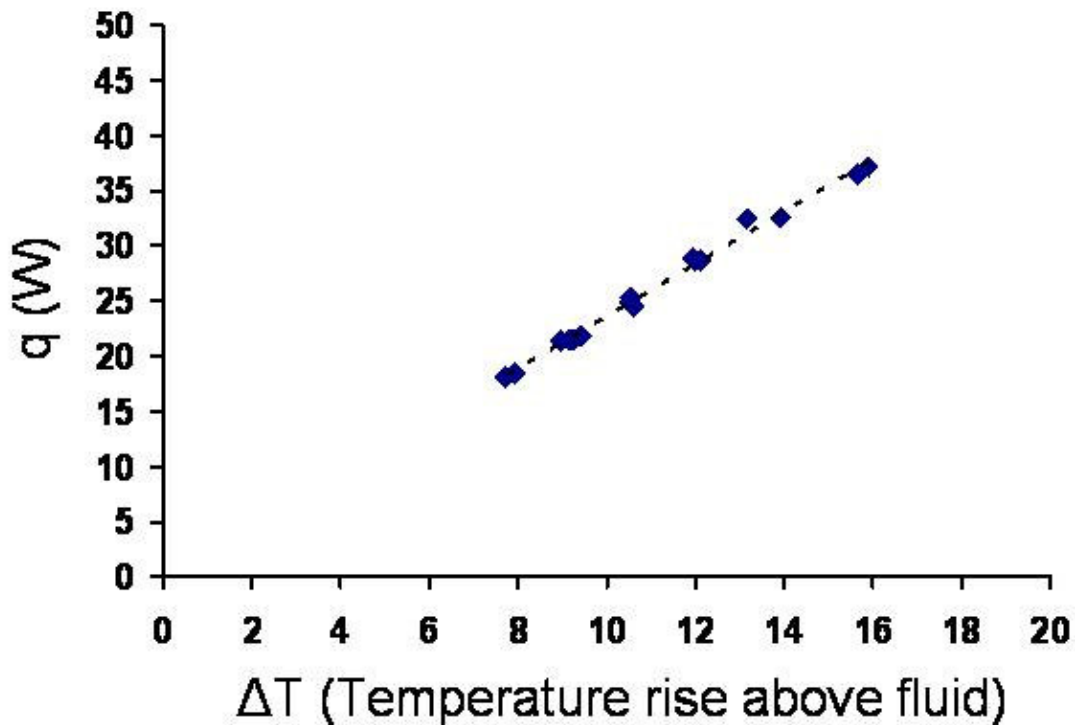
Figure 9.4 Heat flow rate vs. temperature rise above fluid curve

The heat transfer rate of the copper fin is shown in Fig 9.4, where the heat flow rate is seen to increase linearly with the average pin fin excess temperature in the range of 8 to 16 K. As shown in Fig 9.5, this behavior can be related to a nearly constant

average Nusselt number for the tested pin fin of nearly 30 as the Raleigh number increases from 3.7×10^7 to 8.2×10^7. The Raleigh number range indicates that the flow remains laminar over the entire wetted surface of the copper cylinder.
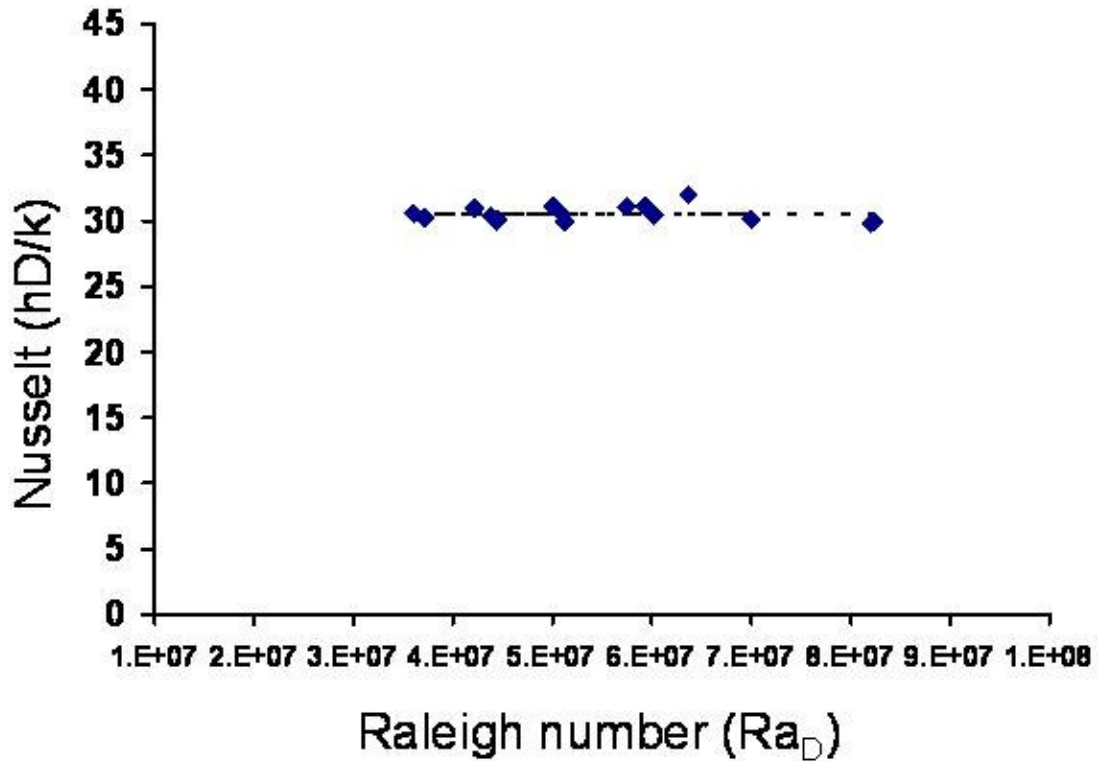
Figure 9.5 Nusselt vs. Raleigh number for water cooled free convection copper fin

Using these results, the Nusselt-Raleigh correlation constant in Eq. (9.1) is found to equal 0.36 +/- 0.024 (see Fig. 9.6), yielding an empirical Nusselt- Raleigh correlation for the test apparatus and pin fin configuration as

$$\overline{Nu_d} = \overline{h}d/k = 0.36Ra^{1/4}{}_d \qquad (9.3)$$

This expression can now be used to calculate the heat transfer coefficient values for each section of the PPS pin fin by calculating diameter based Raleigh number (Eq. 9.2). This expression then provides the average Nusselt number over the entire circumference of an isothermal cylinder.
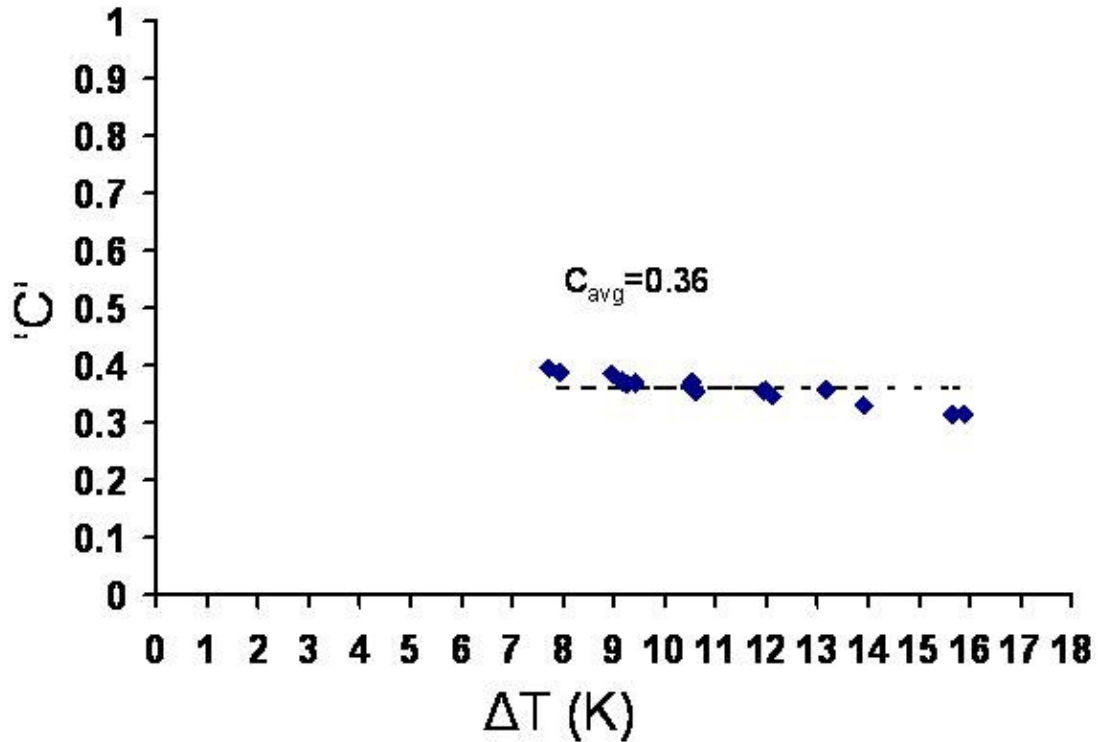
Figure 9.6 Nusselt – Raleigh Correlation constant value for the test setup

9.5 PPS Composite Pin Fin Temperature Measurements

9.5.1 Thermocouple Locations and Measurements

The first three sets of thermocouples were located 0.5 cm above the fin base, followed by the middle thermocouples at 3.5 cm above, and the last three thermocouples at 7.5 cm away from the fin base. Three thermocouples were placed at each axial distance, including one on the pin fin axis, one 6.4 mm away from axis, and the third 9.5 mm from the axis. The holes for these nine thermocouples took 0.9555 mm^3, or only 0.00026 % of total PPS pin fin volume.

Typical results for an experimental run with a PPS composite pin fin, immersed in the previously described water cooled apparatus are displayed in Fig. 9.7. The top

three curves indicate the thermocouple readings closest to the pin fin base, at a fin height of 0.5 cm from the base.
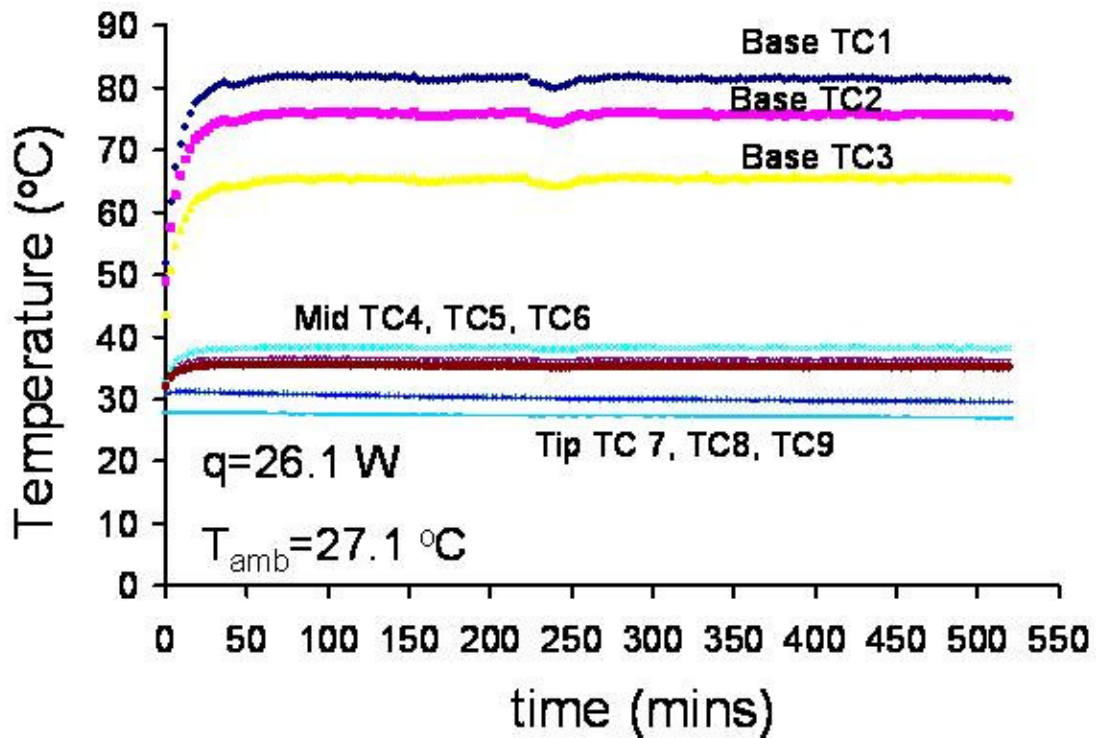
Figure 9.7 PPS pin fin temperature measurement curve

The topmost blue curve is for the thermocouple at the pin fin axis; followed by the purple curve for the pin fin at a radial distance of 6.35 mm, and the yellow curve for the thermocouple at 9.53 mm from the axis. Clearly, a significant radial temperature variation is observed in the low radial thermal conductivity PPS composite pin fin. Similar trends are obtained for the thermocouples at an axial distance of 3.5 cm from the fin base. The third set of thermocouples at 7.5 cm away from the base, depict similar trends, although with a much reduced magnitude, due to the 45K temperature drop from the fin base.. The temperature measurements in the PPS composite pin fin were performed for various power settings ranging from 13.6-27.4 W. The measured

fin excess temperatures (0.5-37.4K) produced by this range of heat rejection rates used to calculate local heat transfer coefficient values in Fig. 9.8**.**

9.5.3 Local Heat Transfer Coefficient Values
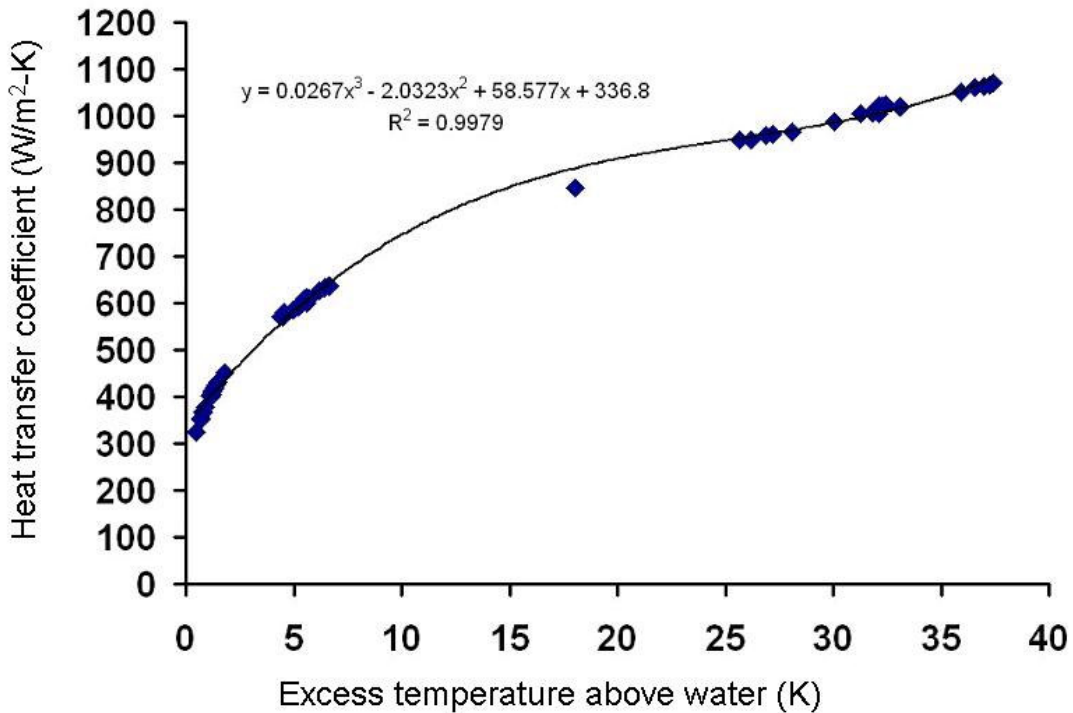
Figure 9.8 PPS pin fin average heat transfer coefficient curve

The observed axial base-to-tip temperature difference can be expected to lead to a noticeable variation in the pin fin heat transfer coefficient along the PPS composite pin fin height. This local heat transfer coefficient value can be calculated using Eq. (9.3) and is shown in Fig. 9.8 for different temperature rise readings at each of the three axial thermocouple locations. The ambient fluid temperature was measured for each experimental run around 27.3 ^{o}C (σ~0.9 ^{o}C).

The calculated heat transfer coefficient close to PPS fin tip is seen to increase with increasing temperature rise above the fluid temperature for various heat dissipation

rates. For the 13.6-27.4 W of pin fin heat dissipation examined in these tests, the near-base temperature rise varied from 27 to 37 K, resulting in heat transfer coefficients at the 0.5cm fin height from 950 to 1070 W/m^2-K with an average value of 1010 W/m^2-K ($\sigma\pm4\%$). For thermocouple located at a fin height of 3.5 cm the local excess temperatures varied from 5 to 7 K resulting in a heat transfer coefficient variation from 570-640 W/m^2-K with an average value of 610 W/m^2-K ($\sigma\pm4\%$). For the PPS composite thermocouple located at fin height of 7.5 cm towards the least effective portion of the pin fin,, the local temperature rose from 1 to 1.3 K, resulting in local heat transfer coefficient values ranging from 325-451W/m^2-K with an average value of approximately 400 W/m^2-K($\sigma\pm8\%$).

9.6 Numerical Modeling

9.6.1 Geometry

Commercial FEM software, ANSYS 8.0, was used to simulate the experimental runs. The pin fin and its base plate assembly, including the copper spreader plate (Fig. 9.2) and all the associated layers, were represented in an axisymmetric 2D model of the pin fin assembly.

9.6.2 Boundary Conditions and Properties

   A constant heat flux boundary condition was applied at the base of the pin fin, representing the different operating conditions of the fin. The external surface of the pin fin is insulated from 0-1.6 cm. The heat transfer coefficient values obtained from Eq. (9.3) after single iteration were applied to the various sections of the wetted surface of the fin, with an average value 850 W/m^2-K for near the base for fin heights of 1.6-2.6 cm, 609 W/m^2-K from 2.6 to 7.6 cm, and towards the tip of the PPS pin fin,

from 7.6 to 9.1 cm, heat transfer coefficients of 408 W/m^2-K. The experimentally measured ambient water temperature values are applied in the numerical runs.

9.6.3 Mesh Generation

Plane 75 elements that provide axisymmetric solution capability are used in order to obtain temperature distribution in the fin. In order to monitor grid independence at various critical locations in the PPS pin fin, structured mesh with increasing node density was used.
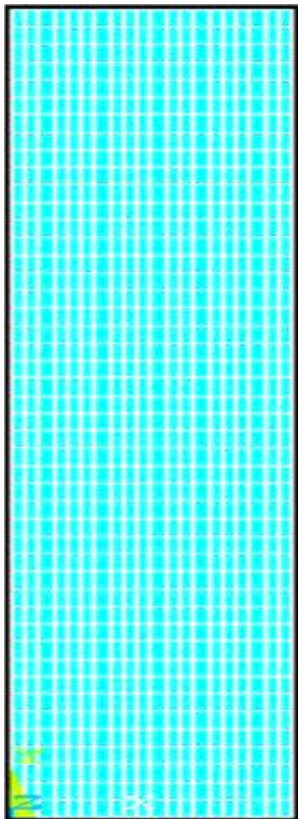
Plane 75 elements
elements=24840
nodes=25315

Figure 9.9 Pin fin assembly finite element mesh diagram

9.6.5 Numerical Grid Independence

The node density in the axisymmetric model was varied in five steps from 6448 to 83611 nodes in order to ensure grid independence in the numerical runs. Temperature values at three different key locations were monitored. Based on the grid independence results shown in Fig 9.10, a mesh with 25315 nodes was used for obtaining the numerical solutions.
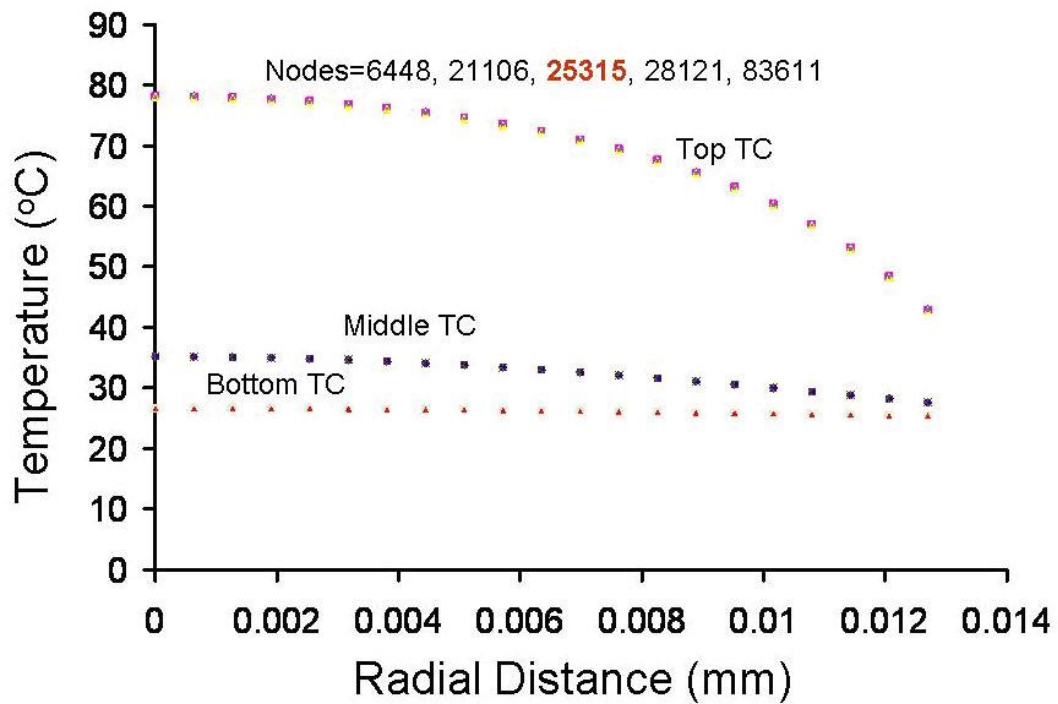
Figure 9.10 Pin fin assembly finite element grid independence plots

9.7 PPS Composite Pin Fin Results and Analysis

9.7.1 Heat Flow Rate of 26.2 W

9.7.1.1 FEM Results

The numerically obtained converged and grid independent temperature distribution plot is shown in Fig. 9.11 for a heat flux value of 51634 W/m^2 (corresponding to

26.2W of heat input) applied at the bottom of the copper spreader plate. The copper

spreader plate then acts as a constant temperature source at the base of the pin fin.

The temperature drop across the width of the copper spreader plate was found to be

insignificant, i.e. <0.5K. The PPS composite thermal conductivity values are taken to

be previously measured values in Chapter 3. The pin fin temperature at the water

surface and at a fin height of 0.5 cm depicts a significant temperature variation, along

the radius of the pin fin, with the temperature highest at the center and decreasing

with the radial distance.
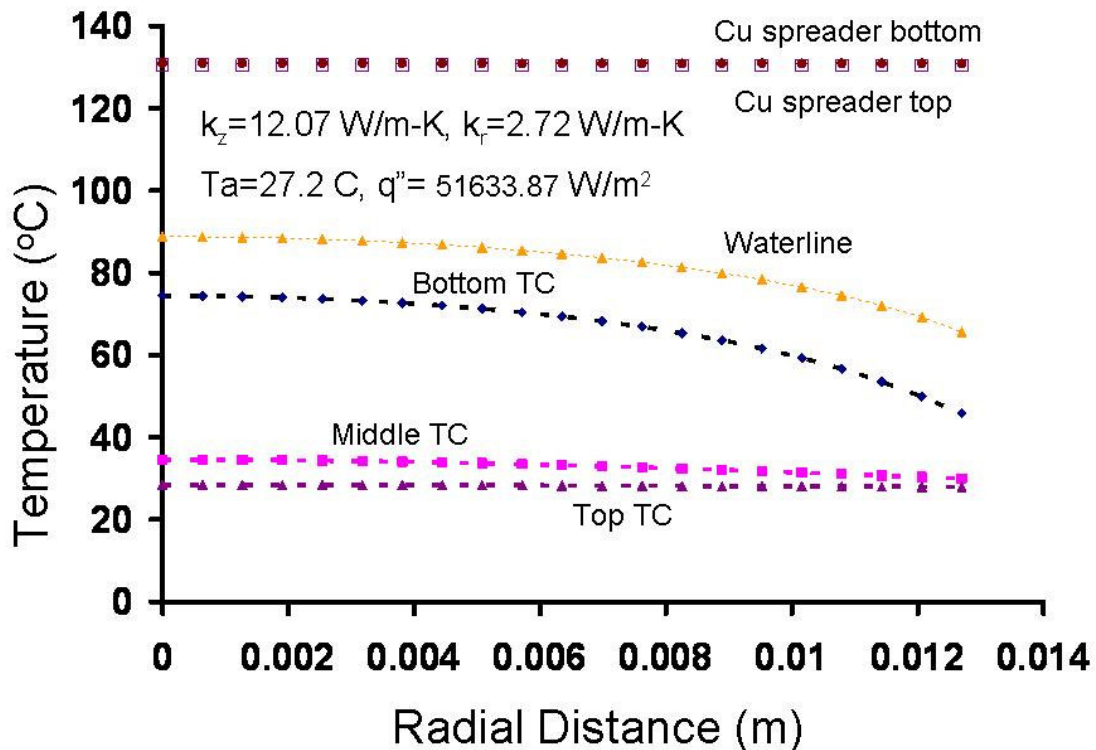
Figure 9.11 Numerical Temperature distribution at PPS composite pin fin for 26.2 W
(k_z=12, k_r=2.72 W/m-K)
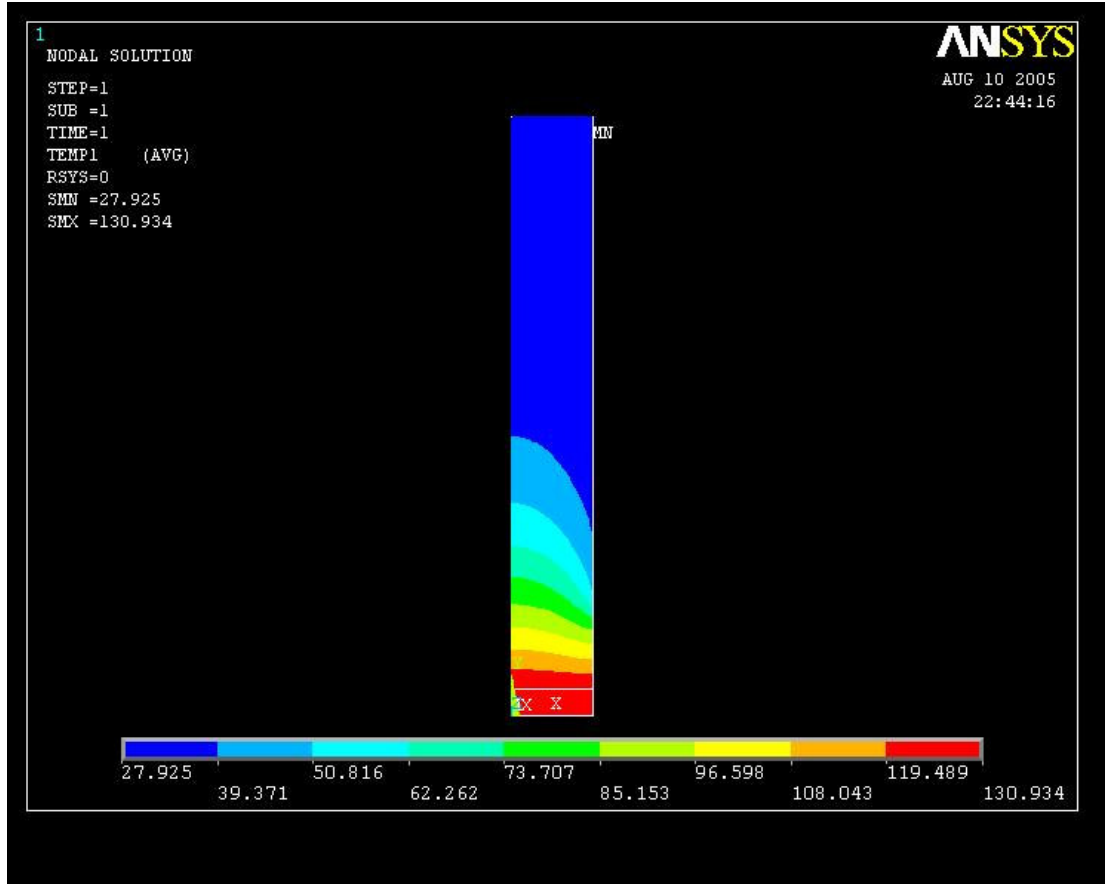
Figure 9.12 Numerical predicted temperature distribution for PPS composite pin fin at 26.2 W (k_z=12, k_r=2.72 W/m-K)

The complete temperature contour plot for this condition is shown in Fig. 9.12. The radial temperature variation diminishes as the axial distance increases from the fin base to the tip. At the base of the fin, the temperature drops approximately 23K from the axis to the wetted surface of the fin. At 0.5 cm fin height the radial temperature variation increases to 29K (Fig. 9.11). At 3.5 cm fin height it decreases to a moderate radial temperature variation of 4.6K and at the fin height of 7.5 cm radial temperature variation is only 0.5K, ranging from 28.5 at the center to 28 on the surface.

9.7.1.2 Experimental Data Points

Average readings from four different runs at the previously described thermocouple locations are plotted in Fig. 9.13 for a power supply of 26.2 W. The results of the uncertainty in Table 9.1 indicate that the average associated uncertainty in the measured values was less than 1K.

9.7.1.2.1 Precision Analysis

Each experimental run involved dissembling and reassembling the pin fin assembly in the test apparatus. The experimental runs were repeated four times and temperature readings were taken at steady state.

The standard deviation in the experimental data was calculated in using the expression

$$\sigma = [\Sigma \, (x_i - x_o)^2 / (n\text{-}1)]^{0.5}$$

Where,

x_i observed value

x_o mean value

n   number of values

σ standard deviation

9.7.1.2.2 Uncertainty Analysis

An uncertainty analysis [88], [117] was conducted, in which the total uncertainty is composed of the precision and bias errors encountered during the experiments.

$$\delta_T^2 = \Sigma(\delta_p^2) + \Sigma(\delta_b^2)$$

The standard deviation represents the precision component (δ_p) of the uncertainty.

The bias component of the uncertainty (δ_b) was determined by considering the thermocouples inaccuracy used in the experiments. Table 9.1 shows the different components of the uncertainty analysis for a specific power dissipation of 26.2W.

Table 9.1 Temperature measurement and uncertainty table at 26.2 W

Thermocouple number	Avg Temp (^{o}C)	Deviation ($\pm^o$C)	Bias error ($\pm^o$C)	Total uncertainty ($\pm^o$C)	% Total Uncertainty On excess temperature
TC1	80.6	0.78	0.5	0.93	1.73
TC2	74.6	0.89	0.5	1.02	2.15
TC3	64.6	0.84	0.5	0.98	2.62
TC4	37.3	0.87	0.5	1.00	9.90
TC5	35.3	0.84	0.5	0.98	12.13
TC6	34.5	0.83	0.5	0.97	13.29
TC7	29.3	0.59	0.5	0.77	36.64
TC8	29.2	0.61	0.5	0.79	39.24
TC9	27.1	0.095	0.5	0.51	510

The total percentage uncertainty increases towards the fin tip due to shrinking excess temperature values above fluid temperature, that becomes nearly zero for TC9 resulting in very high percentage uncertainty. Focusing on the thermocouples located near the pin fin base TC1- TC3 where there is minimum uncertainty due to very high excess temperature above water. It can be seen that the radial temperature variation

from center axis towards the surface is about 16K with average value of 73.3 $^{\circ}$C. This results in uncertainty value of some 22% in the average radial temperature value.

9.7.1.3 Experimental – Numerical Agreement

The Figure 9.13 displays the above tabulated values for PPS composite pin fin in the form of colored squares. The dashed curves indicate the numerical results earlier obtained using the ANSYS 8.0 2D axisymmetric model. The comparison between experimental and numerical temperature results is achieved at 9 key points in the tested PPS composite pin fin assembly with previously measured axial thermal conductivity value of 12.07 W/m-K and radial thermal conductivity value of 2.72 W/m-K.
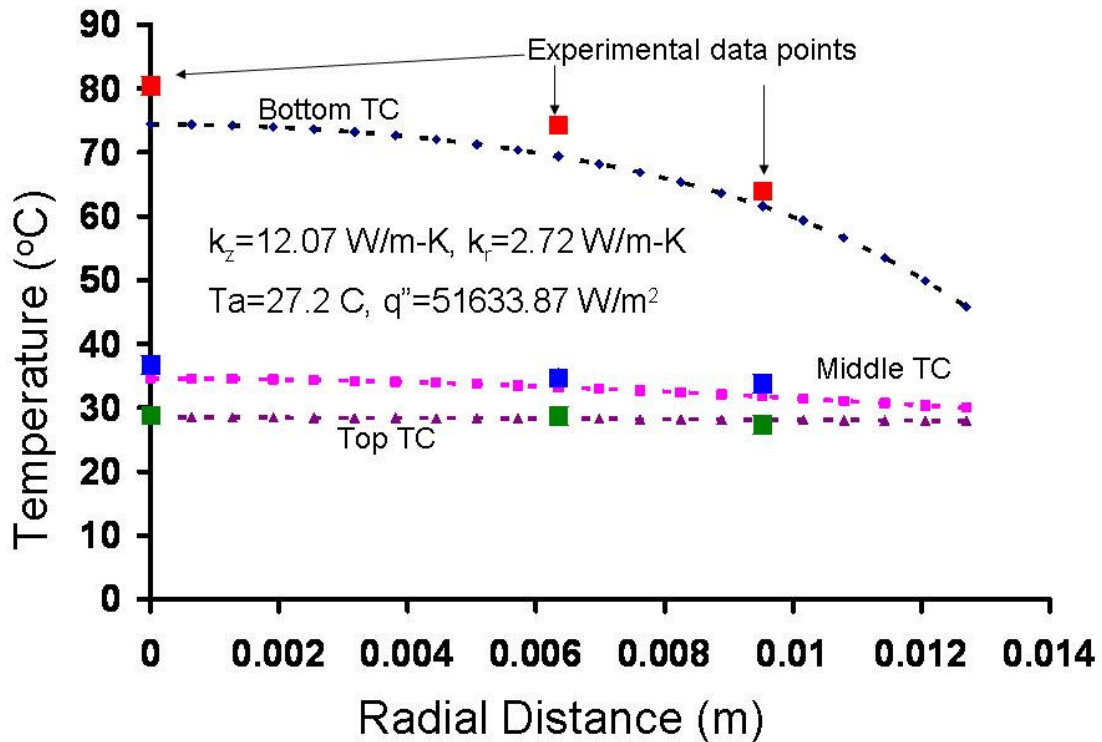
Figure 9.13 Experimental-numerical comparisons at heat transfer rate of 26.2 W (k_z=12, k_r=2.72 W/m-K)

At 0.5 cm fin height – where the largest radial temperature variation is found – the agreement between the numerical and experimental excess temperatures is within 9%. The highest numerical and experimental excess temperature discrepancy of 168% is obtained for at an axial distance of 7.5 cm and on the largest radial distance of 9.5 mm.

Extensive parametric analysis was carried out in order to obtain axial and radial thermal conductivity values that can provide closest agreement with experimentally obtained results. It was found that the values that provide closest agreement are axial thermal conductivity value of 13 W/m-K and radial thermal conductivity value of 2 W/m-K.
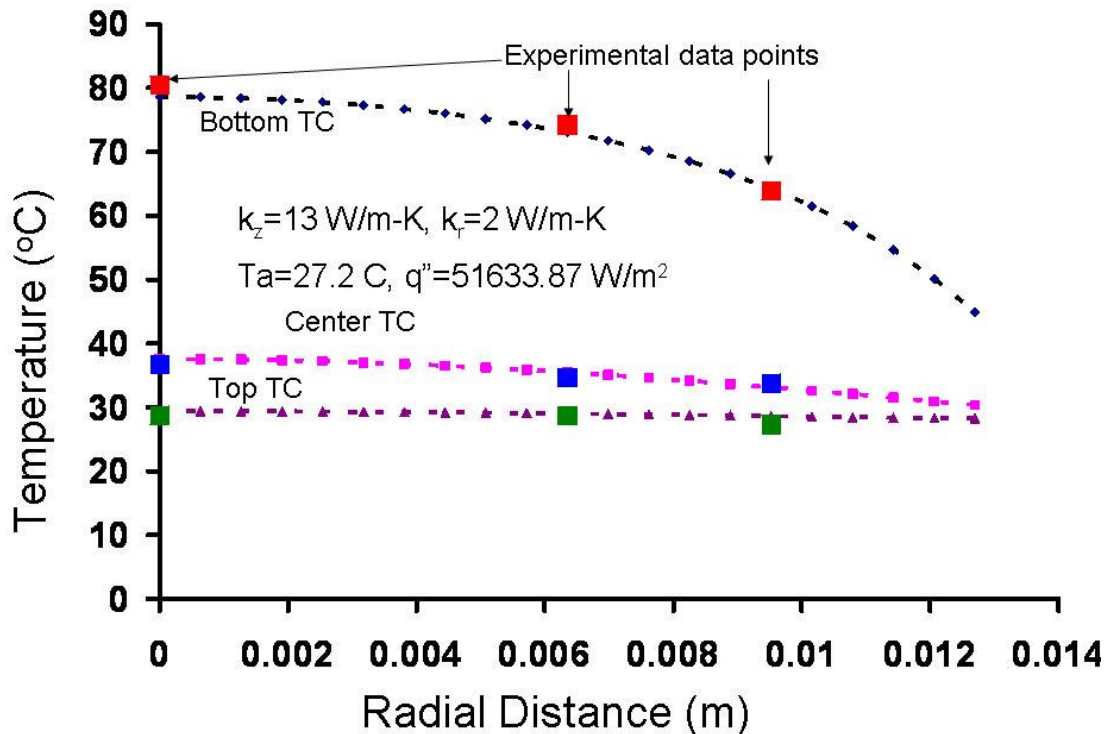
Figure 9.14 Experimental-numerical comparisons at heat transfer rate of 26.2 W (k_z=13, k_r=2W/m-K)

These modified conductivity values of 13 and 2 W/m-K results in much closer agreement with experimental results as indicated in Fig. 9.14. At 0.5 cm fin height – where the largest radial temperature variation is found – the agreement between the numerical and experimental excess temperatures is within 2.5%. The highest numerical and experimental excess temperature discrepancy of 74% is obtained for at an axial distance of 7.5 cm and on the largest radial distance of 9.5 mm. In the following sections these values are used for PPS composite pin fin analysis.
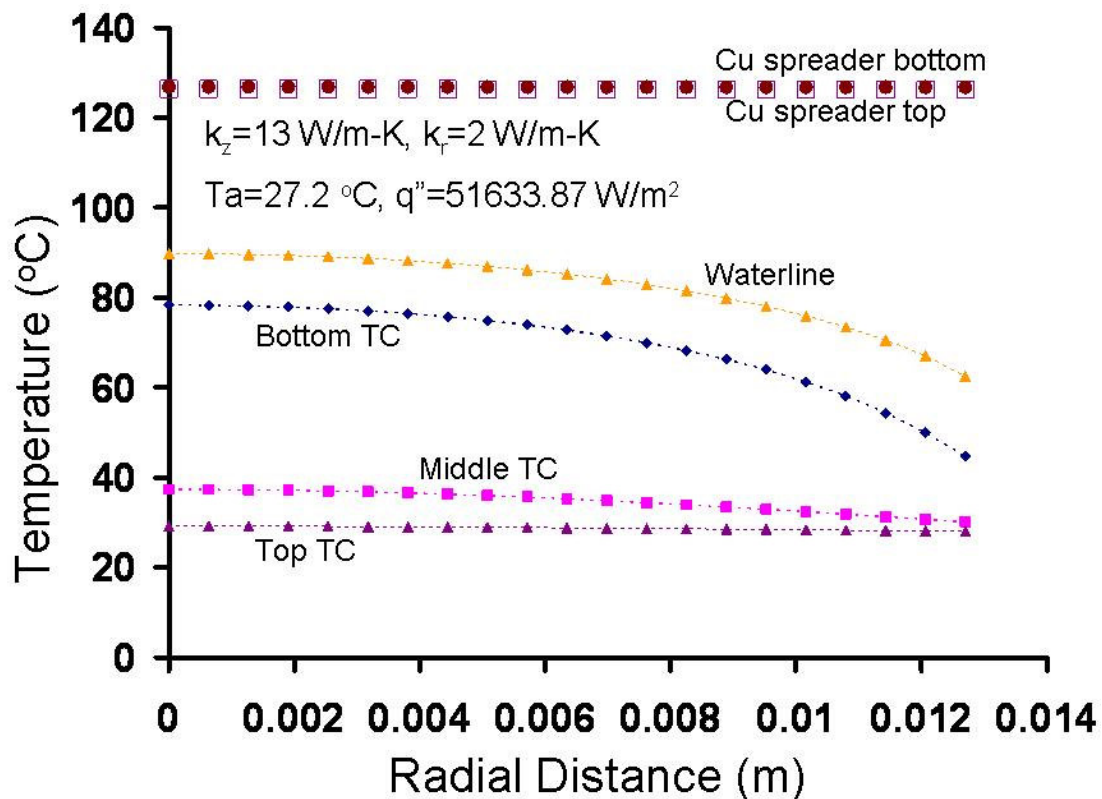
Figure 9.15 Numerical temperature distribution at PPS composite pin fin of 26.2 W ($k_z=13$, $k_r=2$W/m-K)

The numerically obtained converged temperature distribution plot is shown in Fig. 9.15 for a heat flux value of 51634 W/m^2 (corresponding to 26.2W of heat input) applied at the bottom of the copper spreader plate. The copper spreader plate then acts

207

as a constant temperature source at the base of the pin fin. The temperature drop

across the width of the copper spreader plate was found to be insignificant, i.e. <0.5K.
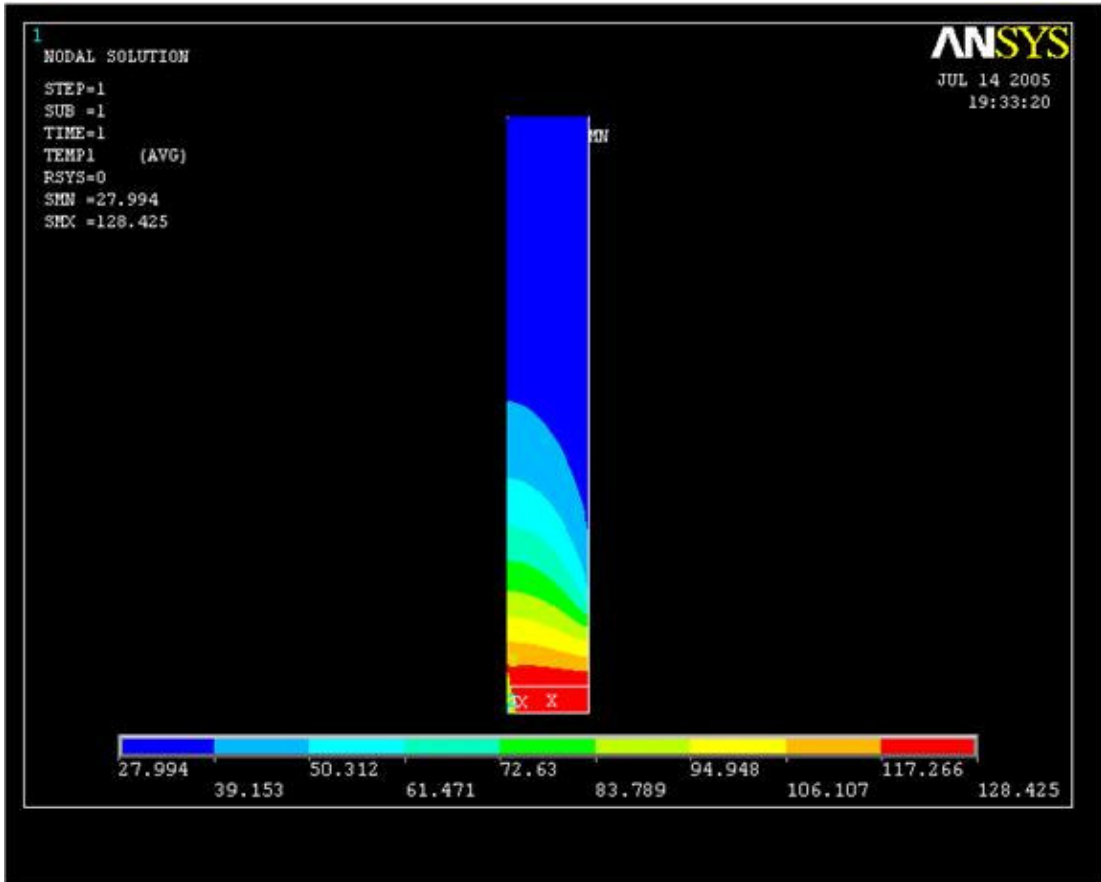
Figure 9.16 Numerical predicted temperature contours for PPS composite pin fin at heat transfer rate of 26.2 W (k_z=13, k_r=2W/m-K)

The complete temperature contour plot for this condition is shown in Fig. 9.16. The

radial temperature variation diminishes as the axial distance increases from the fin

base to the tip. At the base of the fin, the temperature drops approximately 27K from

the axis to the wetted surface of the fin. At 0.5 cm fin height the radial temperature

variation increases to 34K (Fig. 9.16). At 3.5 cm fin height it decreases to a moderate

radial temperature variation of 7.2K and at the fin height of 7.5 cm radial temperature variation is only 1.1K, ranging from 29.4 at the center to 28.3 on the surface.

9.7.2 Heat Flow Rate of 23.5 W

9.7.2.1 FEM Results

The numerically obtained converged temperature distribution plot for lower power value of 23.5 W is shown in Fig. 9.17. The temperature profile at the water surface and 0.5 cm axial distance away in the water has similar curvature and gap from the center axis all the way to the surface (Fig. 9.17). The copper spreader plate acts as a constant temperature source at the base of the pin fin. The temperature drop across the width of the copper spreader plate was found to be insignificant, i.e. <0.5K.The radial temperature variation on the water surface starting at the fin base is from 82.6 to 58.2 ^{o}C for 24.4 ^{o}C temperature difference and at 0.5 cm away it is from 70.9-40.7 ^{o}C for a 30.2 ^{o}C temperature difference value. The radial temperature variation diminishes as axial distance increases from the fin base. At 3.5 cm away there is only moderate radial temperature variation of 6.5 ^{o}C ranging from 34.2-27.7 ^{o}C (Fig. 9.17). On the fin tip the radial temperature variation is only 1°C ranging from 26.8 to 25.8 ^{o}C. The complete contour plot is shown in Fig. 9.18.
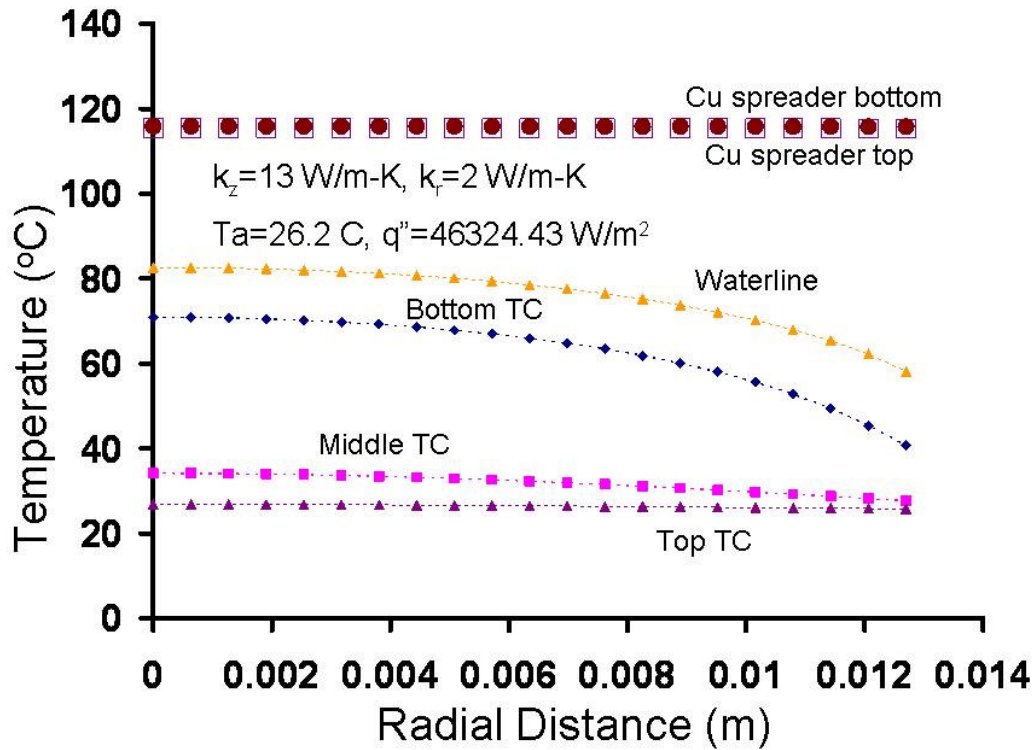
Figure 9.17 Numerical temperature distribution at PPS composite pin fin locations

Figure 9.18 Numerical predicted temperature contours for PPS composite pin fin at

heat transfer rate of 23.5 W

9.7.2.2 Experimental Data Points

The experimental results obtained at power supply of 23.5 W are shown in Table 9.2.

The total maximum uncertainty is within 1.5K as indicated in the table.

Table 9.2 Temperature measurement and uncertainty table at 23.5 W

Thermocouple number	Avg Temp (^{o}C)	Deviation (±^{o}C)	Bias error (±^{o}C)	Total uncertainty (± ^{o}C)	% Total uncertainty On excess temperature
TC1	74.3	1.35	0.5	1.44	3.0
TC2	68.6	1.3	0.5	1.39	3.3
TC3	59.2	1.2	0.5	1.3	3.9
TC4	34.7	0.69	0.5	0.85	9.98
TC5	32.9	0.66	0.5	0.83	12.43
TC6	32.1	0.73	0.5	0.88	15.02
TC7	27.4	0.49	0.5	0.70	56.59
TC8	27.4	0.5	0.5	0.71	60.63
TC9	27.4	0.49	0.5	0.70	640

9.7.2.3 Experimental – Numerical Agreement

The Figure 9.19 demonstrates the above tabulated experimentally measured values in the form of colored squares. The dashed curves indicate the numerical results earlier obtained using ANSYS 8.0 2D axisymmetric model. Clearly, good agreement between experimental and numerical results is achieved at 9 key points in the tested PPS composite pin fin assembly with axial thermal conductivity value of 13 W/m-K

and radial thermal conductivity value of 2 W/m-K. At 0.5 cm fin height – where the largest radial temperature variation is found – the agreement between the numerical and experimental excess temperatures is within 3%. The highest numerical and experimental excess temperature discrepancy of 118% is obtained for at an axial distance of 7.5 cm and on the largest radial distance of 9.5 mm.

Figure 9.19 Experimental-numerical comparisons for a heat transfer rate of 23.5 W

9.7.3 PPS Composite Fin at Heat Flow Rate of 27.4 W

9.7.3.1 FEM Results

The numerically obtained converged temperature distribution plot for higher power value of 27.4 W, shown in Fig. 9.20, indicate similar trends. The temperature profile at the water surface and 0.5 cm axial distance away in the water has similar curvature

and gap from the center axis all the way to the surface (Fig. 9.20). The radial temperature variation on the water surface starting at the fin base is from 91.7 to 63.2 ^{o}C for a 28.5 ^{o}C temperature difference and at 0.5 cm away it is from 78.1-42.8 ^{o}C for a 35.3 ^{o}C temperature difference value.
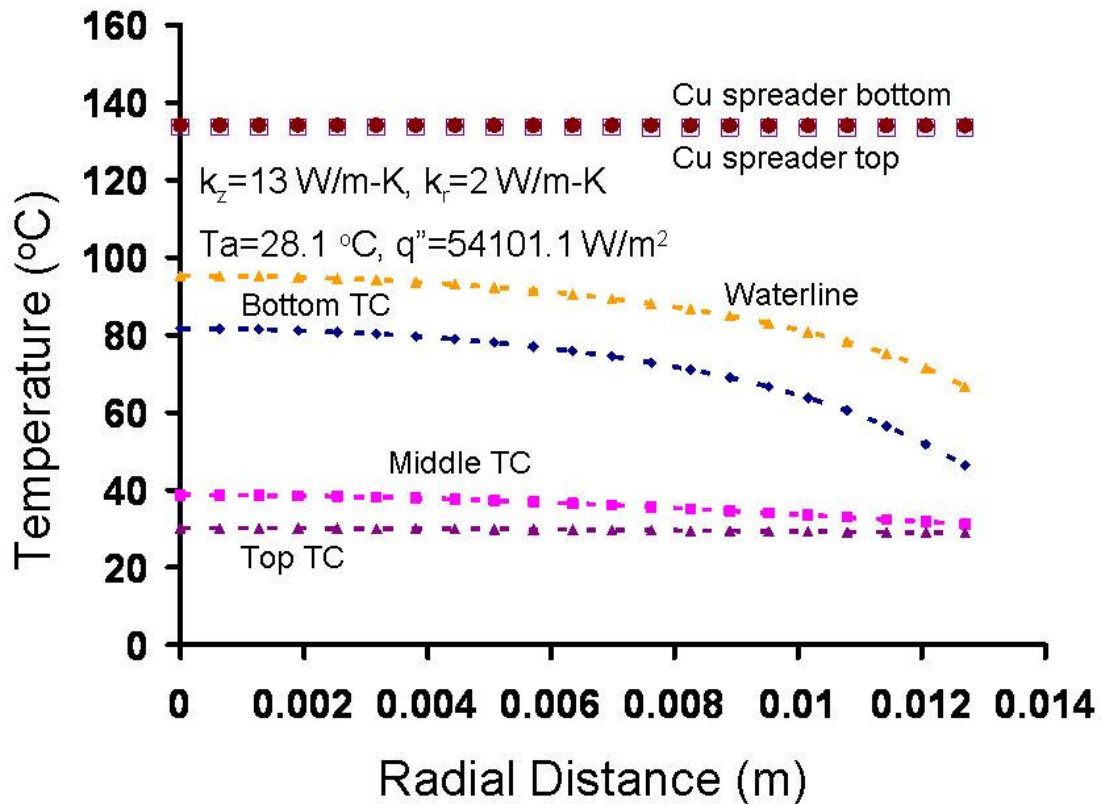
Figure 9.20 Numerical temperature distributions at PPS composite pin fin key locations for heat transfer rate of 27.4W

This suggests similar curvature plots in the intermediate axial distance values. The radial temperature variation diminishes as axial distance increases from the fin base. At 3.5 cm away there is only moderate radial temperature variation of 7.5 ^{o}C ranging from 35.1-27.6 ^{o}C (Fig. 9.20). On the fin tip the radial temperature variation is only 1.2^{o}C ranging from 26.6 to 25.4 ^{o}C. The complete contour plot is shown in Fig. 9.21.
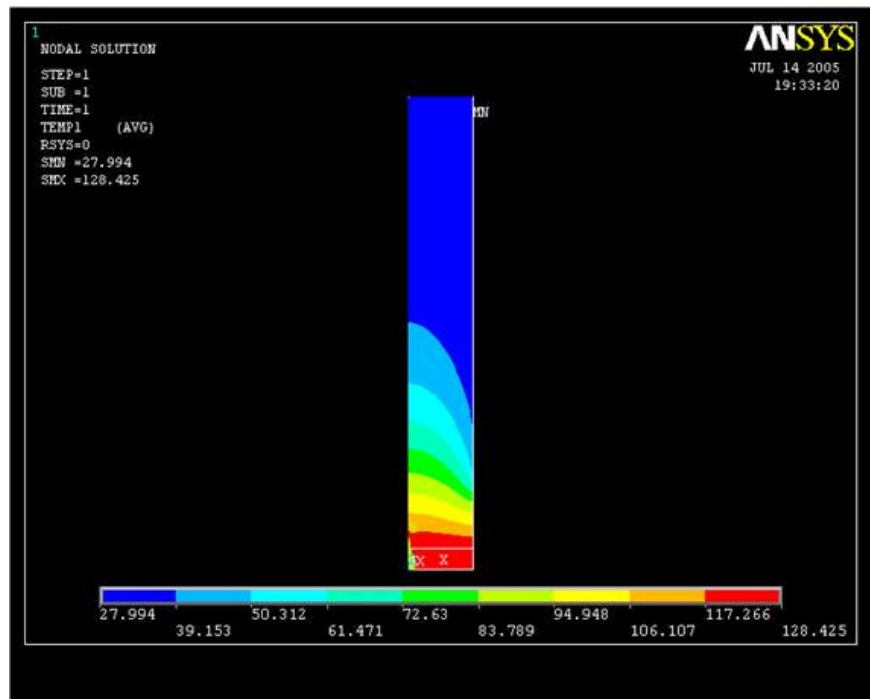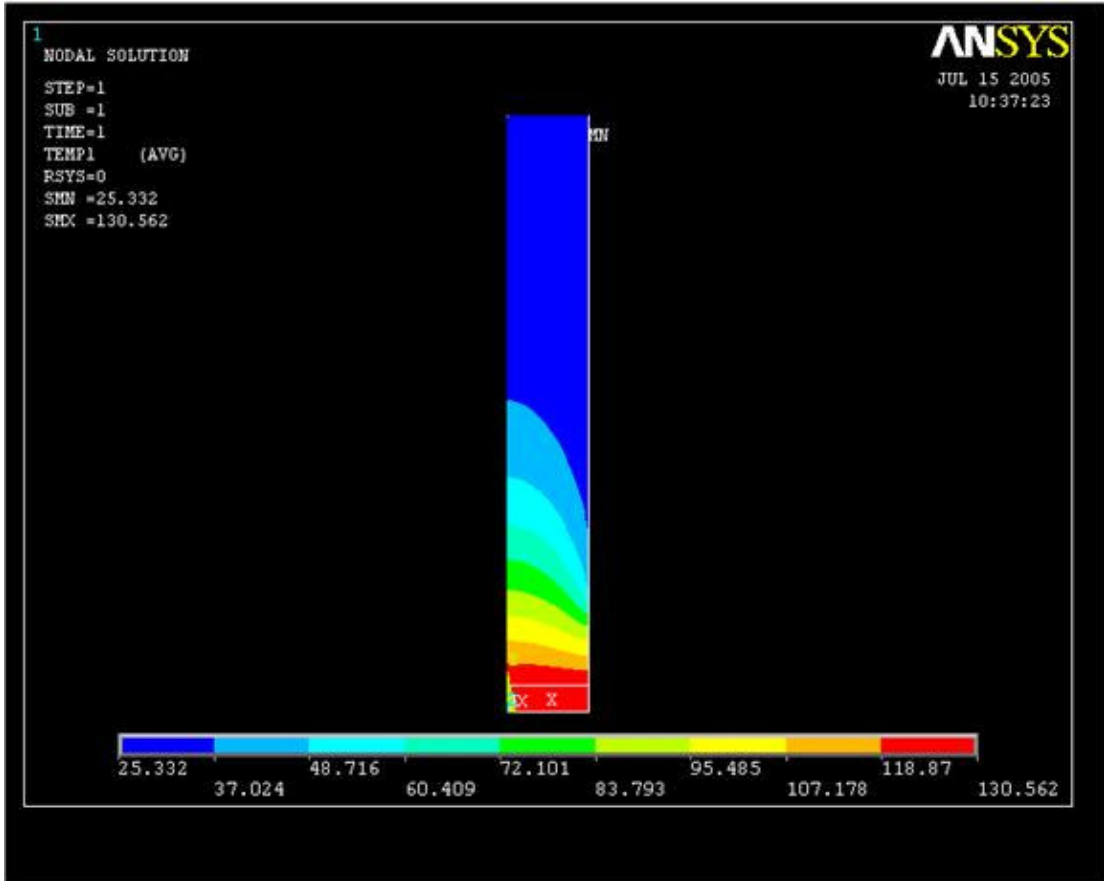
Figure 9.21 Numerical predicted temperature contour plots for PPS composite pin fin at heat transfer rate of 27.4 W

9.7.3.2 Experimental Data Points

The experimental results obtained at power supply of 27.4 W are shown in Table 9.3.

The total maximum uncertainty is within 1.44K as indicated in the table.

Table 9.3: Temperature measurement and uncertainty table at 27.4 W

Thermocouple number	Avg Temp (^{o}C)	Deviation (±^{o}C)	Bias error (±^{o}C)	Total uncertainty (± ^{o}C)	% Total uncertainty on excess temperature
TC1	82.5	1.28	0.5	1.44	2.64
TC2	76.4	1.23	0.5	1.39	2.87
TC3	66.3	1.11	0.5	1.3	3.4
TC4	39.6	0.95	0.5	0.85	7.38
TC5	37.6	0.95	0.5	0.83	8.69
TC6	36.8	0.93	0.5	0.88	10.05
TC7	31.7	0.99	0.5	0.70	19.35
TC8	31.6	1.02	0.5	0.71	19.81
TC9	27.9	0.33	0.5	0.70	540

9.7.3.3 Experimental – Numerical Agreement

The experimental results obtained at power supply of 27.4 W are shown in Table 9.3 and in Fig. 9.22 as colored squares. The dashed curves in Fig. 9.22 indicate the numerical results earlier obtained using ANSYS 8.0 2D axisymmetric model. Clearly, good agreement between experimental and numerical results is achieved at 9 key points in the tested PPS composite pin fin assembly with axial thermal conductivity value of 13 W/m-K and radial thermal conductivity value of 2 W/m-K. At 0.5 cm fin height – where the largest radial temperature variation is found – the agreement between the numerical and experimental excess temperatures is within 1.2%. The highest numerical and experimental excess temperature discrepancy of 172% is

obtained for at an axial distance of 7.5 cm and on the largest radial distance of 9.5 mm.
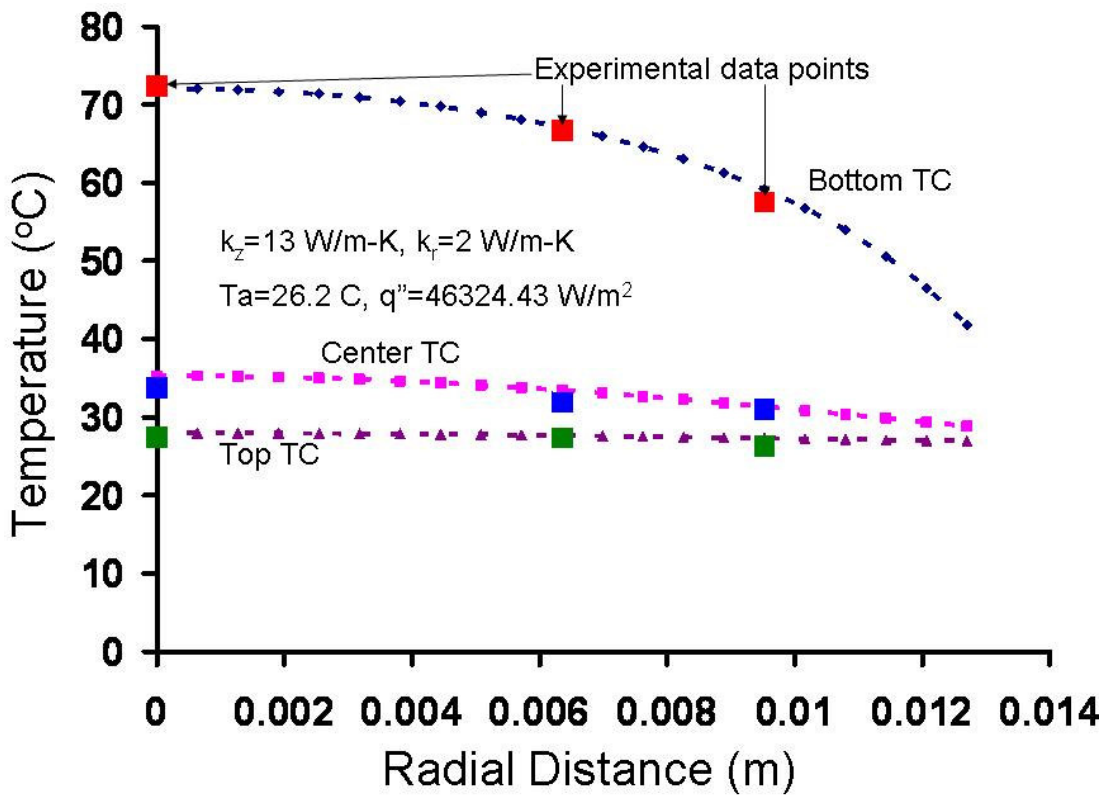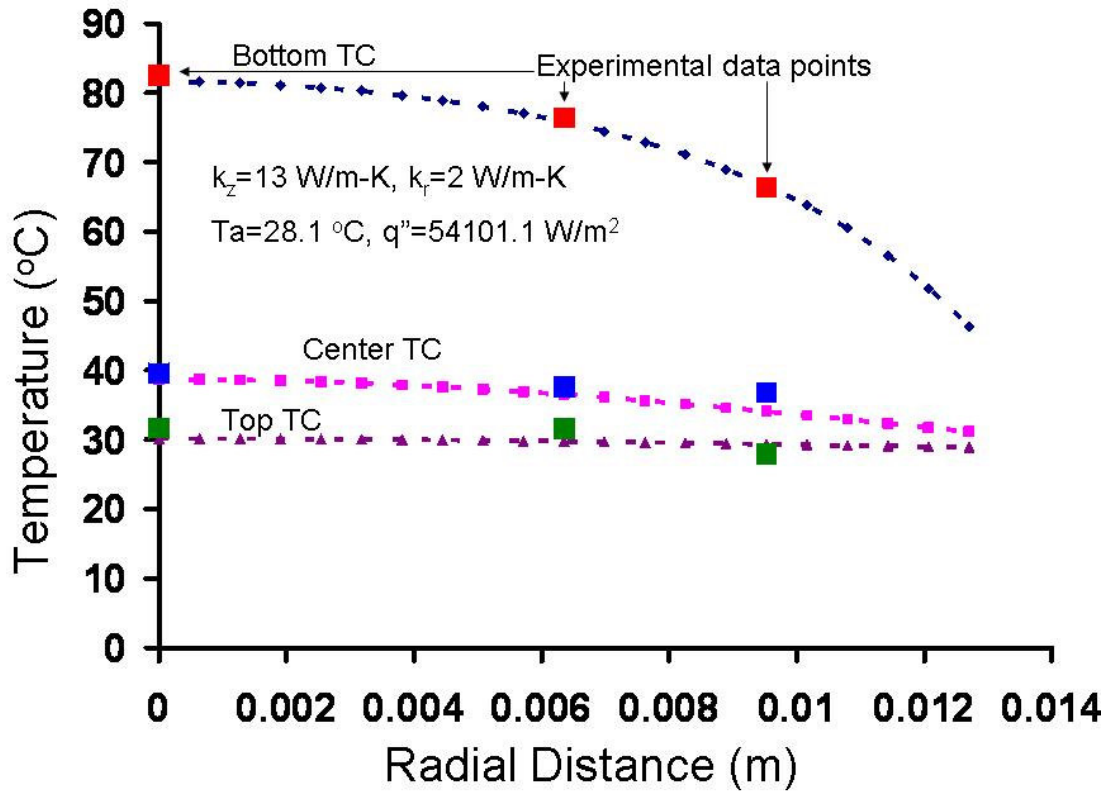

Figure 9.22 Experimental-numerical comparisons for a heat transfer rate of 27.4 W

9.7.4 Base temperature rise

The measured temperature and FEM modeling temperature rise at the bottom center of the copper spreader is depicted in Fig. 9.23 for each of the above 3 heat flow rate cases. The experimentally measured temperature rise is slightly higher than FEM modeling temperature rise due to intermediate contact resistance between the copper spreader and PPS composite pin fin. As previously indicated the FEM predictions on the PPS composite pin fin surface are in good agreement with measured values.
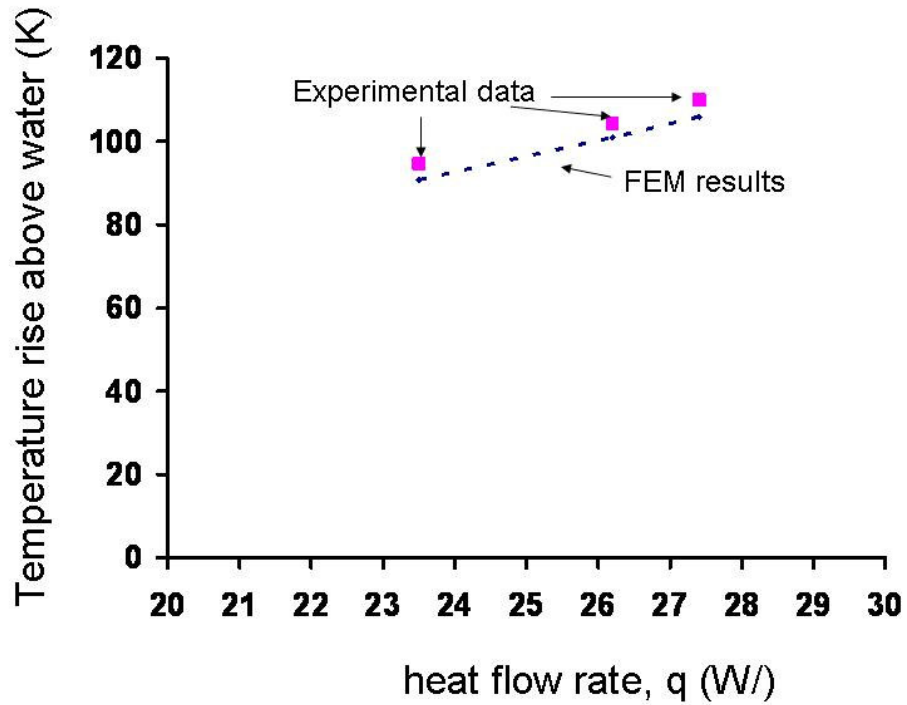
Figure 9.23 Heat transfer rate vs. temperature rise above water at the bottom of copper spreader plate.

9.8 Summary

The foregoing has presented experimental confirmation of the anisotropy encountered in polymer composite fins. An oversized enhanced PPS fin immersed in water was used to create the range of Biot Numbers at which orthotropy was anticipated to produce significant radial temperature variations in the fin. A numerical model, using experimentally-determined orthotropic thermal conductivity values, has been used to simulate the experimental runs and to obtain detailed temperature distributions in the pin fin. Experimental results for measured temperature values at 0.5 cm fin height indicated agreement within 3% of the numerical results. Experimentally obtained temperatures at several key locations were found to agree with the predicted values.

Chapter 10: Contributions and Future Scope

10.1 Contributions

10.1.1 2D Exact Orthotropic Thermal Conductivity Pin Fin Equations

10.1.1.1 Methodology

Single pin fin equations are derived including orthotropic thermal conductivity values for an axisymmetric cylindrical pin fin. The closed form mathematical solution is derived using separation of variables and utilizing orthogonal properties of Bessel functions. The final form of the equations is complex involving finding roots of Bessel functions and carrying out summation over some 100 terms in order to obtain converged final solution. A Matlab program was developed in order to obtain the correct solutions to the final derived 2D orthotropic thermal conductivity temperature and heat transfer rate equation. The final analytical equation for heat transfer and temperature distribution from a cylindrical pin fin is validated using detailed finite-element results.

10.1.1.2 Application

There is a growing interest in the use of polymer composites with enhanced thermal conductivity for high performance fin arrays and heat sinks. However, the thermal conductivity of these materials is relatively low compared to conventional fin metals, and strongly orthotropic. Therefore, the design and optimization of such polymer pin fins requires extension of the one dimensional classical fin analysis to include two-dimensional orthotropic heat conduction effects.

10.1.1.3 Outcome

The thermal performance of such fins was found to be dominated by the axial thermal conductivity, but to depart from the classical fin solution with increasing values of a radius- and radial conductivity-based Biot number. Using these relations, it is determined that fin orthotropy does not materially affect the behavior of typical air-cooled fins. Alternatively, for heat transfer coefficients achievable with water cooling and conductivity ratios below 0.1, the fin heat transfer rate can fall more than 25% below the "classical" heat transfer rates. Detailed orthotropic fin temperature distributions are used to explain this discrepancy.

10.1.2 2D Simplified orthotropic pin fin equations

10.1.2.1 Methodology

Extensive analysis is carried out using developed axisymmetric 2D orthotropic pin fin equation to obtain simplified closed form solutions for a broad range of radial Biot numbers. The summation terms are substituted by constants derived using broad parametric study for specified radial Biot number range.

10.1.2.2 Application

One major limitation of complete exact 2D orthotropic equation is the calculation of eigen values accurately using the constant heat transfer coefficient boundary condition from Bessel function equation. Therefore it was not possible to do heat transfer rate calculations quickly without using codes. This increases the design optimization time for fin arrays. The proposed simplified equations lend itself for quick easy calculation within 7% accuracy for a broad range of radial Biot numbers and fin aspect ratios. These simplified equations can be easily incorporated in the

design and optimization of pin fins within 7% accuracy without time consuming codes.

10.1.2.1 Outcome

The classical 1D pin fin heat transfer rate equation gives 4% accurate results within radial Biot of 0.4 and simplified intermediate Biot range equation is proposed for 0.4<Bi<2 that provides accuracy within 7% compared to 2D exact orthotropic pin fin heat transfer rate equation. Another high radial Biot range equation is proposed for 2<Bi<35 that provides accuracy within 7% for aspect ratio greater than 2.4, and thermal conductivity ratio 0.05-1.

10.1.3 Least-material orthotropic pin fin equation

10.1.3.1 Methodology

It was found from extensive parametric study by keeping pin fin volume constant that there exists an optimum pin fin diameter corresponding to a given heat transfer medium that provides highest heat transfer rate. Increasing or decreasing pin fin diameter decreases heat flow rate. From extensive parametric study by varying heat transfer coefficient, pin fin volumes, and thermal conductivity values, it was deduced that the orthotropic least material pin fin dimensions are very close to the classical pin fin least material pin fin dimension using axial thermal conductivity value. Therefore it was logically deduced that the existing least material pin fin equation can be effectively used with axial thermal conductivity value in it for determining orthotropic thermal conductivity least material pin fin.

10.1.3.2 Application

Since the temperature profile for orthotropic thermal conductivity polymer composite pin fin is significantly different than in case of an isotropic pin fin (Fig. 7.8). Therefore it is essential that the least material pin fin in case of an orthotropic thermal conductivity is derived. Such a least material orthotropic pin fin will result in an efficient material and volume utilization leading to energy efficient thermal designs of orthotropic thermal conductivity pin fin arrays.

10.1.3.3 Outcome

The least material orthotropic thermal conductivity pin fin solution is proposed. The proposed solution is simple and easy to use. The solution can be easily incorporated in the least material pin fin heat sink design methodology.

10.1.4 Optimum pin fin radial thermal conductivity value

10.1.4.1 Methodology

The derived 2D orthotropic pin fin governing equation is used to perform a parametric study for fixed pin fin geometry by varying thermal conductivity, heat transfer coefficient values. For fixed pin fin geometry and heat transfer coefficient value of the medium, various axial thermal conductivity value curves are plotted. The cooling rate versus radial thermal conductivity plots containing curves for fixed axial thermal conductivity value is obtained.

10.1.4.2 Application

In order to increase thermal conductivity value in the PPS pin fin radial direction higher carbon fiber volume fraction is required. The radial thermal conductivity does not contribute to overall heat flow rate beyond certain fraction of axial thermal

conductivity values. The higher volume fraction of carbon fibers degrades mechanical properties of the pin fins and increases cost. Therefore it is necessary to find optimum radial thermal conductivity value in orthotropic thermal conductivity pin fin design.

10.1.4.3 Outcome

The optimum radial thermal conductivity value is $1/10^{th}$ of the axial thermal conductivity. Increasing radial thermal conductivity beyond that results in only small increase in overall pin fin heat flow rate. Therefore for air cooled pin fin heat sink designs optimum radial thermal conductivity value is $1/10^{th}$ of the axial thermal conductivity value.

10.1.5 PPS composite pin fin natural convection heat sink thermal performance

10.1.5.1 Methodology

The design and optimization methodology of a thermally conductive PPS (Polyphenylene Sulphide) polymer staggered pin fin heat sink are described using existing analytical equations. The geometric dependence of heat dissipation and the relationships between the pin fin height, pin diameter, horizontal spacing, and pin fin density for a fixed base area and excess temperature are discussed. Experimental results of a pin finned thermally conductive PPS heat sink in natural convection indicate substantially high thermal performance. Numerical results substantiate analytical modeling results for heat sinks within the Aihara et al fin density range. The cooling rates and coefficient of thermal performance, COP_T, that relates cooling capability to the energy invested in the formation of the heat sink, has been determined for such heat sinks and compared with conventional aluminum heat sinks.

10.1.5.2 Application

PPS composite pin fin heat sink can be used for natural convection air cooled microprocessor and surface mount components with reduced mass, and better matched CTE. Moldability and lower cost provide significant advantages of using thermally conductive PPS composites for heat sinks.

10.1.5.3 Outcome

Cooling rate as high as 16 W can be achieved at 10x10 cm base at temperature rise of 25 K above 45 ^{o}C ambient temperature using optimized free convection air cooled PPS (20 W/m-K) pin finned heat sink. Thermal performance is comparable to aluminum pin finned heat sink upto fin heights of 5 cm.

10.1.6 PPS composite pin fin forced convection heat sink thermal performance

10.1.6.1 Methodology

The thermal performance of forced convection air cooled heat sinks made up of a polyphenylene sulphide composite (PPS, 20W/m-K), are predicted and compared to aluminum and copper pin fin heat sinks, using a defined heat sink volume and a range of pumping powers. The thermal performance is analytically predicted across an extensive parametric space in terms of the primary thermal metrics and identifies the thermal performance limits. PPS heat sinks are seen to constitute a viable alternative material for energy efficient heat sink design and show comparable thermal performance to aluminum and copper heat sinks at low fin densities and pumping power. The analytical model used to predict the heat sink thermal performance is seen to provide good agreement with typical aluminum pin fin heat sink experimental and CFD modeling results.

10.1.6.2 Application

PPS composite pin fin heat sink can be used for forced convection air cooled microprocessor with reduced mass, and better matched CTE. Moldability and lower cost provide significant advantages of using thermally conductive PPS composites for heat sinks.

10.1.6.3 Outcome

Cooling rate as high as 110 W can be achieved at 10x10 cm base at temperature rise of 25 K above 45 ^{o}C ambient temperature using 0.4 W pumping power for an optimized forced convection air cooled PPS (20 W/m-K) pin finned heat sink. Higher coefficient of total thermal performance is achieved at lower pumping power compared to aluminum heat sinks due to savings in fabrication energy and comparable cooling rates.

10.2 Future Scope

10.2.1 Anisotropic Pin Fin Modeling

The PPS composite thermal conductivity measurements indicate that some fin sections has varying thermal conductivity values across various planes. Therefore next step will be to study anisotropic pin fin modeling with variable conductivity along the circumference of the pin fin. This will help in understanding the effect of truly anisotropic thermal conductivity on overall pin fin heat transfer rate and temperature distribution.

10.2.2 Percolation Modeling

Presently Modified Nielsen model is proposed to capture the effects of fiber volume fraction, fiber thermal conductivity, and aspect ratio on effective thermal conductivity value. More elaborate percolation modeling can be performed in order to study the fiber effects in more depth. Monte Carlo or similar methodology can be utilized to divide the whole domain into discrete thermal resistances for each of the matrix and fiber thermal resistances. It is also possible to incorporate a third interfacial thermal resistance. By using a random generator to arrange these three thermal resistances it is possible to obtain an effective thermal conductivity versus fiber volume fraction, aspect ratio and thermal conductivity effects.

10.2.3 Mechanical strength

PPS composite pin fin with 70% volume fraction carbon fiber tends to be brittle. It is important to perform mechanical testing for fracture failures due to vibrations and shocks during handling of manufactured heat sinks. The pin fins tend to break off from the base of the heat sink due to shear forces. The mechanical study could provide detailed insight into failure mechanisms and optimal fiber volume fractions.

10.2.4 Reliability studies such as corrosion, fouling

Corrosion causes fouling and also increases friction coefficients. This results in decreasing fluid flow rates using fixed pumping power fans. This will lead to decreasing cooling rates and may cause system overheating and failures. In order to prevent such scenarios it is required to find out the corrosion resistance, chances of fouling and achievable friction coefficient values using these PPS composite pin fin

heat sinks for reliable heat sink design. It is expected that polymer based composite fins will have significantly reduced corrosion resistance compared to metal based fins. This will result in increase in the reliability of the thermal system.

10.2.5 Design for Sustainability

Detailed analysis involving fabrication energy requirement for each of the listed process step in carbon fiber manufacturing can provide more accurate fabrication energy number. There are new biodegradable polymers made from corn that are in horizon that provide more environment friendly polymer matrix materials. Also use of carbon nanotubes and nano wires provide alternative filler material for increasing thermal conductivity at much reduced filler concentration and hence significantly smaller fabrication energy requirements. Using carbon fibers and polymers for structural components such as heat sinks and heat exchanger designs instead of burning oil will reduce the CO_2 level in the atmosphere. The polymer composites provide light weight thermal systems that save energy in transportation. Clearly there exists a possibility of energy efficient and environment friendly thermal designs using polymer composites that provide many exciting tailorable properties that are not possible with metals.

Appendices

A Orthotropic Equation Derivation
B SEM Images of PPS Composite Samples
C TGA Run Plots
D Laser Flash Plots
E Forced Convection Plate Fin Using MathCAD codes
F Plate/Pin Fin Heat Sink Design Using EES codes
G PPS Composite Fabrication Energy Calculation

A Orthotropic Equation Derivation

The orthotropic pin fin heat transfer governing is given as,

$$k_r \frac{\partial^2 \theta}{\partial r^2} + k_r \frac{1}{r} \frac{\partial \theta}{\partial r} + k_z \frac{\partial^2 \theta}{\partial z^2} = 0 \tag{1}$$

Referring to Fig. 7.1and applying the following boundary conditions:

$r = 0 \qquad \dfrac{\partial \theta}{\partial r} = 0 \qquad$ Symmetric boundary condition at fin center line $\qquad$ (2)

z=0 $\qquad k_z \dfrac{\partial \theta}{\partial z} = h\theta$ Assuming constant heat transfer coefficient at the fin tip $\quad$ (3)

$r = R \quad -k_r \dfrac{\partial \theta}{\partial r} = h\theta$ Assuming constant heat transfer coefficient at fin surface $\quad$ (4)

z=H $\qquad \theta = \phi(r) \qquad$ Fin base radial temperature variation $\qquad$ (5)

We assume that

$$\theta = P(r)S(z) \tag{6}$$

Where, P and S are unknown functions of r and z, respectively. Substituting Eq. (6) into Eq. (1) and dividing through by the product PS yields

$$k_r \frac{P''}{P} + k_r \frac{P'}{rP} + k_z \frac{S''}{S} = 0 \tag{7}$$

$$k_r \frac{P''}{P} + k_r \frac{P'}{rP} = -\sigma^2 \tag{8}$$

$$k_z \frac{S''}{S} = \sigma^2 \tag{9}$$

$$k_z S'' - \sigma^2 S = 0 \tag{10}$$

$$k_r P'' + k_r \frac{P'}{r} + \sigma^2 P = 0 \tag{11}$$

Now both the equations are ordinary differential equations.

Their solutions are

$$S = A \sinh(\frac{\sigma z}{k_z^{1/2}}) + B \cosh(\frac{\sigma z}{k_z^{1/2}}) \tag{12}$$

$$P = C J_o(\frac{\sigma r}{k_r^{1/2}}) + D Y_o(\frac{\sigma r}{k_r^{1/2}}) \tag{13}$$

Where $J_o(\frac{\sigma r}{k_r^{1/2}})$ and $Y_o(\frac{\sigma r}{k_r^{1/2}})$ are the Bessel functions of order zero of the first and second kind, respectively. Hence the solution for the temperature reads

$$\theta = [CJ_o(\frac{\sigma r}{k_r^{1/2}}) + DY_o(\frac{\sigma r}{k_r^{1/2}})] \, [A\sinh(\frac{\sigma z}{k_z^{1/2}}) + B\cosh(\frac{\sigma z}{k_z^{1/2}})] \tag{14}$$

Now applying the first boundary condition we have

$$D=0 \tag{15}$$

Applying second boundary condition we obtain

$$A = \frac{h}{\sigma(k_z^{1/2})}B \tag{16}$$

Applying, Eqs. (15), (16) into (14) the expression for the temperature now reads

$$\theta = KJ_o(\frac{\sigma r}{k_r^{1/2}}) \, [\frac{h}{\sigma k_z^{1/2}}\sinh(\frac{\sigma z}{k_z^{1/2}}) + \cosh(\frac{\sigma z}{k_z^{1/2}})] \tag{17}$$

The values of σ that satisfy boundary condition are obtained after substituting Eq. (17) into the Eq. (4),

The resulting expression reads

$$J_1(\frac{\sigma r}{k_r^{1/2}}) = \frac{h}{\sigma(k_r^{1/2})}Jo\frac{\sigma r}{k_r^{1/2}} \tag{18}$$

Equation can be solved numerically if the exact values of h, k, and r are prescribed to yield the eigenvalues σ_n, n=1, 2, 3, …………
Once the eigenvalues are known, the general solution for θ is the linear superposition of the solutions corresponding to $\sigma_1, \sigma_2, \sigma_3, $ ……….; that is

$$\theta = \sum_{n=1}^{\infty} K_n [\frac{h}{\sigma(k_z^{1/2})}\sinh(\frac{\sigma z}{k_z^{1/2}}) + \cosh(\frac{\sigma z}{k_z^{1/2}})]J_o(\frac{\sigma_n r}{k_r^{1/2}}) \tag{19}$$

Applying the Eq. (5) together with the orthogonality property of $J_o(\frac{\sigma r}{k_r^{1/2}})$, we have

$$K_n = \frac{\int_0^R \phi(r) J_o(\frac{\sigma_n r}{k_r^{1/2}}) r dr}{[\frac{h}{\sigma_n (k_z^{1/2})} \sinh(\frac{\sigma_n H}{k_z^{1/2}}) + \cosh(\frac{\sigma_n H}{k_z^{1/2}})] \int_0^R J_o^2(\frac{\sigma_n r}{k_r^{1/2}}) r dr} \tag{20}$$

$$K_n = \frac{2\int_0^R \phi(r) J_o(\frac{\sigma_n r}{k_r^{1/2}}) r dr}{[\frac{h}{\sigma_n (k_z^{1/2})} \sinh(\frac{\sigma_n H}{k_z^{1/2}}) + \cosh(\frac{\sigma_n H}{k_z^{1/2}})] R^2 [J_1^2(\frac{\sigma_n R}{k_r^{1/2}}) + J_o^2(\frac{\sigma_n R}{k_r^{1/2}})]} \tag{21}$$

$$K_n = \frac{2\int_0^R \phi(r) J_o(\frac{\sigma_n r}{k_r^{1/2}}) r dr}{R^2 [\frac{h}{\sigma_n (k_z^{1/2})} \sinh(\frac{\sigma_n H}{k_z^{1/2}}) + \cosh(\frac{\sigma_n H}{k_z^{1/2}})][\frac{h^2}{\sigma_n^2 k_r} + 1] J_o^2(\frac{\sigma_n R}{k_r^{1/2}})} \tag{22}$$

$$\theta = \sum_{n=1}^{\infty} \frac{2\int_0^R \phi(r) J_o(\frac{\sigma_n r}{k_r^{1/2}}) r dr}{R^2 [\frac{h}{\sigma_n (k_z^{1/2})} \sinh(\frac{\sigma_n H}{k_z^{1/2}}) + \cosh(\frac{\sigma_n H}{k_z^{1/2}})][\frac{h^2}{\sigma_n^2 k_r} + 1] J_o^2(\frac{\sigma_n R}{k_r^{1/2}})} \ \times$$

$$[\frac{h}{\sigma (k_z^{1/2})} \sinh(\frac{\sigma z}{k_z^{1/2}}) + \cosh(\frac{\sigma z}{k_z^{1/2}})] J_o(\frac{\sigma_n r}{k_r^{1/2}}) \tag{23}$$

Using Fourier's law to calculate the heat flux through the fin base,

$$q_b = \int_0^R -k_z (\frac{\partial \theta}{\partial z})_{z=L} 2\pi r dr \tag{24}$$

$$q_b = -4\pi k_z \sum_{n=1}^{\infty} \int_0^R \frac{\int_0^R \phi(r) J_o(\frac{\sigma_n r}{k_r^{1/2}}) r dr}{R^2 [\frac{h}{\sigma_n (k_z^{1/2})} \sinh(\frac{\sigma_n H}{k_z^{1/2}}) + \cosh(\frac{\sigma_n H}{k_z^{1/2}})][\frac{h^2}{\sigma_n^2 k_r} + 1] J_o^2(\frac{\sigma_n R}{k_r^{1/2}})}$$

$$[\frac{h}{\sigma (k_z^{1/2})} \cosh(\frac{\sigma H}{k_z^{1/2}}) + \sinh(\frac{\sigma H}{k_z^{1/2}})] J_o(\frac{\sigma_n r}{k_r^{1/2}}) \frac{\sigma_n}{k_z^{1/2}} r dr \tag{25}$$

If $\phi(r) = \theta_b$ at z=H i.e. constant fin base temperature. The expression for the temperature in the fin and the heat flux through the fin base become.

$$\theta = 2\theta_b \sum_{n=1}^{\infty} \frac{k_r^{1/2} J_1(\frac{\sigma_n R}{k_r^{1/2}})}{\sigma_n R [\frac{h}{\sigma_n(k_z^{1/2})}\sinh(\frac{\sigma_n H}{k_z^{1/2}})+\cosh(\frac{\sigma_n H}{k_z^{1/2}})][\frac{h^2}{\sigma_n^2 k_r}+1]J_o^2(\frac{\sigma_n R}{k_r^{1/2}})} [\frac{h}{\sigma(k_z^{1/2})}\sinh(\frac{\sigma_n z}{k_z^{1/2}})+\cosh(\frac{\sigma_n z}{k_z^{1/2}})]J_o(\frac{\sigma_n r}{k_r^{1/2}}) \quad (26)$$

$$q_b = -4\pi k_z \theta_b \sum_{n=1}^{\infty} \frac{k_r J_1^2(\frac{\sigma_n R}{k_r^{1/2}})}{\sigma_n k_z^{1/2}[\frac{h}{\sigma_n(k_z^{1/2})}\sinh(\frac{\sigma_n H}{k_z^{1/2}})+\cosh(\frac{\sigma_n H}{k_z^{1/2}})][\frac{h^2}{\sigma_n^2 k_r}+1]J_o^2(\frac{\sigma_n R}{k_r^{1/2}})}$$

$$[\frac{h}{\sigma(k_z^{1/2})}\cosh(\frac{\sigma H}{k_z^{1/2}}) + \sinh(\frac{\sigma H}{k_z^{1/2}})] \quad (27)$$

In order to simplify the Eq. (27) we make a substitution

$$\lambda_n = \frac{\sigma_n R}{k_r^{1/2}} \quad (28)$$

$$\theta = 2\theta_b \sum_{n=1}^{\infty} \frac{J_1(\lambda_n)}{\lambda_n[\frac{hR}{k_r^{1/2}k_z^{1/2}\lambda_n}\sinh(\frac{\lambda_n k_r^{1/2}H}{k_z^{1/2}R})+\cosh(\frac{\lambda_n k_r^{1/2}H}{k_z^{1/2}R})][(\frac{Bi}{\lambda_n})^2+1]J_o^2(\lambda_n)}$$

$$\times \; [\frac{hR}{\lambda_n(k_r^{1/2}k_z^{1/2})}\sinh(\frac{\lambda_n k_r^{1/2}z}{k_z^{1/2}R})+\cosh(\frac{\lambda_n k_r^{1/2}z}{k_z^{1/2}R})]J_o(\frac{\lambda_n r}{R}) \quad (29)$$

$$q_b = -4\pi k_z \theta_b \sum_{n=1}^{\infty} \frac{k_r R J_1^2(\lambda_n)}{\lambda_n k_r^{1/2}k_z^{1/2}[\frac{hR}{\lambda_n k_r^{1/2}(k_z^{1/2})}\sinh(\frac{\lambda_n k_r^{1/2}H}{k_z^{1/2}R})+\cosh(\frac{\lambda_n k_r^{1/2}H}{k_z^{1/2}R})][\frac{h^2 R^2}{\lambda_n^2 k_r^2}+1]J_o^2(\lambda_n)}$$

$$\times [\frac{hR}{\lambda_n k_r^{1/2}(k_z^{1/2})}\cosh(\frac{\lambda_n k_r^{1/2}H}{k_z^{1/2}R}) + \sinh(\frac{\lambda_n k_r^{1/2}H}{k_z^{1/2}R})] \quad (30)$$

Let $Bi_r = \frac{hR}{k_r}$ $\quad Bi_{gm} = \frac{hR}{(k_r k_z)^{1/2}}$ $\quad \gamma = \frac{H}{R}$ $\quad k^* = \frac{k_r}{k_z}$ $\quad (31)$

$$\theta = 2\theta_b \sum_{n=1}^{\infty} \frac{\lambda_n J_1(\lambda_n)J_o(\lambda_n \frac{r}{R})[\lambda_n \cosh(\lambda_n(k^*)^{1/2} z/R)+Bi_{gm}\sinh(\lambda_n(k^*)^{1/2} z/R)]}{J_o^2(\lambda_n)[\lambda_n^2 + Bi_r^2][\lambda_n \cosh(\lambda_n(k^*)^{1/2}\gamma)+Bi_{gm}\sinh(\lambda_n(k^*)^{1/2}\gamma)]} \quad (32)$$

$$q_b = -4\pi k_z \theta_b R(k^*)^{\frac{1}{2}} \sum_{n=1}^{\infty} \frac{\lambda_n J_1^2(\lambda_n)[Bi_{gm}\cosh\lambda_n(k^*)^{\frac{1}{2}}\gamma + \lambda_n \sinh\lambda_n(k^*)^{\frac{1}{2}}\gamma]}{J_o^2(\lambda_n)[\lambda_n^2 + Bi_r^2][Bi_{gm}\sinh\lambda_n(k^*)^{\frac{1}{2}}\gamma + \lambda_n \cosh\lambda_n(k^*)^{\frac{1}{2}}\gamma]} \quad (33)$$

Let $A_n = (\lambda_n^2 - Bi_{gm}^2)^{\frac{1}{2}}$

$$\cosh(\beta) = \frac{\lambda_n}{A_n} \qquad\qquad \sinh(\beta) = \frac{Bi_{gm}}{A_n} \qquad\qquad \beta = \tanh^{-1}(\frac{Bi_{gm}}{\lambda_n}) \qquad (34)$$

$$\frac{[Bi_{gm}\sinh(\lambda_n(k^*)^{\frac{1}{2}}\gamma) + \lambda_n \cosh(\lambda_n(k^*)^{\frac{1}{2}}\gamma)]}{[Bi_{gm}\sinh(\lambda_n(k^*)^{\frac{1}{2}}\gamma) + \lambda_n \cosh(\lambda_n(k^*)^{\frac{1}{2}}\gamma)]} = \frac{\cosh(\lambda_n(k^*)^{\frac{1}{2}} z/R + \beta)}{\cosh(\lambda_n(k^*)^{\frac{1}{2}}\gamma + \beta)} = \frac{\exp(\lambda_n(k^*)^{\frac{1}{2}} z/R + \beta) + \exp-(\lambda_n(k^*)^{\frac{1}{2}} z/R + \beta)}{\exp(\lambda_n(k^*)^{\frac{1}{2}}\gamma + \beta) + \exp-(\lambda_n(k^*)^{\frac{1}{2}}\gamma + \beta)}$$

$$= \frac{[1 + \exp(-2[\lambda_n(k^*)^{\frac{1}{2}} z/R + \tanh^{-1}(\frac{Bi_{gm}}{\lambda_n})])]}{[1 + \exp(-2[\lambda_n(k^*)^{\frac{1}{2}}\gamma + \tanh^{-1}(\frac{Bi_{gm}}{\lambda_n})])]} \exp(-\lambda_n(k^*)^{\frac{1}{2}}(H-z)/R) \qquad (35)$$

$$\theta = 2\theta_b \sum_{n=1}^{\infty} \frac{\lambda_n J_1(\lambda_n) J_o(\lambda_n \frac{r}{R})}{J_o^2(\lambda_n)[\lambda_n^2 + Bi_r^2]} \frac{[1 + \exp(-2[\lambda_n(k^*)^{\frac{1}{2}} z/R + \tanh^{-1}(\frac{Bi_{gm}}{\lambda_n})])]}{[1 + \exp(-2[\lambda_n(k^*)^{\frac{1}{2}}\gamma + \tanh^{-1}(\frac{Bi_{gm}}{\lambda_n})])]} \exp(-\lambda_n(k^*)^{\frac{1}{2}}(H-z)/R) \quad (36)$$

Similarly,

$$\frac{[Bi_{gm}\cosh(\lambda_n(k^*)^{\frac{1}{2}}\gamma) + \lambda_n \sinh(\lambda_n(k^*)^{\frac{1}{2}}\gamma)]}{[Bi_{gm}\sinh(\lambda_n(k^*)^{\frac{1}{2}}\gamma) + \lambda_n \cosh(\lambda_n(k^*)^{\frac{1}{2}}\gamma)]} = \frac{\sinh(\lambda_n(k^*)^{\frac{1}{2}}\gamma + \beta)}{\cosh(\lambda_n(k^*)^{\frac{1}{2}}\gamma + \beta)} = \frac{\exp(\lambda_n(k^*)^{\frac{1}{2}}\gamma + \beta) - \exp-(\lambda_n(k^*)^{\frac{1}{2}}\gamma + \beta)}{\exp(\lambda_n(k^*)^{\frac{1}{2}}\gamma + \beta) + \exp-(\lambda_n(k^*)^{\frac{1}{2}}\gamma + \beta)}$$

$$= \frac{[1 - \exp(-2[\lambda_n(k^*)^{\frac{1}{2}}\gamma + \tanh^{-1}(\frac{Bi_{gm}}{\lambda_n})])]}{[1 + \exp(-2[\lambda_n(k^*)^{\frac{1}{2}}\gamma + \tanh^{-1}(\frac{Bi_{gm}}{\lambda_n})])]} \qquad (37)$$

$$q_b = -4\pi k_z \theta_b R(k^*)^{\frac{1}{2}} \sum_{n=1}^{\infty} \frac{\lambda_n J_1^2(\lambda_n)}{J_o^2(\lambda_n)[\lambda_n^2 + Bi_r^2]} \frac{[1 - \exp(-2[\lambda_n(k^*)^{\frac{1}{2}}\gamma + \tanh^{-1}(\frac{Bi_{gm}}{\lambda_n})])]}{[1 + \exp(-2[\lambda_n(k^*)^{\frac{1}{2}}\gamma + \tanh^{-1}(\frac{Bi_{gm}}{\lambda_n})])]} \qquad (38)$$

$$J_1(\lambda_n) = \frac{Bi_r}{\lambda_n} Jo(\lambda_n) \qquad (39)$$

Where setting Eq. (39) into Eq. (38) gives,

$$q_b = -4\pi k_z \theta_b R(k*)^{1/2} \sum_{n=1}^{\infty} \frac{Bi_r^{\,2}}{\lambda_n[\lambda_n^{\,2} + Bi_r^{\,2}]} \frac{[1 - \exp(-2[\lambda_n \gamma(k*)^{1/2} + \tanh^{-1}(\frac{Bi_{gm}}{\lambda_n})])]}{[1 + \exp(-2[\lambda_n \gamma(k*)^{1/2} + \tanh^{-1}(\frac{Bi_{gm}}{\lambda_n})])]} \qquad (40)$$

Setting, $k_r = k_z = k$ we have $Bi_r = Bi_{gm} = Bi = \dfrac{hR}{k}$, and k*=1

Setting all this in Eq. (40) we have,

$$q_b = -4\pi k\, \theta_b R \sum_{n=1}^{\infty} \frac{Bi_r^{\,2}}{\lambda_n[\lambda_n^{\,2} + Bi_r^{\,2}]} \frac{[1 - \exp(-2[\lambda_n \gamma + \tanh^{-1}(\frac{Bi}{\lambda_n})])]}{[1 + \exp(-2[\lambda_n \gamma + \tanh^{-1}(\frac{Bi}{\lambda_n})])]} \qquad (41)$$

B SEM Images of PPS Composite Samples
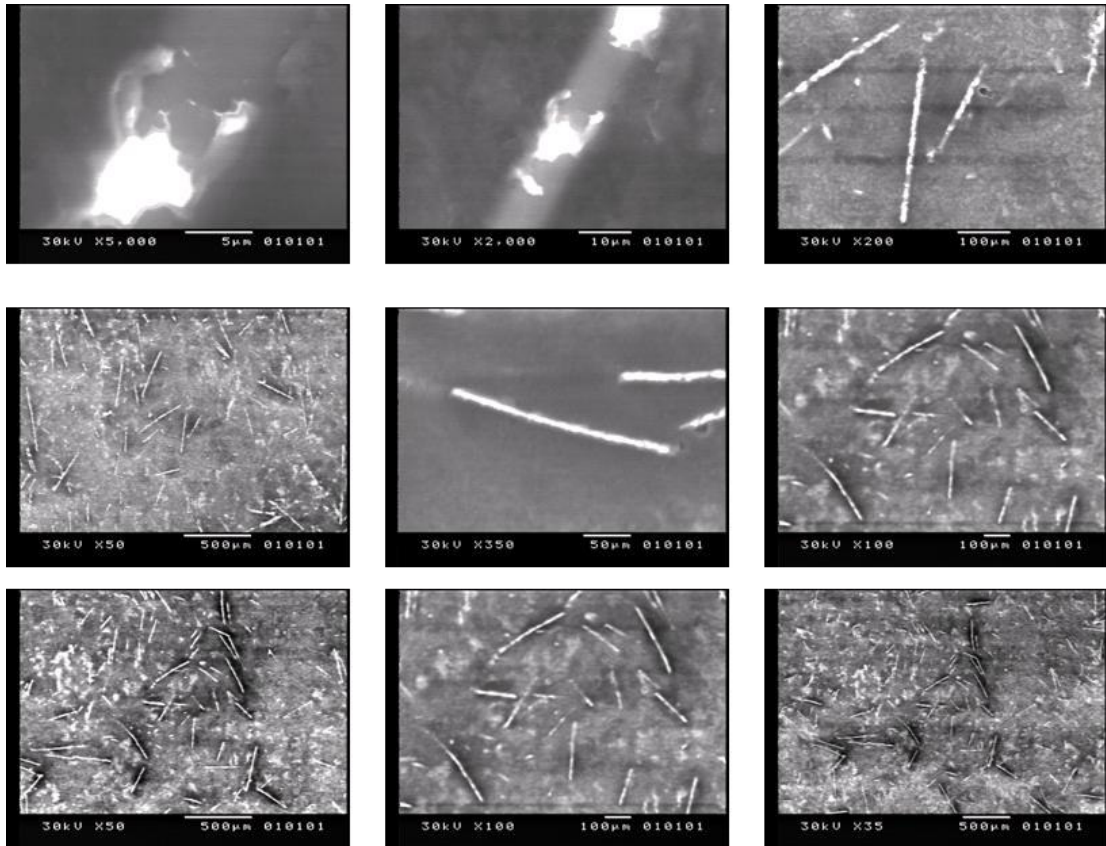
Figure B1 PPS thermally conductive composite (20 W/m-K, [10])
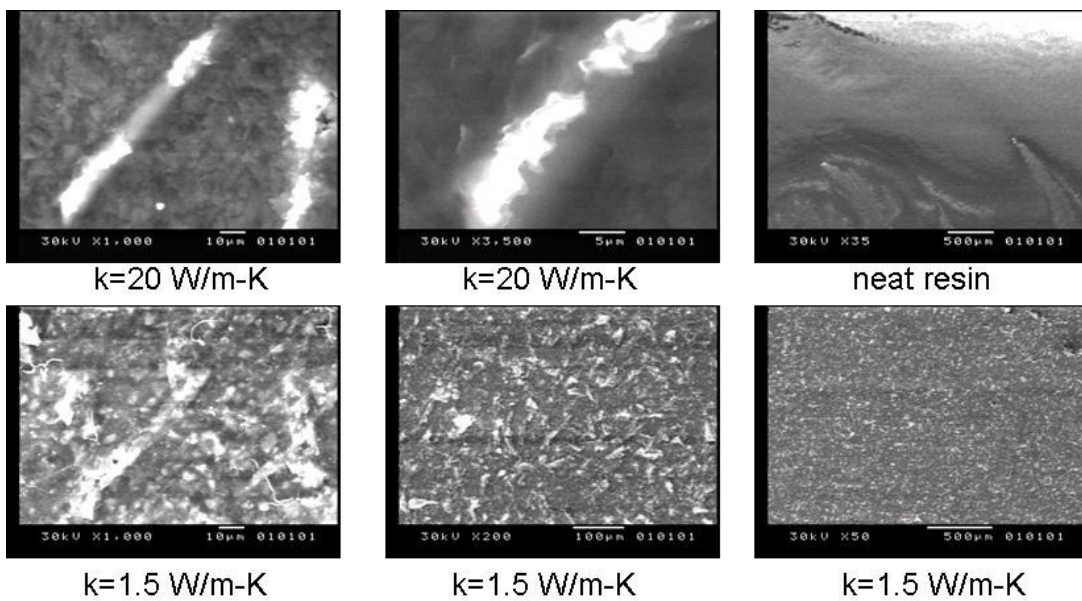

Figure B2 Various PPS composite samples ([10])

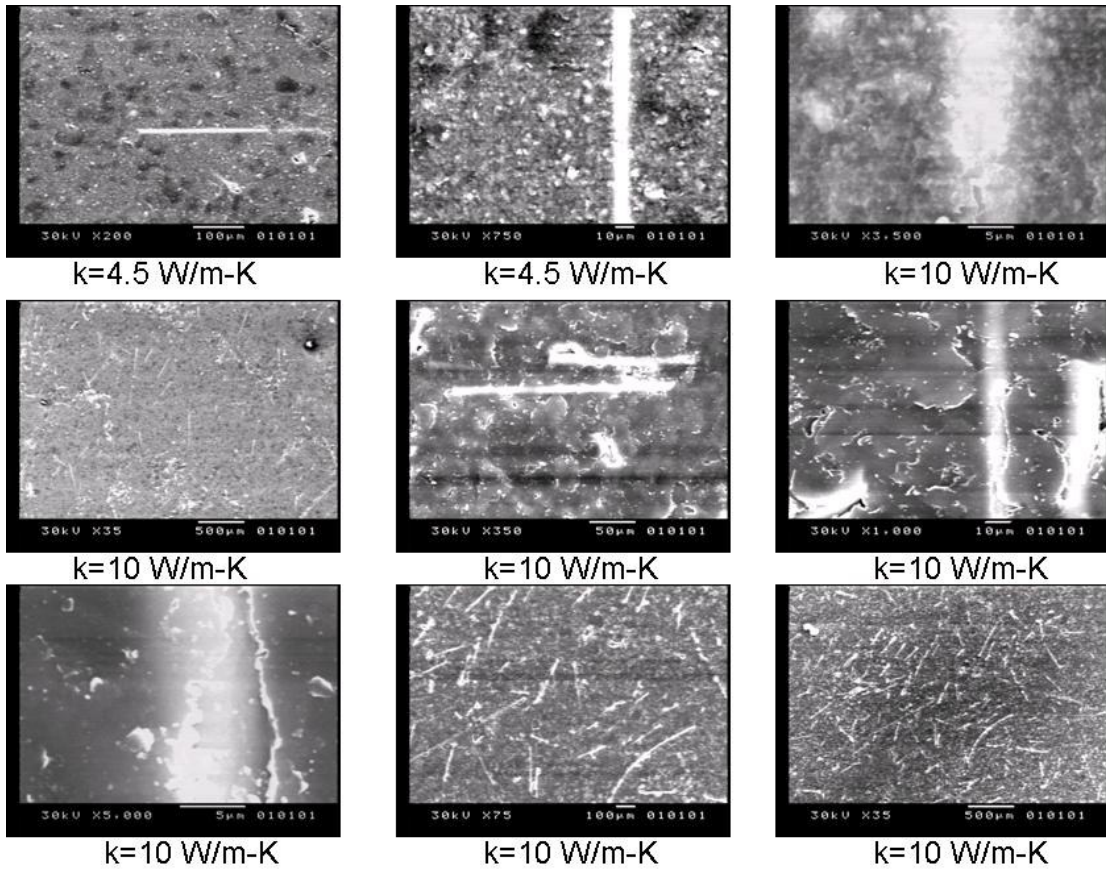SEM Images of PPS Composite Samples Continued...

Figure B3 various thermally conductive PPS composite samples ([10])
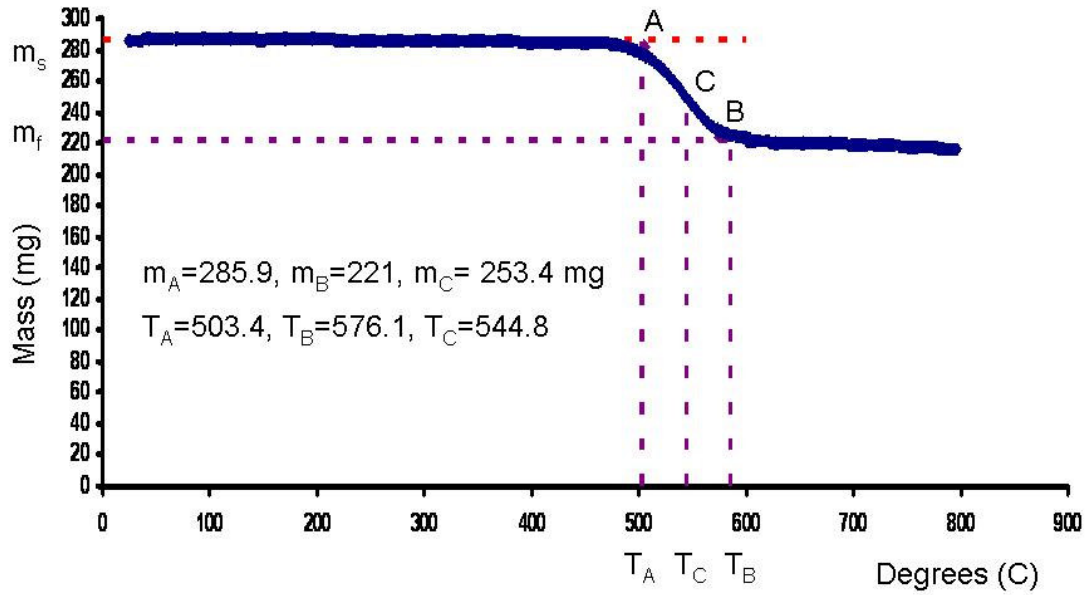
C TGA run plots

m_s

m_f

Mass (mg)

m_A=285.9, m_B=221, m_C= 253.4 mg

T_A=503.4, T_B=576.1, T_C=544.8

T_A T_C T_B

Degrees (C)

Figure C1 TGA run 2 plot for RB020 ([10]) sample using temperature cycle A

Weight (Gm)

m_s=166.304, m_f=132.223 mg

Temperatuer (Celsius)
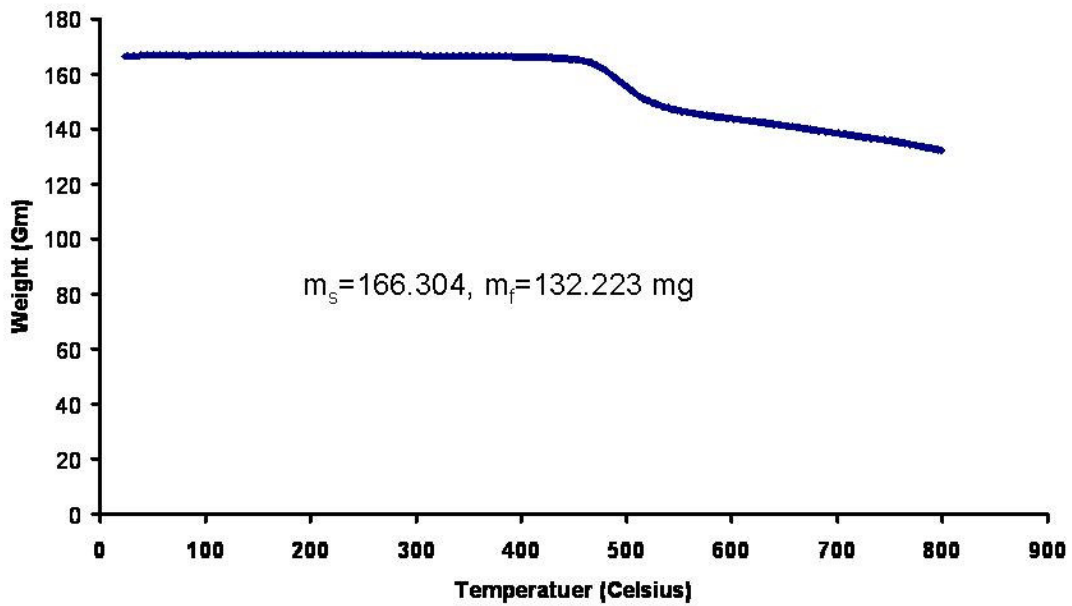
Figure C2 TGA run 1 plot for RB020 ([10]) sample using temperature cycle B

236

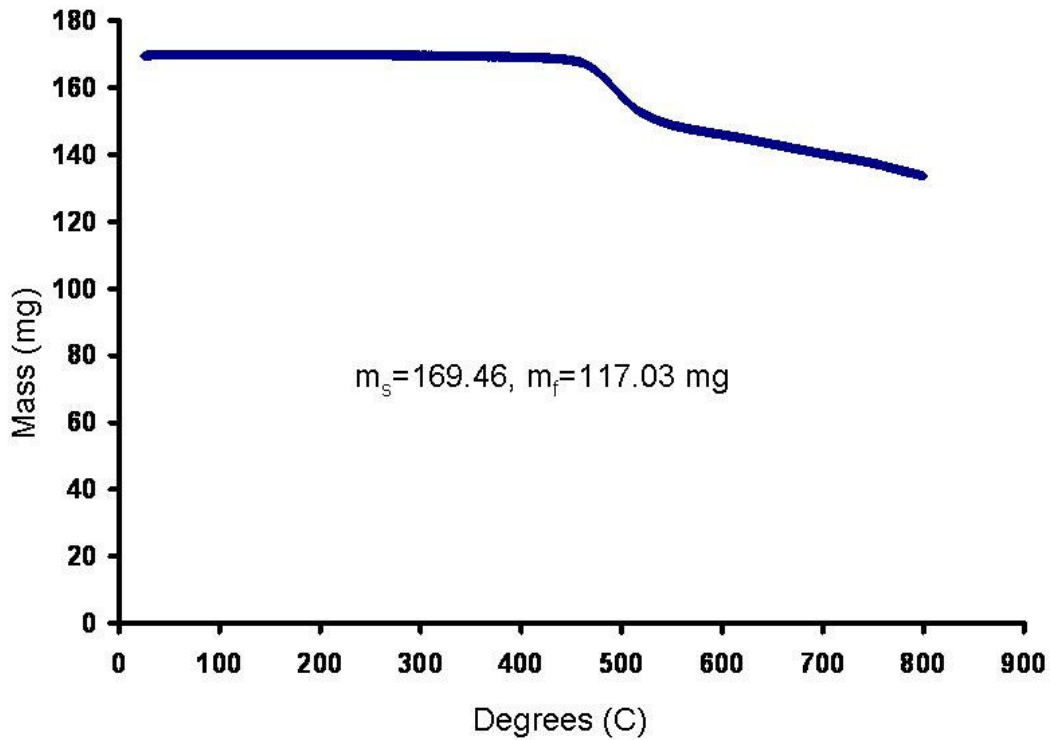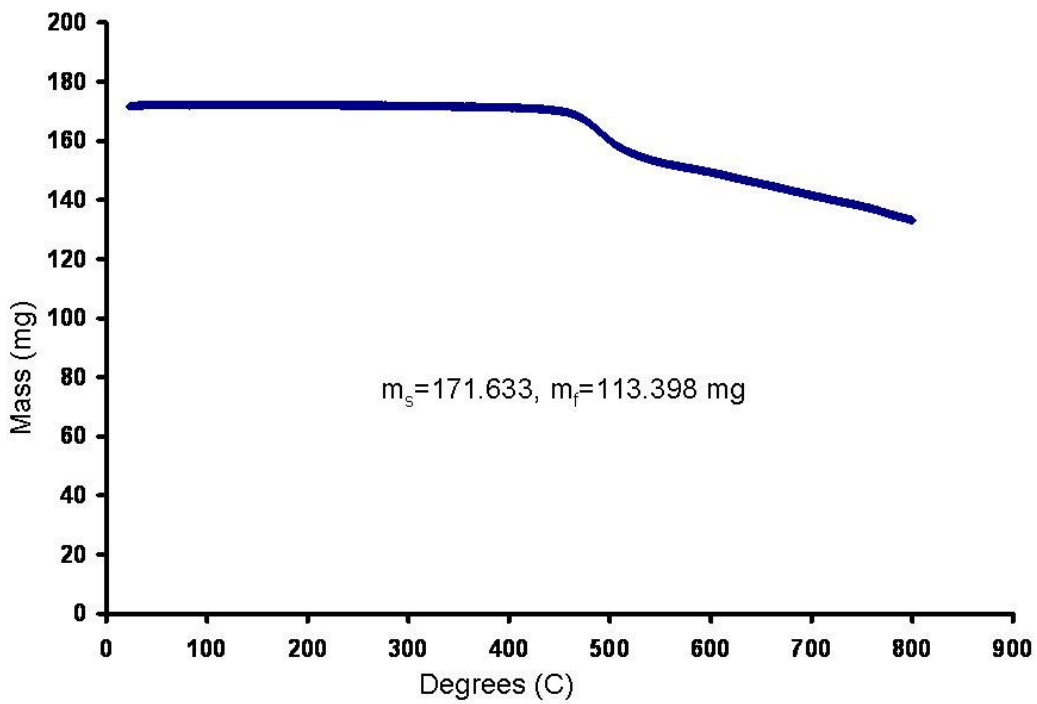Figure C3 TGA run 2 plot for RB020 ([10]) sample using temperature cycle B

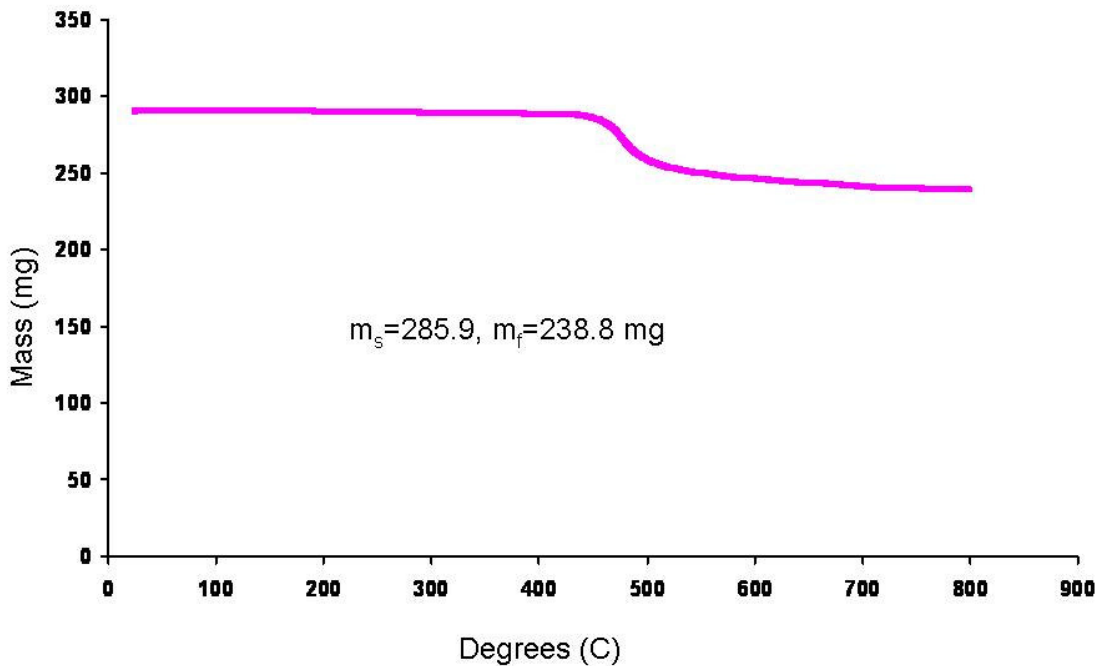Figure C4 TGA run3 plot for RB020 (10)) sample using temperature cycle B

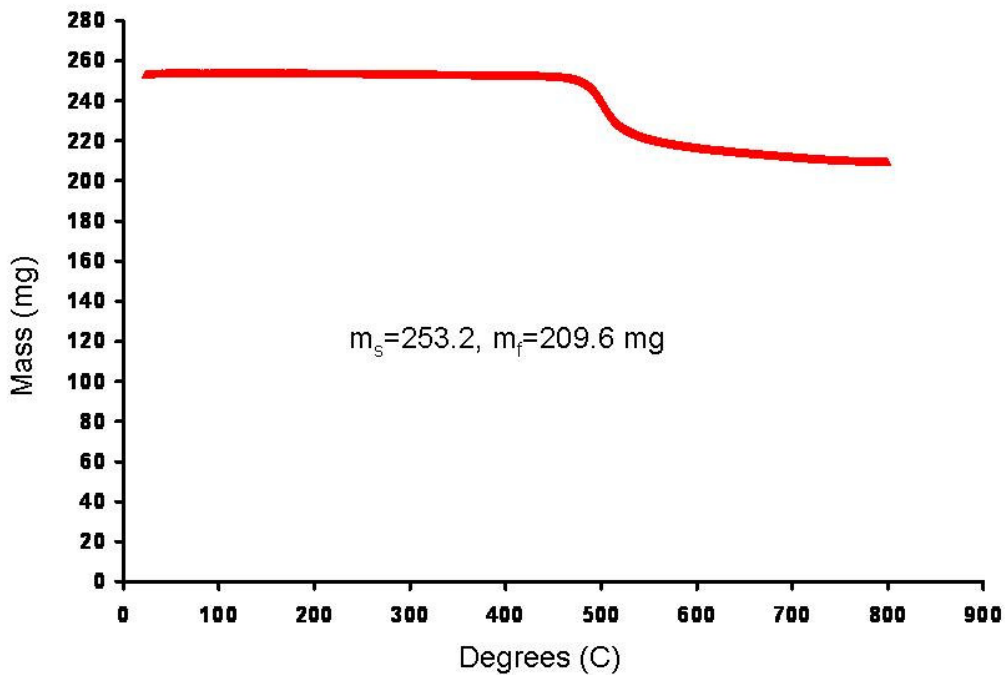Figure C5 TGA run1 plot for E5101 ([10]) sample using temperature cycle B

Figure C6 TGA run2 plot for E5101 ([10]) sample using temperature cycle B

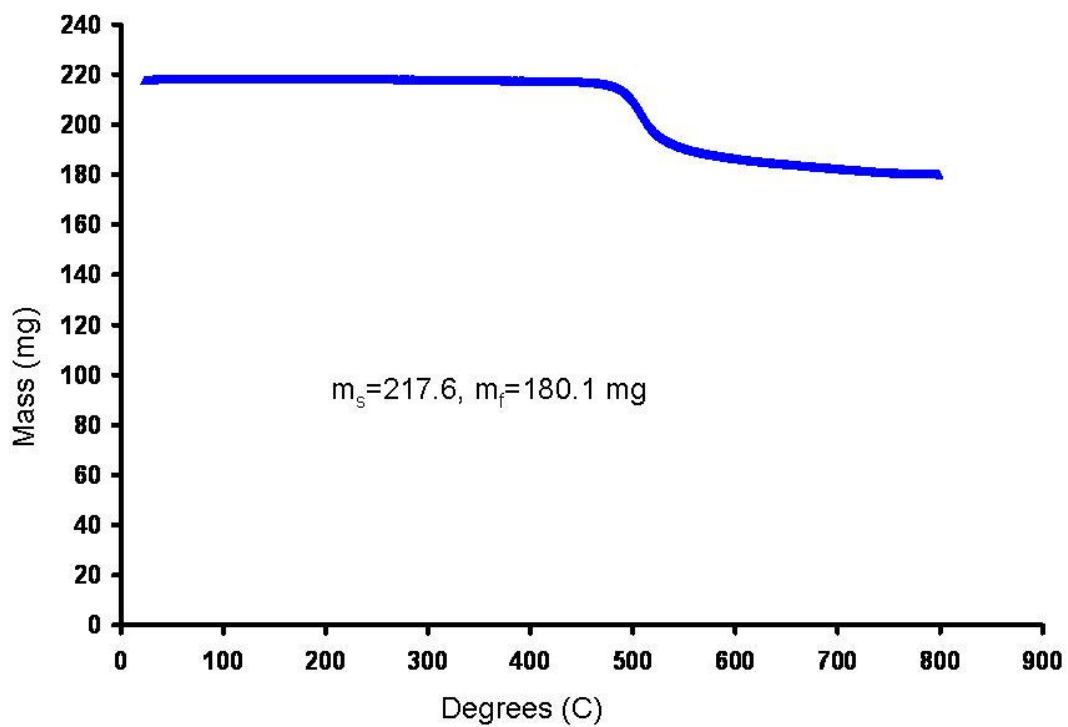m_s=217.6, m_f=180.1 mg

Figure C7 TGA run3 plot for E5101 ([10]) sample using temperature cycle B
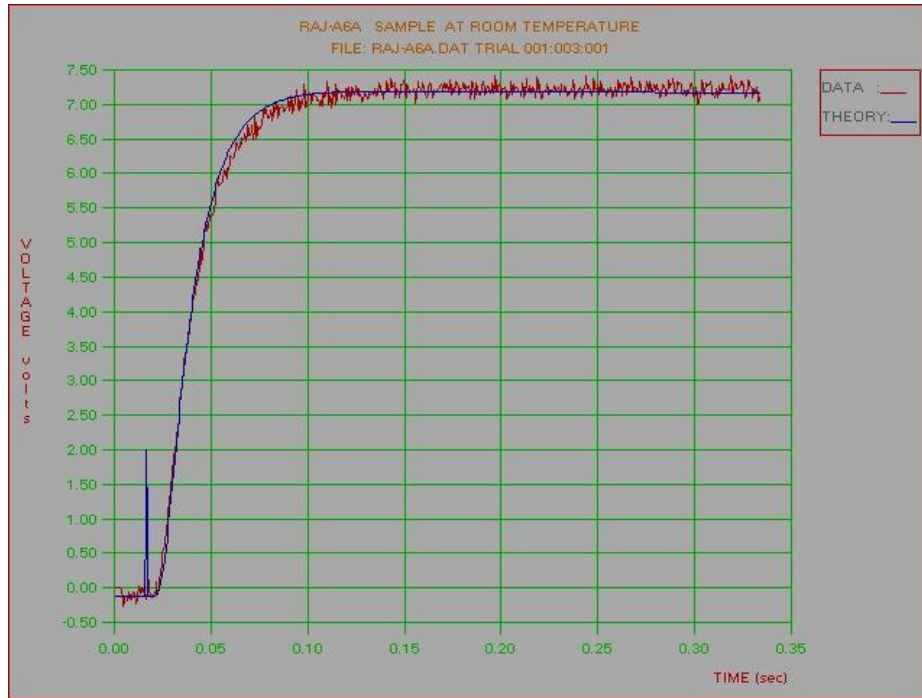
D Laser Flash Plots

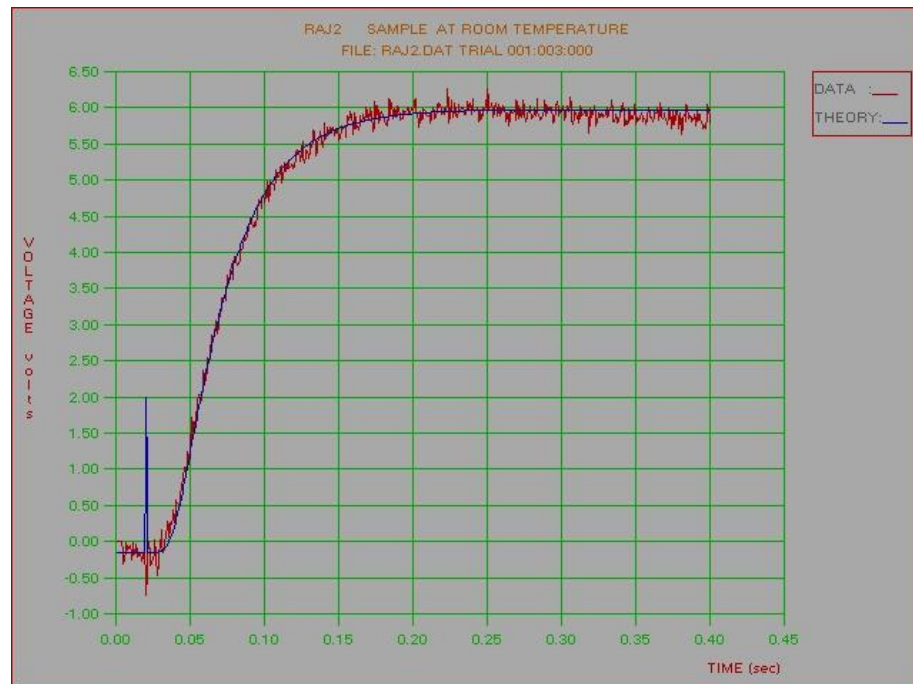Figure D1 Voltage plot for RB020A [10] sample

Figure D2 Voltage plot for E5101B [10] sample

Figure D3 Voltage plot for E5101B [10] sample

Figure D4 Voltage plot for E2-A [10] sample
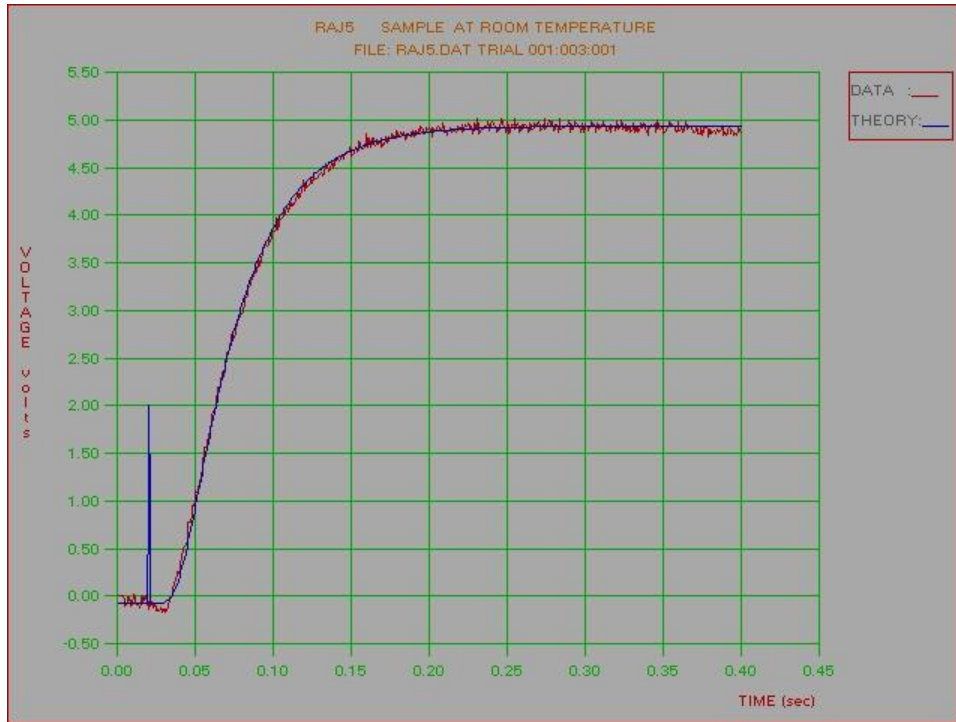
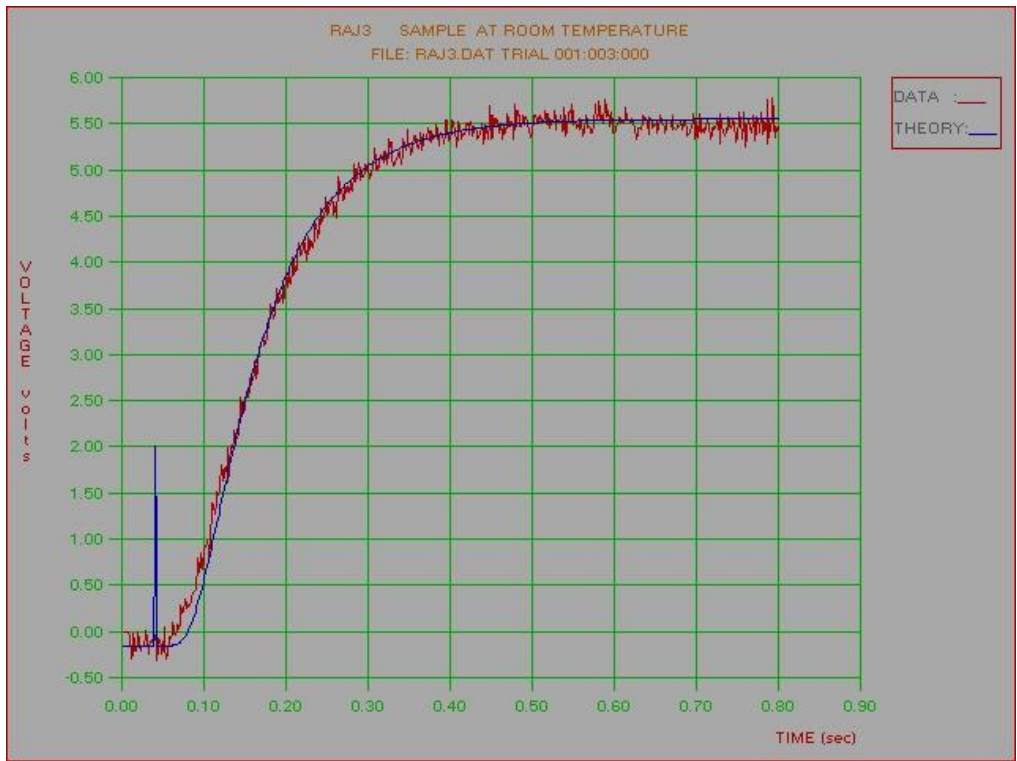Figure D5 Voltage plot for E5101-A2 [10] sample
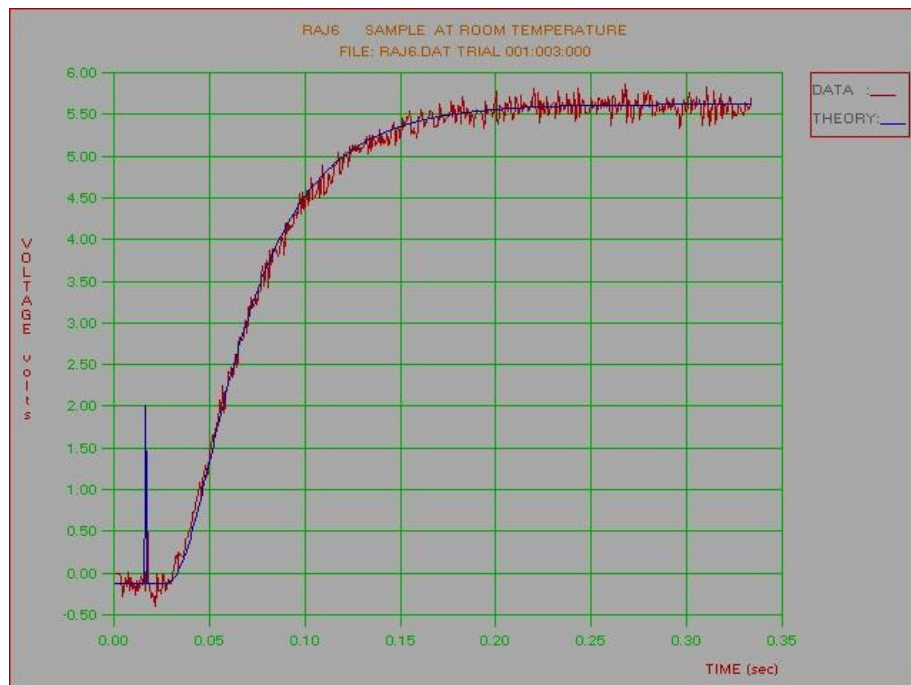
Figure D6 Voltage plot for E5101-B2 [10] sample
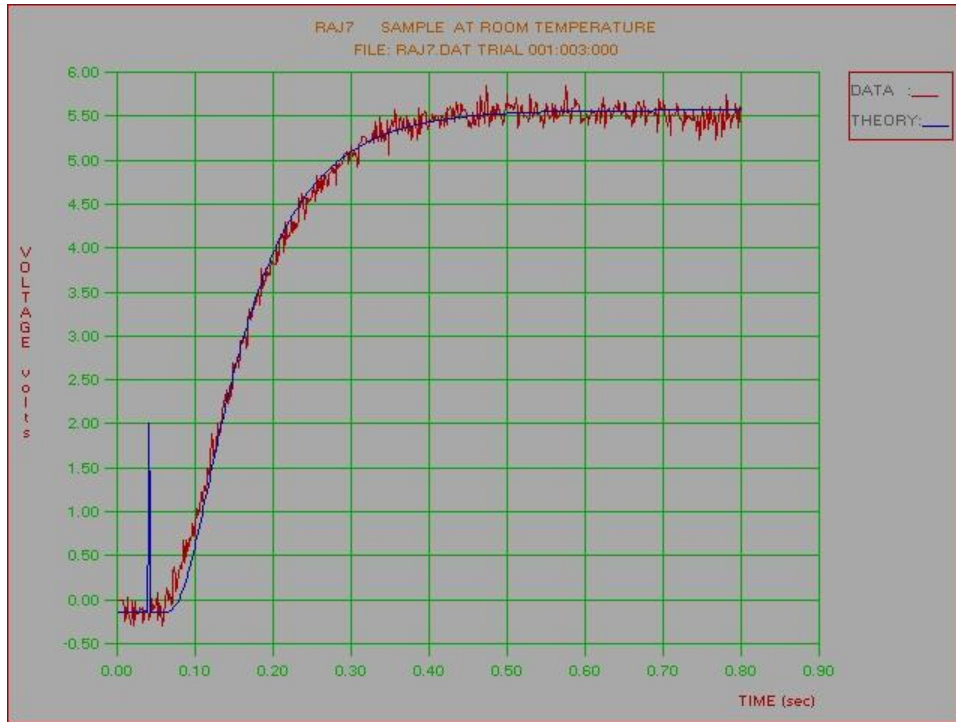
Figure D7 Voltage plot for E2-B [10] sample
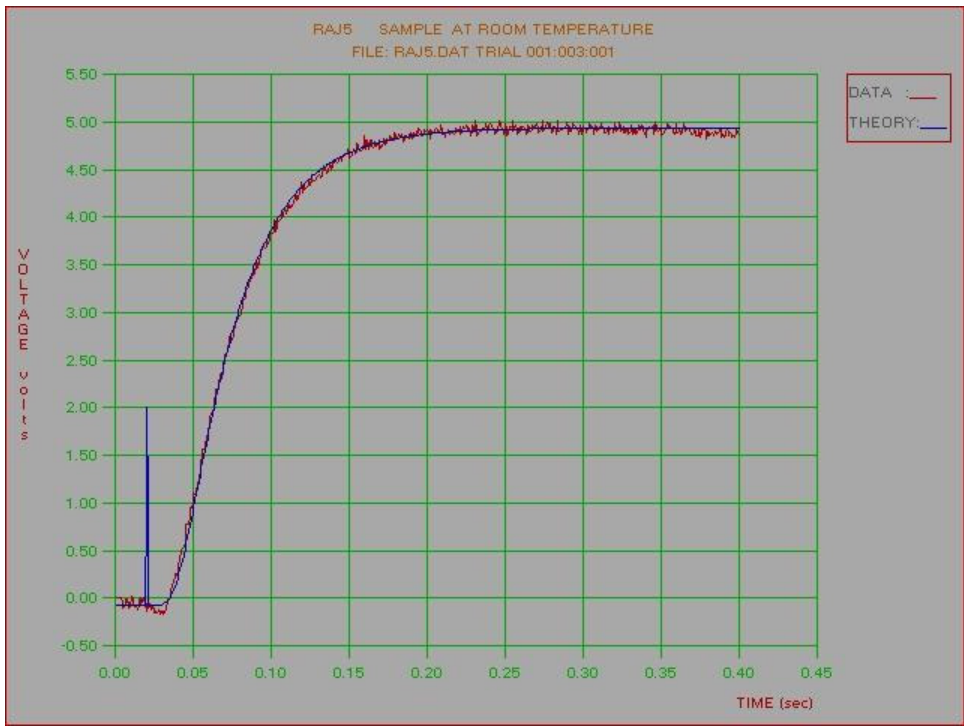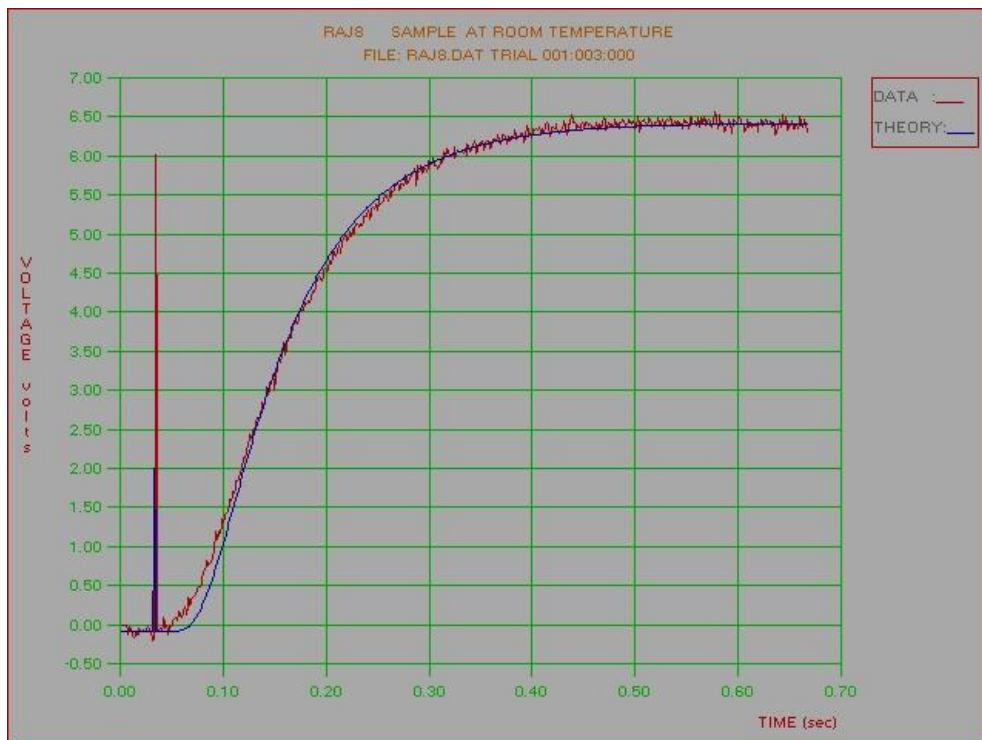

Figure D8 Voltage plot for E2-A2 [10] sample

Figure D9 Voltage plot for E2-B2 [10] sample
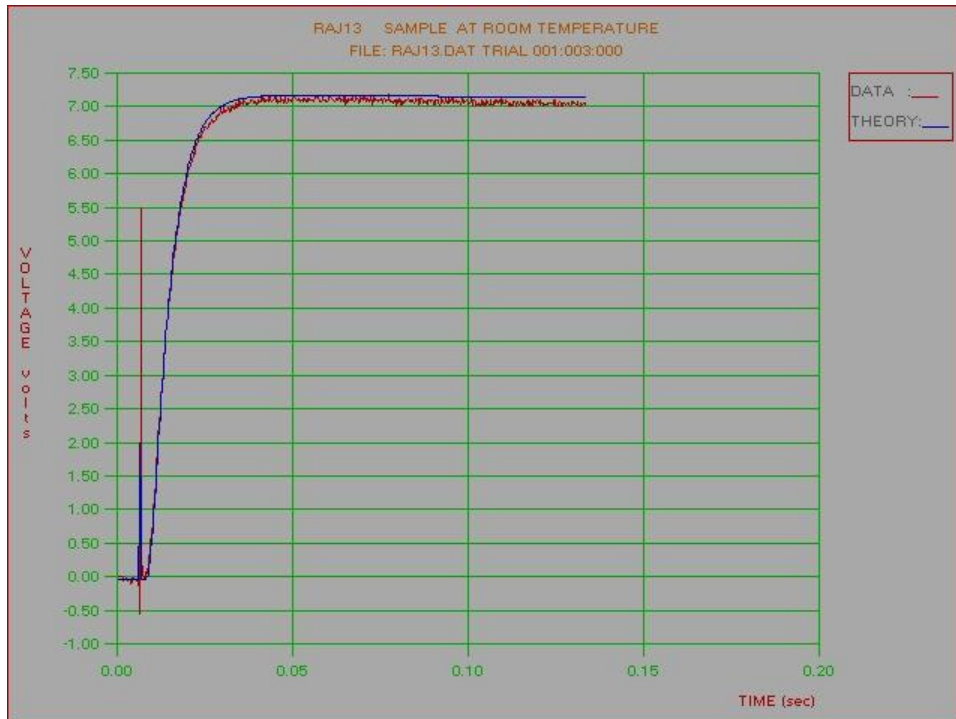
Figure D10 Voltage plot for RB020S axial [10] sample
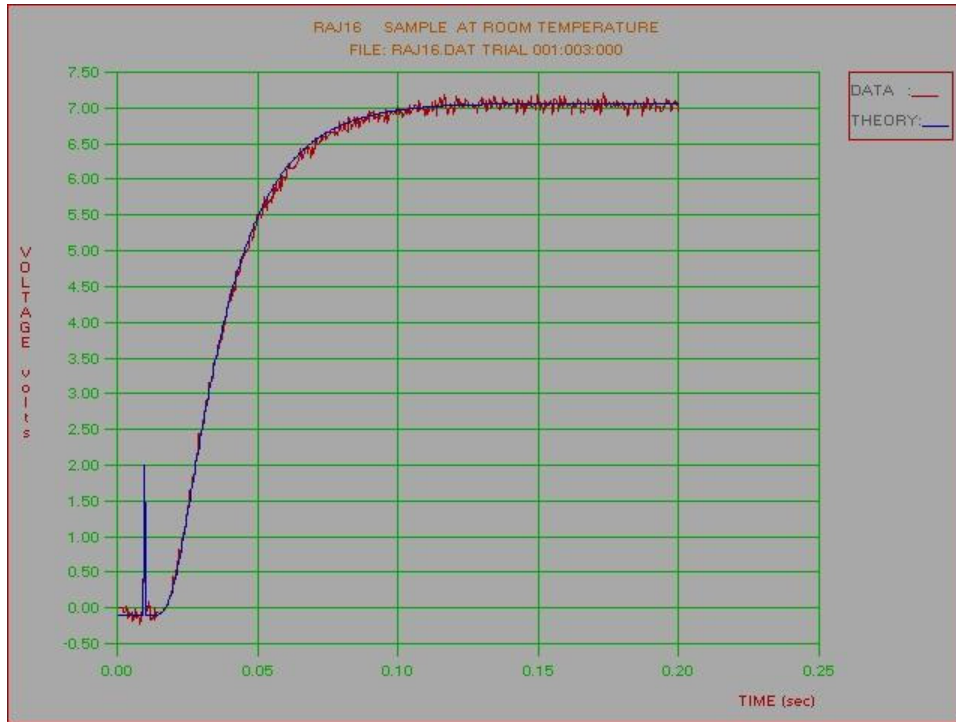
Figure D11 Voltage plot for RB020T inplane [10] sample
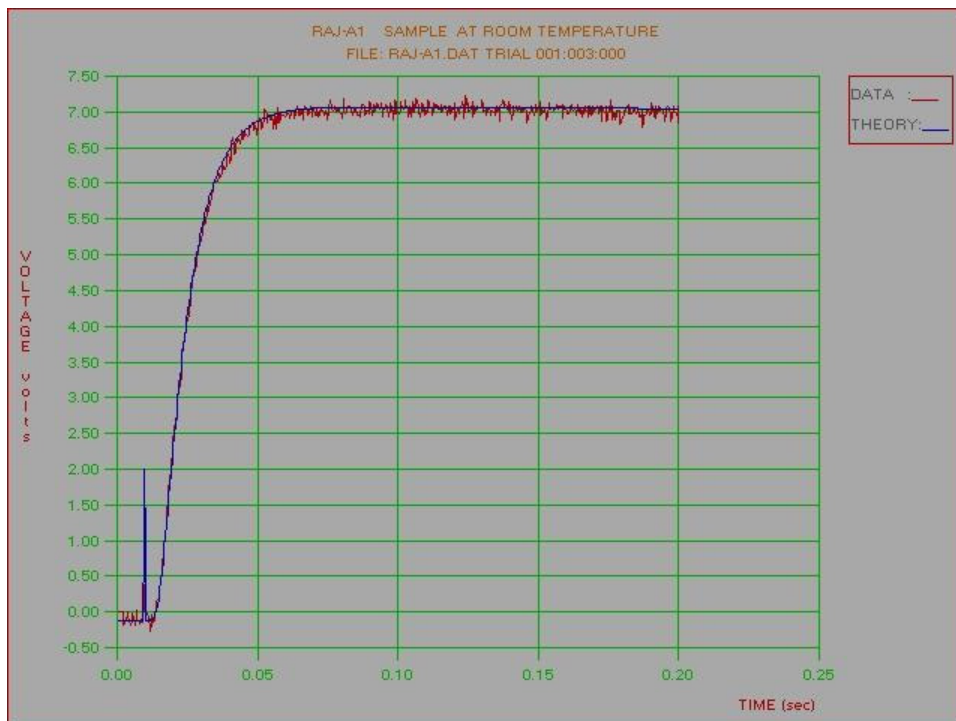
Figure D12 Voltage plot for RB020V inplane [10] sample
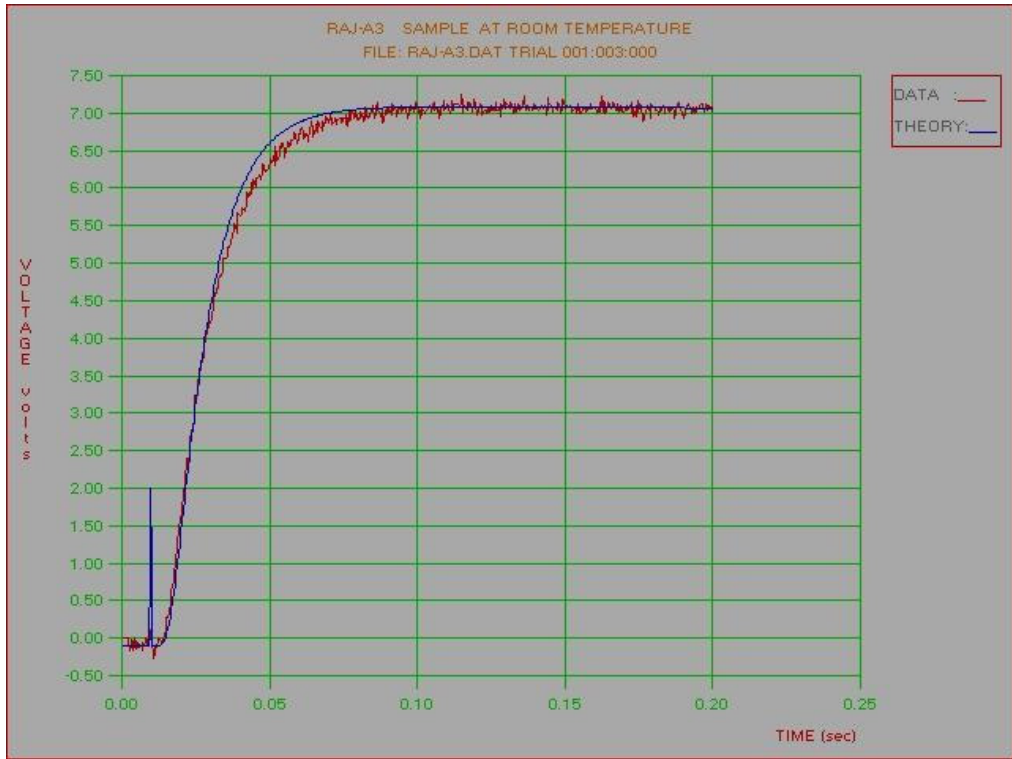
Figure D13 Voltage plot for RB020W axial [10] sample

Figure D14 Voltage plot for RB020A2 inplane [10] sample

E Forced Convection Plate Fin Using MathCAD codes
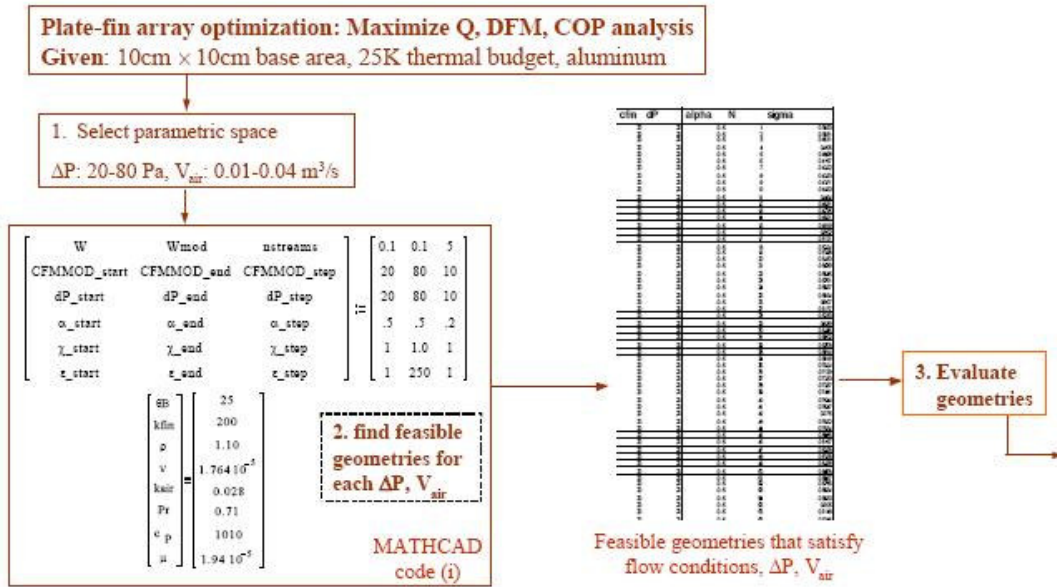
Figure E1 Part I of Description of Heat Sink CAD Tool for Forced Convection Heat Sinks– Use of Mathcad Codes
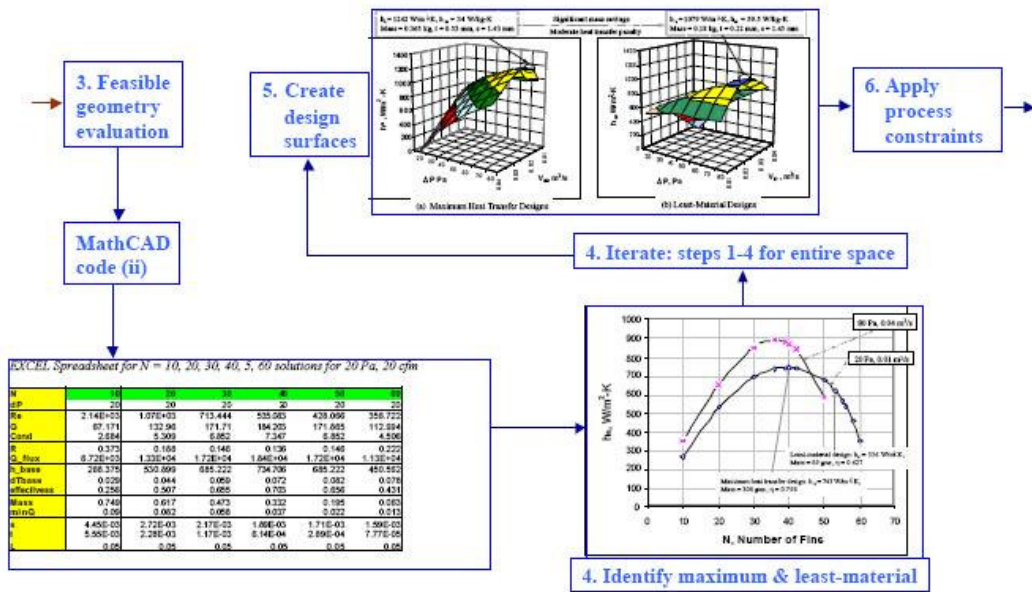
Figure E2 Part II of Description of Heat Sink CAD Tool for Forced Convection Heat Sinks– Use of Mathcad Codes

F Heat Sink Plate/Pin Fin Using EES codes
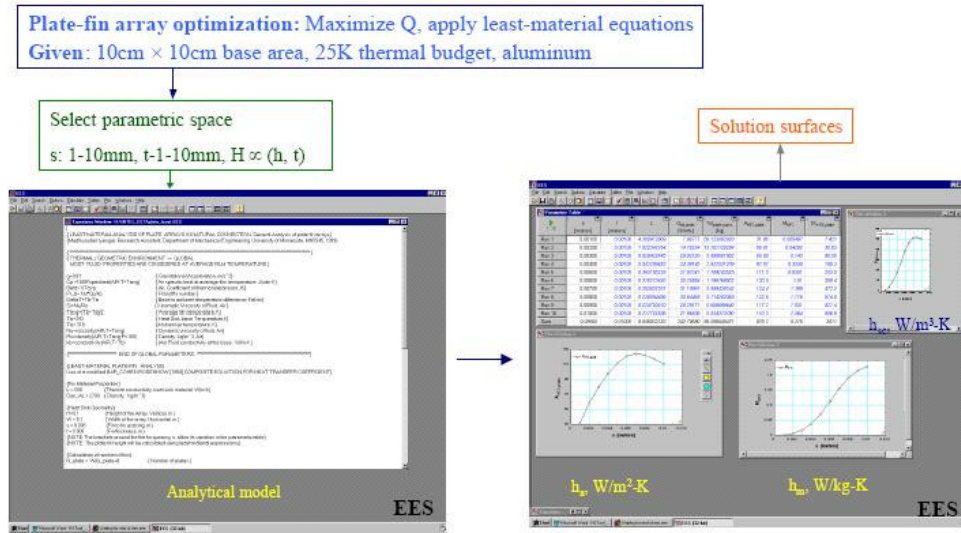
F1 Description of Heat Sink CAD Tool for Natural Convection Heat Sinks– Use of EES Codes

G PPS Composite Fabrication Energy Calculation

Presently the fabrication energy value of 75 MJ/kg approximated for neat PPS resin

is based on the tabulated values [11] obtained for various polymers such as

polypropylene (75 MJ/Kg). This includes the feedstock energy value as well, that is

not the fabrication energy requirement. Therefore it is expected that the approximated

75 MJ/kg for fabrication of PPS neat resin is a conservative number. Similar analysis

as tabulated for fabrication energy requirements for various other polymers will

reveal the actual fabrication energy requirement of the PPS neat resin. The acrylic

fiber required 125 MJ/kg of fabrication energy including 20 MJ/kg of feedstock

energy and therefore it is taken as the carbon fiber fabrication energy requirement.

This results in 115 MJ/kg for 80% by mass of carbon fiber and 20% by mass of PPS

composite.

Bibliography

[1] Computer Industry Almanac Inc. Nearly 600 million computers-in-use in year 2000, Press release; November, 1999.

[2] Spooner, J. G., 2003 a banner year for PC market? CNET news article, August 14th, 2003

[3] US energy requirements for aluminum production. Prepared for the office of industrial technologies (OIT), Department of Energy (DOE), USA, January 2003.

[4] Energy and environmental profile of the US mining industry, Dec 2002, online reports.

[5] Lea, A. C. Low life cycle energy consumption in car and truck radiators: another plus for Copper/Brass, International Copper Organization, USA, online article.

[6] Zweben, C., Emerging high-volume commercial applications for thermally conductive carbon fibers, sixth international business conference on the global outlook for carbon fiber, San Diego, California, USA, November 5 – 7, 2003.

[7] Gary Shives et. al., Comparative thermal performance evaluation of graphite/epoxy fin heat sinks, Proceedings, ITHERM 2004, pp. 410-417.

[8] M. J. Biercuk, M. C. Laguno, M. Radosavljevic, J. K. Hyun, A. T. Johnson, and J. E. Fischer, Carbon nanotube composites for thermal management, Applied Physics Letters, 80, 2002, pp. 2767-2769.

[9] Xuejiao Hu; Linan Jiang; Goodson, K.E, Thermal conductance enhancement of particle-filled thermal interface materials using carbon nanotube inclusions, Thermal and Thermomechanical Phenomena in Electronic Systems, 2004. ITHERM '04. The Ninth Intersociety Conference on 1-4 June 2004 Page(s):63 - 69 Vol.1.

[10] Coolpolymers Inc. Warwick, RI 02886, USA.

[11] Andrady, A., L., Plastics and Environment. John Wiley and Sons New York: 2003 (chapter 3).

[12] D. M. Bigg, Thermally conductive polymer compositions, Polymer Composites, Vol. 7, No. 3, 1986, pp. 125.

[13] D. Hansen, and G. A. Bernier, Thermal conductivity of polyethylene: the effects crystal size, density, and orientation on the thermal conductivity, Polymer Engineering and Science, Vol. 12, No. 3, 1972, pp. 204.

[14] Y. Agari, and T. Uno, Thermal conductivity of polymer filled with carbon materials: effect of conductive particle chains on thermal conductivity, Journal of Applied Polymer Science, Vol. 30, 1985, pp. 2225-2236.

[15] Y. Agari, A. Ueda, and S. Nagai, Thermal conductivities of composites in several types of dispersion systems, Journal of Applied Polymer Science, Vol. 42, 1991, pp. 1655-1669.

[16] R. C. Progelhof, J. L. Throne, and R. R. Ruetsch, Methods of predicting thermal conductivity of composite systems: a review. Reg. Tech. Cond. – Soc. Plast. Eng, 1975, pp. 221-257.

[17] L. E. Nielsen, The thermal and electrical conductivity of two-phase systems, I&EC Fundamentals, Vol. 13, No. 1, 1974, pp. 17-20.

[18] J. R. Fried, Polymer Science and Technology. Prentice Hall, New Jersey, 1995.

[19] GE Engineering Thermoplastic Product Guide: Material Selection, GE Plastics.

[20] L. Piraux, E. Ducarme, and J-P. Issi, Thermal conductivity of oriented polyacetylene films. synthetic metals, 41-43, 1991, pp 129-132.

[21] D. W. Sundstrom and Y. Lee, Thermal conductivity of polymer filled with particulate solids, Journal of Applied Polymer Science, Vol. 16, 1972 pp. 3159-3167.

[22] J-P. Issi, B. Nysten, A. Jonas, A. Demain, L. Piraux, and B. Poulaert, Tailoring the thermal conductivity of organic materials. Thermal conductivity 21, Plenum Press, 1990, pp. 629-646.

[23] Weber, E., Development and modeling of thermally conductive polymer/carbon composites, PhD thesis in chemical engineering at Michigan Technology University, 1999.

[24] S.T. Peters, Handbook of Composites, Published in 1998 by Chapman & Hall, London. ISBN 0412 54020 7, chapter 9, pp. 172.

[25] Zoltek companies Inc., Missouri 63044, USA.
(http://www.zoltek.com/company_information/price_vs_volume.shtml)

[26] Operating manual for Thermotron TG 2121 TGA equipment

[27] Test Method E1461-01, Standard test method for thermal diffusivity of solids by the flash method, American Society for Testing and Materials, Annual Book of ASTM Standards, Vol. 14.02, 2001.

[28] Test Method E1530-99, Standard test method for evaluating the resistance to thermal transmission of thin specimens of materials by the guarded heat flow meter technique, Annual Book of ASTM Standards, Vol. 14.02, 1999.

[29] Test Method E1225-99, Standard test method for thermal conductivity of solids by means of the guarded-comparative-longitudinal heat flow technique, Annual Book of ASTM Standards, Vol. 14.02, 1999.

[30] Test Method D5470-01, Standard test methods for thermal transmission properties of thin thermally conductive solid electrical insulation materials, Annual Book of ASTM Standards, Vol. 10.02, 2001.

[31] Cowan, J., Pulse Method of Measuring Thermal diffusivity at high temperatures, Applied Physics 34, 926 (1963).

[32] Parker, W.J., Jenkins, R.J., Butler, C.P., and Abbott, G.L., A flash method of determining thermal diffusivity, heat capacity, and thermal conductivity, Journal of Applied Physics, 32 (9), 1961, pp. 1679-1684.

[33] Mathis Instruments Inc., NB, Canada.

[34] NETZSCH Instruments, Inc., MA 01803-3305 USA, and Holometrix microflash manual.

[35] R. McCullough, Generalized combining rules for predicting transport properties of composite materials, Composites Science and Technology, Vol. 22, 1985.

[36] H. J. Ott, Thermal conductivity of composite materials, Plastic and rubber processing and applications, Vol. 1, 1981, pp. 9-24.

[37] Matweb.com, automation creations Inc., VA, USA.

[38] BP Amoco Polymers Inc., Thermalgraph high thermal conductivity fibers.

[39] Zhao, Z. and Avedisian, C. T., Enhancing forced air convection heat transfer from an array of parallel plate fins using a heat pipe. Int. J. Heat Mass Transfer 1997; 40(13): 3135-3147.

[40] Garner, S. D., and Toth, J. E., Heat Pipes: A Practical and cost effective method for maximizing heat sink effectiveness, Proceedings of the ASME Advances in Electronic Packaging, USA. 1997; 19(2): 1897-1902.

[41] Ben Achour, M. F., and Bar-Cohen, A., Heat sink optimization for maximum performance and minimum mass, Proceedings of Interpack Conference, USA. 1999; 26(1), pp. 737-744.

[42] Kraus, A. D., Aziz, A., Welty, J., Extended Surface Heat Transfer. John Wiley & Sons New York: 2001.

[43] Bar-Cohen, A., Iyengar, M., and Kraus, A. D., Design of optimum plate-fin natural convective heat sinks. ASME Transactions – Journal of Electronic Packaging 2003; 125(2), pp. 208-216.

[44] Iyengar, M., and Bar-Cohen, A., Least-material optimization of vertical pin-fin, plate-fin, and triangular-fin heat sinks in natural convective heat transfer, Proceedings of the ITHERM conference, USA. 1998, pp. 295-302.

[45] Raj Bahadur, Avram Bar-Cohen, Thermal design and optimization of polymer based pin fin natural convection heat sinks, Components and Packaging Technologies, IEEE Transactions on [see also Components, Packaging and Manufacturing Technology, Part A: Packaging Technologies, IEEE Transactions on] Volume 28, Issue 2, June 2005, pp. 238 - 246.

[46] Iyengar, M., and Bar-Cohen, A., Design for manufacturability of SISE parallel plate forced convection heat sinks. Trans. of the IEEE-CPT 2001; 24(2):150-158.

[47] Shuja, S. Z., Zubair, S. M., and Khan, M. S., Thermo economic design and analysis of constant cross-sectional area fins, Heat and Mass Transfer 1999; 34: 357-364.

[48] Osigo, K., Assessment of overall cooling performance in thermal design of electronics based on thermodynamics. ASME Journal of Heat Transfer 2001; 123: 999-10005.

[49] Lin, W. W. and Lee, D. J., Second law analysis on a flat plate-fin array under cross flow. International Communications in Heat and Mass Transfer 2000; 27(2):179-190.

[50] Culham, J. R., and Muzychka, Y. S., Optimization of plate fin heat sinks using entropy generation minimization. Trans. of the IEEE-CPT 2001; 24(2):159-165.

[51] Bejan, A., Entropy Generation Minimization. CRC Press New York: 1995.

[52] Iyengar, M. and Bar-Cohen, A., Least-energy optimization of SISE forced convection heat sinks. Proceedings of the 8th ITHERM, USA. 2002, pp. 792.

[53] Iyengar, M., and Bar-Cohen, A., Design for manufacturability of SISE parallel plate forced convection heat sinks. Trans. of the IEEE-CPT 2001; 24(2):150-158.

[54] Kern, D. Q., and Kraus, A. D., Extended surface heat transfer. McGraw-Hill New York: 1992.

[55] Sonn, A., and Bar-Cohen, A., Optimum cylindrical pin fin. ASME - Journal of Heat Transfer 1981; 103: 814-815.

[56] Iyengar, M., and Bar-Cohen, A., Least-material optimization of vertical pin-fin, plate-fin, and triangular-fin heat sinks in natural convective heat transfer, Proceedings of the ITHERM conference, USA. 1998, pp. 295-302.

[57] Bar-Cohen, A., and Rohsenow, W., Thermally optimum spacing of vertical, natural convection cooled parallel plates. Journal of Heat Transfer 1984; 106: pp. 116-122.

[58] Elenbaas, W., Heat dissipation of parallel plates by free convection. Physica 1942; 9(1): 665-671.

[59] Bar-Cohen, A., Fin thickness for an optimized natural convection array of rectangular fins, ASME Journal of Heat Transfer 1979;101: 564-566.

[60] Kraus, A.D., Bar-Cohen, A., Design and analysis of heat sinks. John Wiley and Sons NY: 1995 (chapter 10).

[61] Elenbaas, W., Heat dissipation of parallel plates by free convection. Physica 1942; 9(1): 665-671.

[62] Aihara, T., Maruyama et. al., & Kobayakawa et. al., Free convective/radiative heat transfer from pin-fin arrays with a vertical base plate. Int. J. of Heat and Mass Transfer 1990;33(6):1223-1232.

[63] Incropera, F. P. and DeWitt, W. P., Fundamentals of Heat and Mass Transfer. John Wiley New York: 1990 (chapter 9).

[64] Bar-Cohen, A., Iyengar, M., and Benjaafar, S., Design for manufacturability of natural convection cooled heat sinks. International Journal of Transport Phenomena 2002; 4: 43-57.

[65] Bar-Cohen, A., Bahadur, R., M., Iyengar, Least energy optimization of air cooled heat sinks for sustainability - theory, geometry and material selection, Proceedings of the ASME – ZSIS International Thermal Science Seminar II, Bled, Slovenia, June 13 – 16, 2004, pp. 33-53 (submitted for publication in the Journal Energy, November 2004).

[66] Sparrow, E., and Vemuri, S., 1986, Orientation effects on natural convection/radiation heat transfer from pin-fin arrays, Int. J. Heat Mass Transfer, vol.29, No.3, pp. 359-368

[67] LCA (Life Cycle Assessment) committee report, summary of inventory data, Japan Aluminum Association, July 1999.

[68] Khan, W. A., Culham, J. R., Yovanovich, M. M, Optimization of pin-fin heat Ssnks using entropy generation minimization, Components and Packaging Technologies, IEEE Transactions on [see also Components, Packaging and Manufacturing Technology, Part A: Packaging Technologies, IEEE Transactions on] Volume 28, Issue 2, June 2005, pp. 247- 254.

[69] Cool innovations Inc. – www.coolinnovations.com

[70] Gardner, K. A., Efficiency of extended surfaces, Trans. ASME, vol. 67, 1945, pp. 621-631.

[71] Harper, D. R., and Brown, W. B., Mathematical equations for heat conduction in the fins in air cooled engines, NACA technical report, p. 188, 1922.

[72] Aparecido, J. B., Cotta, R. M., Improved one dimensional fin solutions, Heat transfer engineering, vol. 11, 1, 1990, pp. 49-59.

[73] Levitsky, M. J., The criterion for the validity of the fin approximation, Int. J. Heat M. Transfer, 15, 1960, pp. 1960-63.

[74] Ozisik, M., N., Heat conduction, 2nd ed. Wiley, New York, (1993).

[75] Poulikakos, D., Conduction heat transfer, Prentice Hall, Englewood Cliffs, NJ, 1994.

[76] Gebhart, B., Heat Conduction and mass diffusion, McGraw-Hill, New York, 1993.

[77] Irey, R.K., Error in one dimensional fin solution, J. Heat Transfer, 90, 1968, pp. 175-176.

[78] Lau, W., and Tan, C. W., Errors in one dimensional heat transfer analysis in straight and annular fins, J. Heat Transfer, 95, November 1973, pp. 549-551.

[79] Mikhailov, M.D., and Ozisik, M.N., Unified analysis and solutions of heat and mass diffusion, John Wiley, 1984.

[80] Aziz, A., and Nguyen, H., Two dimensional performance of conducting-radiating fins of different profile shapes, Waerme and Stoffuebertrag, 28, 1993, pp. 481.

[81] Davidson, J.H., et al., Are plastic heat exchangers feasible for solar water heaters? Part I: A review of codes and standards and commercial products. in 1999 ASME International Solar Energy Conference. 1999. Maui, Hawaii.

251

[82] Liu, W., et al., Thermal and economic analysis of plastic heat exchangers for solar heating in solar 99, the 1999 American Solar Energy Conference. 1999, Portland, OR.

[83] Raj Bahadur and Avram Bar-Cohen, Orthotropic thermal conductivity effect on cylindrical pin fin heat transfer, 2005 ASME/Pacific rim technical conference, IPACK2005-73181, July 17-22, 2005, USA.

[84] V.T. Morgan, The overall convective heat transfer from smooth circular cylinders, in: T.F. Irvine, Jr., J.P. Hartnett (Eds.), Advances in Heat Transfer, vol. 11, Academic Press, New York, pp. 199–264.

[85] Electronics cooling magazine technical resources, http://www.electronics-cooling.com/html/2001_may_techdata.html

[86]RS Components Ltd., NN17 9RS, UK, www.rsww.com

[87] Watlow Electric Manufacturing Company, Missouri, USA 63146, www.watlow.com

[88] Raj Bahadur, Bahgat Sammakia, Frank Andros, Thermal management of a micro display engine assembly, Inter Society Conference on Thermal Phenomena (ITHERM 2004), 1-4 June 2004, pp. 381-388, vol. 1.

[89] Bruggeman, D.A.G., Ann Physics. 24, 636 (1935).

[90] Kerner, E.H., Proc. Phys. Soc. B69, 802, 808 (1956).

[91] Tsao, G.T., Ind. Eng. Chem. 53, 395 (1961).

[92] Hamilton, R.L., Crosser, O.K., Ind. Eng. Chem. Fundam. 1, 187 (1962).

[93] Springer, G.S., Tsai, S.W., J. Compos. Mater. 1, 166 (1967).

[94] Sundstrom, D., Chen, S., J. Compos. Mater., 1, 166 (1967).

[95] Behrens, E.J. Compos. Mater. 2, 2 (1968).

[96] Cheng, S.C., Vachon, R.I., Intl. J. Heat Mass Transfer 12, 249 (1969).

[97] Zinsmeister, G.E., Purohit, K.S., J. Compos. Mater. 4, 278 (1970).

[98].Ashton, J.E., Halpin, J.C., Petit, P.H., "Primer on Composite Analysis," Chapter 5, p. 72, Technomic Stamford, Conn., 1969.

[99] Agari, Y., Uno, T., "Estimation on thermal conductivities of filled polymers," J. Appl. Polym. Sci., 32, p. 5705-5712 (1986).

[100] Agari, Y., Ueda, A., Nagai, S., " Thermal conductivity of polymer composite," J. Appl. Polym. Sci., 49, p.1625-1634 (1993).

[101] Agari, Y., Tanaka, M., Nagai, S., " Thermal conductivity of a polymer composite filled with mixtures of particles," J. Appl. Polym. Sci., 34, 1429-1437 (1987).

[102] Shoji Okamoto, Hatsuo Ishida, " A new theoretical equation for thermal conductivity of two phase systems," J. Appl. Polym. Sci., 72, pp-1689-1697 (1999).

[103] X. Lu, G. Xu, "Thermally conductive polymer composites for electronic packaging," J. Appl. Polym. Sci., 65, pp-2733-2738 (1997).

[104] Wong, C.P., Bollampally, R.S., "Thermal conductivity, elastic modulus, and coefficient of thermal expansion of polymer composites filled with ceramic particles for electronic packaging," J. Appl. Polym. Sci., 74, pp-3396-3403 (1999).

[105] Amit Devpura, Phelan, P.E., Prasher, R.S., "Percolation theory applied to the analysis of thermal interface materials in flip chip technology,", Inter Society Conference on Thermal Phenomenon, pp-21-28 (2000).

[106] NSF-61, NSF Listings: Drinking Water Additives. 1997, National Sanitary Foundation International, Michigan.

[107] NSF-14, NSF Listings: Plumbing System Components. 1998, National Sanitary Foundation International, Michigan.

[108] Mettler-Toledo Inc., OH, USA.

[109] Mitutoyo America corporation, IL, USA

[110] Holahan, M. F., Kang S. S., Bar-Cohen, A. A Flow stream based analytical model for design of parallel plate heat sinks. Proceedings of the 31st ASME National Heat Transfer Conference, USA. 1996; 329(7): 63-71.

[111] Kakac, S., Shah, R. K., Aung, W. Handbook of Single-Phase Convective Heat Transfer. 2nd Ed. Wiley NY:1987 (p. 3-42).

[112] Kays and London. Compact heat exchangers. 3rd edition, 1997.

[113] Iwasaki, H., Sasaki, T., and Ishizuka, M. Cooling performance of plate fins for multichip modules. Trans. of the IEEE-CPT part A 1995; 18(3): 592-595.

[114] GB Electrical, Milwaukee, WI, USA

[115] Deborah D. L. Chung, Carbon fiber composites, 1994

[116] Khalid Lafdi and Maurice A. Wright, Carbon fiber chapter in the Handbook of Composites. Edited by S.T. Peters. Published in 1998 by Chapman & Hall, London. ISBN 0 412 540207

[117] William Gary Solbrekken, Kazuaki Yazawa, Bar-Cohen, "Experimental modeling of the passive cooling limit of notebook computers," 2002 IEEE pp15-21.